UNIVERSITÉ DE MONTRÉAL

DÉVELOPPEMENT ET VALIDATION EXPÉRIMENTALE DE FACTEURS DE RÉPONSE THERMIQUE POUR CHAMPS DE PUITS GÉOTHERMIQUES

MASSIMO CIMMINO

DÉPARTEMENT DE GÉNIE MÉCANIQUE

ÉCOLE POLYTECHNIQUE DE MONTRÉAL

THÈSE PRÉSENTÉE EN VUE DE L'OBTENTION

DU DIPLÔME DE PHILOSOPHIAE DOCTOR (Ph.D.)

(GÉNIE MÉCANIQUE)

DÉCEMBRE 2014

UNIVERSITÉ DE MONTRÉAL

ÉCOLE POLYTECHNIQUE DE MONTRÉAL

Cette thèse intitulée:

DÉVELOPPEMENT ET VALIDATION EXPÉRIMENTALE DE FACTEURS DE RÉPONSE THERMIQUE POUR CHAMPS DE PUITS GÉOTHERMIQUES

présentée par : CIMMINO Massimo

en vue de l'obtention du diplôme de : Philosophiae Doctor

a été dûment accepté par le jury d'examen constitué de :

M. MARCOTTE Denis, Ph.D., président

M. BERNIER Michel, Ph.D., membre et directeur de recherche

M. ROBERT Étienne, Doctorat Sc., membre

M. CLAESSON Johan, Ph.D., membre

REMERCIEMENTS

Ce projet de thèse fut une tâche colossale qui aurait certainement été impossible à accomplir sans l'aide et le support des personnes que j'ai côtoyées durant mes années au doctorat.

Pour débuter, je me dois d'exprimer ma reconnaissance envers mon directeur de recherche, le professeur *Michel Bernier*. Grâce à lui, mon projet de thèse a été stimulant, enrichissant et rempli de défis. Ses précieux conseils me suivront tout au long de ma carrière.

J'ai beaucoup apprécié la compagnie des étudiants du groupe Bâtiment et Efficacité Énergétique du département de génie mécanique et le plaisir que j'ai eu lors de nos discussions, sérieuses ou moins sérieuses: mes collègues au doctorat, *Ali*, *Amin*, *Benoît*, *Katherine* et *Parham*; les étudiants du C-315, *Arny*, *Bruno*, *Nicolas*, *Patricia*, *Yannick* et *Vivien*; et tous les autres.

Je souhaiterais souligner le support des professeurs *B.R. Baliga*, *M. Kummert*, *M. Laforest*, *P. Pasquier* et *A. Ross*. J'ai énormément appris de chacun d'eux.

Le banc d'essai expérimental a été réalisé grâce à la collaboration de *Thierry Lafrance* (Mëkanic) et à l'assistance technique de *Philippe Massé*.

J'aimerais remercier les professeurs *J. Claesson*, *D. Marcotte* et *É. Robert* d'avoir accepté d'être membres du jury.

Le projet a été rendu possible grâce au financement du *Fonds de recherche du Québec - Nature et technologies (FRQNT)*, du *Conseil de recherches en sciences naturelles et en génie du Canada (CRSNG)*, du *Réseau de recherche stratégique du CRSNG sur les bâtiments intelligents à consommation énergétique nette zéro (SNEBRN)*, de *l'American Society of Heating, Refrigerating and Air-Conditioning Engineers (ASHRAE)*, de la *Coalition canadienne de l'énergie géothermique (CCÉG)*, de *CanmetÉnergie Varennes* et d'*Électricité de France (EDF)*.

À tous un grand merci,

Massimo CIMMINO

Montréal, Décembre 2014

RÉSUMÉ

Le design et la simulation des systèmes géothermiques à puits verticaux reposent sur une modélisation précise du transfert de chaleur entre le fluide caloporteur circulant dans les puits et le sol. Les facteurs de réponse thermique, ou g-functions, sont couramment utilisés afin de prédire la variation de température à la paroi des puits suite à l'extraction ou à l'injection de chaleur dans le sol.

Cette thèse présente un modèle utilisant la solution analytique de la source ligne finie afin de calculer les g-functions avec une exactitude comparable et une efficacité supérieure aux modèles numériques relevés dans la littérature. Les puits sont divisés en segments et une solution étendue de la source ligne finie est présentée afin d'évaluer la variation de température à la paroi des segments de puits suite à l'extraction de chaleur à chacun des segments. Le modèle tient compte de l'interaction thermique entre les puits géothermiques en imposant une condition de température uniforme à la paroi des puits, égale pour tous les puits. Un système d'équations est construit à partir des superpositions spatiale et temporelle dans le domaine de Laplace afin de considérer la variation temporelle des taux d'extraction de chaleur de tous les segments de puits. La solution du système d'équations donne la g-function du champ de puits. Le modèle est comparé à des g-functions obtenues à partir d'un modèle numérique.

Le modèle analytique est utilisé dans une application pratique afin d'étudier l'effet de la position et du nombre de puits dans un champ de puits géothermiques sur la longueur totale requise. Des champs de puits sont dimensionnés pour deux scénarios de charges au sol en faisant varier la position et le nombre de puits dans les champs. L'analyse montre que la position des puits dans les champs a peu d'effet (moins de 1%) sur la longueur totale requise. En retirant des puits, la longueur totale requise a pu être réduite de 2%.

La g-function d'un puits géothermique miniature de 400 mm de longueur est obtenue expérimentalement à partir d’un montage conçu et fabriqué pour la présente étude. La température à la paroi du puits est mesurée à partir d'une série de 22 thermocouples. Le puits est inséré au centre d'un réservoir de sable dont les propriétés thermiques sont connues. Une puissance thermique constante est injectée dans le puits et la g-function est évaluée à partir de cette puissance et des mesures de température à la paroi du puits. La différence entre la g-function expérimentale et celle obtenue avec le modèle analytique est de 4.7% lorsque l’état

permanent est atteint soit après près une semaine d’injection de chaleur. La g-function théorique est à l'intérieur de l'intervalle d'incertitude sur l'ensemble de l'essai ce qui permet d’affirmer la validité du modèle analytique.

ABSTRACT

The design and simulation of geothermal systems coupled with vertical boreholes relies on the precise modelling of the heat transfer between the heat carrier fluid circulating through the boreholes and the ground. Thermal response factors, or g-functions, are commonly used for the prediction of the borehole wall temperature variation due to the extraction or the injection of heat into the ground.

This thesis presents a model based on the finite line source analytical solution for the calculation of g-functions with an accuracy similar to and a greater efficiency than numerical models available in literature. The boreholes are divided into segments and an extended finite line source solution is presented to evaluate the temperature variation at the wall of the borehole segments due to the extraction of heat at all segments. The model accounts for thermal interaction among boreholes by imposing a uniform borehole wall temperature equal for all boreholes. A system of equations is built from the spatial superposition and the temporal superposition in the Laplace domain to consider the temporal variation of the heat extraction rate at each of the borehole segments. The solution to the system of equations gives the g-function of the bore field. The model is compared against a numerical model.

The analytical model is used in a practical application to study the effect of the position and number of boreholes in a bore field on the required length of the boreholes. Bore fields are sized for two ground load scenarios and the number and position of boreholes in the fields are varied. Results show that the position of boreholes has only a small effect (less than 1%) on the total required borehole length. A reduction of 2% on the total required borehole length was obtained by removing boreholes from the bore fields.

The g-function of a small-scale 400 mm long geothermal borehole is determined experimentally using an apparatus designed and built for the present study. The borehole wall temperature is obtained from the temperature measurement of 22 thermocouples welded to the borehole surface. The borehole is installed at the center of a sand tank with known thermal properties. A constant thermal power is injected into the borehole. The g-function is evaluated from the measured power injection and borehole wall temperature measurements. The difference between the experimental g-function and the g-function calculated with the analytical model is 4.7% at steady-state after

one week of heat injection. The theoretical g-function is within the uncertainty bounds throughout the test thus validating the analytical model.

TABLE DES MATIÈRES

LISTE DES TABLEAUX

LISTE DES FIGURES

LISTE DES ANNEXES

INTRODUCTION

Les systèmes de pompes à chaleur reliées à des champs de puits géothermiques verticaux sont couramment utilisés en raison de leur haute performance énergétique. Une vue schématique d'un tel système géothermique est montrée à la Figure 0-1. Un système géothermique comporte trois éléments : le champ de puits géothermiques, la pompe à chaleur (PAC) et le bâtiment.

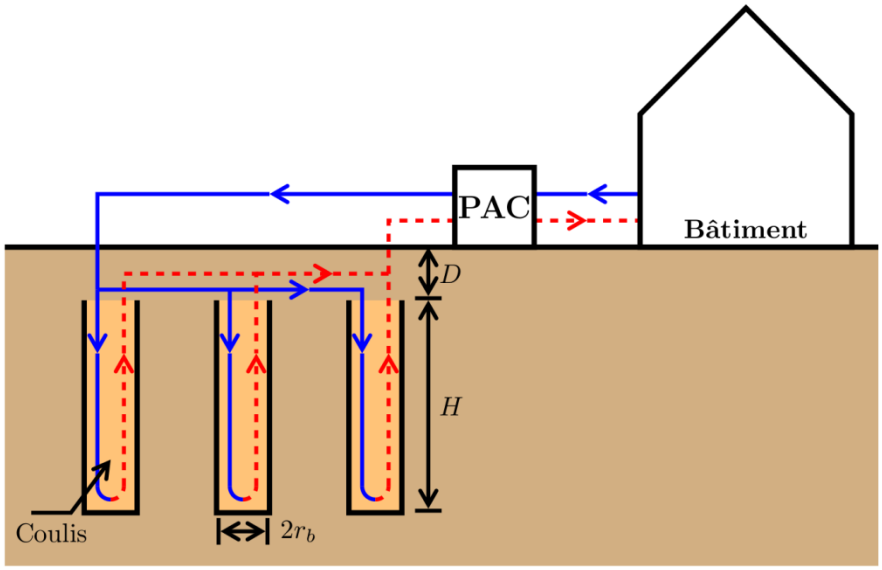

Figure 0-1: Système géothermique à puits verticaux

Les puits géothermiques sont forés jusqu'à une profondeur H variant généralement entre 15 m et 180 m (ASHRAE, 2011), dépendamment de l'application. Après l'insertion de la boucle en U de tuyauterie, les puits sont remplis d'un coulis afin de protéger l'aquifère et d'améliorer le transfert thermique. Un fluide caloporteur, typiquement un mélange d'eau et d'antigel, circule à travers le réseau de puits reliés à la PAC. Lors de l'utilisation du système géothermique pour le chauffage d'un bâtiment, le fluide caloporteur circule dans le champ de puits à une température plus basse que la température du sol. En échangeant de la chaleur avec le sol, le fluide caloporteur sort du champ de puits à une température plus élevée et la chaleur ainsi extraite du sol est transférée au bâtiment par la PAC. À l'inverse, lors de l'utilisation du système géothermique pour la climatisation du bâtiment, la PAC extrait la chaleur du bâtiment et la transfère au fluide caloporteur circulant dans le champ de puits à une température plus élevée que celle du sol.

La conception d'un système géothermique à puits verticaux consiste à évaluer le nombre et la longueur des puits qui sont nécessaires afin de satisfaire les besoins de chauffage et de climatisation du bâtiment. Il importe de s'assurer que la température du fluide caloporteur à la sortie du champ de puits (à l'entrée de la PAC) soit au-dessus d'une température $T_{f,min}$ et en dessous d'une température $T_{f,max}$ afin, entre autres, d'éviter le gel du fluide caloporteur et d'assurer le bon fonctionnement de la PAC. Or, la température du fluide caloporteur dépend à la fois de la puissance extraite ou injectée dans le champ de puits et de la température du sol dans le champ de puits. La puissance extraite ou injectée dépend, quant à elle, de la capacité et de l'efficacité de la PAC qui dépendent toutes deux de la température du fluide alimentant la PAC.

Il existe des approches de dimensionnement permettant de calculer la longueur totale de puits requise pour un système géothermique. Il est également possible d'obtenir les températures minimale et maximale du fluide à l'entrée de la PAC en simulant l'opération du système géothermique. Les différentes approches ont en commun de nécessiter un modèle permettant de calculer les variations de température du sol et du fluide dans le système géothermique.

Plusieurs phénomènes thermiques apparaissent à différentes échelles de temps lors de l'opération d'un système géothermique. À court terme, à l’échelle de quelques minutes à plusieurs heures, la capacité thermique du fluide caloporteur et le transfert de chaleur à travers le coulis ont un impact important sur la température du fluide à la sortie des puits. À plus long terme, voire sur plusieurs années, l'interaction thermique entre les puits géothermiques ainsi que l'interaction thermique entre les puits et la surface du sol ont un effet important sur les températures dans le champ de puits.

Le premier objectif de cette étude est le développement d’un modèle pour le calcul des facteurs de réponse thermique de champs de puits géothermiques, aussi appelées g-functions (Eskilson, 1987), tenant compte de l’interaction thermique entre puits géothermiques et de l’interaction thermique entre les puits géothermiques et la surface du sol. Le modèle, basé sur des solutions analytiques du transfert de chaleur par conduction, se veut d’approcher la capabilité des modèles numériques existants par sa flexibilité quant à la condition frontière utilisée à la paroi des puits et par sa capacité à modéliser des champs de puits à dimensions et positions quelconques.

Le second objectif de l’étude est de valider expérimentalement les facteurs de réponse thermique pour la prédiction à long terme des températures des puits géothermiques. Étant donnée

l’impossibilité d’obtenir expérimentalement les facteurs de réponse thermique à long terme sur un système géothermique de taille réelle, nécessitant alors des mesures durant des dizaines d’années, un puits géothermique de taille réduite est utilisé. La réduction d’échelle permet de mesurer le facteur de réponse thermique du puits jusqu’à l’atteinte du régime permanent à l’intérieur d’un test d’une semaine.

CHAPITRE 1 REVUE CRITIQUE DE LA LITTÉRATURE

Le problème du transfert thermique entre le fluide caloporteur circulant dans le puits géothermique et le sol est généralement séparé en deux régions: le transfert thermique entre la paroi du puits et le sol entourant le puits et le transfert thermique entre le fluide caloporteur et la paroi du puits.

La section 1.1 de cette revue de littérature traite de la première région et plus particulièrement des facteurs de réponse thermique des puits géothermiques qui permettent d'obtenir l'évolution de la température du sol entourant les puits géothermiques. La section 1.2 traite de l'intérieur du puits et de la résistance thermique qui lie les températures du fluide caloporteur et de la paroi du puits à la puissance thermique injectée ou extraite du sol. Finalement, la section 1.3 présente les algorithmes de superposition temporelle utilisés lors de la simulation de champs de puits géothermiques.

1.1 Facteurs de réponse thermique pour échangeurs géothermiques

Les facteurs de réponse thermique des échangeurs géothermiques sont utilisés afin d'obtenir la variation de la température à la paroi d'un puits ou des puits d'un champ de puits due à l'injection ou l'extraction d'une puissance thermique par unité de longueur de puits constante. Il existe des solutions analytiques, notamment la source ligne et la source cylindrique, permettant d'obtenir de tels facteurs de réponse. Plusieurs modèles numériques ont également été proposés afin de modéliser le transfert thermique transitoire entre les champs de puits géothermiques et le sol.

Les modèles numériques ont l'avantage, aux coûts d'une plus grande complexité d'implémentation et de temps de calcul généralement plus longs, d'être plus flexibles en termes de conditions frontières et de propriétés thermiques du puits et du sol. Par exemple, il est possible pour un modèle numérique de considérer plusieurs couches horizontales de sol avec des propriétés thermiques différentes représentant des milieux géologiques différents, ce qui est relativement difficile à réaliser avec des modèles analytiques.

1.1.1 Modèles analytiques à une dimension

Source linéique infinie

La solution de la source linéique infinie a d'abord été proposée par Lord Kelvin en 1882, puis appliquée aux échangeurs géothermiques horizontaux par Ingersoll & Plass (1948) et par Ingersoll et al. (1950; 1954). La solution donne la variation de température ΔT à une distance r d'une source ligne infinie injectant une puissance thermique par unité de longueur Q à r = 0 dans un milieu infini. Un schéma de la géométrie est montré à la Figure 1-1.

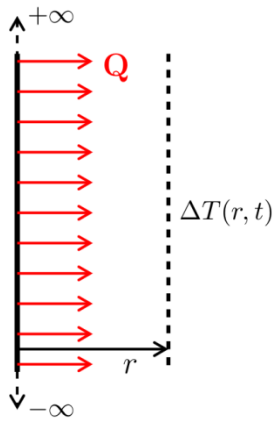

Figure 1-1: Schéma de la source ligne infinie

La solution de la source linéique infinie est applicable aux puits géothermiques verticaux. La variation de température ΔT à une distance r du centre d'un puits est donnée par:

$$\Delta T(r,t) = T(r,t) - T_g = \frac{Q}{2\pi k_s} \int_{\frac{r}{2\sqrt{\alpha_s t}}}^{\infty} \frac{e^{-\beta^2}}{\beta} d\beta \qquad (1.1)$$

où T_g est la température initiale du sol, Q est la puissance thermique injectée par unité de longueur de puits, k_s est la conductivité thermique du sol et α_s est la diffusivité thermique du sol. La solution est évaluée à $r = r_b$ le rayon du puits afin d'obtenir la variation de la température à la paroi du puits.

Pour des temps courts, la capacité thermique du puits ne peut être négligée et le puits ne peut donc pas être approximé par une source linéique. Ingersoll et al. (1950) estiment que la solution

de la source ligne infinie est valide pour $t \geq \frac{20\, r_b^2}{\alpha_s}$. Eskilson (1987) mentionne que la solution est valide pour $t \geq \frac{5\, r_b^2}{\alpha_s}$. À ces instants, le taux de transfert de chaleur à $r = r_b$ tend vers Q et les écarts entre la solution de la source ligne infinie et celle de la source cylindrique infinie sont respectivement d'environ 2 % et 10 % (Philippe, Bernier, & Marchio, 2009).

Source cylindrique infinie

Ingersoll et al. (1950) utilisent la solution proposée par Carslaw & Jaeger (1946a) pour évaluer la température du sol entourant un tuyau enterré transférant une puissance thermique par unité de longueur de tuyau Q au sol environnant. La géométrie du problème est présentée à la Figure 1-2.

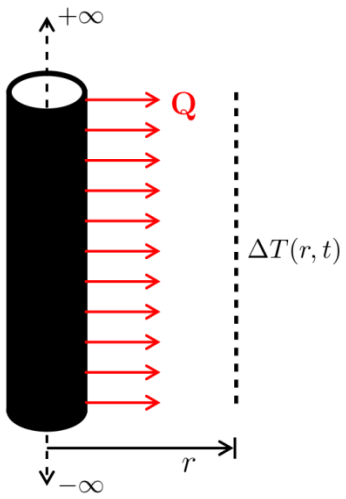

Figure 1-2: Schéma de la source cylindrique infinie

La solution de la source cylindrique infinie est applicable aux puits géothermiques verticaux. La variation de température ΔT à une distance $p = r/r_b$ est donnée par le G-factor (à ne pas confondre avec les g-functions):

$$G(Fo, p) = \frac{1}{\pi^2} \int_0^{\infty} \frac{\exp(-s^2 Fo) - 1}{J_1^2(s) + Y_1^2(s)} [J_0(ps)Y_1(s) - J_1(s)Y_0(ps)] \cdot \frac{ds}{s^2}$$
$$\Delta T(Fo, p) = \frac{Q}{k_s} G(Fo, p) \qquad (1.2)$$

où G est le G-factor, $Fo = \frac{\alpha_s t}{r_b^2}$ est le nombre de Fourier, J_n et Y_n sont les fonctions de Bessel du premier et second type et d'ordre n.

À l'origine, le G-factor était difficile à obtenir numériquement et les valeurs du G-factor étaient précalculées et présentées sous forme de tables (Ingersoll et al., 1954). Carslaw & Jaeger ont donné dans leur ouvrage (Carslaw & Jaeger, 1946a) une expansion en série valable pour $Fo \ll 1$ ainsi qu'une relation pour $Fo \gg 1$. Cooper (1976) utilise la transformation d'Euler pour obtenir un développement en série valide pour $Fo > 0$. Bernier (2000, 2001) fournit des corrélations obtenues à partir des valeurs tabulées de Ingersoll et al. (1954) pour $p = 1, 2, 5, 10$. D'autres corrélations sont données par Bernier & Salim-Shirazi (2007) pour $p = 1, 2, 5, 10, 20, 50, 100$.

1.1.2 g-functions d'Eskilson

Le concept des g-functions est introduit dans la thèse d'Eskilson (1987). Les g-functions sont en fait des facteurs de réponse donnant la relation entre la puissance thermique extraite à la paroi par unité de longueur de puits Q et la température à la paroi des puits T_b. Les g-functions sont définies par la relation:

$$T_b = T_g - \frac{Q}{2\pi k_s} \cdot g(t/t_s, r_b/H, B/H) \tag{1.3}$$

où g est la g-function, $t_s = \frac{H^2}{9\alpha_s}$ est la constante de temps du champ de puits géothermiques, B est l'espacement entre les puits géothermiques et H est la longueur des puits géothermiques.

Chaque g-function est unique à une seule configuration de champ de puits. Un exemple de g-function pour un champ de 3 × 2 puits est présenté à la Figure 1-3. Les g-functions obtenues par Eskilson sont documentées sous forme de graphes dans sa thèse. Elles incluent une variété de géométries de champ de puits et d'espacement B/H. Elles sont cependant produites pour une seule valeur du rapport $r_b/H = 0.0005$ (équivalent à r_b = 0.075 m pour H = 150 m) et pour une seule valeur de tête de puits $D \approx 4$ m. Les g-functions sont généralement données pour un rapport $r_b/H = 0.0005$. Eskilson donne cependant une relation afin de corriger les g-functions pour un rapport $r_b/H \neq 0.0005$.

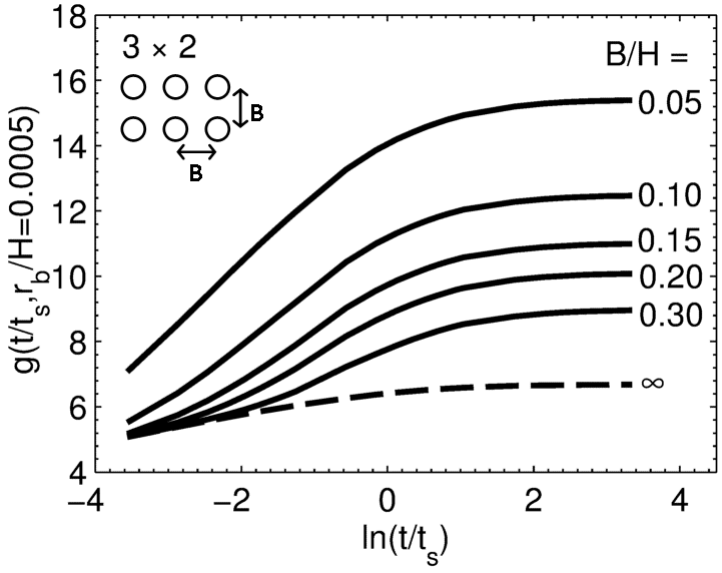

Figure 1-3: g-function d'Eskilson pour un champ de 3 × 2 puits

Les g-functions d'Eskilson sont obtenues par la méthode des différences finies. Chaque puits est représenté par une source de chaleur cylindrique dans un maillage radial-axial. La Figure 1-4 présente un exemple de maillage pour le modèle d'Eskilson. La hauteur des mailles est plus petite près des extrémités du puits – là où les variations de température sont plus importantes. Les mailles sont également plus étroites près du puits et plus larges à mesure qu'on s'éloigne du puits.

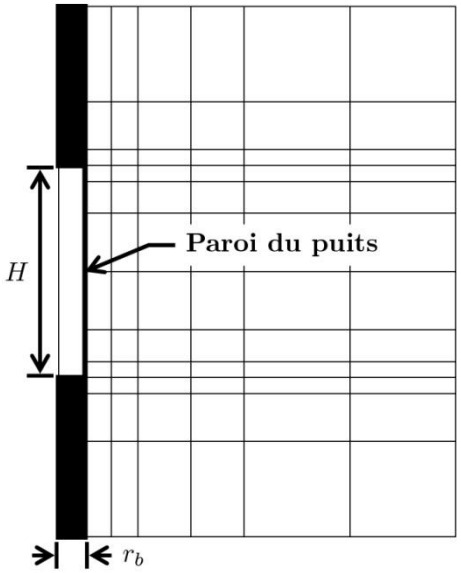

Figure 1-4: Exemple de maillage dans le modèle d'Eskilson

La variation totale de la température dans le champ de puits est obtenue en superposant les variations de température autour des différents puits du champ. La température à la surface du sol est maintenue constante en superposant des sources images avec la surface du sol comme plan de symétrie. Les puissances thermiques extraites à chaque cellule le long de la paroi des puits sont différentes et sont calculées de façon à obtenir une température uniforme à la paroi des puits et la même pour tous les puits du champ (Eskilson, 1986). La puissance thermique totale extraite dans tout le champ est toutefois gardée constante. Les g-functions (Figure 1-3) représentent alors la réponse indicielle de la température à la paroi des puits d'un champ à une puissance thermique extraite du champ de puits.

La condition de température uniforme à la paroi des puits s'approche de celle observée en pratique pour l'opération d'un champ de puits connectés en parallèle. Considérant que la température moyenne du fluide descendant et remontant un puits varie très peu sur la longueur du puits, la variation de la température à la paroi du puits devrait également peu varier sur sa longueur. De plus, puisque la température d'alimentation est la même pour tous les puits, alors les températures à la paroi des puits d'un même champ devraient tendre vers la même valeur.

1.1.3 Solutions analytiques à 2 et 3 dimensions

Source linéique finie

Lorsque les temps considérés deviennent longs, la longueur finie des puits géothermiques verticaux et l'interaction avec la surface du sol deviennent importantes et les solutions à une dimension ne sont plus adéquates. Eskilson (1987) estime que les effets axiaux apparaissent pour des temps $t \geq \frac{t_s}{10} = \frac{H^2}{90\alpha_s}$. La solution de la source linéique finie (SLF) doit alors être utilisée. Elle donne la variation de la température à une position (r, z) sous la surface du sol causée par une source linéique de longueur H enterrée à une distance D sous la surface du sol. La surface du sol est maintenue à la température initiale du sol T_g. La géométrie du problème est montrée à la Figure 1-5.

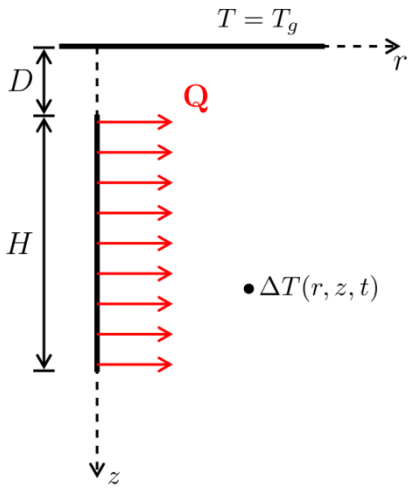

Figure 1-5: Schéma de la source linéique finie

Eskilson (1987) a proposé l'utilisation de la SLF pour l'approximation de la g-function d'un puits géothermique. Zeng et al. (2002) ont ensuite utilisé la SLF pour générer les facteurs de réponse thermique de champs de puits pour le cas $D = 0$. La variation de la température ΔT à une position (r, z) sous la surface du sol est donnée par la superposition de sources de chaleur ponctuelles sur la longueur du puits géothermique. La température T_g à la surface est maintenue par l'utilisation d'une source image.

$$\Delta T(r,z,t) = \frac{Q}{4\pi k_s}\int_D^{D+H}\left[\frac{\operatorname{erfc}\left(\frac{\sqrt{r^2+(z-h)^2}}{2\sqrt{\alpha_s t}}\right)}{\sqrt{r^2+(z-h)^2}} - \frac{\operatorname{erfc}\left(\frac{\sqrt{r^2+(z+h)^2}}{2\sqrt{\alpha_s t}}\right)}{\sqrt{r^2+(z+h)^2}}\right]dh \qquad (1.4)$$

où *erfc* est la fonction d'erreur complémentaire.

Zeng et al. (2002) ont proposé la superposition spatiale de la SLF afin de modéliser les champs de puits géothermiques. Les auteurs ont également comparé l'utilisation de la température à la mi-longueur du puits à celle de la température moyenne intégrale le long du puits pour le cas $D = 0$. La différence entre l'une ou l'autre des alternatives s'est révélée négligeable et la température à la mi-longueur a donc été utilisée par Diao et al. (2004) pour représenter la température à la paroi du puits puisque l'obtention de cette température ne requiert que l'évaluation d'une intégrale simple, plutôt qu'une intégrale double dans le cas de la température moyenne intégrale.

Lamarche & Beauchamp (2007b) ont simplifié la solution de la SLF pour obtenir une formulation permettant d'obtenir la température moyenne à la paroi du puits au moyen d'une intégrale simple pour le cas où $D = 0$. La superposition spatiale est utilisée afin d'obtenir la réponse thermique des champs de puits géothermiques. Les résultats sont comparés aux g-functions d'Eskilson pour des champs de 2 et 4 puits. L'utilisation de la température moyenne intégrale donne une meilleure approximation des g-functions que l'utilisation de la température à la mi-longueur. La solution de Lamarche & Beauchamp a été reprise par Costes & Peysson (2008) et étendue pour les cas $D \geq 0$. La solution de Costes & Peysson est également présentée dans le mémoire de Chapuis (2009).

Une solution pour $D \geq 0$ a également été proposée par Claesson & Javed (2011). La variation de la température moyenne sur la longueur du puits ($D \leq z \leq D + H$) à une distance r du puits est donnée par:

$$\Delta T(r,t) = \frac{Q}{4\pi k_s} \cdot \int_{1/\sqrt{4\alpha_s t}}^{\infty} \exp(-r^2 s^2) \cdot \frac{Y(Hs, Ds)}{Hs^2} \cdot ds$$
$$Y(h,d) = 2 \cdot ierf(h) + 2 \cdot ierf(h + 2d) - ierf(2h + 2d) - ierf(2d) \qquad (1.5)$$
$$ierf(X) = X \cdot erf(X) - \frac{1}{\sqrt{\pi}}(1 - \exp(-X^2))$$

où erf est la fonction d'erreur.

Fossa (2011) a comparé les facteurs de réponse thermique obtenus avec la SLF aux g-functions d'Eskilson pour des champs de 3 × 3 et 8 × 2 puits. L'auteur remarque que, pour de petites valeurs de B/H et de grandes valeurs de $\ln(t/t_s)$, la SLF surestime les g-functions. Fossa propose également une expression pour le calcul de la température moyenne à une distance r d'un puits. L'expression est utilisée pour calculer les facteurs de réponse thermique des champs de puits. Pour les cas étudiés, les facteurs de réponse obtenus ont des écarts maximums d'environ 10 % avec ceux calculés avec la SLF.

Marcotte et al. (2010) comparent l'utilisation de la source ligne infinie à celle de la SLF pour la simulation de champ de puits géothermiques. Les auteurs montrent que l'utilisation de la source ligne infinie — et donc le fait de négliger les effets axiaux — conduit à la surestimation des variations de température dans les champs de puits. L'utilisation de la SLF permet alors de diminuer le nombre de puits requis lors du design du système.

La SLF a également été utilisée pour modéliser les puits géothermiques inclinés. Cui et al. (2006), Marcotte & Pasquier (2009) et Lamarche (2011) ont proposé des solutions pour le calcul de la température à la paroi de puits inclinés basées sur la SLF. Lamarche (2011) a comparé sa solution aux g-functions d'Eskilson pour des champs de 2, 4 et 6 puits inclinés. L'écart avec les g-functions est inférieur à 2 % pour l'ensemble des cas étudiés.

Marcotte & Pasquier (2014) proposent un modèle pour le calcul des facteurs de réponse thermique de champs puits avec des combinaisons de puits en parallèle et en série se basant sur la SLF. Ces facteurs de réponse thermique donnent la variation de la température d'entrée du champ de puits plutôt que la température à la paroi des puits puisque le modèle tient compte de la résistance thermique des puits et des débits massiques dans les différents circuits. Le modèle est comparé à des simulations par éléments finis pour un champ de 12 puits. La température d'entrée du fluide ainsi que les taux de transferts de chaleur de chacun de puits prévus par le modèle analytique sont similaires à ceux obtenus par la simulation par éléments finis.

La SLF pour un seul puits vertical de 100 m est comparée à la g-function, à la source cylindrique infinie et à la source linéique infinie à la Figure 1-6. Comme le montre la figure, les sources linéiques finie et infinie sous-estiment la variation de la température à la paroi du puits pour des temps $t \leq 5\frac{r_b^2}{\alpha_s}$. Pour des temps $t \geq \frac{t_s}{10}$ $\left(\ln\left({}^{t}/_{t_s}\right) \geq -2.3\right)$, les sources cylindrique infinie et ligne infinie surestiment la variation de température à la paroi du puits tandis que la SLF et la g-function convergent vers une valeur constante des g-functions représentant un état permanent.

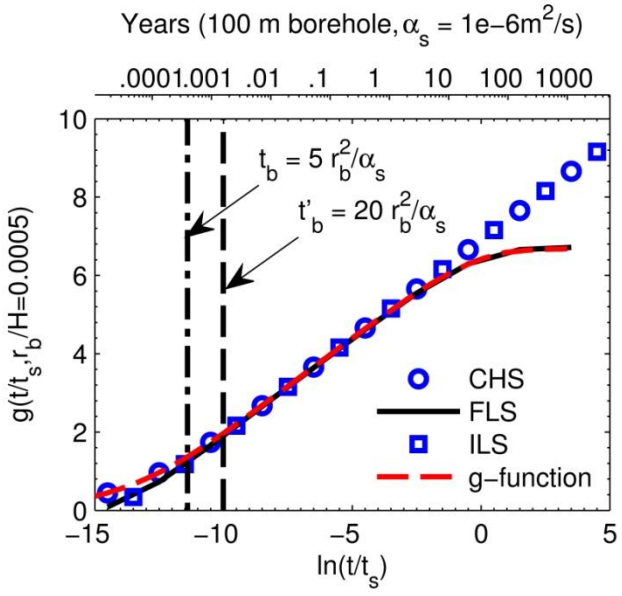

Figure 1-6: Comparaison de la source ligne finie (SLF), de la source cylindrique infinie (CHS), de la source ligne infinie (ILS) et de la g-function pour un puits de 100 m

La SLF a également été appliquée au transfert de chaleur entre des pylônes électriques et le sol. Duan et al. (2007) ont étudié la distribution de la température autour de la fondation d'un pylône électrique pour un profil de taux de transfert thermique sur la longueur de la fondation obtenu par la solution du problème de conduction axiale à travers la fondation. Duan & Naterer (2008b) ont proposé une solution pour une température à la surface du sol variant dans le temps. Duan & Naterer (2008a) comparent des solutions pour différents profils de taux de transfert thermique à des résultats expérimentaux.

Autres solutions analytiques

Man et al. (2010) ont obtenu des solutions pour les sources cylindriques dites "solides" infinie et finie. La solution de la source cylindrique solide infinie est en fait la réponse thermique à une source cylindrique de rayon $r = r_b$ dans un milieu infini $r \geq 0$, contrairement à la source cylindrique infinie (Ingersoll et al., 1950) qui donne la réponse thermique dans un milieu semi-infini $r \geq r_b$. La solution de la source cylindrique solide finie donne la réponse thermique à une source cylindrique finie de longueur H dans un milieu semi-infini $r \geq 0,\ z \geq 0$. Les deux

solutions sont obtenues par la superposition spatiale de sources de chaleur ponctuelles sur la circonférence et la longueur de la source. Pour la solution de la source cylindrique solide finie, la surface du sol à $z = 0$ est maintenue à une température constante par l'utilisation d'une source image de signe opposé. Un schéma de la source cylindrique solide finie est présenté à la Figure 1-7a.

Cui et al. (2011) ont proposé une solution pour la réponse thermique due à une série de sources anneaux espacés régulièrement. Les sources anneaux servent à modéliser un échangeur hélicoïdal. La solution est obtenue par la superposition spatiale de sources de chaleur ponctuelles. Des solutions sont données pour des sources de longueur finies et infinies. Un schéma pour une série de sources anneaux de longueur finie est présenté à la Figure 1-7b.

Li & Lai (2012a) proposent des facteurs de réponse pour des puits géothermiques dans un milieu anisotrope ayant des conductivités thermiques k_x, k_y, k_z différentes dans chaque direction. Des solutions sont données pour les sources linéiques infinie et finie, les sources cylindriques solides infinie et finie en plus de proposer les sources spirales infinie et finie. Les sources spirales sont utilisées afin de modéliser des échangeurs hélicoïdaux. Les auteurs comparent la température à la paroi du puits obtenue avec les sources cylindrique solide et spirale. Ils notent que la différence entre les deux solutions est négligeable et que l'utilisation de la source spirale ne permet donc pas d'obtenir de meilleurs résultats. Un schéma de la source spirale finie est présenté à la Figure 1-7c.

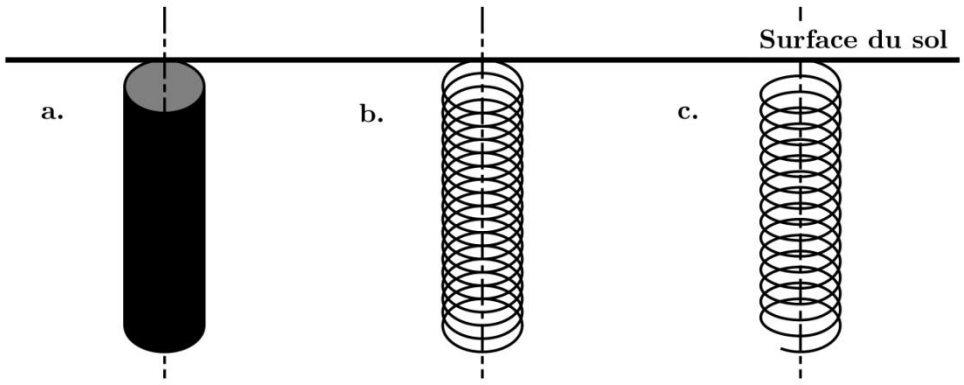

Figure 1-7: Schémas des sources cylindrique solide (a), anneaux (b) et spirale (c)

Abdelaziz et al. (2014) présentent un modèle se basant sur la SLF pour le calcul de la température entourant un puits géothermique dans un sol divisé en une série de couches verticales ayant des

propriétés thermiques différentes. Le puits est représenté par une série de lignes sources, soit une par couche verticale. La température en un point dans le sol est obtenue par la superposition de la contribution de toutes les lignes sources du puits et de sources images au-dessus de la surface du sol. La contribution du segment primaire, celui qui partage la même couche verticale que le point où l'on évalue la température, est évaluée avec la SLF (Équation 1.4). Pour évaluer la contribution des autres segments, dits secondaires, des propriétés thermiques équivalentes sont d'abord calculées afin de considérer les propriétés thermiques des différentes couches séparant les segments du point où la température est évaluée. Les auteurs corrigent également la puissance thermique injectée par chacun des segments selon les propriétés thermiques des différentes couches. Le modèle analytique est vérifié en comparant les profils de température calculés à différentes distances à ceux obtenus à partir de simulation par éléments finis.

1.1.4 Solutions numériques

Le modèle d'Eskilson (1987) (présenté à la section 1.1.2) est l'un des premiers modèles numériques permettant de simuler les champs de puits géothermiques. L'autre contribution classique est celle d'Hellström (1989) qui présente un modèle numérique pour la simulation de stockages thermiques saisonniers par puits géothermiques. Dans son modèle, Hellström divise le sol en deux régions: la région globale, qui sert à modéliser le transfert thermique entre le volume de stockage et le sol environnant, et la région locale, qui sert à modéliser le transfert thermique entre les puits et le sol du volume de stockage. Le maillage de la région globale est un maillage 2D axisymétrique tandis que le maillage de la région locale est un maillage 1D. Le maillage de la région globale est divisé en sous-régions, les puits sont répartis uniformément entre les sous-régions. Il est à noter que la position exacte des puits n'est pas définie, ils sont liés au maillage global par l'entremise du maillage local. Le transfert thermique dans chacun des maillages est résolu par différences finies. De plus, les maillages global et local n'utilisent pas les mêmes pas de temps. Le modèle DST, basé sur la méthodologie d'Hellström, est implémenté dans l'environnement de simulation TRNSYS, tel que décrit par Chapuis & Bernier (2009).

Récemment, plusieurs modèles numériques ont été proposés. L'intérêt des modèles numériques est de pouvoir représenter fidèlement la géométrie de l'échangeur géothermique et les propriétés thermiques des différents matériaux impliqués. Quelques-uns des modèles récents sont décrits dans cette section.

Li & Zheng (2009), puis Li (2012) développent un modèle 3D par volumes finis permettant de prédire les températures d'entrée et sortie du fluide dans un puits géothermique et également de calculer le facteur de réponse thermique du puits. L'espace est divisé en 3 régions: le sol, le coulis et le fluide. La capacité thermique des tuyaux est négligée. Pour le calcul des facteurs de réponse thermique, la température du fluide requise à l'entrée du puits pour maintenir un taux d'extraction de chaleur constant est recalculée à tous les pas de temps.

Kim & al. (2011; 2010) développent un modèle par éléments finis pour la simulation de champs de puits géothermiques. Les auteurs utilisent la technique de réduction du modèle d'état afin de diminuer le temps de calcul. L'espace est divisé en plusieurs régions: les régions plus près des puits géothermiques ont des maillages plus denses et un pas de temps plus petit. La solution du modèle est décomposée en modes et seuls les modes dominants sont retenus afin d'obtenir une bonne approximation de la solution tout en limitant la mémoire requise pour le calcul.

Acuña et al. (2012) et Monzó et al. (2013) utilisent un modèle par éléments finis développé dans le logiciel Comsol pour le calcul de la g-function d'un champ de 8 × 8 puits. Le sol est représenté par un domaine cylindrique de 100 m de rayon et de 150 m de profondeur. Une température constante et uniforme est utilisée comme condition frontière pour les frontières extérieure, supérieure et inférieure du domaine du sol. Les puits, d'une longueur de 100 m et espacés de 5 m, sont représentés par des cylindres creux. Une puissance thermique constante et uniforme est utilisée comme condition frontière à l'intérieur des cylindres. La symétrie est utilisée pour simuler que le quart du domaine du sol. Les g-functions calculées pour différents rapports D/H sont similaires à celles obtenues avec la SLF et surestiment les g-function d'Eskilson tirées du logiciel de dimensionnement EED.

Monzó et al. (2014) utilisent un modèle par éléments finis pour calculer la g-function d'un champ de 3 × 2 puits. Une condition frontière de température constante égale à la température initiale du sol est utilisée à l'ensemble des frontières du domaine représentant le sol, à l'exception de la paroi des puits. La condition de température uniforme à la paroi des puits est obtenue en modélisant les puits avec un matériau à très haute conductivité thermique (10^{10} W/m-K). Les puits sont tous connectés au-dessus du sol à une barre à très haute conductivité thermique sur laquelle est imposée la condition de taux d'injection de chaleur uniforme et constant. Les auteurs arrivent

alors à obtenir la g-function du champ de puits en utilisant les mêmes conditions frontières qu'Eskilson (1987).

Zanchini & Lazzari (2013) utilisent un modèle 2D axisymétrique par éléments finis pour calculer les facteurs de réponse thermique de champ de puits. Le sol est modélisé pour $r \geq r_b$ et $z \geq 0$ et pour un rayon extérieur et une profondeur maximale suffisants pour ne pas que la solution soit dépendante de la grandeur du domaine. Une puissance thermique par unité de longueur constante et uniforme est injectée à la paroi du puits. La surface du sol est maintenue à une température constante égale à la température initiale du sol. Le reste des frontières sont adiabatiques. Les auteurs évaluent la température moyenne à la paroi du puits ainsi que la température moyenne à différentes distances du puits. Les facteurs de réponse thermique des champs de puits sont obtenus par la superposition spatiale des températures pour les différentes distances séparant les puits. Les facteurs de réponses thermiques sont présentés sous forme de corrélations. Zanchini & Lazzari (2014) évaluent la réponse à court terme d'un puits géothermique en modélisant par éléments finis une tranche axiale d'un puits à deux tubes en U. Une puissance thermique constante est injectée à la paroi des tubes plutôt qu'à la paroi du puits. La réponse à court terme ainsi calculée est utilisée pour corriger les facteurs de réponse thermique à long terme et de nouvelles corrélations sont présentées.

Loveridge & Powrie (2013) développent un modèle 3D par éléments finis pour le calcul de facteurs de réponse thermique de pieux géothermiques. Le diamètre des pieux géothermiques, pouvant dépasser un mètre, est plus grand que celui des puits géothermiques verticaux et la longueur des pieux géothermiques est aussi généralement plus petite que celle des puits géothermiques verticaux. Une puissance thermique uniforme est injectée sur la longueur des tubes à l'intérieur d'un pieu. La variation de la température à la paroi du pieu est utilisée pour tracer le facteur de réponse thermique. Un modèle 2D d'une tranche axiale du pieu est utilisé pour évaluer le facteur de réponse thermique pour les temps courts. Des corrélations sont fournies pour différentes dimensions de pieux géothermiques. La superposition spatiale est utilisée par Loveridge & Powrie (2014) pour calculer les facteurs de réponse thermique d'arrangements à plusieurs pieux géothermiques.

1.2 Résistance thermique des puits géothermiques

La résistance thermique des puits géothermiques fait la relation entre la température moyenne du fluide T_f dans le puits géothermique, la température à la paroi du puits T_b et la puissance thermique extraite par unité de longueur de puits Q.

$$T_f(t) = T_b(t) - Q(t)R_b \tag{1.6}$$

où R_b est la résistance thermique du puits.

La résistance thermique du puits est évaluée en régime permanent et peut être obtenue expérimentalement à l'aide d'essais de réponse thermique ou analytiquement à partir des propriétés thermiques des matériaux du puits et du sol. Il existe également des modèles permettant de considérer les capacités thermiques du fluide, des tuyaux et du coulis et donc de modéliser la variation de la valeur effective de R_b dans le temps.

1.2.1 Essai de réponse thermique

À partir d'une unité d'essai de réponse thermique, un fluide est circulé dans le puits d'essai et une puissance thermique constante est injectée. Les températures à l'entrée et à la sortie du puits ainsi que le débit de fluide sont mesurés (Austin, Yavuzturk, & Spitler, 2000; Gehlin & Hellström, 2003; Shonder & Beck, 1999). L'essai de réponse thermique permet d'évaluer la conductivité thermique du sol k_s, et la résistance thermique du puits R_b.

La durée minimale d'un essai de réponse thermique est normalement d'environ 50 h (Austin et al., 2000; Shonder & Beck, 1999). Cependant, une étude menée par Beier & Smith (2003) indique que la durée requise de l'essai de réponse thermique afin d'obtenir une bonne précision sur les propriétés thermiques peut varier d'un facteur 100 dépendamment des propriétés du coulis et du sol.

Les résultats de l'essai de réponse thermique sont comparés à un modèle analytique ou numérique du transfert de chaleur dans le sol. Les propriétés thermiques qui permettent d'obtenir les plus petits écarts avec les résultats de l'essai sont retenues. La méthode la plus simple pour identifier les propriétés thermiques du sol est celle de la source linéique infinie (Gehlin & Hellström, 2003). Dans cette méthode, les résultats de l'essai de réponse thermique sont tracés dans un

graphique semi-logarithmique (T_f *vs* $\ln(t)$) pour les valeurs $t \geq \frac{5r_b^2}{\alpha_s}$. Une régression linéaire est effectuée sur les résultats. On obtient les propriétés thermiques avec la relation:

$$T_f(t) = T_g + \frac{Q}{4\pi k_s H}\left[\ln\left(\frac{4\alpha_s}{r_b^2}t\right) - \gamma\right] + \frac{Q}{H}R_b \qquad (1.7)$$

où Q est la puissance thermique moyenne injectée durant l'essai et $\gamma = 0.5772$ est la constante d'Euler. D'autres méthodes pour l'estimation des propriétés thermiques font appel à la source cylindrique infinie ou à des méthodes numériques (Austin et al., 2000; Marcotte & Pasquier, 2008b).

La température non-perturbée doit être mesurée avant l'essai de réponse thermique. Gehlin & Nordell (2003) présentent plusieurs méthodes pour l'obtention de cette température: la mesure de la température du fluide à l'intérieur du puits sans circulation par l'insertion d'une sonde de température; la mesure de la température de sortie du fluide après la mise en marche de la pompe durant un aller-retour du fluide dans la boucle; la mesure de la température du fluide après 20 min de circulation sans injection de chaleur. Dans l'étude, les températures obtenues par chacune des méthodes sont équivalentes à 0.1 °C près.

Bandos et al. (2009) obtiennent une solution pour la température moyenne à la paroi d'un puits à partir d'un développement en série de la solution de la SLF. L'effet de la variation de la température à la surface du sol ainsi que l'effet du gradient géothermique sont superposés à la solution. La méthode présentée par les auteurs permet de retirer les variations de température causées par la variation de la température ambiante durant les essais de réponse thermique afin d'améliorer les résultats de l'analyse des essais. La méthode est étendue par Bandos et al. (2011) afin d'évaluer les pertes dans la tuyauterie au-dessus du sol dues à la variation de la température ambiante.

1.2.2 Modèles en régime permanent

La résistance thermique équivalente d'un puits géothermique est la combinaison de trois résistances, soient la résistance thermique due à la convection dans les tuyaux R_f, la résistance thermique des tuyaux R_p et la résistance thermique du coulis R_g.

Une revue des méthodes pour l'évaluation de la résistance thermique des puits géothermiques a été effectuée par Lamarche et al. (2010). L'approche classique pour l'évaluation de la résistance thermique des puits consiste à représenter l'intérieur du puits comme un circuit de résistances thermiques reliant le fluide dans chacun des tuyaux et la paroi du puits. Cette approche est illustrée à la Figure 1-8. Les auteurs répertorient des méthodes basées sur des résultats expérimentaux, des méthodes utilisant des sources linéiques ou des multipoles ainsi que des méthodes numériques.

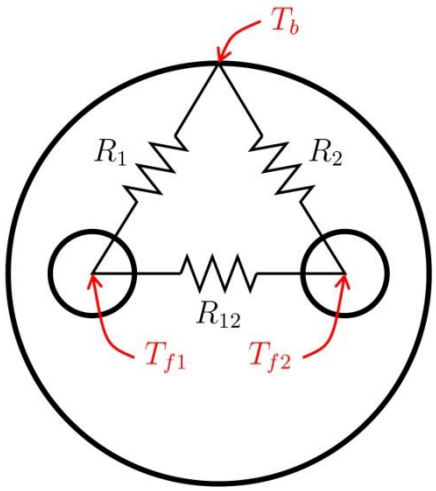

Figure 1-8: Résistances thermiques dans un puits géothermique

Hellström (1991) présente 2 solutions permettant d'obtenir les résistances internes d'un puits géothermique. La première est basée sur la solution de la ligne source. La seconde est une approximation de la méthode multipole présentée dans des rapports internes par Claesson & Bennet (1987) et par Bennet et al. (1987). La méthode multipole est la solution au transfert thermique entre des sources de chaleur à la position des tuyaux dans le puits et la paroi du puits entouré d'un milieu annulaire avec des propriétés thermiques différentes du puits. Claesson & Hellström (2011) ont récemment amélioré la méthode multipole.

Eskilson & Claesson (1988) présentent une solution pour la variation de température du fluide dans un puits géothermique pour un profil arbitraire de la température à la paroi du puits. L'expression finale prend la forme suivante:

$$T_{f1}(z,t) = T_{f1}(0,t)f_1(z) + T_{f2}(0,t)f_2(z) + \int_0^z T_b(\eta,t)f_4(z-\eta)d\eta \qquad (1.8)$$

$$T_{f2}(z,t) = -T_{f1}(0,t)f_2(z) + T_{f2}(0,t)f_3(z) - \int_0^z T_b(\eta,t)f_5(z-\eta)d\eta \qquad (1.9)$$

où T_{f1} et T_{f2} sont les températures du fluide descendant et remontant le puits et $f_{1\text{-}5}$ sont des fonctions donnant la variation de la température du fluide selon la profondeur *z*. Hellström (1991) donne des solutions pour les cas particuliers où la température à la paroi du puits est uniforme sur sa longueur et où la puissance thermique extraite est uniforme sur la longueur du puits.

Zeng et al. (2003) étendent la solution de Hellström pour le cas où la température à la paroi du puits est uniforme et l'appliquent à des puits à quatre tuyaux. Les auteurs étudient différents branchements en parallèle et en série des deux boucles en U. Eslami-Nejad & Bernier (2011) appliquent la même méthode pour des puits à quatre tuyaux ayant deux circuits de fluide indépendants avec des débits différents à travers chacun des circuits.

1.2.3 Modèles transitoires

Les modèles transitoires pour la réponse thermique à court terme des puits géothermiques ont été revus par Javed et al. (2010; 2009) . Les modèles présentés dans cette section sont généralement couplés à des facteurs de réponse thermique à long terme (section 1.1) afin de couvrir l'intégralité des échelles de temps. Elles sont plus particulièrement intéressantes pour les temps $t \leq \frac{5r_b^2}{\alpha_s}$ ou $t \leq \frac{20r_b^2}{\alpha_s}$, après quoi la résistance thermique en régime permanent (section 1.2.2) est adéquate pour traiter le transfert de chaleur dans le puits.

Modèles numériques et analytiques à 1 et 2 dimensions

Yavuzturk et al. (1999) ont développé un modèle par volumes finis pour le transfert de chaleur transitoire à l'intérieur du puits. Le puits est représenté dans un maillage 2-D en coordonnées polaires. Chaque tuyau est approximé par un ensemble de cellules pour former une région ayant un volume équivalent au tuyau. Un schéma du maillage utilisé est présenté à la Figure 1-9. Le facteur de réponse à court terme est donné par la température moyenne à la paroi du puits due à

une injection de chaleur à la paroi interne des tuyaux: le modèle considère donc les propriétés thermiques des tuyaux et du coulis. La puissance totale injectée est répartie entre les deux tuyaux dans des proportions de 60 % et 40 %. La sensibilité du facteur de réponse thermique à court terme à la répartition de la puissance entre les deux tuyaux est négligeable. Les auteurs présentent la réponse thermique sous forme de g-function et pour se faire, l'effet de la résistance thermique en régime permanent est retiré de la solution (Yavuzturk & Spitler, 1999). À cause de cet ajustement, la réponse thermique est négative pour les très petites valeurs de temps. Le modèle a été validé grâce à des données mesurées sur un puits géothermique en opération pour une durée d'un an (Yavuzturk & Spitler, 2001). Les températures prédites par le modèle sont en bon accord avec les données mesurées sur le site.

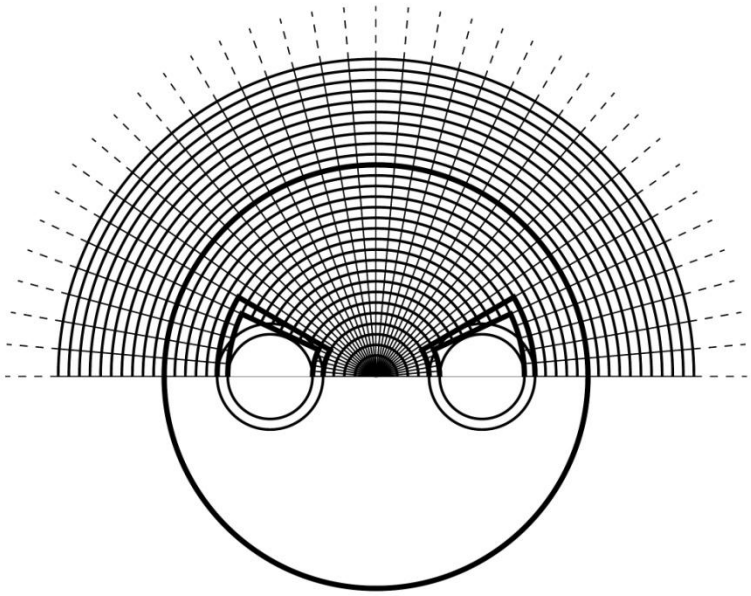

Figure 1-9: Schéma du maillage du modèle par volumes finis de Yavuzturk et al.

Yavuzturk et al. (2009) développent un modèle par éléments finis de l'intérieur du puits. Les deux tuyaux de la boucle en U sont remplacés par un tuyau de diamètre équivalent. Le modèle par éléments finis est alors développé en coordonnées 1D axisymétriques. Les conditions frontières utilisées sont le taux d'injection de chaleur à la paroi externe du tuyau et la température à la paroi du puits. La température à la paroi du puits est obtenue en couplant le modèle à la source

cylindrique infinie (Bernier, 2001). La température du fluide est obtenue en considérant le coefficient de convection du fluide caloporteur et la résistance thermique du tuyau.

Beier & Smith (2003) obtiennent une solution dans le domaine de Laplace pour la variation de la température du fluide due à une injection constante de chaleur dans le sol. Les tuyaux de la boucle en U sont remplacés par un tuyau de diamètre équivalent. La résistance thermique du tuyau et la résistance thermique par convection dans le tuyau sont négligées. Les auteurs proposent l'utilisation de l'algorithme Gaver-Stehfest (Stehfest, 1970) pour l'inversion de la solution. Ils suggèrent qu'une solution existe dans le domaine temporel mais la solution impliquerait une intégrale impropre de fonctions de Bessel, ce que les auteurs jugent serait trop complexe à évaluer.

Lamarche & Beauchamp (2007c) obtiennent une solution dans le domaine du temps pour le problème présenté par Beier & Smith (2003). La solution est obtenue par l'intégration par contour dans le plan complexe. Cette technique est décrite par Carslaw & Jaeger (1946c). La solution est vérifiée numériquement par éléments finis en utilisant le logiciel Comsol.

Bandyopadhyay et al. (2008) obtiennent une solution pour une puissance thermique constante injectée au centre du puits par un solide virtuel à température uniforme représentant le fluide caloporteur. Le solide virtuel a un diamètre équivalent aux deux tuyaux de la boucle en U et est lié au coulis par une résistance thermique incluant la résistance thermique du tuyau et la résistance due à la convection dans le tuyau. Il possède la même densité que le fluide et sa capacité thermique est ajustée de façon à tenir compte de la capacité thermique du fluide et de l'écoulement de fluide dans les tuyaux. La solution est en bon accord avec la solution par éléments finis présentée mais n'est applicable que pour les cas où le coulis et le sol ont les mêmes propriétés thermiques. Bandyopadhyay et al. (2008) proposent plus tard une solution semi-analytique pour le cas où les propriétés du coulis et du sol sont différentes. La solution est obtenue dans le domaine de Laplace et inversée avec l'algorithme Gaver-Stehfest (Stehfest, 1970).

Javed et al. (2011; 2010) développent une solution analytique pour l'intérieur d'un puits géothermique où les tuyaux de la boucle en U sont remplacés par un tuyau de diamètre équivalent. Le modèle tient compte des propriétés thermiques du fluide, du tuyau, du coulis et du sol environnant. Les auteurs montrent que le problème peut être réduit à un circuit de résistances

thermiques dans le domaine de Laplace, tel que montré à la Figure 1-10. La solution dans le domaine temporel est obtenue par la transformée inverse de la solution dans le domaine de Laplace. Un modèle par différences finies est développé pour vérifier la solution analytique. Des données d'expérience en laboratoire sont également utilisées afin de valider le modèle analytique. Les résultats du modèle analytique, du modèle numérique et les résultats expérimentaux sont équivalents.

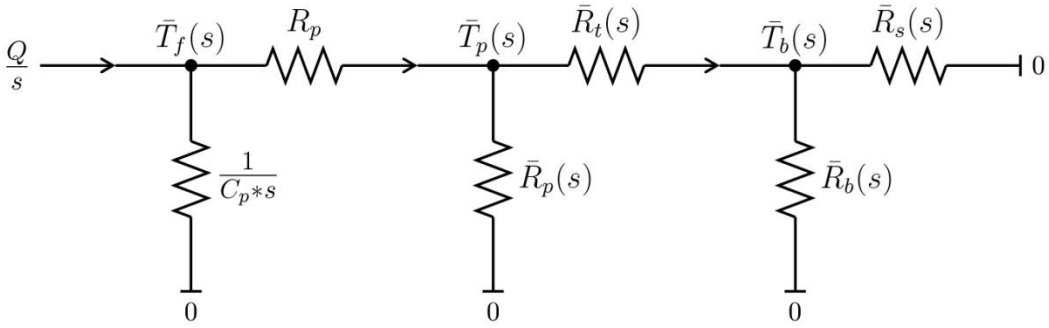

Figure 1-10: Réseau de résistances thermiques utilisé par Javed & Claesson

Li & Lai (2012b) utilisent la solution de la source linéique infinie dans un milieu composite obtenue par Jaeger (1944) pour obtenir des facteurs de réponse à court terme de puits géothermiques. Les milieux $r < r_b$ et $r > r_b$ possèdent des propriétés thermiques k, α différentes. Les sources lignes sont positionnées selon la position des tuyaux dans le puits et superposées spatialement. La réponse thermique est évaluée à la paroi des tuyaux, la résistance thermique du puits est donc gérée implicitement. Selon les auteurs, la solution est valide pour des petites et moyennes valeurs de temps (entre 15 min et 10 ans), à partir du moment où le tuyau peut être approximé par une source ligne jusqu'à ce qu'apparaissent les effets axiaux. Li & Lai (2013) raffinent le modèle pour le calcul des températures d'entrée et sortie du fluide dans le puits géothermique. Le modèle est validé à partir de l'essai de réponse thermique conduit en laboratoire par Beier et al. (2011). La comparaison entre le modèle et les résultats de l'essai de réponse thermique montre des différences importantes entre les températures prédites et mesurées, soit entre 2°C et 3°C de différences sur les températures du fluide et de la paroi du puits. Une comparaison avec un modèle numérique (Y. Yang & Li, 2014) révèle qu'une part des différences sont dues aux incertitudes lors de l'essai de réponse thermique, notamment sur la puissance thermique transférée au sol. Li et al. (2014) intègre cette approche dans un modèle multi-étage de

puits géothermiques, dans lequel le transfert de chaleur à court terme est calculé avec la source ligne infinie dans un milieu composite et le transfert de chaleur à moyen et à long termes est évalué avec la source ligne finie.

Al-Khoury (2010) étudie l'interaction thermique entre le fluide descendant et remontant un puits, le coulis et le sol. Les capacités thermiques du fluide et du coulis sont considérées. Les deux tuyaux de fluide interagissent par l'intermédiaire du coulis et le coulis interagie avec les deux tuyaux et le sol. Le sol est à une température connue, variable dans la direction axiale. Le système d'équations est résolu en utilisant la transformée de Fourier discrète. Les résultats sont comparés à des résultats numériques. Al-Khoury (2012) étend le modèle afin d'inclure la variation temporelle et axiale de la température du sol. La condition frontière à $r = 0$ est obtenue par un bilan d'énergie sur le coulis. Plutôt que de considérer un milieu semi-infini dans la direction radiale, l'auteur impose une température $T = T_g$ à $r = R$, où R est suffisamment grand pour que le puits géothermique ait un impact négligeable sur la température à cette distance. Les solutions pour les températures du fluide, du coulis et du sol peuvent alors être présentées sous forme de développements en séries.

Salim Shirazi & Bernier (2013) développent un modèle par volumes finis pour la simulation de puits géothermiques permettant de tenir compte de l'effet de la capacité thermique du coulis. Le tube en U est remplacé par un seul tuyau de diamètre équivalent au centre du puits. Le diamètre équivalent est choisi de façon à obtenir une résistance thermique entre le tuyau de diamètre équivalent et la paroi du puits égale à la résistance thermique entre le tube en U et la paroi du puits. La capacité thermique du fluide et le temps de résidence sont considérés en utilisant des valeurs équivalentes pour la densité, la chaleur spécifique et la vitesse d'écoulement du fluide à travers le tuyau de diamètre équivalent. La variation axiale des températures dans le puits est négligée. Le modèle est couplé à la solution de la source cylindrique infinie pour le calcul du transfert thermique dans le sol. Des simulations d'un bâtiment durant une saison de chauffage révèlent que le fait de ne pas tenir compte de la capacité thermique du coulis et du fluide conduit à une sous-estimation du coefficient de performance de la pompe à chaleur et donc à une surestimation de la consommation d’énergie de la pompe à chaleur.

Modèles résistances-capacitances

À la section 1.2.2, il a été montré que l'interaction entre le fluide, les tuyaux, la paroi du puits et le sol peut être représenté sous forme de circuit de résistances thermiques. En ajoutant des capacitances dans le circuit, il est possible de tenir compte des effets transitoires à l'intérieur du puits.

Bauer et al. (2011; 2010) proposent des modèles par circuits de résistances-capacitances pour des puits à tubes concentriques, à un tube en U et à deux tubes en U. Les auteurs ajoutent des capacitances thermiques afin de modéliser la capacité thermique du coulis dans les régions occupées par les tuyaux. Ainsi, il y a deux capacitances dans un puits à un tube en U et quatre dans un puits à deux tubes en U. Le schéma du circuit de résistances-capacitances pour un puits à un tube en U est montré à la Figure 1-11. Zarella et al. (2011) utilisent une démarche similaire, mais ne considèrent qu'une seule capacité thermique pour la région centrale entre les 4 tuyaux d'un puits à deux tubes en U.

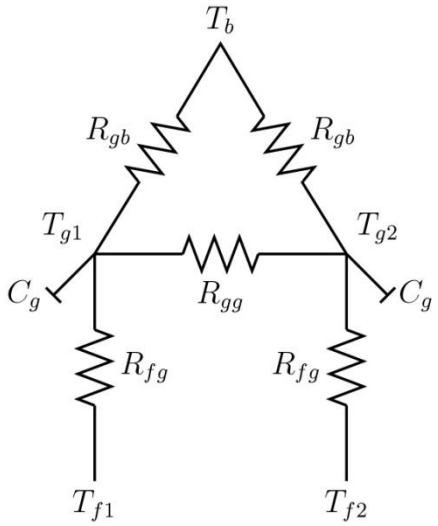

Figure 1-11: Circuit de résistances-capacitances pour le modèle de puits à deux tuyaux proposé par Bauer et al. (2010)

Pasquier & Marcotte (2012, 2014) décomposent chacun des éléments du puits (fluide, tuyaux, coulis) en une série de résistances et capacitances. De cette façon, les auteurs tiennent compte de la capacité thermique de tous les éléments du puits et arrivent à prédire la réponse thermique à

court terme avec une bonne précision. Le modèle est comparé à des résultats d'un essai de réponse thermique conduit en laboratoire par Beier et al. (2011).

1.3 Simulation des systèmes géothermiques

À la section 1.1, il a été décrit comment obtenir la variation de la température ΔT_b à la paroi des puits due à l'injection d'une puissance thermique constante dans le sol. Cependant, dans le cadre des simulations des systèmes géothermiques, la puissance thermique injectée ou extraite varie dans le temps. Pour une puissance thermique extraite par unité de longueur de puits $Q(t_i)$ débutant au temps $t_{i\text{-}1}$ et se terminant au temps t_i, la variation de la température à la paroi des puits est donnée par la superposition temporelle d'une puissance thermique extraite $Q(t_i)$ au temps $t_{i\text{-}1}$ et d'une puissance thermique extraite -$Q(t_i)$ au temps t_i:

$$\Delta T_b(t) = T_g - T_b(t) = \frac{Q(t_i)}{2\pi k_s} \cdot [f(t - t_{i-1}) - f(t - t_i)] \tag{1.10}$$

où f est le facteur de réponse thermique du champ de puits géothermiques (par exemple, la g-function) et $t \geq t_i$.

Pour une succession de puissances thermiques extraites $Q(t_i)$, la variation de température au temps t_k est donnée par:

$$\Delta T_b(t_k) = \sum_{i=1}^{k} \left(\frac{Q(t_i)}{2\pi k_s} \cdot [f(t_k - t_{i-1}) - f(t_k - t_i)] \right) \tag{1.11}$$

où $\Delta t = t_i - t_{i\text{-}1}$ et $t_0 = 0$.

L'équation (1.11) peut être réarrangée pour être exprimée en fonction de l'incrément de puissance thermique extraite par unité de longueur $q(t_i) = Q(t_i) - Q(t_{i\text{-}1})$:

$$\Delta T_b(t_k) = \sum_{i=1}^{k} \left(\frac{q(t_i)}{2\pi k_s} \cdot f(t_k - t_{i-1}) \right) \tag{1.12}$$

où $q(t_1) = Q(t_1)$.

On réfère généralement aux équations (1.11) et (1.12) en tant que « superposition temporelle des charges ». Dans le cadre de simulations pluriannuelles, l'évaluation de la superposition temporelle devient de plus en plus demandante en temps de calcul. Des simplifications sont alors nécessaires afin de réduire le temps requis pour les simulations.

Agrégation des charges

Yavuzturk & Spitler (1999) proposent la méthode d'agrégation des charges afin de réduire le temps de calcul nécessaire à la simulation. La méthode consiste à moyenner toutes les puissances thermiques extraites $Q(t_i \leq t_k - n_{ag}\Delta t)$, où n_{ag} est le nombre de pas de temps non-moyennés. La superposition temporelle des charges s'écrit alors (pour $k > n_{ag}$):

$$\begin{aligned}\Delta T_b(t_k) = {} & \frac{\sum_{i=1}^{k-n_{ag}} \left(\frac{Q(t_i)}{2\pi k_s}\right)}{k - n_{ag}} \left(f(t_k) - f\left(t_k - t_{k-n_{ag}}\right)\right) \\ & + \frac{Q\left(t_{k-n_{ag}+1}\right)}{2\pi k_s}\left[f\left(t_k - t_{k-n_{ag}}\right) - f\left(t_k - t_{k-n_{ag}+1}\right)\right] \\ & + \sum_{i=k-n_{ag}+2}^{k} \left(\frac{q(t_i)}{2\pi k_s} \cdot f(t_k - t_{i-1})\right)\end{aligned} \qquad (1.13)$$

Les auteurs ont utilisé une valeur $n_{ag} = 192$ pour effectuer des simulations horaires. Les auteurs arrivent à réduire le temps de calcul de 90 % pour une simulation d'un an et de 99 % pour une simulation de 20 ans.

Bernier et al. (2004) introduisent la méthode d'agrégation des charges multiple. La méthode consiste à considérer plusieurs groupes d'agrégation regroupant différents nombres de pas de temps. Les puissances thermiques extraites sont regroupées en différents groupes N_h, N_d, N_w, N_m et N_y. N_h représente le nombre de pas de temps gardés intacts; N_d, N_w, N_m représentent différents groupes d'agrégation et N_y représente le reste des pas de temps, tel que montré à la Figure 1-12.

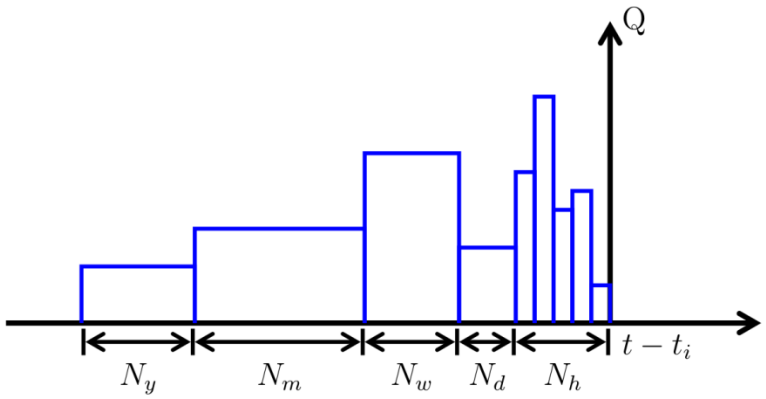

Figure 1-12: Groupes d'agrégation de la méthode d'agrégation des charges multiple

Les auteurs ont choisi les valeurs de N_h, N_d, N_w, N_m de façon à optimiser la précision des résultats de simulation et le temps de calcul. Les valeurs retenues sont $N_h = 12$, $N_d = 48$, $N_w = 168$ et $N_m = 360$.

Liu (2005) propose une méthode similaire à l'agrégation des charges multiple appelée la procédure d'agrégation hiérarchique des charges (hierarchical load aggregation procedure). La procédure consiste à regrouper les puissances thermiques extraites en petits, moyens et grands blocs d'agrégation. Un grand bloc contient N_g moyens blocs, un moyen bloc contient N_m petits blocs et un petit bloc contient N_p puissances thermiques instantanées. Un petit bloc est formé en prenant la moyenne de N_p puissances thermiques instantanées lorsque le nombre de puissances thermiques instantanées atteint la période d'attente PA_p pour la création d'un petit bloc. De façon similaire, un moyen ou un grand bloc sera formé lorque le nombre de petits ou de moyens blocs atteindront la période d'attente PA_m ou PA_g pour la création d'un moyen ou grand bloc. Cette méthode présente une amélioration par rapport à la méthode d'agrégation des charges multiple, car elle ne nécessite pas de garder en mémoire l'entièreté de l'historique des puissances thermiques extraites. La Figure 1-13 montre un exemple de création de petit et moyen blocs. Étant données les grandeurs de blocs $N_p = 2$, $N_m = 3$ et $N_g = 4$ et les périodes d'attente $PA_p = PA_m = PA_g = 6$, le cas présenté à la Figure 1-13 nécessite la création d'un petit bloc (a) car l'historique des charges contient $PA_p = 6$ charges instantanées. Ceci amène le nombre de petits blocs à atteindre la période d'attente pour la création d'un moyen bloc $PA_m = 6$ et entraîne alors la création d'un moyen bloc (b).

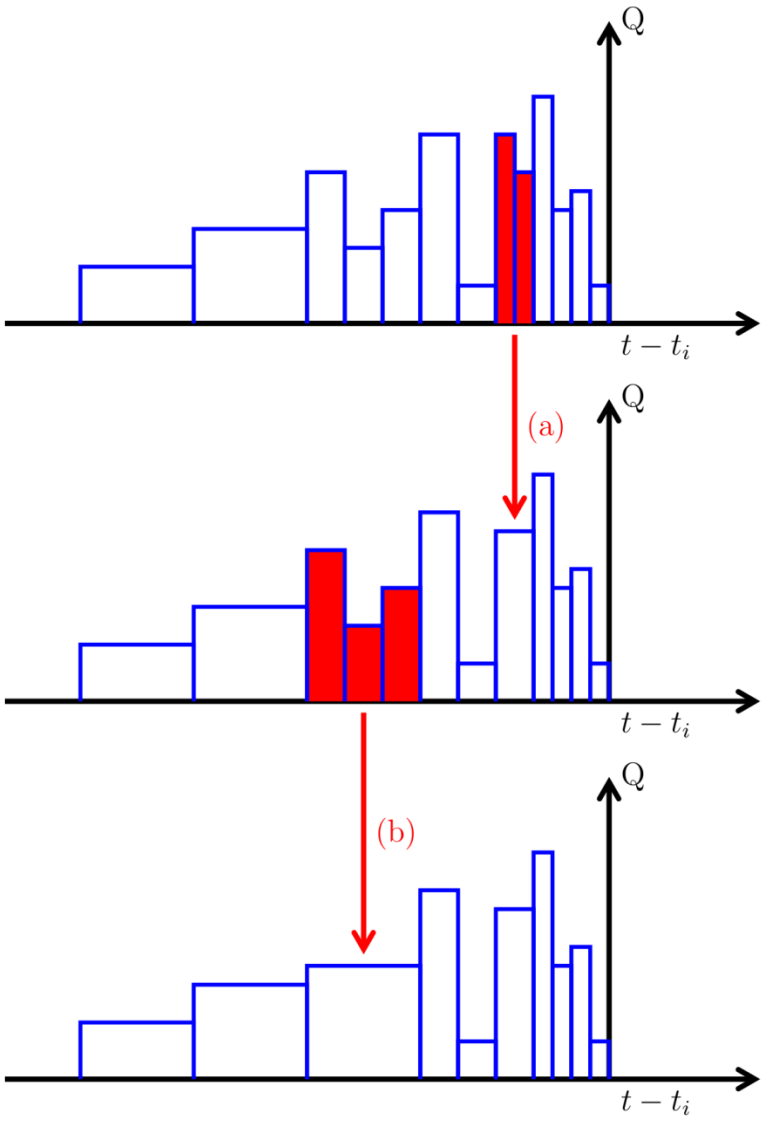

Figure 1-13: Création de blocs d'agrégation avec l'algorithme d'agrégation de Liu

Claesson & Javed (2012) proposent une autre amélioration à l'agrégation des charges. Les auteurs utilisent des cellules d'agrégation de nombre et de largeur fixés au début de la simulation. Les cellules sont de largeur croissante à mesure qu'on s'éloigne dans l'historique des charges. Les puissances thermiques sont dispersées d'une cellule à la suivante lorsque l'on passe d'un pas de temps au suivant. La charge moyenne $\bar{Q}_{i+1}^{(n+1)}$ de la cellule *i+1* au $(n+1)^{\text{ème}}$ pas de temps est alors calculée à partir des charges moyennes des cellules *i* et *i*+1 au $n^{\text{ème}}$ pas de temps:

$$\bar{Q}_{i+1}^{(n+1)} = \bar{Q}_i^{(n)} \frac{\Delta t}{\Delta t_{i+1}} + \bar{Q}_{i+1}^{(n)} \frac{\Delta t_{i+1} - \Delta t}{\Delta t_{i+1}} \tag{1.14}$$

Δt_i est la largeur de la cellule i et Δt est le pas de temps de la simulation. Un exemple de la dispersion des puissances thermiques est montré à la Figure 1-14. Tout comme la procédure d'agrégation de Liu (2005), cette méthode ne nécessite pas de garder en mémoire l'historique complet des puissances thermiques afin de calculer les charges moyennes à tous les pas de temps. De plus, puisque le nombre et la largeur des cellules sont connus au début de la simulation, le facteur de réponse thermique du champ de puits n'a besoin d'être calculé que pour les temps $t_k = \sum_{i=1}^{k} \Delta t_i$.

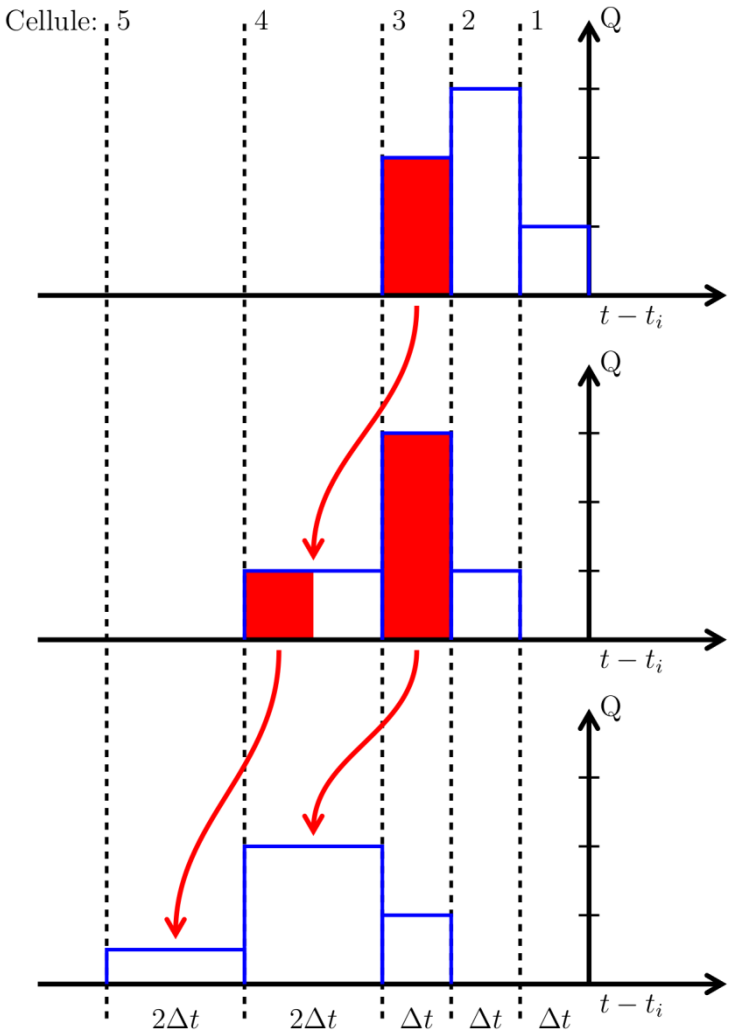

Figure 1-14: Dispersion des puissances thermiques avec l'algorithme d'agrégation de Claesson & Javed

Méthode de Lamarche & Beauchamp

Lamarche & Beauchamp (2007a) proposent un algorithme utilisant la solution de la source cylindrique infinie pour la simulation de systèmes géothermiques. La solution de la source cylindrique infinie est présentée sous forme de fonction de Green:

$$T_b(\tilde{t}) - T_g = \frac{-1}{\pi^2 k_s} \int_0^{\tilde{t}} Q(\tilde{\tau}) \int_0^{\infty} e^{-z^2(\tilde{t}-\tilde{\tau})} \frac{J_0(\tilde{r}_b z)Y_1(z) - J_1(z)Y_0(\tilde{r}_b z)}{J_1^2(z) + Y_1^2(z)} dz d\tilde{\tau} \qquad (1.15)$$

où $\tilde{t} = \frac{\alpha_s t}{r_b^2}$ et $\tilde{\tau} = \frac{\alpha_s \tau}{r_b^2}$ sont des nombres de Fourier, $\tilde{r}_b = \frac{r_b}{r_b} = 1$ est le rayon adimensionnel du puits.

En inversant l'ordre d'intégration:

$$\begin{aligned} T_b(\tilde{t}) - T_g &= \frac{-1}{\pi^2 k_s} \int_0^{\infty} \frac{J_0(\tilde{r}_b z)Y_1(z) - J_1(z)Y_0(\tilde{r}_b z)}{J_1^2(z) + Y_1^2(z)} \int_0^{\tilde{t}} e^{-z^2(\tilde{t}-\tilde{\tau})} Q(\tilde{\tau})\, d\tilde{\tau} dz \\ T_b(t) - T_g &= \frac{-1}{\pi^2 k_s} \int_0^{\infty} F(\tilde{t}, z)\, dz \end{aligned} \qquad (1.16)$$

La température au temps $\tilde{t} = \tilde{t} + \Delta\tilde{t}$ est donnée par:

$$\begin{aligned} & T_b(\tilde{t} + \Delta\tilde{t}) - T_g \\ &= \frac{-1}{\pi^2 k_s} \int_0^{\infty} \frac{J_0(\tilde{r}_b z)Y_1(z) - J_1(z)Y_0(\tilde{r}_b z)}{J_1^2(z) + Y_1^2(z)} \left(\int_0^{\tilde{t}} e^{-z^2(\tilde{t}+\Delta\tilde{t}-\tau)} Q(\tilde{\tau}) d\tilde{\tau} \right. \\ &+ \left. \int_{\tilde{t}}^{\tilde{t}+\Delta\tilde{t}} e^{-z^2(\tilde{t}+\Delta\tilde{t}-\tau)} Q(\tilde{\tau}) d\tilde{\tau} \right) dz \end{aligned} \qquad (1.17)$$

Supposant que $Q(\tilde{\tau})$ est constant sur l'intervalle $[\tilde{t}, \tilde{t} + \Delta\tilde{t}\,]$, la seconde intégrale pour $\tilde{\tau}$ peut être évaluée et la température au temps $\tilde{t} + \Delta\tilde{t}$ s'obtient à partir de la fonction $F(\tilde{t}, z)$.

$$
\begin{aligned}
&T_b(\tilde{t}+\Delta\tilde{t}) - T_g \\
&= \frac{-1}{\pi^2 k_s}\int_0^\infty e^{-z^2\Delta\tilde{t}}\frac{J_0(\tilde{r}_b z)Y_1(z) - J_1(z)Y_0(\tilde{r}_b z)}{J_1^2(z)+Y_1^2(z)}\int_0^{\tilde{t}} e^{-z^2(\tilde{t}-\tilde{\tau})}Q(\tilde{\tau})d\tilde{\tau}\,dz \\
&+ \frac{-1}{\pi^2 k_s}\int_0^\infty \frac{J_0(\tilde{r}_b z)Y_1(z) - J_1(z)Y_0(\tilde{r}_b z)}{J_1^2(z)+Y_1^2(z)}\left[Q(\tilde{t})\cdot\left(\frac{1-e^{-z^2\Delta\tilde{t}}}{z^2}\right)\right]dz
\end{aligned}
\tag{1.18}
$$

$$
\begin{aligned}
&T_b(\tilde{t}+\Delta\tilde{t}) - T_g \\
&\quad= \frac{-1}{\pi^2 k_s}\int_0^\infty e^{-z^2\Delta t}\,\boldsymbol{F}(\tilde{\boldsymbol{t}},\boldsymbol{z}) \\
&\quad+ \frac{J_0(\tilde{r}_b z)Y_1(z) - J_1(z)Y_0(\tilde{r}_b z)}{J_1^2(z)+Y_1^2(z)}\left[Q(\tilde{t})\cdot\left(\frac{1-e^{-z^2\Delta\tilde{t}}}{z^2}\right)\right]dz
\end{aligned}
\tag{1.19}
$$

$$
T_b(\tilde{t}+\Delta\tilde{t}) - T_g = \frac{-1}{\pi^2 k_s}\int_0^\infty F(\tilde{t}+\Delta\tilde{t},z)\,dz \tag{1.20}
$$

L'intégrale sur *z* converge rapidement et est résolue numériquement par les auteurs. Le gain en vitesse de calcul vient du fait que la fonction $F(\tilde{t}+\Delta\tilde{t},z)$ est obtenue à partir de sa valeur précédente $F(\tilde{t},z)$. L'algorithme est plus rapide que la méthode d'agrégation des charges multiple. Par exemple, une simulation horaire sur 2 ans est calculée en 1.39 s alors que la même simulation est calculée en 25.1 s avec la méthode d'agrégation des charges.

Lamarche (2009) généralise l'algorithme de Lamarche & Beauchamp (2007a) afin de permettre son application à n'importe quel facteur de réponse. Il s'agît de trouver une fonction *u(z)* satisfaisant:

$$
T_b(\tilde{t}) - T_g = -\frac{Q}{k_s}\cdot h(\tilde{t}) = -\frac{Q}{k_s}\cdot\int_0^\infty \left(1-e^{-z^2\tilde{t}}\right)u(z)dz \tag{1.21}
$$

où $h(\tilde{t})$ est le facteur de réponse thermique du champ de puits. La fonction $u(z)$ s'obtient par la transformée de Laplace inverse du facteur de réponse thermique:

$$
u(z^2) = -2z\mathcal{L}^{-1}\left(h(\tilde{t})\right) \tag{1.22}
$$

où $\mathcal{L}^{-1}$ représente la transformée de Laplace inverse. Lamarche effectue la transformée inverse à l'aide de l'algorithme Gaver-Stehfest (Stehfest, 1970). Connaissant la fonction $u(z)$, il est possible d'appliquer l'algorithme de Lamarche & Beauchamp:

$$T_b(\tilde{t}) - T_g = \frac{-1}{k_s}\int_0^{\infty} u(z)\int_0^{\tilde{t}} e^{-z^2(\tilde{t}-\tilde{\tau})}Q(\tilde{\tau})\,d\tilde{\tau}dz = \int_0^{\infty} F(\tilde{t},z)\,dz \tag{1.23}$$

$$T_b(\tilde{t}+\Delta\tilde{t}) - T_g = \frac{-1}{k_s}\int_0^{\infty} e^{-z^2\Delta\tilde{t}}\,\boldsymbol{F}(\tilde{\boldsymbol{t}},\boldsymbol{z}) + \left[Q(\tilde{t})\cdot\left(1-e^{-z^2\Delta\tilde{t}}\right)\cdot u(z)\right]dz \tag{1.24}$$

$$T_b(\tilde{t}+\Delta\tilde{t}) - T_g = \frac{-1}{k_s}\int_0^{\infty} F(\tilde{t}+\Delta\tilde{t},z)\,dz \tag{1.25}$$

Méthode spectrale

Marcotte & Pasquier (2008a) notent que la superposition temporelle des charges (Équation 1.12) est en fait un produit de convolution. Conformément au théorème de convolution, la somme peut être remplacée par un produit simple dans le domaine de Fourier:

$$\Delta T_b(t) = \mathcal{F}^{-1}\left(\mathcal{F}\left(\frac{q}{2\pi k_s}\right)\cdot\mathcal{F}(f)\right) \tag{1.26}$$

où $\mathcal{F}$ et $\mathcal{F}^{-1}$ sont les transformées de Fourier directe et inverse. Dans le cadre de simulations numériques, les transformées directe et inverse peuvent être évaluées à l'aide d'un algorithme de type *Fast Fourier Transform* (FFT).

L'utilisation de la méthode spectrale pour la simulation de systèmes géothermiques est décrite par Cimmino et al. (2012). La Figure 1-15 illustre la méthode spectrale. La longueur des vecteurs d'incrément de taux d'extraction de chaleur par unité de longueur (a) et de facteur de réponse thermique (b) est doublée par l'ajout de zéros. Un algorithme de type FFT est utilisé pour obtenir les incréments de taux d'extraction de chaleur (c) et le facteur de réponse thermique (d) dans le domaine de Fourier. Les deux vecteurs dans le domaine de Fourier sont multipliés (e) et la transformée de Fourier inverse donne la variation de température à la paroi du puits (f).

Pasquier & Marcotte (2013) montrent qu'il est possible d'utiliser la méthode spectrale pour évaluer les taux de transfert de chaleur requis, variables dans le temps, d'un nombre quelconque de sources de chaleur afin d'obtenir une température désirée à chacune des sources de chaleur. Les superpositions temporelles et spatiales sont effectuées dans le domaine de Fourier. Les taux de transfert de chaleur de chacune des sources sont déterminés suivant un processus itératif jusqu'à convergence des températures des sources de chaleur aux valeurs voulues.

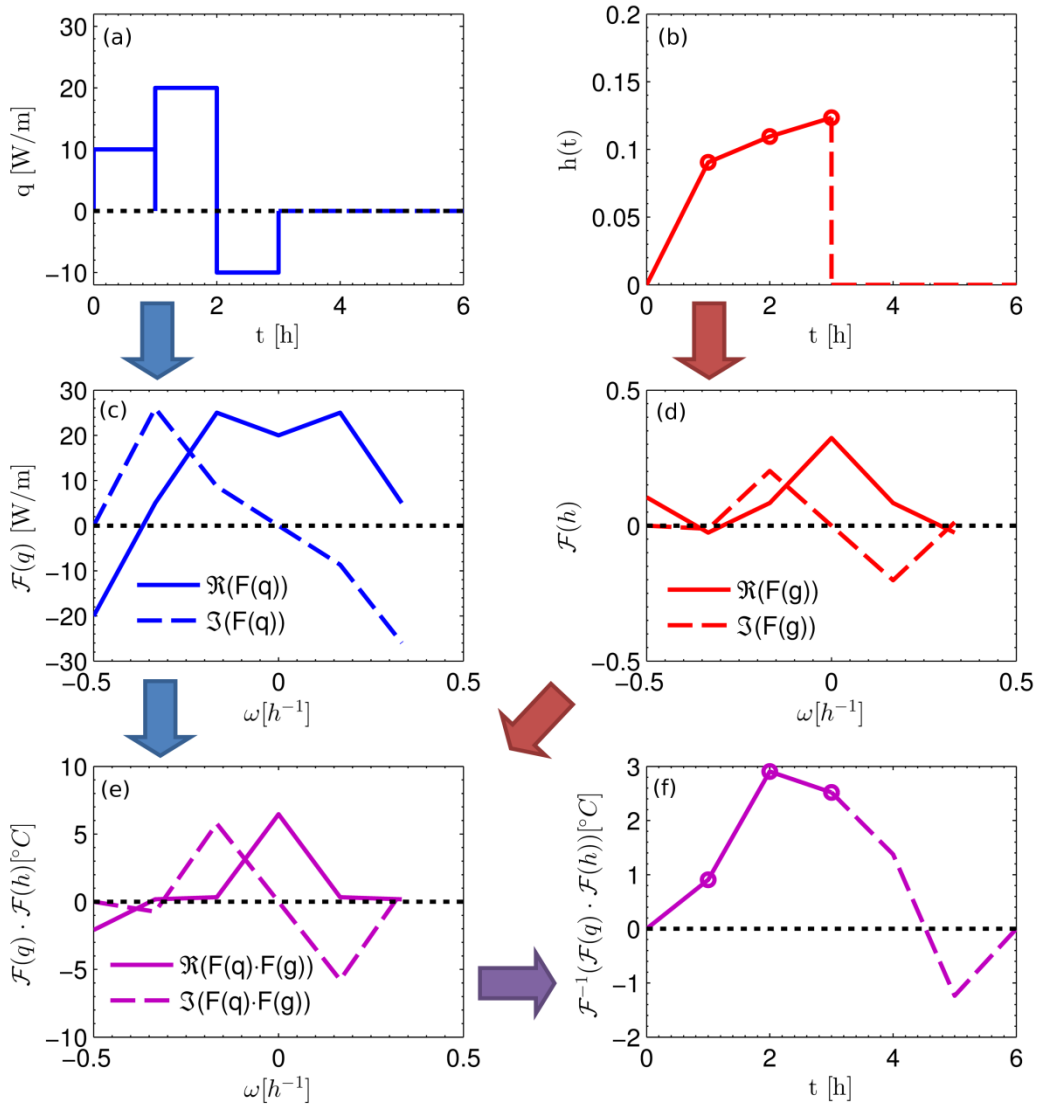

Figure 1-15: Illustration de la méthode spectrale pour la superposition temporelle des charges

La méthode spectrale est utilisée par Cimmino et al. (2013) pour simuler un système de capteurs géothermiques novateurs de faible profondeur. La superposition temporelle est effectuée dans le domaine de Laplace en utilisant un algorithme FFT pour calculer la transformée de Laplace numérique. Des bilans d'énergie sur le fluide caloporteur sont utilisés afin de tenir compte des différences de température entre les différents capteurs reliés en série. Une solution analytique du transfert de chaleur dans un milieu semi-infini permet de tenir compte de la variation de la température de l'air ambiant. Le modèle est validé à partir de mesures sur un système réel au cours d'une saison de chauffage (1289 h). Après une période transitoire initiale de 500 h, l'écart maximal entre les températures de fluide prédites et mesurées est de 1.4°C.

La simulation de systèmes géothermiques par l'emploi de la transformée de Fourier est plus rapide que les autres méthodes présentées précédemment, entre autres parce que les températures sont évaluées pour tous les pas de temps en une seule opération. Contrairement à la méthode d'agrégation des charges et à l'algorithme proposé par Lamarche & Beauchamp, la méthode par transformée de Fourier est une méthode exacte: il n'y a pas d'erreurs dues au moyennement des taux d'extraction de chaleur ou à l'inversion numérique d'une transformée de Laplace. Cependant, il faut noter que la méthode par transformée de Fourier s'intègre difficilement aux logiciels de simulation énergétique des bâtiments. En effet, la méthode nécessite de connaître à priori les taux d'extraction de chaleur — ou la température — à tous les pas de temps, tandis que les logiciels de simulation calculent les taux d'extraction de chaleur et les températures dans le champ de puits géothermique un pas de temps à la fois.

1.4 Conclusion

La revue de littérature présentée illustre les enjeux de la modélisation des systèmes géothermiques à puits verticaux. Un modèle complet pour la simulation de systèmes géothermiques se doit de considérer divers phénomènes thermiques apparaissant à des échelles de temps différentes. À court terme ($t \lesssim 12$ h), la capacité thermique du fluide circulant dans l'échangeur géothermique et celle du coulis jouent un rôle prédominant sur la réponse thermique de l'échangeur géothermique. À moyen ($12\text{ h} \lesssim t \lesssim 3$ ans) et long ($t \gtrsim 3$ ans) termes, l'interaction thermique entre les puits géothermiques et entre les puits et la surface du sol influencent la réponse thermique du champ de puits. À ces échelles de temps, les capacités

thermiques du fluide et du coulis peuvent être négligées et le lien entre le fluide et le sol peut être modélisé par une résistance thermique en régime permanent. Finalement, plusieurs techniques pour diminuer le temps nécessaire au calcul de la réponse thermique ont été présentées.

CHAPITRE 2 DÉMARCHE DE L'ENSEMBLE DU TRAVAIL DE RECHERCHE ET ORGANISATION GÉNÉRALE DU DOCUMENT

Le sujet principal du travail de recherche est la modélisation du transfert de chaleur dans les champs de puits géothermiques. Un modèle, basé sur des solutions analytiques, est proposé pour calculer les facteurs de réponse thermique des champs de puits géothermiques. Ces facteurs de réponse thermique peuvent être utilisés afin de faire la simulation des systèmes géothermiques et de dimensionner les champs de puits lors de leur conception.

En plus des articles de revues présentés dans la thèse, les travaux effectués ont mené à des collaborations avec d'autres chercheurs. La simulation des systèmes géothermiques en utilisant les facteurs de réponse thermique a été étudiée et les résultats ont été présentés à la conférence eSim 2012 (Cimmino et al., 2012). La modélisation de capteurs géothermiques novateurs de faible profondeur a été étudiée en collaboration avec EDF et les résultats ont été présentés au XI^{e} colloque interuniversitaire franco-québécois sur la thermique des systèmes (Cimmino, Bernier, & Cauret, 2013).

Un outil logiciel pour le calcul des facteurs de réponse thermique a été développé et présenté à la conférence BS2013 (Cimmino & Bernier, 2013).

2.1 Objectifs de la thèse

La thèse comporte deux objectifs principaux pouvant être séparés en multiples objectifs secondaires:

- Développer un modèle pour le calcul des facteurs de réponse thermique des champs de puits géothermiques:
    - Développer un modèle analytique qui tient compte de l'interaction thermique entre puits géothermiques;
    - Évaluer l'impact de la profondeur de tête de puits sur la réponse thermique des champs de puits;
    - Vérifier le modèle développé à partir de solutions numériques;

- Évaluer l'effet du positionnement des puits sur le dimensionnement des champs de puits.

- Déterminer expérimentalement le facteur de réponse thermique d'un puits géothermique:
  - Concevoir et construire un banc d'essai pour l'étude de la réponse thermique d'un puits géothermique;
  - Comparer la réponse thermique du puits obtenue expérimentalement au facteur de réponse thermique obtenu à partir du modèle développé.

2.2 Organisation de la thèse

La thèse comprend sept chapitres et suit le format d'une thèse par articles. Une revue critique de la littérature, présentée au Chapitre 1, couvre la modélisation du transfert de chaleur dans les champs de puits géothermiques et les algorithmes utilisés pour leur simulation. Le Chapitre 2 décrit les objectifs et l'organisation de la thèse.

Le Chapitre 3 présente le premier article intitulé « A contribution towards the determination of g-functions using the finite line source » et publié dans la revue *Applied Thermal Engineering* (Cimmino, Bernier, & Adams, 2013). L'article fait la revue détaillée des méthodes classiques pour l'obtention des facteurs de réponse thermique des champs de puits géothermiques et propose un modèle basé sur des solutions analytiques pour le calcul des facteurs de réponse thermique. Le modèle tient compte de la variation temporelle des taux d'extraction de chaleur de chacun des puits des champs en appliquant une condition de température moyenne à la paroi des puits égale pour tous les puits.

Le Chapitre 4 présente le second article intitulé « A semi-analytical method to generate g-functions for geothermal bore fields » et publié dans la revue *International Journal of Heat and Mass Transfer* (Cimmino & Bernier, 2014b). L'article présente un modèle étendu pour le calcul des facteurs de réponse thermique des champs de puits. Le modèle permet le calcul des facteurs de réponse thermique pour des puits de longueurs inégales disposés de façon arbitraire. Les facteurs de réponse thermique sont calculés pour trois différentes conditions frontières à la paroi des puits et sont comparés à des facteurs de réponse thermique obtenus à l'aide d'un modèle numérique de référence. Ce chapitre complète le premier objectif de la thèse, soit le

développement d'un modèle pour le calcul des facteurs de réponse thermique des champs de puits géothermiques.

Le Chapitre 5 présente le troisième article intitulé « Unequal borehole spacing to reduce borehole length » et publié dans *ASHRAE Transactions* (Cimmino & Bernier, 2014a). Le modèle présenté dans les deux chapitres précédents est utilisé pour étudier l'effet du positionnement des puits et du nombre de puits sur le dimensionnement des champs de puits géothermiques. Les dimensions des champs de puits sont obtenues à partir de simulations horaires sur vingt années d'opération pour deux scénarios de charges au sol. La longueur requise des puits est présentée pour différentes configurations de champs puits.

Le Chapitre 6 présente le quatrième et dernier article intitulé « Experimental determination of the g-functions of a small-scale geothermal borehole » et soumis à la revue *Geothermics*. L'article fait la description d'un banc d'essai conçu et construit pour obtenir expérimentalement le facteur de réponse thermique d'un puits géothermique. Un puits miniature est instrumenté et la variation de la température à la paroi du puits suite à l'injection d'une puissance thermique constante durant une semaine est utilisée pour déterminer le facteur de réponse du puits. Le facteur de réponse thermique est ensuite comparé au facteur de réponse thermique obtenu avec le modèle analytique. Ce chapitre complète le second objectif de la thèse, soit la détermination expérimentale du facteur de réponse thermique d'un puits géothermique.

Le Chapitre 7 présente une discussion des résultats obtenus. Ce chapitre est suivi des recommandations pour les futurs travaux.

CHAPITRE 3 ARTICLE 1 : A CONTRIBUTION TOWARDS THE DETERMINATION OF G-FUNCTIONS USING THE FINITE LINE SOURCE

Cimmino, M., Bernier, M., & Adams, F. (2013). A contribution towards the determination of g-functions using the finite line source. *Applied Thermal Engineering*, 51(1-2), 401-412.

ABSTRACT

This paper examines the thermal response of bore fields using the concept of g-functions introduced by Eskilson. In the first part of the paper, the original concept of the g-functions is reviewed. Then, a new method is proposed to approximate the g-functions. The method accounts for the variation of heat extraction rates among boreholes due to thermal interaction among boreholes and for the buried depth to borehole height ratio (D/H) which was not included in Eskilson's original work. The new method is based on the analytical finite line source and the solution is not limited to regular borehole spacing. Borehole-to-borehole and group-to-borehole response factors are evaluated and then temporal superposition of heat extraction rates is applied in the Laplace domain. The heat extraction rates obtained with the proposed method showed good agreement with Eskilson's numerical model. The differences observed can be explained by the fact that two different boundary conditions are used at the borehole wall. However, for small simulation times, the differences are small and the response factors are almost identical for up to 10 and 6 years for 3 × 2 and 10 × 10 bore fields, respectively. For large bore fields, thermal interactions among boreholes become important and the differences observed between the proposed model and the g-function increase. For instance, the g-function of a 10 × 10 bore field obtained with the proposed method overestimates the g-function by 32 % at steady-state. Finally, the effect of the buried depth (D) is examined using the proposed method. It is shown that the response factor of a 5 m borehole buried at depths of 1 and 3 m differ by 19%.

3.1 Introduction

A typical bore field geometry is presented in Figure 3-1. It consists of 6 boreholes of radius rb, separated by a distance B and positioned in a rectangular 3×2 pattern. The height of the borehole is H and the head of each borehole is buried at a distance D from the ground surface. Generally, as indicated in Figure 3-1, boreholes are hooked up in parallel and each borehole is fed with a fluid at the same temperature, $T_{in,ground}$. Heat transfer inside the borehole is a function of the pipe positions and of the thermal resistance and thermal capacity caused by the presence of the grout. The heat transfer rate from the borehole wall to the ground depends on the ground thermal conductivity, k_s, thermal diffusivity, α_s, and far-field temperature, T_g.

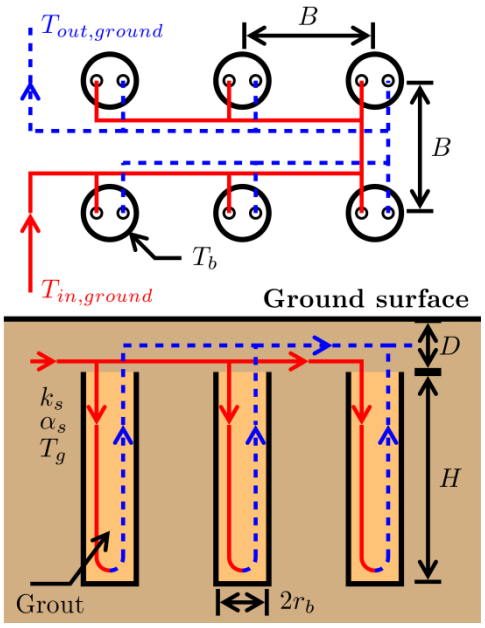

Figure 3-1: Typical bore field geometry

Eskilson introduced the concept of g-functions in 1987 (Eskilson, 1987). The g-functions give a relation between the heat extracted from the ground at the borehole wall $q(t)$ and the borehole wall temperature T_b. The borehole wall temperature is given by:

$$T_b = T_g - \frac{q(t)}{2\pi k_s} g(t/t_s, r_b/H, B/H) \tag{3.1}$$

where g represents the g-function. As shown in Equation 3.1, g-functions depend on three non-dimensional parameters: B/H, the bore field aspect ratio; r_b/H, the non-dimensional borehole radius; and t/t_s, a non-dimensional time where t_s is a characteristic time (= $H^2/9\alpha_s$). Eskilson's non-dimensional analysis introduced a fourth non-dimensional parameter, *D/H*. However, it was not explicitly used in his studies as he used a fixed value of D (= 4 or 5 m). These g-functions have been generated using two-dimensional (radial and axial) numerical simulations combined with spatial superposition to effectively obtain a three-dimensional response of the bore field subjected to a uniform (over the height) borehole wall temperature, T_b, for every borehole in the bore field. Typical g-functions, digitized from Eskilson's original work, are presented in Figure 3-2 for a 3 × 2 bore field.

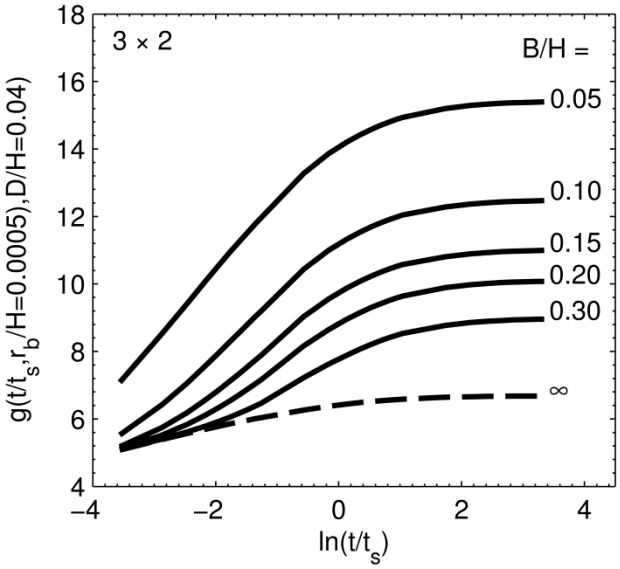

Figure 3-2: g-functions for a 3 × 2 bore field

As shown in Figure 3-2, the g-functions are presented graphically for a particular geometry as a function of $\ln(t/t_s)$ for a bore field spacing (B/H) and for a given value of r_b/H. The curve for $B/H = \infty$ corresponds to the g-function of a single borehole.

The curves are linear for small values of time, when axial heat conduction is negligible and heat transfer is essentially one-dimensional in the radial direction. For very long times $\ln(t/t_s) > 3$, the curves reach a plateau indicating that the bore field operates in steady-state, i.e. the borehole

wall temperature is constant for a given $q(t)$. For large values of B/H and small values of time, thermal interaction among boreholes is negligible and the resulting g-functions are equal to the g-function for a single borehole.

It is important to note that the borehole thermal capacity is not accounted for in the original g-functions. Therefore, if only the heat transfer rate in the fluid is known, then one has to evaluate the time it takes for a heat impulse in the fluid to reach steady-state at the borehole wall in order to properly use the g-functions which are valid for a heat transfer rate applied to the borehole wall. This time has been evaluated by Eskilson to be equal to $t_b = 5r_b^2/\alpha_s$, where t_b is defined by Eskilson as the borehole time and α_s is the thermal diffusivity of the ground. The borehole time corresponds to the time at which the difference between the g-function and the infinite line source (ILS) solution falls below 10 %. Ingersoll et al. (Ingersoll et al., 1950) proposed a lower time limit of $20r_b^2/\alpha_s$, which corresponds to a difference of 3 % between the ILS and the g-function (Philippe et al., 2009). For times greater than t_b, the heat extraction rate at the borehole wall is assumed to be the same as at the U-tube pipes and the interior of the borehole is approximated by a steady-state thermal resistance. Typical values of t_b are of the order of 3 to 6 hours (Yavuzturk & Spitler, 1999) which can be a serious limitation when performing annual hourly simulations. The lower time limit is the reason why Eskilson's g-function are sometimes referred to "long-time response factors" (Yavuzturk & Spitler, 1999).

The present authors consider that the inside and outside of boreholes should be modelled separately with the borehole wall acting as the interface. The model for the borehole interior should account for the thermal capacity as well as the thermal interactions between the fluid loop and the borehole wall. The outside model should take care of the thermal phenomenon from the borehole wall to the surrounding ground and the other boreholes. The lower time limit for the validity of the g-functions depends mainly on the model of the interior of the borehole. The g-function as a model of the borehole exterior is valid for all times since it is the solution to the thermal response of a borehole extracting heat at its wall.

As noted in Figure 3-2, g-functions are usually calculated for r_b/H = 0.0005. Eskilson proposes a correlation for small variations of the r_b/H ratio. For a ratio $\frac{r_b^*}{H} \neq \frac{r_b}{H}$, the g-function becomes:

$$g\left(\frac{t}{t_s},\frac{r_b^*}{H},\frac{B}{H}\right) = g\left(\frac{t}{t_s},\frac{r_b}{H},\frac{B}{H}\right) - \ln\left(\frac{r_b^*}{r_b}\right) \quad (3.2)$$

where $\ln(r_b^*/r_b)$ is the non-dimensional thermal resistance of an annulus with inner and outer radii r_b and r_b^*.

Eskilson's g-functions are used in a number of ground heat exchanger design tools and energy simulation software programs (H. Yang, Cui, & Fang, 2010), e.g. EED, GLHEPRO, EnergyPlus (Fisher, Rees, Padhmanabhan, & Murugappan, 2006). In these tools g-functions have been pre-calculated and included in a database containing a large number of bore field configurations. Users, however, are restricted to these configurations.

The objective of this paper is twofold: first, provide a comprehensive review of Eskilson's model and to illustrate the difference between the g-functions provided by Eskilson and those obtained using the Finite Line Source (FLS) analytical solution often used to model boreholes which assumes that each borehole is subjected to the same heat transfer rate at the borehole wall. Secondly, a new method based on the FLS solution is proposed to approximate the g-functions while accounting for thermal interaction among boreholes.

Thermal interaction affects the thermal response of boreholes based on their proximity to each other and their position in the bore field. In a field of boreholes that are fed in parallel, heat is extracted from the ground through a fluid entering all boreholes at the same temperature. However, heat extracted by individual boreholes varies as each borehole is surrounded by a different thermal surrounding. The new method presented in this paper accounts for the time variation of the heat extraction rates among boreholes. The resulting g-functions obtained using the new method are compared to Eskilson's g-functions.

3.2 Litterature review

Eskilson (1987) solved the heat transfer problem in a bore field using a finite difference method. The problem is solved for zero initial temperature and for a constant average heat flux extracted from the ground. All boreholes within a field share the same uniform (over the height) wall temperature. This approximation is reasonable considering that all boreholes are connected in parallel and that the fluid experiences small temperature variations along the borehole height. The temperature of the ground is obtained by spatial superposition of the individual two-dimensional

(radial-axial) temperature distributions for each borehole in the field. The zero ground surface temperature boundary condition is assured by applying the method of images to the numerical solution.

Yavuzturk and Spitler (1999) extended Eskilson's g-functions for shorter time steps. The heat transfer from the fluid to the borehole wall and the borehole surroundings was modelled using a finite volume approach. The grout and pipe thermal resistance and thermal capacitance were taken into account. In order to adhere to Eskilson's definition of the g-functions (Equation 3.1), the authors subtracted the contribution of the steady-state thermal resistance of the borehole to the thermal response. This resulted in a negative borehole wall temperature for times approaching zero, as later noted by Yavuzturk et al. (2009). The model was validated using monitored field data and results were presented for a time period of 1 year (Yavuzturk & Spitler, 2001). The results showed good agreement between the model and the measurements. Yavuzturk et al. (2009) proposed a one-dimensional finite element model of the borehole interior and coupled this model to the cylindrical heat source analytical solution (CHS) (Bernier, 2001; Carslaw & Jaeger, 1946a; Cooper, 1976). In the finite element model, the U-tube is replaced by an equivalent diameter pipe at the center of the borehole. Therefore, thermal interaction between pipes inside the borehole is neglected.

The problem of short-time response of boreholes was addressed by several other authors. Beier & Smith (Beier & Smith, 2003) obtained an analytical solution in the Laplace domain. The solution used a single pipe of equivalent diameter and was based on the assumption that the fluid and pipe temperatures are equal. The time domain solution was obtained through the numerical inversion of the analytical solution using the Gaver-Stehfest algorithm for the numerical inversion of the Laplace transform (Stehfest, 1970). Bandyopadhyay et al. (Bandyopadhyay, Kulkarni, et al., 2008) developed an analytical solution in the time domain where the grout and the surrounding ground have the same properties. The fluid is modeled as a virtual solid and the convection coefficient between the fluid and the pipe as well as the resistance of the pipe are accounted for. Even though the model is only applicable to boreholes backfilled with borehole cuttings, the solution proposed is relatively simple to use. Bandyopadhyay et al. (Bandyopadhyay, Gosnold, et al., 2008) proposed an analytical solution in the Laplace domain that takes into account the thermal capacities of the fluid and the grout and can handle different thermal properties for the grout and the ground. The solution in the time domain is obtained by a numerical inversion of the

analytical solution using the Gaver-Stehfest algorithm, as used in (Beier & Smith, 2003). Lamarche & Beauchamp (2007c) proposed an analytical solution in the time domain for heat injected at the wall of an equivalent diameter pipe. This solution takes into account the thermal properties of both the grout and the ground. Javed & Claesson (2011) developed an analytical solution that considers the thermal properties of the fluid, the pipes, the grout and the surrounding ground. The U-tube pipes are replaced by an equivalent diameter pipe. The authors showed that the problem can be illustrated as a thermal network in the Laplace domain. The solution is given in the time domain in the form of a single integral. The model has been validated using a finite differences numerical model. An exhaustive review for the short-time response of borehole heat exchangers was made by Javed et al. (2010; 2009).

Since the number of available configurations is limited, one might prefer an analytical solution over the use of g-functions. Eskilson (1987) proposed an analytical approximation of the g-functions in the form of a finite line source (FLS) evaluated at the mid-height of the borehole and at $r = \sqrt{1.5} \cdot r_b$. This radius corresponds to the radius of an ellipsoid with the same volume as the borehole. As noted by Eskilson, isotherms created by the FLS tend to resemble to slightly distorted ellipsoids and thus, the chosen radius for the evaluation of the FLS approximates the borehole wall temperature better than if the FLS were evaluated at the borehole radius. Zeng et al. (2002) later presented a methodology to calculate the temperature in a bore field using the FLS. The authors compared results for the temperature calculated at mid-height as suggested by Eskilson and the integral mean temperature over the borehole height. The integral mean temperature showed better results. Lamarche & Beauchamp (2007b) simplified the FLS solution from a double integral to a single integral, thereby reducing considerably the time required to calculate the integral mean temperature over the borehole height. The g-functions obtained using the FLS were compared with the results of Eskilson for fields of 2 boreholes and 4 boreholes in a square configuration. Lamarche (2009) later presented a comparison for a 2 × 8 bore field. The g-function evaluated by the FLS tended to overestimate Eskilson's g-function for large values of time. Fossa (2011) presented g-functions calculated using the FLS for bore fields of 9 boreholes in a square and for 2 × 8 boreholes in a rectangle. Fossa's results were similar to Lamarche's as the g-functions of Eskilson were overestimated by the FLS solution. The difference becomes more important as the spacing to height ratio (B/H) becomes smaller and thermal interaction between boreholes becomes more important.

Bandos et al. (2009) gave an approximation for the integral mean temperature obtained by the FLS. The approximation was used to estimate the thermal properties of the ground from thermal response test data (Bandos et al., 2011), taking into account the variation of air temperature at the ground surface. The thermal conductivity of the ground obtained using the FLS approximation were lower than those obtained using the standard one-dimensional infinite line source (ILS) approximation, as a result of modelling the finite length of the borehole.

Claesson & Javed (2011) proposed a formulation for the integral mean temperature in a bore field where boreholes are buried at a distance D from the ground surface. Contrary to Zeng et al. (2002) and Lamarche & Beauchamp (2007b), the point heat source integral used to define the FLS was integrated in space first and the solution is given in the form of an integral in the time domain. This results in a simpler formulation of the solution and it leads to identical results. The FLS solution of Claesson & Javed was coupled to the author's short-time response model (Javed & Claesson, 2011) by defining a breaking time at 100 hours. The temperature for times below the breaking time are obtained using the short-time response model. The temperature for times greater than the breaking point are obtained by adding the difference between the short-time response and the FLS solution at the breaking time to the FLS solution. The model was compared to Eskilson's g-functions for fields of one borehole, 3 boreholes in a line and 9 boreholes in a square. The results are in good agreement with the g-functions for a period up to approximately 25 years and then they underestimate the g-functions. However, the model evaluates the temperature of the fluid in the borehole while the g-functions can only calculate the borehole wall temperature.

The differences observed between the FLS solution and the g-functions of Eskilson can be explained by the differences between the boundary conditions at the borehole wall. In Eskilson's model, all boreholes within a field share the same wall temperature and the total heat extraction rate in the field is constant. As a result, the heat injected into the ground varies from borehole to borehole, along their height and in time. On the other hand, the FLS solution is based on a heat extraction rate that is constant along the height of the boreholes, from borehole to borehole and in time.

Zeng et al. (2003) coupled the FLS evaluated at mid-height to a resistance model of the interior of a borehole equipped with double U-tube pipes. The steady-state resistances between the

U-tube pipes and between each pipe and the borehole wall are taken into account. Eslami-Nejad and Bernier (2011) expanded the model to take into account different fluids and flow rates in each circuit. However, these models neglect the thermal capacitance of the borehole. Man et al. (2011) used Zeng's model to design and simulate a hybrid ground-coupled heat pump system.

Duan et al. (2007) used the FLS in order to model the heat exchange between a power transmission tower and the surrounding ground. The authors calculated the temperature distribution in the surrounding ground for an assumed heating strength profile over the tower foundation height. Results were in good agreement with the classical pin fin solution. Duan & Naterer (2008b) later proposed a method for time-varying surface temperature and heating strength from the tower foundation. An approximation for a sinusoidal variation of the heating strength over time is also developed. The model is validated experimentally (Duan & Naterer, 2008a) and the results are compared for different assumptions on the heating strength profile.

3.3 The case of a single borehole

A number of analytical source solutions are hereby compared to Eskilson's g-function for a single borehole. The three analytical heat sources (infinite line source, cylindrical heat source and finite line source) are presented and expressed in terms of r_b/H and t/t_s in order to adhere to Eskilson's definition of the g-functions (Equation 3.1).

3.3.1 Infinite line source

The use of the Infinite line source (ILS) for modeling borehole heat exchangers was introduced by Ingersoll et al. (1950). It consists of a one-dimensional solution to heat transfer from a heat source of infinite length. The response factor at a distance r from the line source obtained using the ILS is as follows:

$$f(t,r) = \int_{\frac{r}{2\sqrt{\alpha t}}}^{\infty} \frac{\exp(-\beta^2)}{\beta} d\beta \tag{3.3}$$

It can be shown that the terms in Equation 3.3 can be rearranged to express the response factor in terms of t/t_s and r_b/H by introducing a variable change $s = \beta^2$:

$$g_{ILS}(t/t_s, r_b/H) = \frac{1}{2}\int_{\frac{9}{4}\cdot\frac{(r_b/H)^2}{t/t_s}}^{\infty} \frac{\exp(-s)}{s}\,ds \tag{3.4}$$

3.3.2 Cylindrical heat source

The solution to the heat transfer from an infinite hollow cylinder in the radial direction was introduced by Carslaw & Jaeger (1946a) and applied to borehole heat exchangers by Ingersoll et al. (1950). The solution was presented by Ingersoll et al. in terms of the G-factor:

$$G(Fo, p) = \frac{1}{\pi^2}\int_0^{\infty} \frac{\exp(-s^2 Fo) - 1}{J_1^2(s) + Y_1^2(s)}\left[J_0(ps)Y_1(s) - J_1(s)Y_0(ps)\right]\frac{ds}{s^2} \tag{3.5}$$

where J and Y are Bessel functions of the first and second kind, $Fo = \alpha t/r_b^2$ is the Fourier number and $p = r/r_b$ is the ratio of the radius of evaluation of the temperature response to the radius of the borehole. The response factor for a single borehole can be obtained from the G-factor by expressing Fo in terms of r_b/H and t/t_s and for p = 1:

$$g_{CHS}(t/t_s, r_b/H) = 2\pi \cdot G\left(\frac{1}{9}\left(\frac{r_b}{H}\right)^{-2}\frac{t}{t_s}, 1\right) \tag{3.6}$$

The Cylindrical heat source (CHS) is particularly useful when modelling the borehole wall temperature response at shorter time-steps when the borehole can't be approximated by a line source. However, the evaluation of the integral in Equation 3.5 is computationally intensive. Ingersoll et al. (1950) presented tabulated values of the G-factor for values of $p = \{1, 2, 5, 10\}$. Bernier (2001) presented an approximation of the G-factor obtained by curve fitting the solution of Equation 3.5.

3.3.3 Finite line source

Claesson & Javed (2011) presented the following formulation for the integral mean temperature at a distance r of a finite length line heat source extending from $z = D$ to $z = D + H$. The surface z = 0 is maintained at a temperature T = 0. The heat source has a strength q_0.

$$\overline{T}(r, t) = \frac{q_0}{4\pi k_s}\int_{1/\sqrt{4\alpha_s t}}^{\infty} \frac{\exp(-r^2 s^2)\, Y(Hs, Ds)}{Hs^2}\,ds \tag{3.7}$$

$$Y(h,d) = 2 \cdot \text{ierf}(h) + 2 \cdot \text{ierf}(h+2d) - \text{ierf}(2h+2d) - \text{ierf}(2d) \quad (3.8)$$

$$\text{ierf}(X) = X \cdot \text{erf}(X) - \frac{1}{\sqrt{\pi}}(1 - \exp(-X^2)) \quad (3.9)$$

From Equations 3.1 and 3.7-3.9, the response factor g_{FLS} at a distance r of a borehole at a time t is:

$$g_{FLS}(t/t_s, r/H, D/H) = \frac{1}{2}\int_{\sqrt{9/(4\alpha_s t/t_s)}}^{\infty} \frac{\exp(-(r/H)^2 s^2)\, Y(s, D/H\, s)}{s^2} ds \quad (3.10)$$

this expression forms the basis of the proposed method to approximate the g-functions of bore fields. It is worth noting that an additional non-dimensional parameter, D/H, has been added. This parameter is not explicitly included in Eskilson's original g-functions.

3.3.4 g-function

The g-functions presented by Eskilson (1987) are the result of a numerical simulation of the heat transfer between the ground and the borehole wall using a finite difference method. The ground surrounding the borehole is divided in a two-dimensional radial-axial mesh with cells of variable sizes with smaller mesh heights near the borehole extremities. Similarly, the width of the cells is smaller close to the borehole wall. An illustration of the type of cell used by Eskilson is shown in Figure 3-3.

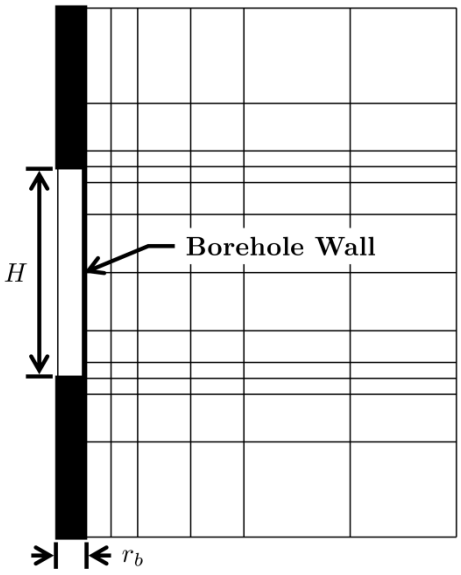

Figure 3-3: Example of a mesh used by Eskilson for the calculation of the g-functions

The total heat extraction rate in the bore field is constant. However, the heat extraction rate over each cell along the borehole height may vary and is calculated at every time step in order to obtain a uniform temperature at the borehole wall over the full height. The zero ground surface temperature is obtained using the method of images. As such, the temperature field around the borehole is superimposed to a symmetric temperature field with temperatures of opposite sign, taking the ground surface as an axis of symmetry. A near-complete description of the model is given in Eskilson's Manual for Computer Code (Eskilson, 1986) which is often referred to as the Superposition Borehole Model (SBM). Figure 3-4 shows the g-function for a field of one borehole with r_b/H = 0.0005 and D/H = 0.04 along with the response factors calculated with the three analytical source solutions presented earlier. The top x-axis has been added to relate the non-dimensional x-axis on the bottom to real times for a typical borehole height and ground thermal diffusivity.

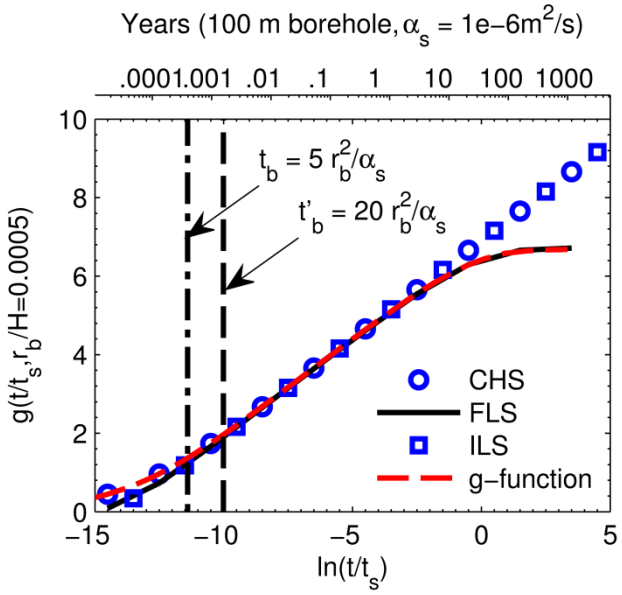

Figure 3-4: Comparison of the analytical heat sources solutions and the g-function for a single borehole

For small values of time, the response factor calculated with the CHS is equal to the g-function while the ILS and the FLS give a smaller value for the response factor. The difference can be explained by the fact that heat is extracted at the borehole wall in the case of the g-function and

the CHS, while it is extracted at the center of the borehole in the case of the ILS and the FLS. Also, the similar values obtained by the CHS and the g-function and by the ILS and the FLS show that axial conduction effects are negligible for small values of time. The borehole time tb, as defined by Eskilson, gives a good approximation of the time at which the ILS and the FLS can be used to approximate the g-function. The time t_b' defined by Ingersoll gives a more severe criterion of validity for the ILS and FLS. As shown on the top-axis in Figure 3-4, this time is attained after 3.5 and 14 hours for Eskilson and Ingersoll criteria, respectively.

For times $t > t_s/10$ ($\ln(t/t_s) > -2.3$), axial conduction effects become more important: the response factors calculated with the CHS and the ILS both continue to grow indefinitely while the FLS and the g-function both converge to a steady-state value of 6.7. The g-function and the FLS are almost identical for large values of time. However, as will be demonstrated later, this might not be the case for bore fields.

3.4 Proposed method

The proposed method aims to approximate the g-functions of Eskilson using the FLS. The method takes into consideration the time variation of the heat extraction rate among boreholes, while keeping the overall heat extraction rate of the bore field constant over time, to obtain a mean borehole wall temperature common to all boreholes. This boundary condition is used to replicate the operation of boreholes that are fed in parallel. Since all boreholes receive the same inlet fluid temperature and that the fluid temperature rise is small (3-5 ºC), the mean fluid temperatures inside the boreholes should be similar for every borehole. The borehole wall temperatures should therefore tend to the same value provided that the borehole completion methods (grouting and pipe spacing) are similar. This condition differs from the classical spatial superposition of the FLS (Sherrif, 2007), where the heat extraction rates are the same for all boreholes and the temperature distributions around every borehole are added in order to calculate the borehole wall temperatures. In this case, thermal interaction among boreholes is not properly taken into account since the ability of an individual borehole to extract heat is not affected by the presence of the other boreholes in the field.

The method is best explained using an example. The case of a field of 3 × 2 boreholes of height H = 100 m and radius r_b = 0.05 m buried at a distance D = 4 m from the ground surface and

equally spaced at a distance B = 5 m is studied in this section. The ground thermal conductivity is k_s = 2 W/m.K and the ground thermal diffusivity is α_s = 1 e-6 m^2/s. Figure 3-5 shows the corresponding borehole geometry.

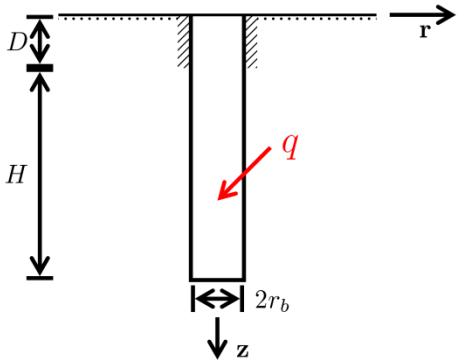

Figure 3-5: Borehole geometry

The boreholes in the field are arranged in N_{sym} symmetry groups. Eskilson (1986) defined a symmetry group as a group of boreholes where every borehole sees the same surroundings. In addition, every borehole in a symmetry group shares the same inlet temperature and fluid flow. Therefore, all boreholes of a symmetry group extract the same amount of heat from the surrounding ground for any given time t. Figure 3-6 shows the two different symmetry groups for the case of a 3 × 2 bore field.

Figure 3-6: Symmetry groups in a 3 × 2 bore field

The borehole-to-borehole response factors g_i' are now evaluated for all different distances d_i separating 2 boreholes and for the case $d_0 = r_b$. Figure 3-7 shows these distances for a 3 × 2 bore field.

The borehole-to-borehole response factors are defined as follows:

$$g_i'(t/t_s) = g_{FLS}(t/t_s\,, d_i/H\,, D/H) \tag{3.11}$$

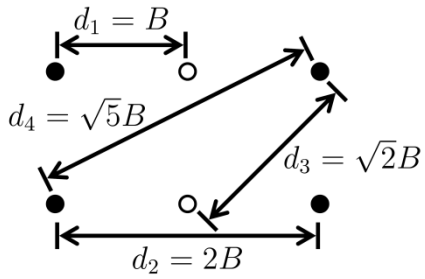

Figure 3-7: Distances in a 3 × 2 bore field

The group-to-borehole response factors G_{uv} are constructed from the borehole-to-borehole response factors. The response factors G_{uv} result from the sum of the borehole-to-borehole response factors for all distances between the boreholes of symmetry group v and an arbitrary borehole from symmetry group u. As a result, the response factors G_{uv} give the thermal response of symmetry group u in reaction to heat being extracted by boreholes in symmetry group v. In the case of a 3 × 2 bore field, the group-to-borehole response factors are as follows:

$$G_{11}(t/t_s) = g_0'(t/t_s) + g_1'(t/t_s) + g_2'(t/t_s) + g_4'(t/t_s) \tag{3.12}$$

$$G_{22}(t/t_s) = g_0'(t/t_s) + g_1'(t/t_s) \tag{3.13}$$

$$G_{12}(t/t_s) = g_1'(t/t_s) + g_3'(t/t_s) \tag{3.14}$$

$$G_{21}(t/t_s) = 2g_1'(t/t_s) + 2g_3'(t/t_s) \tag{3.15}$$

In order to take into account the varying heat fluxes, temporal superposition is applied to the response factors. The non-dimensional average borehole wall temperature Θ_b is obtained from the contribution of all symmetry groups. Since Θ_b is the same for all boreholes, it can be obtained by superposition of the response factors at any symmetry group.

$$\Theta_b(t) = \sum_{i,t_i \le t} [q_1'(t_i) \cdot G_{11}((t - t_i)/t_s) + q_2'(t_i) \cdot G_{12}((t - t_i)/t_s)] \tag{3.16}$$

$$\Theta_b(t) = \sum_{i,t_i \le t} [q_1'(t_i) \cdot G_{21}((t - t_i)/t_s) + q_2'(t_i) \cdot G_{22}((t - t_i)/t_s)] \tag{3.17}$$

where $q'_k(t_i) = q_k(t_i) - q_k(t_{i-1})$ is the non-dimensional heat extraction rate increment for boreholes in symmetry group k. $q_k(t_i)$ is the non-dimensional heat extraction rate for boreholes in symmetry group k at time t_i. It corresponds to the ratio between the heat extraction rate of a borehole in symmetry group k and the average heat extraction rate of all the boreholes in the field. It is convenient to introduce an additional equation to complete the equation set. This equation simply states that the total non-dimensional heat extraction rate is equal to the number of boreholes in the field multiplied by the average non-dimensional heat extraction rate of all boreholes $\bar{q}(t)$:

$$n_t \cdot \bar{q}(t) = \sum_{i=1}^{N_{sym}} n_i \cdot q_i(t) \tag{3.18}$$

where n_t is the total number of boreholes in the field and n_i is the number of boreholes in symmetry group i and $\bar{q}(t) = 1$.

The convolution products in Equations 3.16-3.17 are then expressed in the Laplace domain. The use of spectral methods to solve the temporal superposition of the loads in geothermal bore fields was first proposed by Marcotte & Pasquier (2008a). The authors used fast Fourier transforms to take advantage of the convolution theorem, which states that a convolution product in the time domain is equivalent to a simple multiplication in the frequency domain. The numerical Laplace transform is chosen here to avoid time aliasing errors that are difficult to overcome using Fourier transforms in the present case.

$$\mathcal{L}(\Theta_b) = \mathcal{L}(q'_1) \cdot \mathcal{L}(G_{11}) + \mathcal{L}(q'_2) \cdot \mathcal{L}(G_{12}) \tag{3.19}$$

$$\mathcal{L}(\Theta_b) = \mathcal{L}(q'_1) \cdot \mathcal{L}(G_{21}) + \mathcal{L}(q'_2) \cdot \mathcal{L}(G_{22}) \tag{3.20}$$

An overview on the use of the numerical Laplace transform to solve the temporal superposition is presented in Appendix A. In the Laplace domain, the total non-dimensional heat extraction rate increment q'_t is equal to the sum of the non-dimensional heat extraction rate increment of every borehole in the field.

$$\mathcal{L}(q'_t) = \sum_{i=1}^{N_{sym}} n_i \cdot \mathcal{L}(q'_i) \tag{3.21}$$

where $q'_t(t_1) = n_t$ and $q'_t(t_i)_{i\neq 1} = 0$.

Equations 3.19-3.21 form a system of linear equations. In the case of a 3 × 2 bore field, the system becomes:

$$\begin{bmatrix} 0 \\ 0 \\ \mathcal{L}(q'_t) \end{bmatrix} = \begin{bmatrix} \mathcal{L}(G_{11}) & \mathcal{L}(G_{12}) & -1 \\ \mathcal{L}(G_{21}) & \mathcal{L}(G_{22}) & -1 \\ n_1 & n_2 & 0 \end{bmatrix} \begin{bmatrix} \mathcal{L}(q'_1) \\ \mathcal{L}(q'_2) \\ \mathcal{L}(\Theta_b) \end{bmatrix} \tag{3.22}$$

The solution of the system of equations gives the heat extraction rate for every symmetry group and the resulting non-dimensional temperature response. The non-dimensional temperature response becomes the approximation for the g-function. The reader is referred to Appendix B for an example of the calculation procedure.

The results presented in the present paper are a combination of 2 consecutive resolutions of the system of equations to cover the full range of times for the g-functions. The first resolution is made with a time-step of 10 hours over the first 100 years and the second is made with a time-step of 100 hours up to 1000 years. The system of equations is solved for each term (time-step) of the numerical Laplace transforms.

The computation time varies according to the number of distances in the field, the number of symmetry groups and the number of time-steps. For example, the computation time for the 3 × 2 bore field (5 distances, 2 symmetry groups, 8760 time-steps) is ~1 minute and the computation time for a 10 × 10 bore field (51 distances, 15 symmetry groups, 8760 time-steps) is ~12 minutes. Most of the calculation time is due to the evaluation of the FLS solution. The computer used for the calculations is equipped with an AMD Phenom II X6 processor (2.7 GHz) and 8 Gb of RAM.

In summary, in order to obtain the g-function for a given bore field under the proposed method, one would proceed as follows. First, the symmetry groups in the bore field and the distances between every pair of boreholes need to be identified. Then, the borehole-to-borehole response factors are calculated using the FLS solution (Equation 3.10) for each unique distance between two boreholes and every time step. The group-to-borehole response factors are obtained for each pair of symmetry groups by the summation of the borehole-to-borehole response factors for all distances between an arbitrary borehole of the first group and all boreholes of the second group. Finally, the matrix of Equation 3.22 is constructed and the system is solved for each term of the numerical Laplace transform of the group-to-borehole response factors. The non-dimensional

heat extraction rate increments q_i' and the approximation of the g-function, Θ_b, are obtained by the inverse numerical Laplace transform of the solutions of the system of equations.

Figure 3-8 shows the approximation of the g-function with the proposed method along with Eskilson's g-function for a 3 × 2 bore field. Results are also compared to the response factor obtained by the classical spatial superposition of the FLS solution (Sherrif, 2007) which is given by :

$$g_{FLS,bore\ field}(t/t_s) = \frac{1}{N}\sum_{i=1}^{N}\sum_{j=1}^{N} g_{FLS}\left(t/t_s\,, r_{i,j}/H\,, D/H\right) \tag{3.23}$$

$$r_{i,i} = r_b, \qquad r_{i,j} = \sqrt{\left(x_i - x_j\right)^2 + \left(y_i - y_j\right)^2}, \qquad i \neq j \tag{3.24}$$

where (x_k, y_k) is the position of the k^{th} borehole and N is the total number of boreholes in the field.

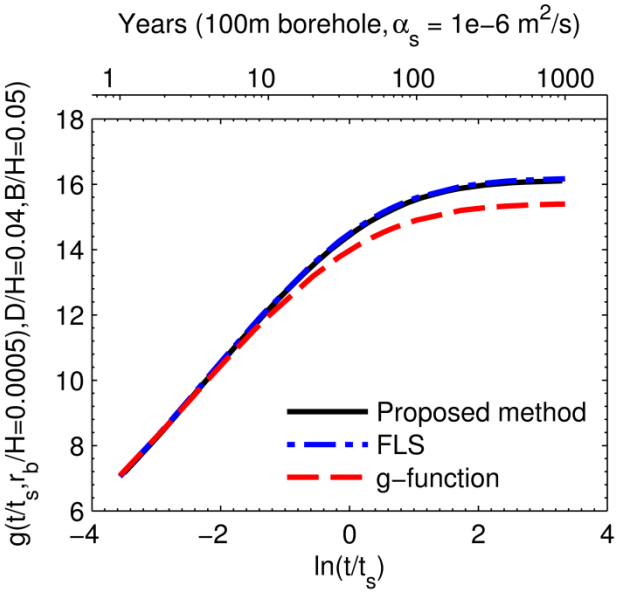

Figure 3-8: g-function of a 3 × 2 bore field computed using the FLS and the proposed method compared to Eskilson's g-function

Contrary to the response factors for a single borehole (Figure 3-4), Figure 3-8 shows that the g-function and the proposed method do not reach the same steady-state value at very large times.

The differences between the models become apparent at around $\ln(t/t_s) = -2$ when thermal interaction among boreholes starts to be significant. In the case of the 3×2 bore field, the proposed method gives results similar to the classical spatial superposition of the FLS solution and the g-function is overestimated by both the proposed method and the FLS. Figure 3-9 shows a comparison of the heat extraction rates obtained by the proposed method (PM) and Eskilson's model (SBM) for the two symmetry groups.

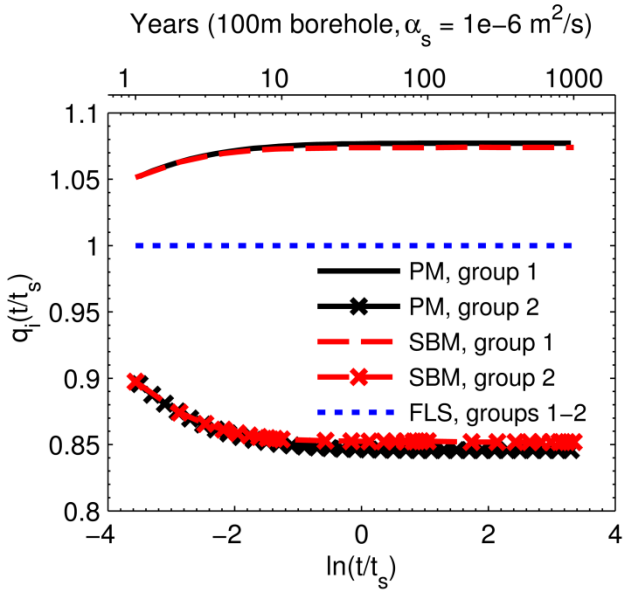

Figure 3-9: Heat extraction rates obtained for the 2 symmetry groups, proposed method (PM) and Eskilson's model (SBM)

Figure 3-9 shows that the heat extracted by the outer boreholes (i.e. symmetry group 1) increases with time while the heat extracted by the inner boreholes (i.e. symmetry group 2) decreases. Since the borehole wall temperature of the inner boreholes is more affected by the outer boreholes than the opposite, the heat extraction rate needed for all the boreholes to have the same average borehole wall temperature is greater for the outer boreholes. The maximum difference between the heat extraction rates calculated with the proposed method and Eskilson's model is 0.6 %. These differences are attributable to the differences on the boundary condition at the borehole wall. While the proposed method uses a condition of uniform heat flux over the borehole height, Eskilson's model uses a condition of uniform temperature over the borehole height.

3.5 Effects of bore field geometry on the temperature response

3.5.1 Bore field size

The effects of the bore field size on the temperature response are illustrated in Figure 3-10 for three bore fields (3 × 2, 6 × 4, 10 × 10).

Figure 3-10 shows that the response factors are similar for small times. The curves start to split at $\ln(t/t_s) \approx$ -1.2 and -2.0 for the 3 × 2 and 10 × 10 bore fields, respectively. For a 100 m borehole and a thermal diffusivity of 1e^{-6} m^2⁄s, this corresponds approximately to 10 and 6 years, respectively.

Overall, the response factors tend to a higher steady-state value for larger fields. This is due to the thermal interactions being more important for larger fields. Also, the difference between the response factors computed using the FLS solution and Eskilson's g-functions is greater for larger fields. For the 10 × 10 bore field, the FLS solution overestimates Eskilson's g-function by 45 % at $\ln(t/t_s)$ = 3.3. The proposed method reduces this difference to 32 %. In order to explain the differences, the heat extraction rates obtained with the FLS and the proposed method are compared to the heat extraction rates obtained with Eskilson's model. Figure 3-11 shows the heat extraction rates for 4 boreholes in the 6 × 4 bore field.

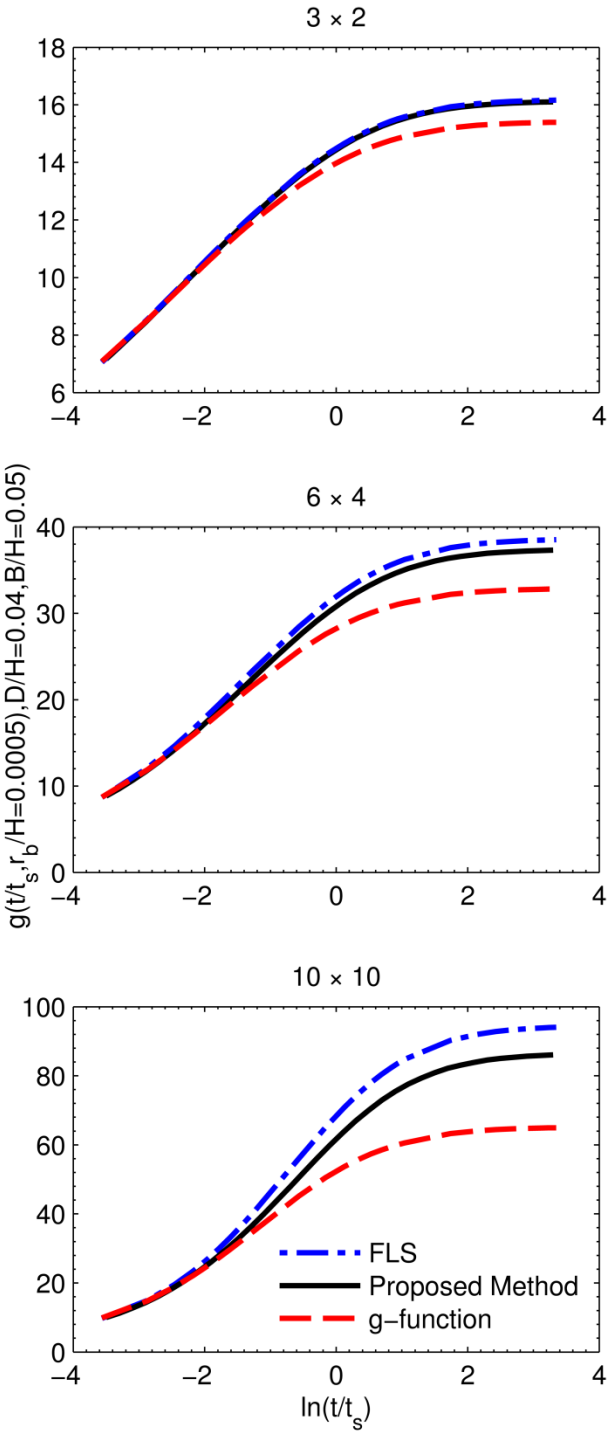

Figure 3-10: Response factors for three bore fields (3 × 2, 6 × 4, 10 × 10) computed using the FLS (top curve), the proposed method (middle curve) and Eskilson's g-function (bottom curve)

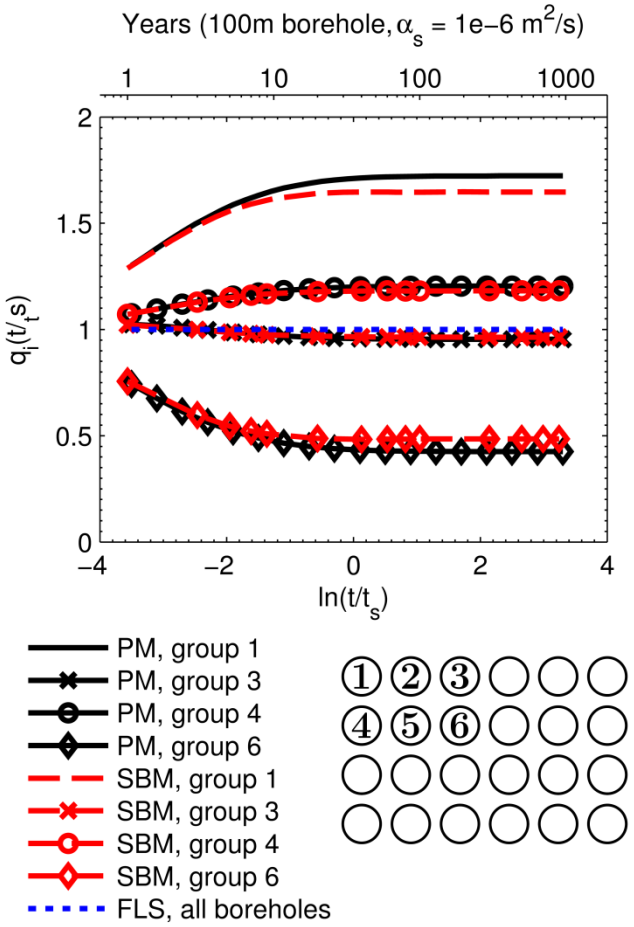

Figure 3-11: Heat extraction rates in a 6 × 4 bore field, proposed method (PM) and Eskislon's model (SBM)

In the case of a 6 × 4 bore field, the maximum difference between the heat extraction rates calculated with the proposed method and Eskilson's g-function is 12 %. As was the case for the 3 × 2 bore field (Figure 3-9), outer boreholes have a greater heat extraction rate than the inner boreholes. In this case, symmetry group 6 has a steady-state heat extraction rate of 0.43 while symmetry group 1 has a steady-state heat extraction rate of 1.72. This means that the contribution of the boreholes in symmetry group 6 to the overall heat exchange is far less than boreholes in symmetry group 1. This explains why Eskilson's g-functions and the g-function calculated with the proposed method have lower values for large times when compared to the classical superposition of the FLS. In the case where all boreholes have the same heat extraction rate, more heat is extracted inside the field and the overall temperature drop is higher.

In order to explain the differences between Eskilson's g-function and the g-function obtained with the proposed method, the temperature profiles along the borehole heights need to be examined. Figure 3-12 shows the non-dimensional temperature profile over the height for a borehole of symmetry group 6 at three given times corresponding to 10, 100 and 1000 years for a 100 m borehole for both the proposed method and Eskilson's g-function.

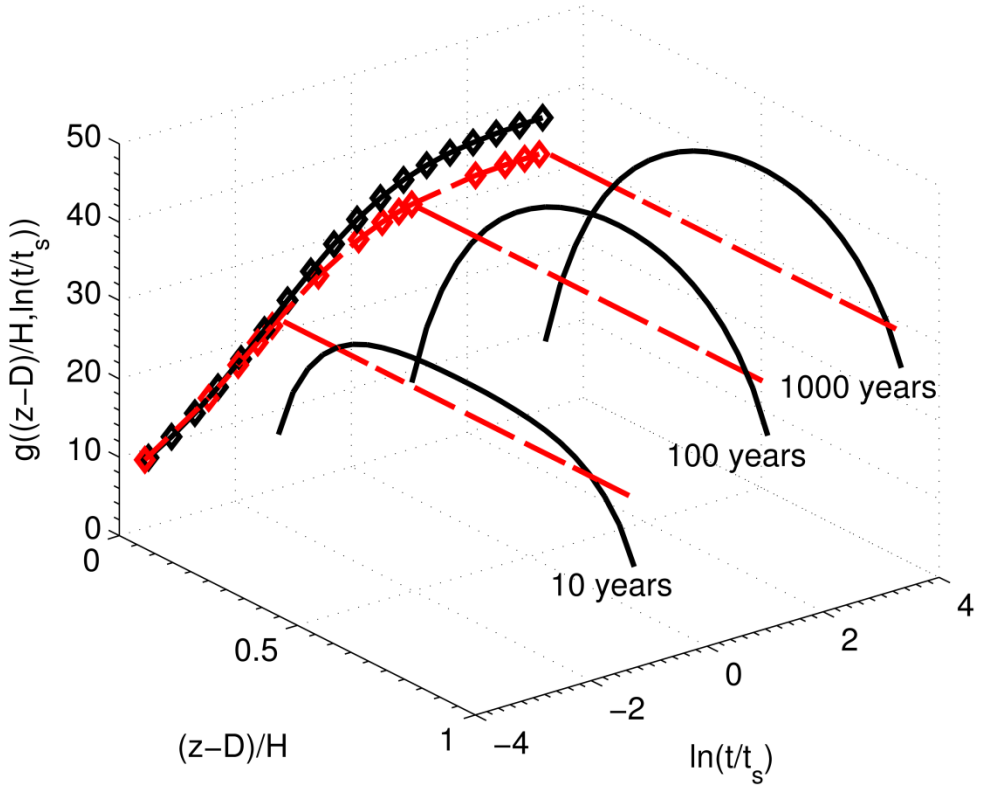

Figure 3-12: Temperature profile along the height of the innermost borehole in a 6 × 4 bore field

The difference between Eskilson's g-function and the proposed method becomes clear. The temperature responses obtained using the proposed method (based on the FLS) are higher at the middle of the borehole and lower at the top and bottom of the borehole while it is uniform for Eskilson's g-function. For example for t = 10 years, the temperature response for the proposed model varies from 12.9 at the bottom to 25.6 at the middle and then down to 6.9 at the top. The corresponding value for Eskilson's g-function is 21.7. As a result, more heat is extracted at the top and at the bottom of the borehole for Eskilson's g-function.

3.5.2 Buried depth

The g-functions presented by Eskilson were calculated for a buried depth (D) of 4 to 5 m (Eskilson, 1987). These values were chosen by Eskilson after numerical simulations that showed only small variations of the borehole wall temperature for buried depth of 2 to 8 m. This might be true for long boreholes, however, when considering boreholes of small height, the buried depth becomes an important parameter. Figure 3-13 shows the g-functions, calculated with the proposed method, for various buried depths of a 6×4 bore field of height H = 5 m and radius r_b = 0.05 m with a spacing B = 1 m.

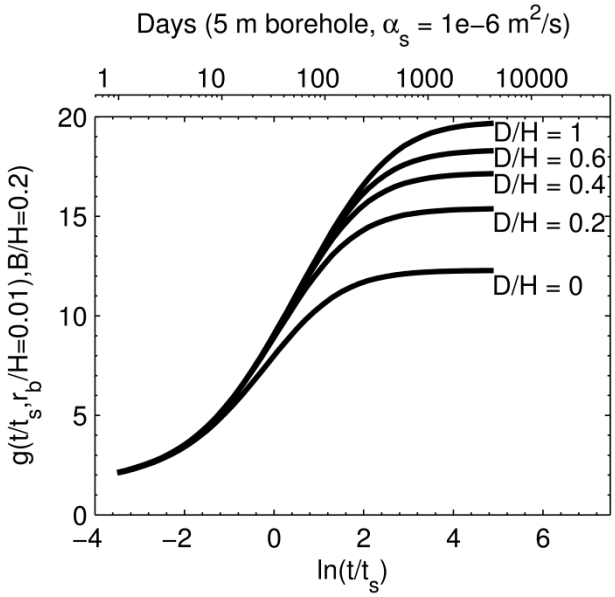

Figure 3-13: g-function of a 6 × 4 bore field for different buried depth to borehole height ratio obtained with the proposed method

As shown on Figure 3-13, the buried depth becomes an important parameter in the evaluation of the g-function when modeling short boreholes. The difference between the steady-state value of the g-function with D/H = 0.2 and D/H = 0.6, which corresponds to a variation of 2 m for a 5 m borehole, is 19 %. Moreover, the steady-state is attained faster in the case of short boreholes than with long boreholes (note that the units of the upper axis of Figure 3-13 are days). The g-functions presented in Figure 3-13 show that the time required to attain steady-state varies

significantly depending on the D/H ratio. The time required to attain 98 % of the steady-state value of the g-function is approximately 16 months for $D/H = 0$ and 4.2 years for $D/H = 1$.

At steady-state, the heat extracted by the boreholes comes essentially from the ground surface (Nouanegue, Shirazi, & Bernier, 2009). As the D/H ratio increases, the boreholes are farther away from the surface and the effective thermal resistance between the ground surface and the boreholes becomes larger. The steady-state temperature drop from a constant heat extraction rate is thus larger. The thermal capacitance of the ground layer above the boreholes slows the heat exchange between the boreholes and the surface. The steady-state is therefore attained faster when the D/H ratio is small. When D/H tends to infinity, the heat transfer between the boreholes and the ground is similar to a heat sink in an infinite medium.

3.6 Conclusion

In the first part of this paper, the characteristics of the g-functions are examined and the classical approach used to approximate the g-functions with the line source (infinite and finite) and the cylindrical source analytical solutions are presented. A comparison between these three methods and the g-function for a single borehole shows the limit of applicability of each solution and indicates that the finite line source (FLS) solution is capable of reproducing the g-function adequately.

In the second part of the paper, a new method, based on the FLS, is proposed to take into account the variation of the heat extraction rate among boreholes of the same bore field while keeping the same mean borehole wall temperature for every borehole in the bore field. The method also takes into account the buried depth to borehole height ratio (D/H). Borehole-to-borehole and group-to-borehole response factors are evaluated and then temporal superposition of heat extraction rates is applied in the Laplace domain. This results in a simple linear system of equations. The heat extraction rates obtained with the proposed method showed good agreement with Eskilson's numerical model. The differences observed, especially for large times, when comparing the g-functions of Eskilson and the ones obtained with the proposed method can be explained by the fact that two different boundary conditions are used at the borehole wall. The numerical model of Eskilson assumes that the temperature at the borehole wall is uniform along the height of each borehole while the proposed method uses a uniform heat transfer rate along the height of the

boreholes. In reality, neither the temperature nor the heat extraction rate is uniform at the borehole wall. The boundary condition at the borehole wall and its effect on the thermal response of the bore field will be addressed in future studies.

For small times, however, the agreement between both methods is much better and the response factors are almost identical for up to 10 and 6 years for the 3×2 and 10×10 bore fields, respectively. For larger bore fields, thermal interactions between boreholes become more important and the differences observed between the proposed model and the g-function increase. For instance, the g-function of a 10×10 bore field obtained with the proposed method overestimates the g-function by 32 % at steady-state. Finally, the effect of the buried depth (D) is examined with the proposed method. It is shown that the difference between the steady-state value of the g-function with D/H = 0.2 and D/H = 0.6, which corresponds to a variation of 2 m for a 5 m borehole, is 19 %. Moreover, the steady-state is attained faster in the case of short boreholes than with long boreholes

3.7 Acknowledgements

This work was partly funded by the NSERC Smart Net-Zero Energy Buildings Strategic Research Network (SNEBRN). The authors also wish to thank the Canadian GeoExchange Coalition and the American Society of Heating, Refrigerating and Air-Conditioning Engineers (ASHRAE) for scholarships awarded to the first author.

3.8 Appendix A : Calculating the thermal response to a variable heat extraction rate

The borehole wall temperature resulting from a variable heat extraction rate can be obtained using temporal superposition. Following equation 3.1, the temperature drop at the borehole wall ΔT_b resulting from a constant heat extraction rate per unit length $Q(t_i)$ starting at time t_{i-1} up to time t_i is obtained by subtracting the response factor evaluated at time $t - t_i$ from the response factor evaluated at time $t - t_{i-1}$.

$$\Delta T_b = \frac{Q(t_i)}{2\pi k_s}[f(t - t_{i-1}) - f(t - t_i)] \tag{3.25}$$

where f is the response factor obtained from any model that can predict heat transfer from a borehole. Some of the available models have been presented in the paper (Equations 3.4, 3.6 and 3.10). For a succession of heat extraction rates $Q(t_i)$, the temperature drop at time t is given by the superposition of the contribution of each extraction rate at time t:

$$\Delta T_b(t) = \sum_{i,t_i \leq t} \frac{Q(t_i)}{2\pi k_s} [f(t - t_{i-1}) - f(t - t_i)] \tag{3.26}$$

Rearranging Equation 3.26, the temperature drop can be expressed as a convolution product between the incremental heat extraction rate $Q'(t_i) = Q(t_i) - Q(t_{i-1})$ and the response factor:

$$\Delta T_b(t) = \sum_{i,t_i \leq t} \frac{Q'(t_i)}{2\pi k_s} f(t - t_{i-1}) = \frac{1}{2\pi k_s} (Q' * f) \tag{3.27}$$

where $Q(t_0) = 0$.

Marcotte & Pasquier (2008a) proposed to solve the convolution product using Fourier transforms. Cimmino et al. (2012) used Fourier transforms to simulate a bore field with a pre-calculated g-function. In the Fourier domain, the convolution theorem states that the convolution product takes the form of a simple multiplication:

$$\Delta T_b(t) = \mathcal{F}^{-1}\left(\mathcal{F}\left(\frac{Q'}{2\pi k_s}\right) \cdot \mathcal{F}(f)\right) \tag{3.28}$$

where $\mathcal{F}$ stands for the Fourier transform and $\mathcal{F}^{-1}$ stands for the inverse Fourier transform. In the discrete case, the Fourier transform can be evaluated using a Fast Fourier Transform (FFT) algorithm. This method offers an improvement over conventional time domain algorithms (i.e. load aggregation algorithms (Bernier et al., 2004; Yavuzturk & Spitler, 1999)) in terms of computational efficiency.

In this study, the numerical Laplace transform is used instead of the FFT in order to avoid time aliasing errors that appeared when computing the g-functions. The convolution theorem also applies to Laplace transforms: the Fourier transforms in Equation 3.28 can be replaced by Laplace transforms. The Laplace transform pairs are expressed as follows:

$$H(s) = \mathcal{L}\big(h(t)\big) = \int_0^{\infty} h(t)\exp(\text{-}st)\,dt \tag{3.29}$$

$$h(t) = \mathcal{L}^{\text{-}1}\big(H(s)\big) = \frac{1}{2\pi j}\int_{\sigma-j\infty}^{\sigma+j\infty} H(s)\exp(st)\,ds \tag{3.30}$$

where $\mathcal{L}$ stands for the Laplace transform and $\mathcal{L}^{\text{-}1}$ stands for the inverse Laplace transform, the complex frequency s is the variable in the Laplace domain, $h(t)$ is an arbitrary function in the time domain and $H(s)$ is the corresponding-function in the Laplace domain, $j = \sqrt{\text{-}1}$ is the imaginary number.

The numerical Laplace transform can be formulated using Fourier transforms by introducing a variable change $s = \sigma + \omega j$ (Moreno & Ramirez, 2008), with ω the angular frequency. The time domain vector is multiplied by a decreasing exponential $\exp(\text{-}\sigma t)$ before ensuing the forward Fourier transform. After the inverse Fourier transform, the time domain vector should then be multiplied by an increasing exponential $\exp(\sigma t)$. The Laplace transform pairs are rewritten as follows:

$$H(s) = \int_0^{\infty} h(t)\exp(\text{-}\sigma t)\exp(\text{-}j\omega t)\,dt = \mathcal{F}(h(t)\exp(\text{-}\sigma t)) \tag{3.31}$$

$$h(t) = \frac{\exp(\sigma t)}{2\pi}\int_{\text{-}\infty}^{+\infty} H(s)\exp(j\omega t)\,d\omega = \exp(\sigma t)\,\mathcal{F}^{\text{-}1}\big(H(s)\big) \tag{3.32}$$

where $\mathcal{L}$ stands for the Laplace transform and $\mathcal{L}^{\text{-}1}$ stands for the inverse Laplace transform. The damping factor σ should be chosen with care: choosing a value that is too small will not attenuate the time domain vector enough to avoid temporal aliasing and choosing a value that is too large will distort the results. In this study, the damping factor was chosen meet Wedepohl's criterion (Wedepohl, 1983):

$$\sigma = 2 \cdot \frac{\ln(N)}{t_{max}} \tag{3.33}$$

where N is the number of terms in the time domain vector which corresponds to the number of time steps and tmax is the maximum value of time, which corresponds to the value of time at the end of the last time step.

3.9 Appendix B : Example of a g-function calculation using the proposed method[1]

An example is hereby presented for a field of 3 × 2 boreholes of height H = 100 m and buried depth D = 4 m. The boreholes have a radius r_b = 0.05 m and they are equally spaced at a distance B = 5 m. As shown in Figure 3-6, the field consists of 2 symmetry groups. The first group includes the 4 outer boreholes and the second includes the 2 inner boreholes. The distances between boreholes (defined in Figure 3-7) are $d_0 = r_b$ = 0.05 m, d_1 = 5 m, d_2 = 10 m, d_3 = 7.07 m, and d_4 = 11.2 m. The distances $d_1 - d_4$ are ordered arbitrarily, but include all distances between 2 boreholes in the 3 × 2 bore field. Note that the number of distances increases with the number of boreholes in the field. For instance, a 6 × 4 bore field consists of 16 distances $d_1 - d_{16}$ while a 10 × 10 bore field consists of 50 distances $d_1 - d_{50}$ (in addition to the borehole radius $d_0 = r_b$). The g-function of the bore field is calculated up to a time of 6 months (t_{max} = 15 768 000 s) with a time step of 1 month (2 628 000 s).

The borehole-to-borehole response factors are calculated for each of the 5 distances using the FLS solution (Equation 3.10). Results are shown in Table 3-1. The resulting group-to-borehole response factors (Equations 3.12-3.15) and the total non-dimensional heat extraction rate increments are presented in Table 3-2.

[1] Cette section comprend des erreurs de calculs qui affectent les données des tableaux. Les tableaux corrigés sont fournis à l'Annexe A.

Table 3-1: Borehole-to-borehole response factors for a 3 × 2 bore field

function	time [yr/12]					
	1	2	3	4	5	6
g_0'	3.87	4.20	4.40	4.54	4.65	4.73
g_1'	1.44E-02	7.89-02	1.53E-01	2.23E-01	2.86E-01	3.43E-01
g_2'	3.48E-06	7.46E-04	5.10E-03	1.42E-02	2.70E-02	4.24E-02
g_3'	7.52E-04	1.43E-02	4.29E-02	7.81E-02	1.15E-01	1.52E-01
g_4'	2.62E-07	1.87E-04	1.92E-03	6.53E-03	1.41E-02	2.41E-02

Table 3-2: Group-to-borehole response factors and total non-dimensional heat extraction rate increment for a 3 × 2 bore field

function	time [yr/12]					
	1	2	3	4	5	6
G_{11}	3.88	4.28	4.56	4.78	4.97	5.14
G_{12}	1.52E-02	9.32E-02	1.96E-01	3.01E-01	4.01E-01	4.94E-01
G_{21}	3.03E-02	1.86E-01	3.93E-01	6.03E-01	8.03E-01	9.88E-01
G_{22}	3.88	4.28	4.55	4.76	4.93	5.08
q_t'	6	0	0	0	0	0
$\exp(-\sigma t)$	0.55	0.30	0.17	0.09	0.05	0.03

The numerical Laplace transforms of the group-to-borehole response factors and the total non-dimensional heat extraction rate increments are calculated as described in Appendix A. The damping factor σ is chosen according to Wedepohl's criterion (Wedepohl, 1983):

$$\sigma = 2 \cdot \frac{\ln(N)}{t_{max}}$$
$$\sigma = 2 \cdot \frac{\ln(6)}{15\,768\,000\ \text{s}} = 2.27 \times 10^{-7}\ \text{s}^{-1} \tag{3.34}$$

The Laplace transforms of the group-to-borehole response factors and the total non-dimensional heat extraction rate increment are then calculated. Results are shown in Table 3-3.

Table 3-3: Numerical Laplace transforms of the group-to borehole response factors and the total non-dimensional heat extraction rate increment

function	Angular frequency ω [rad/yr]					
	−37.7	−25.1	−12.6	0.0	12.6	25.1
$\mathcal{L}(G_{11})$	1.27	1.35+0.559j	1.91+1.44j	5.03	1.91-1.44j	1.35-0.559j
$\mathcal{L}(G_{12})$	-0.00828	-0.011 +0.0018j	-0.025 +0.023j	0.131	-0.025 -0.023j	-0.011 -0.0018j
$\mathcal{L}(G_{21})$	-0.0166	-0.023 +0.0035j	-0.050 +0.047j	0.262	-0.050 -0.047j	-0.023 -0.0035j
$\mathcal{L}(G_{22})$	1.27	1.35+0.560j	1.91+1.44j	5.02	1.91-1.44j	1.35-0.560j
$\mathcal{L}(q_t')$	3.30	3.30	3.30	3.30	3.30	3.30

The matrix system of Equation 3.22 may now be built and solved for each step in the Laplace domain. The matrix system for the first term in the Laplace domain is as follows:

$$\begin{bmatrix} 0 \\ 0 \\ \mathcal{L}(q_t')_1 \end{bmatrix} = \begin{bmatrix} \mathcal{L}(G_{11})_1 & \mathcal{L}(G_{12})_1 & -1 \\ \mathcal{L}(G_{21})_1 & \mathcal{L}(G_{22})_1 & -1 \\ n_1 & n_2 & 0 \end{bmatrix} \begin{bmatrix} \mathcal{L}(q_1')_1 \\ \mathcal{L}(q_2')_1 \\ \mathcal{L}(\Theta_b)_1 \end{bmatrix}$$
$$\begin{bmatrix} 0 \\ 0 \\ 3.30 \end{bmatrix} = \begin{bmatrix} 1.27 & -0.00828 & -1 \\ -0.0166 & 1.27 & -1 \\ n_1 & n_2 & 0 \end{bmatrix} \begin{bmatrix} \mathcal{L}(q_1')_1 \\ \mathcal{L}(q_2')_1 \\ \mathcal{L}(\Theta_b)_1 \end{bmatrix} \tag{3.35}$$

The solutions of the matrix system for each step in the Laplace domain are detailed in Table 3-4. The results in the time domain are obtain with the inverse numerical Laplace transform of the values in Table 3-4 and are presented in Table 3-5. Finally, the non-dimensional heat extraction rates are obtained by taking the cumulative sums of the non-dimensional heat extraction rate increments. The results are shown in Table 3-6. As noted in section 3.4, the approximation of the g-function is equal to the non-dimensional mean borehole wall temperature Θ_b.

Table 3-4: Numerical Laplace transforms of the non-dimensional heat extraction rate increments and the non-dimensional mean borehole wall temperature

function	Angular frequency ω [rad/yr]					
	−37.7	−25.1	−12.6	0.0	12.6	25.1
$\mathcal{L}(\mathrm{q}_1')$	0.549	0.549 + 0.0008j	0.550 + 0.0026j	0.555	0.550 - 0.0026j	0.549 - 0.0008j
$\mathcal{L}(\mathrm{q}_2')$	0.553	0.553 - 0.0015j	0.551 - 0.0052j	0.541	0.551 + 0.0052j	0.553 + 0.0015j
$\mathcal{L}(\Theta_\mathrm{b})$	0.692	0.734 + 0.309j	1.03 + 0.811j	2.86	1.03 - 0.811j	0.734 - 0.309j

Table 3-5: Time domain values of the non-dimensional heat extraction rate increments and the non-dimensional mean borehole wall temperature

function	time [yr/12]					
	1	2	3	4	5	6
$\exp(\sigma t)$	1.82	3.30	6.00	10.90	19.81	36.00
q_1'	1.000	0.0068	0.0081	0.0072	0.0061	0.0050
q_2'	0.999	-0.0137	-0.0162	-0.0145	-0.0122	-0.0101
Θ_b	2.146	2.426	2.653	2.849	3.023	3.179

Table 3-6: Non-dimensional heat extraction rates for a 3 × 2 bore field

function	Time [yr/12]					
	1	2	3	4	5	6
q_1	1.000	1.007	1.015	1.022	1.029	1.034
q_2	0.999	0.986	0.970	0.955	0.943	0.933

3.10 References

Bandos, T. V., Montero, Á., Fernández de Córdoba, P. J., & Urchueguía, J. F. (2011). Improving parameter estimates obtained from thermal response tests: Effect of ambient air temperature variations. Geothermics, 40(2), 136-143.

Bandos, T. V., Montero, Á., Fernández, E., Santander, J. L. G., Isidro, J. M., Pérez, J. (2009). Finite line-source model for borehole heat exchangers: effect of vertical temperature variations. Geothermics, 38(2), 263-270.

Bandyopadhyay, G., Gosnold, W., & Mann, M. (2008). Analytical and semi-analytical solutions for short-time transient response of ground heat exchangers. Energy and Buildings, 40(10), 1816-1824.

Bandyopadhyay, G., Kulkarni, M., & Mann, M. (2008). A New Approach to Modeling Ground Heat Exchangers in the Initial Phase of Heat-Flux Build Up. ASHRAE Transactions, 114(2), 428-439.

Beier, R. A., & Smith, M. D. (2003). Minimum duration of in-situ tests on vertical boreholes. ASHRAE Transactions, 109(2), 475-486.

Bernier, M. A. (2001). Ground-coupled Heat pump system simulation. ASHRAE Transactions, 107(1), 605-616.

Bernier, M. A., Pinel, P., Labib, R., & Paillot, R. (2004). A multiple load aggregation algorithm for annual hourly simulations of GCHP systems. HVAC&R Research, 10(4), 471-487.

Carslaw, H. S., & Jaeger, J. C. (1946a). Chapter 13, The Laplace transformation: Problems on the cylinder and sphere. In O. U. Press (dir.), Conduction of Heat in Solids. (2nde éd., pp. 327-352). Oxford: Oxford University.

Cimmino, M., Bernier, M., & Pasquier, P. (2012). Utilisation des g-functions de Eskilson pour la simulation de systèmes géothermiques. Proceedings of eSim 2012, Halifax NS.(pp. 282-295).

Claesson, J., & Javed, S. (2011). An analytical method to calculate borehole fluid temperatures for time-scales from minutes to decades. ASHRAE Transactions, 117(2), 279-288.

Cooper, L. Y. (1976). Heating of a cylindrical cavity. International Journal of Heat and Mass Transfer, 19, 575-577.

Duan, X., & Naterer, G. F. (2008a). Ground heat transfer from a varying line source with seasonal temperature fluctuations. Journal of Heat Transfer, 130(11), 1-10.

Duan, X., & Naterer, G. F. (2008b). Ground thermal response to heat conduction in a power transmission tower foundation. Heat and Mass Transfer, 44(5), 547-558.

Duan, X., Naterer, G. F., Lu, M., & Mueller, W. (2007). Transient heat conduction from a vertical rod buried in a semi-infinite medium with variable heating strength. Heat and Mass Transfer, 43(6), 547-557.

Eskilson, P. (1986). Superposition Borehole Model: Manual for Computer Code. University of Lund, Lund, Sweden.

Eskilson, P. (1987). Thermal Analysis of Heat Extraction Boreholes. Ph.D. Thesis, University of Lund, Lund, Sweden.

Eslami-Nejad, P., & Bernier, M. (2011). Coupling of geothermal heat pumps with thermal solar collectore using double U-tube boreholes with two independent circuits. Applied Thermal Engineering, 31(14-5), 3066-3077.

Fisher, D. E., Rees, S. J., Padhmanabhan, S. K., & Murugappan, A. (2006). Implementation and validation of ground-source heat pump system models in an integrated building and system simulation environment. HVAC&R Research, 12(3A), 693-710.

Fossa, M. (2011). The temperature penalty approach to the design of borehole heat exchangers for heat pump applications. Energy and Buildings, 43(6), 1473-1479. doi:10.1016/j.enbuild.2011.02.020

Ingersoll, L. R., Adler, F. T., Plass, H. J., & Ingersoll, A. C. (1950). Theory of earth heat exchangers for the heat pump. Heating, Piping & Air Conditioning, 22, 113-122.

Javed, S., & Claesson, J. (2011). New analytical and numerical solutions for the short-term analysis of vertical ground heat exchangers. ASHRAE Transactions, 117(1), 3-12.

Javed, S., Claesson, J., & Fahlén, P. (2010). Analytical modelling of short-term response of ground heat exchangers in ground source heat pump systems. Proceedings of the 10th REHVA world congress; Clima 2010, Antalya Turkey. Clima 2010.

Javed, S., Fahlén, P., & Claesson, J. (2009). Vertical ground heat exchangers: A review of heat flow models. Proceedings of the 11th international conference on thermal energy storage; Effstock 2009, Stockholm Sweden. Effstock 2009.

Lamarche, L. (2009). A fast algorithm for the hourly simulations of ground-source heat pumps using arbitrary response factors. Renewable Energy, 34(10), 2252-2258.

Lamarche, L., & Beauchamp, B. (2007a). A new contribution to the finite line-source model for geothermal boreholes. Energy and Buildings, 39(2), 188-198.

Lamarche, L., & Beauchamp, B. (2007b). New solutions for the short-time analysis of geothermal vertical boreholes. International Journal of Heat and Mass Transfer, 50(7-8), 1408-1419. doi:10.1016/j.ijheatmasstransfer.2006.09.007

Man, Y., Yang, H., Spitler, J. D., & Fang, Z. (2011). Feasibility study on novel hybrid ground coupled heat pump system with nocturnal cooling radiator for cooling load dominated buildings. Applied Energy, 88(11), 4160-4171.

Marcotte, D., & Pasquier, P. (2008). Fast fluid and ground temperature computation for geothermal ground-loop heat exchanger systems. Geothermics, 37(6), 651-665.

Moreno, P., & Ramirez, A. (2008). Implementation of the Numerical Laplace Transform: A review. IEEE Transactions on power delivery, 23(4), 2599-2609.

Nouanegue, H.-F., Shirazi, A. S., & Bernier, M. (2009). Extracted heat from geothermal boreholes: where does the energy come from? 4th Canadian Solar Buildings Conference, Toronto, Ontario.

Philippe, M., Bernier, M., & Marchio, D. (2009). Validity ranges of three analytical solutions to heat transfer in the vicinity of single boreholes. Geothermics, 38(4), 407-413.

Sherrif, F. (2007). Génération de facteurs de réponse pour champs de puits géothermiques verticaux. MA Sc, École Polytechnique de Montréal, Montreal.

Stehfest, H. (1970). Algorithm 368, Numerical inversion of the Laplace transforms [D5]. Communications of the ACM, 13(1), 47-49.

Wedepohl, L. M. (1983). Power system transients: Errors incurred in the numerical inversion of the Laplace transforms. 26th Midwest Symposium on Circuits and Systems, Mexico.(pp. 174-178).

Yang, H., Cui, P., & Fang, Z. (2010). Vertical-borehole ground-coupled heat pumps: A review of models and systems. Applied Energy, 87(1), 16-27.

Yavuzturk, C., Chiasson, A. D., & Nydahl, J. E. (2009). Simulation model for ground loop heat exchangers. ASHRAE Transactions, 115(2), 45-59.

Yavuzturk, C., & Spitler, J. D. (1999). A short time step response factor model for vertical ground loop heat exchangers. ASHRAE Transactions, 105(2), 475-485.

Yavuzturk, C., & Spitler, J. D. (2001). Field validation of a short time step model for vertical ground-loop heat exchangers. ASHRAE Transactions, 107(1), 751-759.

Zeng, H. Y., Diao, N. R., & Fang, Z. (2003). Heat transfer analysis of boreholes in vertical ground heat exchangers. International Journal of Heat and Mass Transfer, 46(23), 4467-4481.

Zeng, H. Y., Diao, N. R., & Fang, Z. H. (2002). A finite line-source model for boreholes in geothermal heat exchangers. Heat Transfer - Asian Research, 31(7), 558-567.

CHAPITRE 4 ARTICLE 2 : A SEMI-ANALYTICAL METHOD TO GENERATE G-FUNCTIONS FOR GEOTHERMAL BORE FIELDS

Cimmino, M., & Bernier, M. (2014). A semi-analytical method to generate g-functions for geothermal bore fields. *International Journal of Heat and Mass Transfer*, 70(c), 641-650.

ABSTRACT

This paper introduces a new methodology for the generation of thermal response factors of geothermal bore fields using the concept of g-functions introduced by Eskilson. Boreholes are divided into segments to consider the variation of the heat extraction rates along the length of the boreholes and the analytical finite line source (FLS) solution is used to calculate the temperature variations at the wall of each borehole segment along the axial direction. The proposed methodology accounts for the time variation of the heat extraction rates among boreholes and along the length of individual boreholes to obtain a uniform borehole wall temperature equal for all boreholes in accordance with the original boundary conditions proposed by Eskilson. In addition, the methodology is generalised to account for boreholes of different lengths and buried depths. g-functions calculated with the proposed methodology are compared to the numerical technique used by Eskilson to derive the g-functions for fields of 1 to 12 × 12 boreholes. The difference between the two models is within 5 % for all studied bore fields, except for fields of boreholes located on a single row. The variation of the heat extraction rates of individual boreholes along their length as well as in time also showed good agreement with the numerical model. It is shown that using 12 borehole segments is adequate to calculate the g-functions in most practical cases. For instance, the error on the g-function of a 10 × 10 bore field calculated using 12 borehole segments is 2.2 % after 20 years and 4.7 % at steady-state.

4.1 Introduction

Ground source heat pump (GSHP) systems coupled to geothermal bore fields are increasing in popularity due to their potential in decreasing energy consumption. The design and simulation of geothermal bore fields relies on modeling the transient heat transfer in the bore fields during the

operation of the systems. A bore field consists in an array of vertical boreholes usually connected in parallel and fed with a heat carrier fluid at a temperature $T_{f,in}$. Figure 4-1 shows a field of 3 arbitrarily sized and positioned boreholes. Each borehole has a length H_i and is buried at a distance D_i from the ground surface.

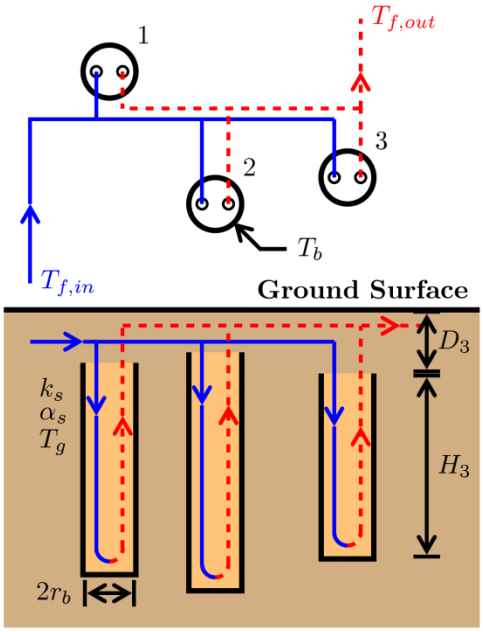

Figure 4-1: Arbitrarily sized and positioned vertical boreholes in an bore field

It is common to separate the regions inside and outside the boreholes and solve the heat transfer problem for each region separately (Eskilson, 1987). In this paper, only transient heat transfer in the ground outside the borehole is considered.

Thermal response factors are widely used to predict the performance of geothermal bore fields. Coupled with suitable temporal superposition schemes (Bernier et al., 2004; Lamarche, 2009; Lamarche & Beauchamp, 2007a; Liu, 2005; Marcotte & Pasquier, 2008a; Yavuzturk & Spitler, 1999), thermal response factors are used in several bore field sizing tools and energy simulation programs (e.g. EED (Hellström & Sanner, 1994), GLHEPRO (Spitler, 2000), EnergyPlus (Fisher et al., 2006), eQuest (Liu & Hellstrom, 2006), etc.).

Eskilson's thermal response factors, also known as g-functions (Eskilson, 1987), are often taken as reference for comparison with other thermal response factors. Eskilson generated his thermal response factors numerically and assumed that the temperature at the borehole walls is uniform

along the length of the boreholes and equal for all boreholes. This reflects the behavior of bore fields where boreholes are connected in parallel: the inlet fluid temperature is the same for all boreholes and varies little inside individual boreholes.

It is possible to generate thermal response factors using analytical solutions to transient heat transfer in the ground such as the finite line source (FLS). Three boundary conditions (BC) for the generation of g-functions using the FLS have been used and are described below. Eskilson's g-functions were derived using BC-III.

- BC-I: Uniform heat extraction rate along the length of the boreholes. Heat extraction rates are equal for all boreholes. The average temperatures along the length of all boreholes are unequal.
- BC-II: Uniform heat extraction rate along the length of the boreholes. The average temperature along the length of the boreholes is equal for all boreholes.
- BC-III: Uniform borehole wall temperature along the length of the boreholes. The borehole wall temperature is equal for all boreholes.

These boundary conditions are shown on Figure 4-2 for two interacting boreholes of unequal lengths. The schematics on the left show the distribution of the heat transfer rate at the borehole wall while the right portion of the figure shows the corresponding temperature profile at the borehole wall for both boreholes. The generation of g-functions with BC-I is straightforward as the temperature drop at the borehole wall due to a known heat extraction rate can be directly obtained from existing analytical solutions. The generation of g-functions with BC-II and BC-III is more complex as both the heat extraction rates and the borehole wall temperatures are unknown. When using BC-I, overestimation of the g-functions for larger bore fields with closely packed boreholes has been observed (Cimmino, Bernier, & Adams, 2013; Fossa, 2011; Malayappan & Spitler, 2013; Monzó et al., 2013). Cimmino et al. (2013) showed that using BC-II improved the estimation of g-functions, but there are still important differences with Eskilson's g-functions when calculating thermal response factors for bore fields with a large number of boreholes.

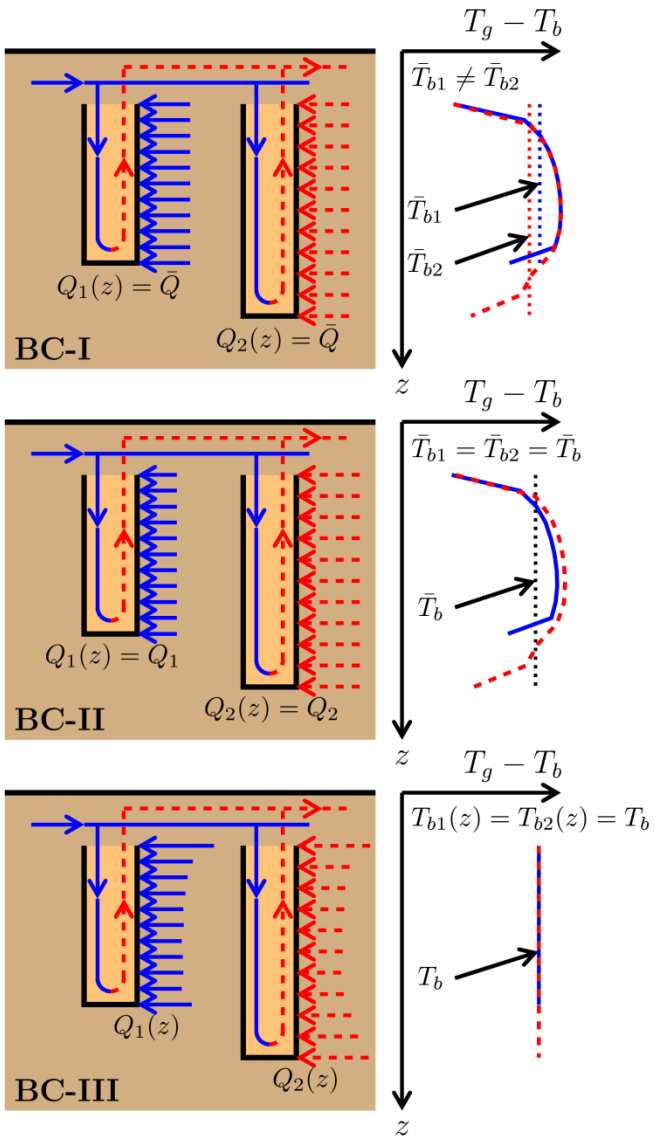

Figure 4-2: Three boundary conditions for the evaluation of thermal response factors

The objective of this paper is to provide a methodology based on the FLS solution that enables the generation of g-functions using BC-III. The proposed methodology accounts for the time variation of the heat extraction rates among boreholes and along the length of individual boreholes. In addition, the methodology is generalised to account for boreholes of different lengths and has several advantages over the numerical method of Eskilson. The calculation time is greatly reduced and therefore the proposed methodology is better adapted to the iterative

design and optimization of bore fields. The solution is independent of any radial mesh of the ground and no interpolation of temperatures is required.

It is shown that Eskilson's results can be replicated accurately, even for bore fields showing strong thermal interactions. Also, it is shown that solutions obtained with BC-I and BC-II can be considered adequate in certain circumstances.

4.2 Litterature review

The concept of g-functions was first introduced by Eskilson (1987). g-functions are defined by the relation:

$$T_b = T_g - \frac{\bar{Q}}{2\pi k_s} \cdot g(t/t_s, r_b/H, B/H, D/H) \tag{4.1}$$

g-functions are in fact thermal response factors that give the non-dimensional temperature drop (i.e. the second term on the right of Equation 4.1) at the borehole walls due to a constant total heat extraction rate in a bore field. In Equation 4.1, T_b is the borehole wall temperature common to all boreholes, T_g is the undisturbed ground temperature, $\bar{Q}$ is the average heat extraction rate per borehole length, k_s is the ground thermal conductivity and g is the g-function. g-functions depend on four non-dimensional parameters: t/t_s the non-dimensional time, with $t_s = H^2/9\alpha_s$ the characteristic time of the bore field and α_s the ground thermal diffusivity; r_b/H the non-dimensional borehole radius; B/H the bore field aspect ratio; D/H the non-dimensional buried depth of the boreholes. The last parameter D/H was not included in Eskilson's original work, as small variations of this parameter for deep boreholes had negligible effect on the g-functions. It is included in the following analysis for completeness.

g-functions are presented in the form of non-dimensional curves as shown on Figure 4-3 for a field of 6 (3 × 2) boreholes. The g-function of a single borehole corresponds to the curve for infinite borehole spacing, i.e. $B/H = \infty$. As indicated in Figure 4-3, the g-functions can be separated into four regions each with its own heat transfer characteristics. The first region (I) corresponds to radial 1-D heat transfer. In this region, the borehole wall temperatures are not affected by the ground surface temperature or by the far-field ground temperature below the boreholes. One-dimensional analytical solutions such as the infinite line source and the cylindrical heat source are more than adequate to describe transient heat transfer in the vicinity of

boreholes (Philippe et al., 2009). The second region (II) corresponds to thermal interactions among boreholes. It is observable on the g-function graph as the g-function curve detaches from the g-function of a single borehole. The starting time of this region depends on the spacing-to-length ratio, it is shown on Figure 4-3 for B/H = 0.05. The third region (III) corresponds to radial-axial 2-D heat transfer. It is observable on the g-function graph as the g-function of a single borehole starts to approach its steady-state value. The starting time of this region was estimated by Eskilson to be equal to $t_s/10$ ($\ln(t/t_s)$ = -2.3). The third region (III) can overlap with the second region (II) for certain spacings between boreholes (e.g. B/H = 0.30 on Figure 4-3). The fourth region corresponds to steady-state heat transfer. In this region, the bore field and the ground are in equilibrium. The extraction of heat does not affect the borehole wall temperatures, which are constant in time. Finally, it should be noted that g-function curves such as those presented in Figure 4-3 are strictly valid for particular values of r_b/H and D/H.

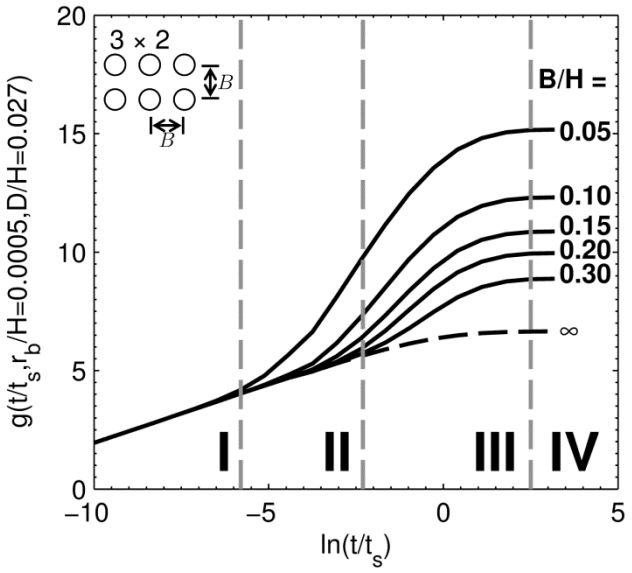

Figure 4-3: Numerical g-functions for a 3 × 2 bore field

The g-functions can be used to calculate the temperature drop at the borehole wall due to a constant heat extraction. It is interesting to note that when $\bar{Q}/2\pi k_s$ = 1, the g-function value gives the borehole wall temperature drop directly. For example, if the boreholes in the 3 × 2 bore field have a length H = 150 m, a buried depth D = 4 m (D/H = 0.027), are equally spaced at a distance B = 7.5 m (B/H = 0.05) and the ground has a thermal diffusivity α_s = 1 × 10^{-6} m^2/s

(t_s = 2.5 × 10^9 s) and a thermal conductivity k_s = 2 W/m-K, the temperature drop at borehole walls ($T_g - T_b$) after 20 years ($\ln(t/t_s)$ = 1.3) of heat extraction at a constant rate $\bar{Q}$ = 12.57 W/m ($\bar{Q}/2\pi k_s$ = 1) is 11.9°C.

Eskilson's g-functions were obtained from finite differences numerical simulations. Each borehole is modelled in a 2-D radial-axial mesh as shown on Figure 4-4. The global ground temperature field is obtained from the spatial superposition of the temperature fields around individual boreholes. At each time-step, the heat extraction rates at every cell along the borehole walls required to obtain a uniform borehole wall temperature across the bore field are calculated. The boundary condition used by Eskilson thus corresponds to BC-III as defined above. Eskilson's numerical model, the Superposition Borehole Model (SBM), is described in his Manual for Computer Code (Eskilson, 1986).

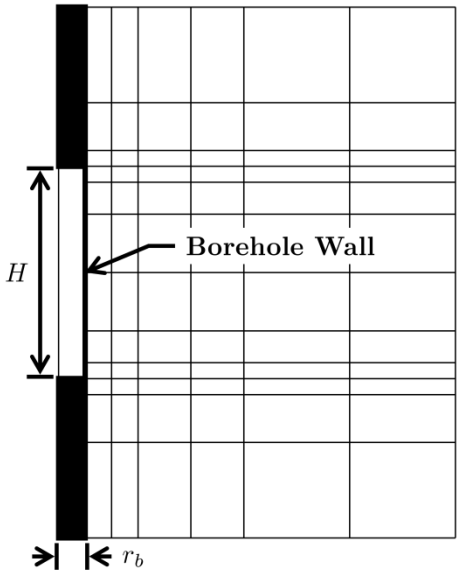

Figure 4-4: Example of the 2-D mesh used by Eskilson for the computation of g-functions

Analytical solutions are often preferred over numerical solutions since they can easily be used to generate thermal response factors for any bore field configuration. The infinite line source (ILS) solution was used by Ingersoll and Plass (1948) to calculate the thermal response of buried pipes. The solution gives the temperature distribution around a line source of infinite length extracting heat at a constant rate. The authors applied the principles of temporal superposition and spatial superposition to calculate the temperature response of multiple pipes with varying heat extraction

rates. Ingersoll et al. (1950) later applied the same methodology to the cylindrical heat source (CHS) solution introduced by Carslaw and Jaeger (1946a). The CHS was originally difficult to solve numerically and the solutions were pre-calculated and given in tables. Later Beaudoin (1988) proposed a solution in the form of a series of Bessel functions by inverting the Laplace domain solution of the CHS using a Gaver-Stehfest algorithm (Stehfest, 1970). Correlations were also proposed by Cooper (1976) and by Bernier (2000, 2001).

Eskilson used the finite line source (FLS) solution to approximate the g-function of a single borehole (Eskilson, 1987). The FLS solution gives the temperature distribution around a line source of length H extracting heat at a uniform rate Q. The temperature distribution around a mirror source is superposed to model the heat transfer with a constant temperature surface at a distance D above the line source. Eskilson proposed to superpose multiple line sources to approximate the g-functions of bore fields.

Zeng et al. (2002) superposed the FLS solution to obtain the average borehole wall temperature in a bore field. This method corresponds to the boundary condition BC-I identified earlier. The authors compared the FLS evaluated at mid-length to the integral mean temperature along the length of the boreholes. Results showed little differences between the two solutions.

Lamarche and Beauchamp (2007b) simplified the FLS solution and obtained a relation for the integral mean temperature at the borehole wall involving a single integral instead of a double integral as was the case for Zeng et al. (2002). The solution was used to calculate thermal response factors for bore fields but was only applicable for the case D = 0. The integral mean temperature gave a better approximation of Eskilson's g-functions than the temperature at mid-length. Costes and Peysson (2008) used the same methodology to obtain a relation for the case D > 0. The solution is included in Chapuis's thesis (Chapuis, 2009).

Claesson and Javed (2011) also proposed a relation for the integral mean temperature at the borehole wall for the case $D \geq 0$. According to the authors, the integral mean temperature at a distance r from the center of the borehole is given by:

$$\Delta\bar{T}(r,t) = -\frac{Q}{4\pi k_s} \cdot \int_{1/\sqrt{4\alpha_s t}}^{\infty} exp(-r^2 s^2) \cdot \frac{Y(Hs, Ds)}{Hs^2} \cdot ds \qquad (4.2)$$

$$Y(h,d) = 2 \cdot ierf(h) + 2 \cdot ierf(h+2d) - ierf(2h+2d) - ierf(2d) \qquad (4.3)$$

$$ierf(X) = X \cdot erf(X) - \frac{1}{\sqrt{\pi}}(1 - exp(-X^2)) \tag{4.4}$$

where $\Delta\bar{T} = \bar{T} - T_g$ is the average (over the length) temperature variation at a distance r from the center of the borehole.

For a field of multiple boreholes, spatial superposition is used to obtain the average temperature variation at the borehole walls:

$$T_b(t) = \frac{1}{n_b}\sum_{j=1}^{n_b}\sum_{i=1}^{n_b}\Delta\bar{T}\left(d_{ij}, t\right) \tag{4.5}$$

$$d_{ij} = \begin{cases} r_b & \text{for } i = j \\ \sqrt{\left(x_i - x_j\right)^2 + \left(y_i - y_j\right)^2} & \text{for } i \neq j \end{cases} \tag{4.6}$$

where ΔT_b is the average temperature variation at the borehole walls, (x_i, y_i) are the coordinates of the i^{th} borehole and n_b is the number of boreholes in the bore field. Equation 4.5 will be referred to as the FLS/BC-I solution.

The FLS was also used to model inclined boreholes using BC-I. Cui et al. (2006), Marcotte and Pasquier (2009) and Lamarche (2011)) presented solutions for the evaluation of the temperature at the wall of inclined boreholes. Lamarche (2011) compared his solution to Eskilson's g-functions for fields of 2, 4 and 6 inclined boreholes. The differences with Eskilson's g-functions were within 2% in all cases studied.

Fossa (2011) compared thermal response factors obtained from the FLS with BC-I to Eskilson's g-functions for fields of 3 × 3 and 8 × 2 boreholes. The author noted that the FLS/BC-I calculation overestimates Eskilson's g-functions for small values of the parameter B/H and large values of the non-dimensional time t/t_s. Fossa et al. (2009) earlier compared the thermal response factor of a 8 × 4 borehole field obtained using the FLS with BC-II. Heat extraction rates of individual boreholes were changed iteratively until a common borehole wall temperature was achieved. The thermal response factor was found to be similar to that of the FLS/BC-I solution.

Acuña et al. (2012) and later Monzó et al. (2013) used 3-D finite elements simulations to calculate thermal response factors. Boreholes were modeled as cylindrical sources of uniform heat injection rate in a cylindrical ground domain with constant temperature boundaries. The case

of a field of 8 × 8 boreholes was studied. Results were compared with thermal response factors obtained from the FLS/BC-I solution and g-functions generated by the software tool EED (1994).

Cimmino et al. (2013) proposed a method based on the FLS for the approximation of Eskilson's g-functions. A system of equation was built in the Laplace domain and solved to obtain thermal response factors of bore fields. The authors considered the time variation of the heat extraction rates of individual boreholes by imposing the average (over the length) borehole wall temperature to be equal for all boreholes. This condition, corresponding to boundary condition BC-II, differs from the FLS/BC-I solution (Equation 4.5) which considers the heat extraction rate to be constant and equal for all boreholes. Noticeable differences between the thermal response factors obtained using this FLS/BC-II approach and Eskilson's were still noted for large bore fields with small spacing between boreholes. The differences are attributed to the boundary condition used at the borehole wall: the FLS/BC-II assumes a uniform (over the length) heat extraction rate at the borehole wall (BC-II) while Eskilson's g-functions assume a uniform borehole wall temperature (BC-III). A simplified version of the method of Cimmino et al. (2013) was presented by Cimmino and Bernier (2013) for boreholes of unequal lengths.

The next logical step, which is the main trust of this paper, is to evaluate thermal response factors analytically with the FLS solution and the BC-III boundary condition to reproduce Eskilson's numerically-generated g-functions. In addition, the methodology is generalized to account for boreholes of different lengths and buried depth.

4.3 Proposed model

A bore field of 3 arbitrarily sized and positioned boreholes was presented in Figure 4-1. Each borehole has a radius r_b, a length H_i, is buried at a distance D_i from the ground surface and positioned at coordinates (x_i, y_i). The ground has a thermal conductivity k_s, a thermal diffusivity α_s and is initially at a uniform temperature T_g.

As per the definition of the g-function (Equation 4.1), the g-function is obtained by calculating the borehole wall temperature T_b, resulting from the simultaneous extraction of heat by all boreholes of the field at an average heat extraction rate per unit length $\bar{Q}$.

4.3.1 Segment-to-segment response factors

Each borehole is modeled as a series of n_q finite line sources segments stacked on top of each other as shown on Figure 4-5 for n_q = 3. n_q is the same for all boreholes. This constitutes a generalization of the method presented by Cimmino et al. (2013), which corresponds to the case n_q = 1. The temperature drop at the wall of a borehole segment caused by the extraction of heat from another borehole segment is given by the finite line source solution provided in Appendix A. For a constant heat extraction rate at the uth segment of the i^{th} borehole:

$$\Delta T_{i\to j,u\to v}(t_k) = -\frac{Q_{i,u}}{2\pi k_s} \cdot h_{i\to j,u\to v}(t_k) \tag{4.7}$$

$$h_{i\to j,u\to v}(t) = h_{FLS}\left(t, d_{ij}, H_{i,u}, D_{i,u}, H_{j,v}, D_{j,v}\right) \tag{4.8}$$

$$\begin{aligned} h_{i\to j,u\to v}(t) = \frac{1}{2H_{j,v}} \int_{1/\sqrt{4\alpha_s t}}^{\infty} \frac{1}{s^2} exp\left(-{d_{ij}}^2 s^2\right) \Big[& ierf\left(\left(D_{j,v} - D_{i,u} + H_{j,v}\right)\mathrm{s}\right) \\ & - ierf\left(\left(D_{j,v} - D_{i,u}\right)\mathrm{s}\right) + ierf\left(\left(D_{j,v} - D_{i,u} - H_{i,u}\right)\mathrm{s}\right) \\ & - ierf\left(\left(D_{j,v} - D_{i,u} + H_{j,v} - H_{i,u}\right)\mathrm{s}\right) \\ & + ierf\left(\left(D_{j,v} + D_{i,u} + H_{j,v}\right)\mathrm{s}\right) - ierf\left(\left(D_{j,v} + D_{i,u}\right)\mathrm{s}\right) \\ & + ierf\left(\left(D_{j,v} + D_{i,u} + H_{i,u}\right)\mathrm{s}\right) \\ & - ierf\left(\left(D_{j,v} + D_{i,u} + H_{j,v} + H_{i,u}\right)\mathrm{s}\right)\Big] ds \end{aligned} \tag{4.9}$$

$$ierf(\mathrm{X}) = \int_0^X erf(x')\, dx' = X\, erf(X) - \frac{1}{\sqrt{\pi}}(1 - exp(-X^2)) \tag{4.10}$$

$$d_{ij} = \begin{cases} r_b & \text{for } i = j \\ \sqrt{\left(x_i - x_j\right)^2 + \left(y_i - y_j\right)^2} & \text{for } i \neq j \end{cases} \tag{4.11}$$

where $\Delta T_{i\to j,u\to v}$ is the temperature variation at the wall of the v^{th} segment of the j^{th} borehole caused by the extraction of heat at the wall of the u^{th} segment of the i^{th} borehole at a rate $Q_{i,u}$, d_{ij} is the distance separating borehole i from borehole j located at coordinates (x_i, y_i) and $\left(x_j, y_j\right)$, $h_{i\to j,u\to v}$ is the segment-to-segment response factor of the u^{th} segment of the i^{th} borehole on the

v^{th} segment of the j^{th} borehole, $H_{i,u}$ and $D_{i,u}$ are the length and buried depth of the u^{th} segment of the i^{th} borehole.

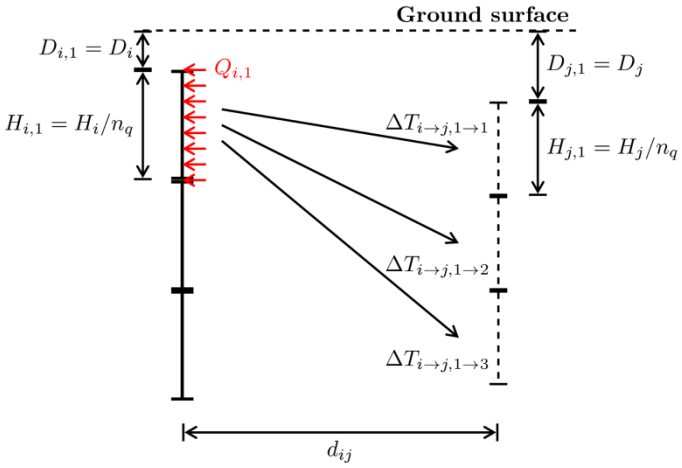

Figure 4-5: Two interacting boreholes each modelled with three stacked finite line sources segments

4.3.2 Temporal and spatial superposition

For a varying heat extraction rate $Q_{i,u}(t)$, the temperature variation is obtained through temporal superposition of the finite line source solution:

$$\Delta T_{i\to j,u\to v}(t_k) = -\sum_{p=1}^{k}\left[\frac{q_{i,u}(t_p)}{2\pi k_s}\cdot h_{i\to j,u\to v}(t_k - t_{p-1})\right] \tag{4.12}$$

where $q_{i,u}(t_p) = Q_{i,u}(t_p) - Q_{i,u}(t_{p-1})$ is the heat extraction rate increment of the u^{th} segment of the i^{th} borehole, $Q_{i,u}(t_0) = 0$ and $\Delta t = t_p - t_{p-1}$ is the calculation time step.

The total temperature variation at the wall of the borehole segments is obtained by superposition of the temperature drops caused by all borehole segments:

$$\Delta T_{b,j,v}(t_k) = -\sum_{p=1}^{k}\sum_{i=1}^{n_b}\sum_{u=1}^{n_q}\frac{q_{i,u}(t_p)}{2\pi k_s}h_{i\to j,u\to v}(t_k - t_{p-1}) \tag{4.13}$$

where $\Delta T_{b,j,v} = T_{b,j,v} - T_g$ is the temperature variation at the wall of the v^{th} segment of the j^{th} borehole, n_b is the total number of boreholes in the field. Equation 4.13 can be evaluated for any

segment v of any borehole j and thus forms a set of $n_b \cdot n_q$ equations with $2 \cdot n_b \cdot n_q$ unknowns ($q_{i,u}$ and $\Delta T_{b,i,u}$). The total heat extraction rate of the bore field is constant:

$$\bar{Q} = \frac{\sum_{i=1}^{n_b} \sum_{u=1}^{n_q} H_{i,u} Q_{i,u}(t_k)}{\sum_{i=1}^{n_b} \sum_{u=1}^{n_q} H_{i,u}} \tag{4.14}$$

Equation 4.14 can be expressed in terms of heat extraction rate increments:

$$\frac{\sum_{i=1}^{n_b} \sum_{u=1}^{n_q} H_{i,u} q_{i,u}(t_k)}{\sum_{i=1}^{n_b} \sum_{u=1}^{n_q} H_{i,u}} = \bar{Q}\delta(t_k - t_1) = \begin{cases} \bar{Q} & \text{for } t_k = t_1 \\ 0 & \text{for } t_k \neq t_1 \end{cases} \tag{4.15}$$

In non-dimensional form:

$$\Theta_{b,j,v}(t_k) = \sum_{p=1}^{k} \sum_{i=1}^{n_b} \sum_{u=1}^{n_q} \tilde{q}_{i,u}(t_p) h_{i \to j,u \to v}(t_k - t_{p-1}) \tag{4.16}$$

$$\frac{\sum_{i=1}^{n_b} \sum_{u=1}^{n_q} H_{i,u} \tilde{q}_{i,u}(t_k)}{\sum_{i=1}^{n_b} \sum_{u=1}^{n_q} H_{i,u}} = \delta(t_k - t_1) = \begin{cases} 1 & \text{for } t = t_1 \\ 0 & \text{for } t \neq t_1 \end{cases} \tag{4.17}$$

where $\Theta_{b,j,v} = \frac{\Delta T_{b,j,v}}{-\bar{Q}/2\pi k_s}$ is the non-dimensional temperature drop at the wall of the v^{th} segment of the j^{th} borehole, $\tilde{q}_{i,u} = q_{i,u}/\bar{Q}$ is the normalized heat extraction rate increment.

4.3.3 Boundary conditions

Additional equations are required to complete the system of equations and satisfy boundary conditions BC-I, BC-II and BC-III. BC-I corresponds to the case of a uniform heat extraction rate equal for all boreholes:

$$Q_{i,u}(t_k) = \bar{Q}, \qquad \tilde{q}_{i,u}(t_k) = \delta(t_k - t_1) \tag{4.18}$$

$$\Theta_b(t_k) = \frac{\sum_{j=1}^{n_b} \sum_{v=1}^{n_q} H_{j,v} \Theta_{b,j,v}(t_k)}{\sum_{j=1}^{n_b} \sum_{v=1}^{n_q} H_{j,v}} \tag{4.19}$$

BC-II corresponds to the case of uniform heat extraction rate along the length of the boreholes (but different from borehole to borehole) and an average borehole wall temperature equal for all boreholes:

$$Q_i(t_k) = Q_{i,u}(t_k), \qquad \tilde{q}_i(t_k) = \tilde{q}_{i,u}(t_k) \tag{4.20}$$

$$\Theta_{b,j}(t_k) = \frac{\sum_{v=1}^{n_q} H_{j,v}\Theta_{b,j,v}(t_k)}{\sum_{v=1}^{n_q} H_{j,v}} \tag{4.21}$$

$$\Theta_b(t_k) = \Theta_{b,j}(t_k) \tag{4.22}$$

Finally, BC-III corresponds to the case of a uniform borehole wall temperature equal for all boreholes:

$$\Theta_b(t_k) = \Theta_{b,j,v}(t_k) \tag{4.23}$$

Equations. 4.16-4.17, along with Equations. 4.18-4.19 (BC-I), 4.20-4.22 (BC-II) or 4.23 (BC-III) form 3 complete systems of equations. The solution of the systems of equations gives the normalized heat extraction rate increments $\tilde{q}_{i,u}$ as well as the non-dimensional temperature drop at the borehole wall Θ_b, corresponding to the thermal response factor, or g-function, of the bore field. It should be noted that the number of borehole segments n_q is irrelevant for boundary conditions BC-I and BC-II and the number of borehole segments is set to n_q = 1 in these two cases.

4.3.4 System of equations in the spectral domain

These systems of equations are however difficult to solve due to the summation over the time variable in Equation 4.16. Marcotte and Pasquier (2008a) showed that this summation takes the form of a convolution product that can be replaced by a product in the Fourier domain. The Laplace transform is used here to avoid temporal aliasing that occurs when using the Fourier transform.

The Laplace transform pairs are expressed as:

$$F(s) = \mathcal{L}\big(f(t)\big) = \int_0^{\infty} f(t)\, exp(\text{-}st)\, dt \tag{4.24}$$

$$f(t) = \mathcal{L}^{\text{-}1}\big(F(s)\big) = \frac{1}{2\pi j}\int_{\sigma-j\infty}^{\sigma+j\infty} F(s)\, exp(st)\, ds \tag{4.25}$$

where $\mathcal{L}$ and $\mathcal{L}^{-1}$ are the direct and inverse Laplace transforms, f is an arbitrary function in the time domain and F the corresponding-function in the Laplace domain, s is the complex frequency in the Laplace domain and $j = \sqrt{-1}$ is the imaginary number.

The Laplace transform can be obtained from the Fourier transform. A variable change $s = \sigma + j\omega$ (Moreno & Ramirez, 2008) leads to:

$$F(s) = \int_0^{\infty} [f(t)\, exp(-\sigma t)]\, exp(-j\omega t)\, dt = \mathcal{F}(f(t) \cdot exp(-\sigma t)) \tag{4.26}$$

$$f(t) = \frac{exp(\sigma t)}{2\pi} \int_{-\infty}^{+\infty} F(s)\, exp(j\omega t)\, d\omega = exp(\sigma t) \cdot \mathcal{F}^{-1}\big(F(s)\big) \tag{4.27}$$

where ω is the angular frequency in the Fourier domain, $\mathcal{F}$ and $\mathcal{F}^{-1}$ are the direct and inverse Fourier transforms, $\sigma = 2 \cdot \frac{\ln(N_t)}{t_{max}}$ is the damping factor chosen according to Wedepohl's criterion (Wedepohl, 1983), N_t is the total number of time steps and t_{max} is the maximum value of the time variable.

Equations 4.16-4.17 are expressed in the Laplace domain:

$$\mathcal{L}\big(\Theta_{b,j,v}\big) = \sum_{i=1}^{n_b} \sum_{u=1}^{n_q} \mathcal{L}\big(\tilde{q}_{i,u}\big) \mathcal{L}\big(h_{i \to j, u \to v}\big) \tag{4.28}$$

$$\mathcal{L}\big(\delta(t - t_1)\big) = \frac{\sum_{i=1}^{n_b} \sum_{u=1}^{n_q} H_{i,u} \mathcal{L}\big(\tilde{q}_{i,u}\big)}{\sum_{i=1}^{n_b} \sum_{u=1}^{n_q} H_{i,u}} \tag{4.29}$$

Equations 4.18-4.19 for BC-I become:

$$\mathcal{L}\big(\tilde{q}_{i,u}\big) = \mathcal{L}\big(\delta(t - t_1)\big) \tag{4.30}$$

$$\mathcal{L}(\Theta_b) = \frac{\sum_{j=1}^{n_b} \sum_{v=1}^{n_q} H_{j,v} \mathcal{L}\big(\Theta_{b,j,v}\big)}{\sum_{j=1}^{n_b} \sum_{v=1}^{n_q} H_{j,v}} \tag{4.31}$$

Equations 4.20-4.22 for BC-II become:

$$\mathcal{L}(\tilde{q}_i) = \mathcal{L}\big(\tilde{q}_{i,u}\big) \tag{4.32}$$

$$\mathcal{L}\left(\Theta_{b,j}\right) = \frac{\sum_{v=1}^{n_q} H_{j,v}\mathcal{L}\left(\Theta_{b,j,v}\right)}{\sum_{v=1}^{n_q} H_{j,v}} \tag{4.33}$$

$$\mathcal{L}(\Theta_b) = \mathcal{L}\left(\Theta_{b,j}\right) \tag{4.34}$$

Equation 4.23 for BC-III becomes:

$$\mathcal{L}(\Theta_b) = \mathcal{L}\left(\Theta_{b,j,v}\right) \tag{4.35}$$

The systems of equations are solved numerically using an FFT algorithm to evaluate the Fourier transforms. The calculation time is mostly dependent on the number of numerical evaluations of the FLS solution (Equation 4.9), which increases with the number of time steps used in the evaluation of the g-function curve and with the square of the total number of borehole segments ($n_b \cdot n_q$) in the bore field. The calculation time for BC-I and BC-II are about the same since both use the same number of borehole segments n_q = 1. The time required for the calculation of the g-function using BC-II and BC-III (using n_q = 12) and 71 time steps for bore fields of 3 × 2, 6 × 4 and 10 × 10 boreholes, is shown in Table 4-1. The calculation time is 13 times greater for BC-III than for BC-II on average for all bore fields studied. The calculation times of the FLS/BC-II and FLS/BC-III solutions are significantly lower than the numerical g-functions. These calculation times were obtained on a computer equipped with an AMD Phenom II X6 processor (2.7 GHz) and 8 Gb of RAM.

Table 4-1: Time required for the calculation of the g-functions for bore fields of 3 × 2, 6 × 4 and 10 × 10 boreholes

Field	FLS/BC-II	FLS/BC-III	numerical g-function
3 × 2	2 s	28 s	3 min
6 × 4	8 s	98 s	26 min
10 × 10	25 s	433 s	7 hrs

4.4 Results

4.4.1 g-functions

The g-functions for bore fields of 3 × 2, 6 × 4 and 10 × 10 boreholes are computed using the proposed methodology. Boreholes have a length H = 150 m, a radius r_b = 0.075 m, are buried at a depth D = 4 m and are equally spaced at a distance B = 7.5 m (B/H = 0.05). The ground has a thermal diffusivity α_s = 1 × 10^6 m^2/s. The solution for BC-III is obtained using n_q = 12 segments. g-functions obtained using the proposed methodology for all three boundary conditions are compared in Figure 4-6 to numerical g-functions obtained using BC-III.

Numerical g-functions are obtained from a finite difference numerical model, based on the work of Eskilson (1986, 1987). Every borehole is modeled in a 2-D radial-axial mesh with 12 uneven cells along the borehole length and 6 cells above and below the borehole. The first cells above and below the two extremities of the boreholes have a height $\frac{H}{2}\frac{\sqrt{2}-1}{\sqrt{2}^{n_q/2}-1}$. The height of the cells expands with a factor 2 above and below the boreholes and with a factor $\sqrt{2}$ towards the middle of the borehole. The size of the cells is expanding in the radial direction, as shown in the example on Figure 4-4. The three first cells have a width $3\sqrt{\alpha_s \Delta t}$. The width of cells then expands with a factor 2 until the maximum radius $3\sqrt{\alpha_s t_{max}}$ is attained. Spatial superposition is used to calculate the global temperature drop at the borehole walls. Image boreholes, symmetric with the ground surface and of opposite signs, are used to obtain the constant temperature condition at the ground surface. The heat extraction rates at every cell along the boreholes are calculated at each time step to obtain a uniform borehole wall temperature equal for all boreholes.

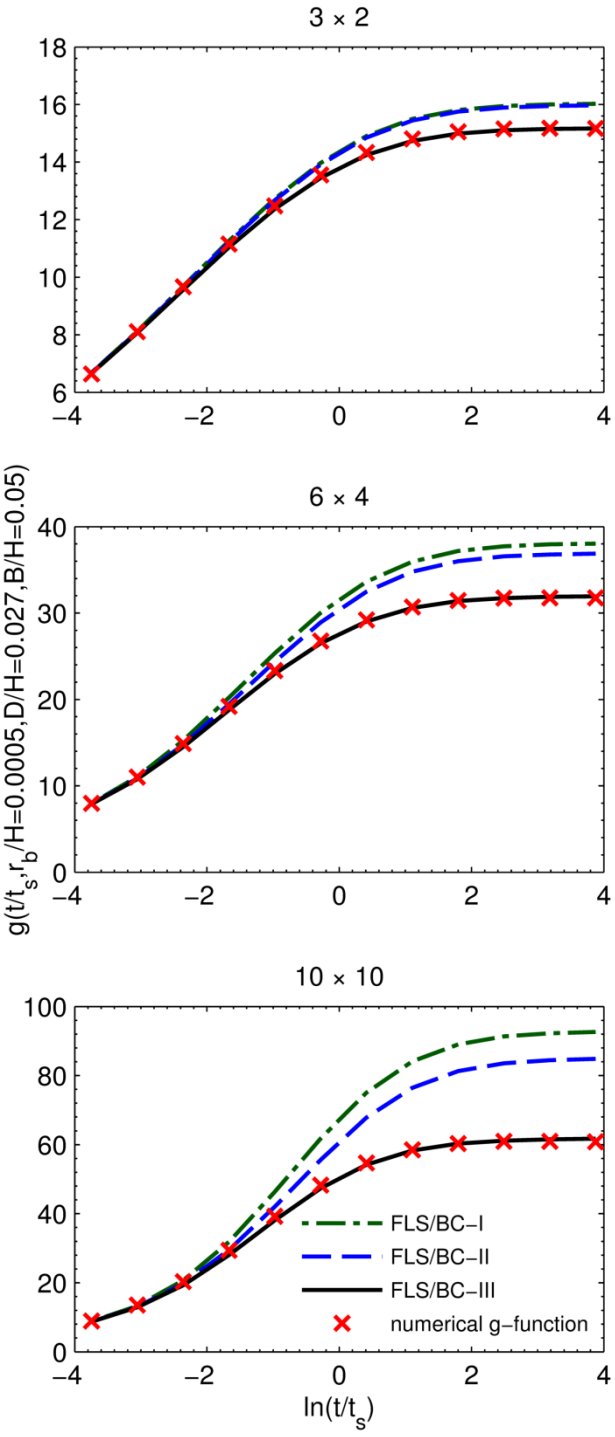

Figure 4-6: Thermal response factors of fields of 3 × 2, 6 × 4 and 10 × 10 boreholes, compared with Eskilson's numerical g-functions

As shown on Figure 4-6, the differences between the g-functions obtained using BC-I, BC-II and BC-III vary as a function of $\ln(t/t_s)$. For values of $\ln(t/t_s)$ below approximately -2.3, all four curves are identical. In practical terms, for the conditions listed above, this corresponds to $t \approx 8$ years. Thus, for these particular conditions the use of the BC-I boundary condition would greatly reduce the calculation speed without any loss of accuracy. This threshold time will of course vary with borehole length and ground thermal diffusivity. As the value of $\ln(t/t_s)$ increases the differences between the FLS/BC-I and FLS/BC-II and the other two curves increases. These differences are greater for larger bore fields. For the 10 × 10 bore field, the difference between the FLS/BC-I and FLS/BC-II curves and the g-function are 52 and 39%, respectively in the steady-state region at $\ln(t/t_s)$ = 3.5. These results are similar to the results of Cimmino et al. (2013) for the same boundary conditions. The FLS/BC-III curve is in very good agreement with the numerical g-function with a difference of 1.5 % and 1.4 % at $\ln(t/t_s)$ = 0 and 3.5, respectively for the 10 × 10 bore field. The lower g-function values obtained using BC-III (either with FLS/BC-III or with the numerical g-function) when compared to the FLS/BC-I solution result from the variation of the normalized heat extraction rates from borehole to borehole and along the length of the boreholes as will be shown in Figures 4-8 and 4-9 in the next section.

Figure 4-7a shows additional comparisons between the FLS/BC-III and the numerical g-functions for 312 bore field configurations ranging from a single borehole up to a field of 12 × 12, evaluated at time $\ln(t/t_s)$ = 3.5 and for spacing-to-length ratios B/H = 0.05, 0.10, 0.20 and 0.50. The results from the two models are in good agreement, with 92 % of the bore fields within ± 5 %. The root mean square (RMS) difference between the two models is 2.4 %. The greatest differences occur for fields of boreholes positioned on a single row. For these fields, the difference between the two models reaches 10 % for the 12 × 1 borehole field with B/H = 0.05. These differences are most likely due to the interpolation of temperatures in the expanding radial mesh used for the calculation of the numerical g-functions. The interpolation error at greater distances from the boreholes is more important since the cells are bigger and are thus more distanced from each other. Thus, the g-functions generated numerically using the approach of Eskilson may not be precise for certain configurations. Nonetheless, they will be used here as the reference for comparison with analytical methods. Figure 4-7b shows the RMS difference with the numerical g-function as a function of $\ln(t/t_s)$ for all three boundary conditions and B/H = 0.05 (78 bore fields). It is shown that the FLS/BC-III solution is able to calculate the

g-function with a RMS difference of approximately 3 % for all values of $\ln(t/t_s)$. Based on these comparisons, the FLS/BC-III solution is in good agreement with the numerical calculation of the g-functions for any value of $\ln(t/t_s)$. The FLS/BC-II and FLS/BC-III are in good agreement with the numerical g-functions up to $\ln(t/t_s) \approx$ -2.3. After this threshold, the FLS/BC-II start to show significant differences with the FLS/BC-III solution and the numerical solution and is inadequate for large values of $\ln(t/t_s)$.

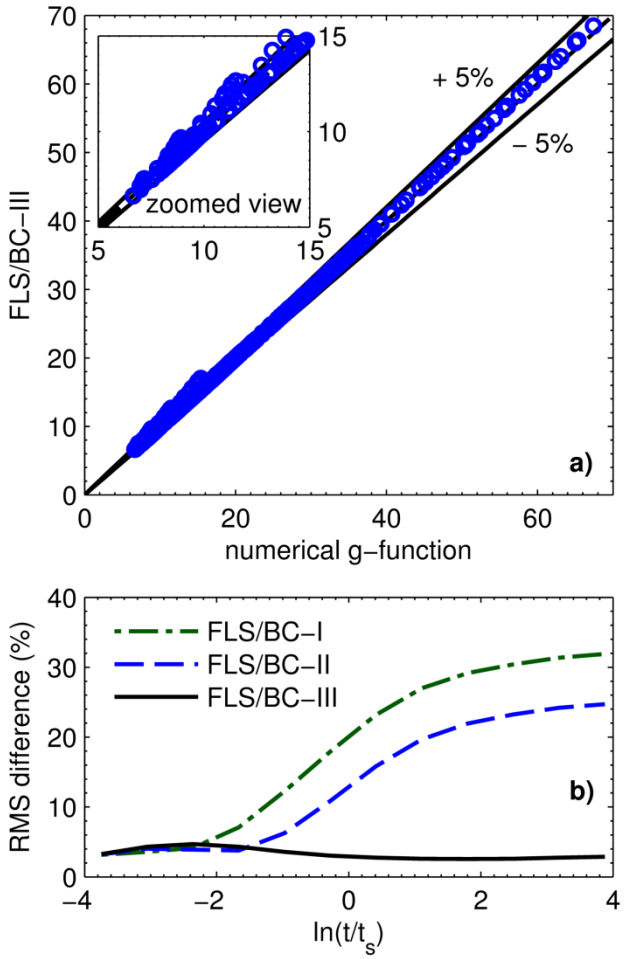

Figure 4-7: a) Comparison of the analytical and numerical g-functions for boundary condition BC-III and b) RMS difference between the analytical solutions and the numerical g-function

4.4.2 Heat extraction rates

The individual normalized heat extraction rates of the different boreholes calculated with FLS/BC-III also correspond to those predicted by the numerical model. Figure 4-8 shows the average normalized heat extraction rate $\tilde{Q}_i$ of different boreholes in a 6 × 4 bore field. It is interesting to note that the extraction rate varies significantly as a function of the borehole position in the bore field. The normalized heat extraction rates are higher for boreholes located further away from the center of the bore field and at the top and bottom of the boreholes (as shown on Figure 4-9). For example, at $\ln(t/t_s) = 0$, the normalized heat extraction rate of corner boreholes (borehole #1) is 1.6 while that of center boreholes (borehole #6) is 0.5. More heat is therefore extracted from the ground outside of the ground volume bounded by the boreholes and the temperature drop for boreholes inside the bore field is thus lower.

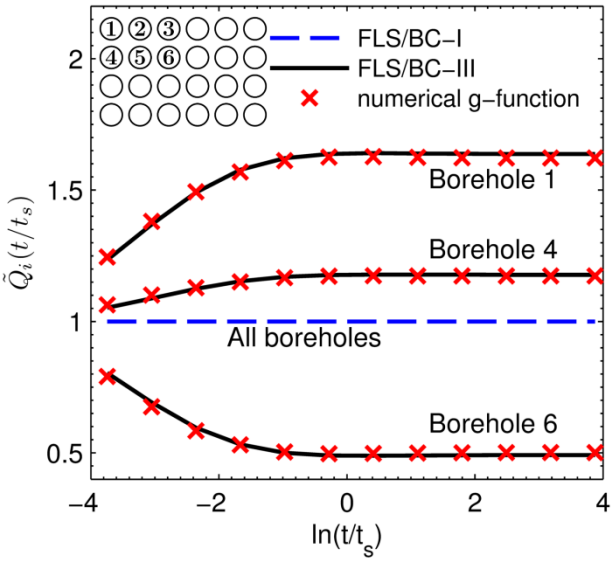

Figure 4-8: Variation of the normalized heat extraction rates in a 6 × 4 bore field

The average normalized heat extraction rate is obtained from the normalized heat extraction rate increments of the borehole segments:

$$\tilde{Q}_i(t_k) = \frac{\sum_{p=1}^{k}\sum_{u=1}^{n_q} H_{i,u}\tilde{q}_{i,u}(t_p)}{\sum_{u=1}^{n_q} H_{i,u}} \tag{4.36}$$

A variation of the normalized heat extraction rates is also seen over the length of the boreholes, which can only be predicted using BC-III. Figure 4-9 shows the normalized heat extraction rates of the segments of a borehole located at the center of a field of 6 × 4 boreholes at time $\ln(t/t_s)$ = 3.5 calculated with FLS/BC-III, compared with results from the numerical g-function model. The heat extraction rates for the numerical solution are shown at the center of each of the 12 cells along the borehole length. The heat extraction rates for the analytical solution are calculated with n_q = 64. Here again the agreement is very good.

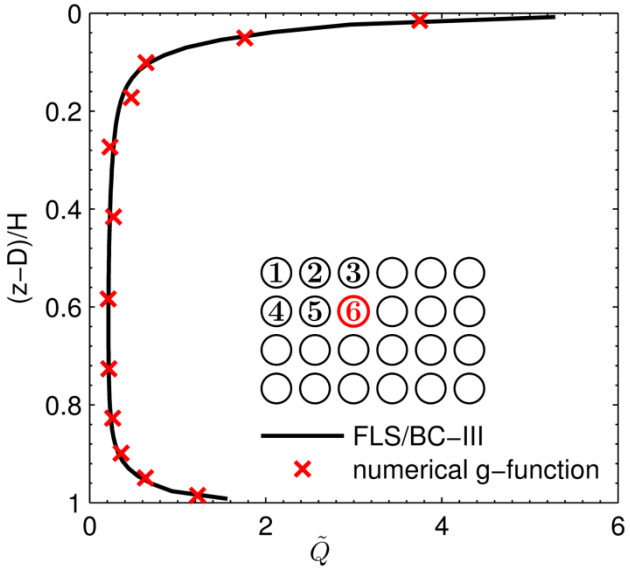

Figure 4-9: Normalized heat extraction rate along the length of a borehole located in the center of a 6 × 4 bore field

4.4.3 Dependence on n_q

The accuracy of the g-functions calculated using FLS/BC-III depends on the number of segments nq used in their calculation. It was shown on Figure 4-7a that the g-functions calculated using BC-III for n_q = 12 were within 5 % of the numerical g-functions for $\ln(t/t_s)$ = 3.5. However, the numerical g-functions were calculated with a limited number of cells along the length of the boreholes in the finite difference mesh. In fact, Eskilson's g-functions were obtained using a maximum of 12 uneven cells along the borehole length (Eskilson, 1987) and as mentioned earlier this may not be sufficient in certain circumstances. The dependence of the FLS/BC-III solution

on the number of segments will now be examined. The error on the solution is defined here using 256 borehole segments as reference:

$$\varepsilon_i(t) = \frac{g_i - g_{256}}{g_{256}} \tag{4.37}$$

where $\varepsilon_i(t)$ is the error on the g-function at time t calculated using i borehole segments, g_i and g_{256} are the values of the g-function calculated with FLS/BC-III using i and 256 borehole segments, respectively. The errors on the values of the g-function at $t \to \infty$ and t = 20 years ($\ln(t/t_s)$ = 1.4) are shown on Figure 4-10 for a field of 7 × 7 boreholes with B/H = 0.05, D/H = 0.027, r_b/H = 0.0005 and α_s = 1 × 10 6 m^2/s. For n_q = 12, the error is 3.4 % at steady-state and 1.8 % at t = 20 years. Additional comparisons for fields of 3 × 2, 6 × 4, 7 × 7 and 10 × 10 boreholes with B/H = 0.05, 0.10 and 0.20 are shown in Table 4-2. The error on the g-function increases with the number of boreholes and decreases as the spacing between boreholes increases. The error at t = 20 years is lower than the steady-state error. The reduction of the error from steady-state to 20 years is greater for bigger bore fields. For instance, the error on the g-function of the 10 × 10 bore field with B/H = 0.05 is 4.7% at steady-state and 2.2% at t = 20 years. In most cases, the g-functions obtained using n_q = 12 segments are a good approximation of the g-function obtained with 256 segments. The error can be reduced by increasing the number of segments. Using n_q = 16 segments, the error on the g-function of a 10 × 10 bore field with B/H = 0.05 is 3.1% at steady-state and 1.4% at t = 20 years. These results also suggest that the axial mesh (12 nodes along the length of the borehole) used in the numerical determination of the g-function may not lead to a grid independent solution.

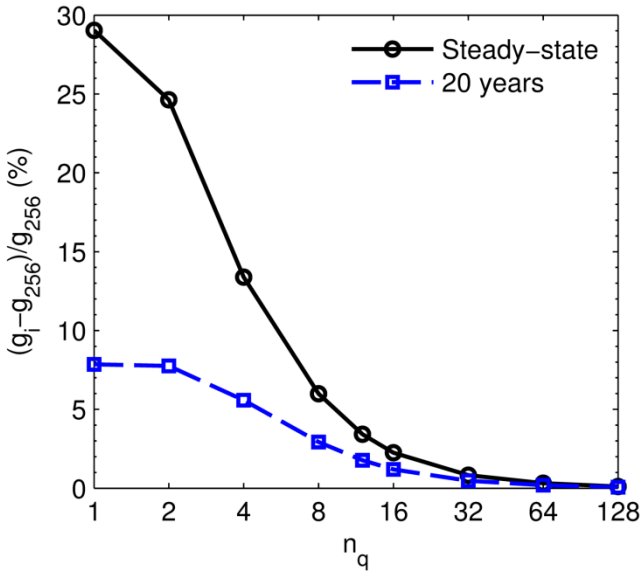

Figure 4-10: Error on the value of the g-function of a 7 × 7 bore field at steady-state and at t = 20 years as a function of the number of borehole segments

Table 4-2: Error on the g-functions at $t \to \infty$ and t = 20 years for various bore field configurations

Field	B/H	$g_{12}(t \to \infty)$	$g_{256}(t \to \infty)$	$\varepsilon_{12}(t \to \infty)$	$g_{12}(t = 20\ \text{yrs})$	$g_{256}(t = 20\ \text{yrs})$	$\varepsilon_{12}(t = 20\ \text{yrs})$
3×2	0.05	15.18	15.03	0.97 %	11.62	11.54	0.73 %
	0.10	12.28	12.20	0.69 %	8.89	8.85	0.48 %
	0.20	9.92	9.87	0.48 %	6.93	6.91	0.32 %
6×4	0.05	31.97	31.24	2.32 %	20.59	20.29	1.46 %
	0.10	21.49	21.20	1.36 %	11.99	11.90	0.74 %
	0.20	14.34	14.23	0.72 %	7.51	7.48	0.38 %
7×7	0.05	45.67	44.16	3.42 %	26.53	26.04	1.87 %
	0.10	27.86	27.36	1.83 %	13.47	13.36	0.85 %
	0.20	17.01	16.86	0.87 %	7.72	7.69	0.39 %
10×10	0.05	61.78	59.00	4.70 %	32.20	31.50	2.21 %
	0.10	34.39	33.61	2.30 %	14.60	14.47	0.91 %
	0.20	19.49	19.29	1.00 %	7.86	7.83	0.39 %

4.4.4 Validity of Eskilson's boundary condition

Eskilson's boundary condition of uniform temperature at the borehole walls, equal for all boreholes (BC-III), and its resulting g-functions were used as reference for comparison of the thermal response factors obtained using the model presented in the current study. In reality, boreholes in a bore field have a common inlet fluid temperature, and both the temperature and extraction rate vary along the length of the boreholes. A preliminary analysis has shown that using a boundary condition of inlet fluid temperature requires the introduction of additional non-dimensional parameters taking into account the fluid mass flow rate $\dot{m}$, the fluid specific heat c_p and the internal thermal resistances between the two U-tube pipes R_{12} and between each pipe and the borehole wall R_{11}, R_{22} (Lamarche et al., 2010):

$$\frac{\dot{m}c_p R_{12}}{H}, \quad \frac{\dot{m}c_p R_{11}}{H}, \quad \frac{\dot{m}c_p R_{22}}{H}, \quad \frac{\dot{m}c_p}{2\pi k_s H} \tag{4.38}$$

The boundary condition of inlet fluid temperature was considered by Eskilson for the simulation of geothermal systems (Eskilson, 1986, 1987). It was demonstrated that, for a system of one borehole, the boundary condition of inlet fluid temperature and uniform temperature (BC-III) resulted in very similar borehole wall temperatures over a simulation of 25 years. However, future work should determine more precisely the validity of the uniform temperature boundary condition and the dependence of the g-functions on the fluid mass flow rate and internal thermal resistances in fields of multiple boreholes.

4.5 Conclusion

A methodology based on the finite line source solution is used to generate g-functions of bore fields. Boreholes are divided into segments to consider the variation of the heat extraction rates along the length of the boreholes. The borehole wall temperature is assumed to be equal for all segments of all boreholes (referred to as boundary BC-III). Segment-to-segment response factors are superposed in space and time to build a system of equations in the Laplace domain. The solution to the system of equations gives the time variation of the borehole wall temperature and the heat extraction rates of the borehole segments.

g-functions calculated with the proposed methodology are compared to the numerical technique used by Eskilson, with relatively coarse grids, to derive the g-functions for fields of 1 to 12 × 12

boreholes. The difference between the two models is within 5 % (with an RMS difference of 2.4%) for all studied bore fields, except for fields of boreholes located on a single row. In this case, these differences are most likely due to the interpolation of temperatures in the expanding radial mesh used for the calculation of the numerical g-functions. The calculated heat extraction rates at the borehole segments are also in close agreement with results from the numerical model.

The dependence of the solution on the number of segments is also examined. In most cases, the g-functions obtained using n_q = 12 segments are a good approximation of the g-function obtained with 256 segments. For instance, the error on the g-function of the 10 × 10 bore field with B/H = 0.05 is 4.7% at steady-state and 2.2% at t = 20 years. These results also suggest that the axial mesh (12 nodes along the length of the borehole) used in the numerical determination of the g-function may not lead to a grid independent solution.

The presented methodology based on analytical solutions for the evaluation of g-functions has several advantages over the numerical method of Eskilson. The calculation time is greatly reduced and therefore the presented methodology is better adapted to the iterative design and optimization of bore fields. For the cases presented here, the calculation time is less than 10 min (e.g. 28 s for 1 borehole and 7 min for 100 boreholes) using the proposed methodology while the calculation of g-functions using the numerical model can take several hours. The solution is independent of any radial mesh in the ground and no interpolation of temperatures is required.

4.6 Acknowledgements

This work was partly funded by the NSERC Smart Net-Zero Energy Buildings Strategic Research Network (SNEBRN). The authors also wish to thank the Canadian GeoExchange Coalition and the American Society of Heating, Refrigerating and Air-Conditioning Engineers (ASHRAE) for a scholarship and a Grant-in-aid awarded to the first author.

4.7 Appendix A : General solution to the average temperature at a distance *r* of a finite line heat source

Claesson and Javed (2011) proposed a solution for the average (over the length) temperature at a radial distance r of a line source. The solution is adapted to allow averaging of the temperature for a length different from that of the line source and off-set in the axial direction.

A line source of length H_1 is extracting heat at constant rate Q in a infinite medium of thermal conductivity k, thermal diffusivity α, specific heat c and density ρ as shown in Figure 4-11. The average temperature drop $\Delta\bar{T}$ over a length H_2, parallel to the line source at a radial distance r and off-set by a distance Δz in the axial direction, is obtained from the spatial integration of the point heat source solution:

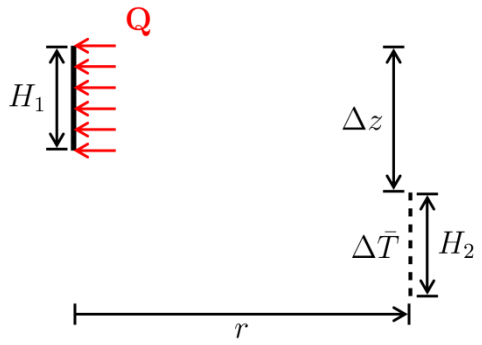

Figure 4-11: Finite line source modelling

$$\Delta\bar{T}(r,t,H_1,H_2,\Delta z) = \frac{1}{H_2}\int_0^t \frac{Q}{\rho c\left(4\alpha\pi(t-t')\right)^{\frac{3}{2}}}\int_{\Delta z}^{\Delta z+H_2}\int_0^{H_1} exp\left(-\frac{r^2+(z_2-z_1)^2}{4\alpha(t-t')}\right)dz_1\,dz_2\,dt' \quad (4.39)$$

The variable change $s = 1/\sqrt{4\alpha(t-t')}$ leads to:

$$\Delta\bar{T} = \frac{2}{H_2\sqrt{\pi}}\int_{1/\sqrt{4\alpha t}}^{\infty}\frac{Q}{4\pi k}exp(-r^2s^2)\int_{\Delta z}^{\Delta z+H_2}\int_0^{H_1} exp(-(z_2 - z_1)^2s^2)\,dz_1\,dz_2\,ds \quad (4.40)$$

The following variable changes are introduced:

$$\Theta = \frac{\Delta\bar{T}}{Q/2\pi k}, \quad sz_1 = v, \quad sz_2 = s\Delta z + u \quad (4.41)$$

$$\Theta = \frac{1}{2H_2}\int_{1/\sqrt{4\alpha t}}^{\infty} exp(-r^2s^2)\frac{2}{s^2\sqrt{\pi}}\int_0^{H_2 s}\int_0^{H_1 s} exp(-(s\Delta z + u - v)^2)\,dv\,du\,ds \quad (4.42)$$

The integrations over v and u lead to a solution involving integrals of the error function:

$$erf(\mathrm{X}) = \frac{2}{\sqrt{\pi}} \int_0^X exp(\text{-}x'^2)\, dx' \tag{4.43}$$

$$ierf(\mathrm{X}) = \int_0^X erf(x')\, dx' = X\, erf(X) - \frac{1}{\sqrt{\pi}}(1 - exp(\text{-}X^2)) \tag{4.44}$$

$$\begin{aligned} &\Theta(r, t, H_1, H_2, \Delta z) \\ &\quad = \frac{1}{2H_2} \int_{1/\sqrt{4\alpha t}}^{\infty} \frac{1}{s^2} exp(\text{-}r^2 s^2) \left[ierf\big((\Delta \mathrm{z} + H_2)\mathrm{s}\big) - ierf(\mathrm{s}\Delta \mathrm{z})\right. \\ &\quad \left. + ierf\big((\Delta \mathrm{z} - H_1)\mathrm{s}\big) - ierf\big((\Delta \mathrm{z} + H_2 - H_1)\mathrm{s}\big)\right] ds \end{aligned} \tag{4.45}$$

The solution to the average temperature variation over a length H_2 at a distance D_2 below a constant temperature surface T = 0 and at a radial distance r from a finite line source of length H_1 located at a distance D_1 below the constant temperature surface is given by superposition of an image source of opposing sign to the previous solution:

$$\begin{aligned} &h_{FLS}(r, t, H_1, H_2, D_1, D_2) \\ &\quad = \Theta(r, t, H_1, H_2, D_2 - D_1) - \Theta(r, t, H_1, H_2, H_1 + D_1 + D_2) \end{aligned} \tag{4.46}$$

$$\begin{aligned} &h_{FLS}(r, t, H_1, H_2, D_1, D_2) \\ &\quad = \frac{1}{2H_2} \int_{1/\sqrt{4\alpha_s t}}^{\infty} \frac{1}{s^2} exp(-r^2 s^2) \left[ierf\big((D_2 - D_1 + H_2)\mathrm{s}\big)\right. \\ &\quad - ierf\big((D_2 - D_1)\mathrm{s}\big) + ierf\big((D_2 - D_1 - H_1)\mathrm{s}\big) \\ &\quad - ierf\big((D_2 - D_1 + H_2 - H_1)\mathrm{s}\big) + ierf\big((D_2 + D_1 + H_2)\mathrm{s}\big) \\ &\quad - ierf\big((D_2 + D_1)\mathrm{s}\big) + ierf\big((D_2 + D_1 + H_1)\mathrm{s}\big) \\ &\quad \left. - ierf\big((D_2 + D_1 + H_2 + H_1)\mathrm{s}\big)\right] ds \end{aligned} \tag{4.47}$$

4.8 References

Acuña, J., Fossa, M., Monzó, P., & Palm, B. (2012). Numerically generated g-functions for ground-coupled heat pump applications. Proceedings of the 2012 COMSOL conference in Milan, Milan.

Baudoin, A. (1988). Stockage intersaisonnier de chaleur dans le sol par batterie d'échangeurs baionnette verticaux; modèle de prédimensionnement. Ph.D. Thesis, Université de Reims Champagne-Ardenne, France.

Bernier, M. A. (2000). A Review of the Cylindrical Heat Source Method for the Design and Analysis of Vertical Ground-Coupled Heat Pump Systems. 4th International Conference on Heat Pumps in Cold Climates.

Bernier, M. A. (2001). Ground-coupled Heat pump system simulation. ASHRAE Transactions, 107(1), 605-616.

Bernier, M. A., Pinel, P., Labib, R., & Paillot, R. (2004). A multiple load aggregation algorithm for annual hourly simulations of GCHP systems. HVAC&R Research, 10(4), 471-487.

Carslaw, H. S., & Jaeger, J. C. (1946a). Chapter 13, The Laplace transformation: Problems on the cylinder and sphere. In O. U. Press (dir.), Conduction of Heat in Solids. (2nde éd., pp. 327-352). Oxford: Oxford University.

Chapuis, S. (2009). Stockage thermique saisonnier dans un champ de puits géothermiques verticaux en boucle fermée. Master's Thesis, École Polytechnique de Montréal, Montréal.

Cimmino, M., & Bernier, M. (2013). Preprocessor for the generation of g-functions used in the simulation of geothermal systems. Proceedings of BS2013, Chambéry, France.

Cimmino, M., Bernier, M., & Adams, F. (2013). A contribution towards the determination of g-functions using the finite line source. Applied Thermal Engineering, 51(1-2), 401-412.

Claesson, J., & Javed, S. (2011). An analytical method to calculate borehole fluid temperatures for time-scales from minutes to decades. ASHRAE Transactions, 117(2), 279-288.

Cooper, L. Y. (1976). Heating of a cylindrical cavity. International Journal of Heat and Mass Transfer, 19, 575-577.

Costes, V., & Peysson, P. (2008). Capteurs géothermiques verticaux enterrés : Validation expérimentale de nouveaux modèles développés dans l'environnement TRNSYS. Tiré de École Polytechnique de Montréal.

Cui, P., Yang, H., & Fang, Z. (2006). Heat transfer analysis of ground heat exchangers with inclined boreholes. Applied Thermal Engineering, 26(11-12), 1169-1175.

Eskilson, P. (1986). Superposition Borehole Model: Manual for Computer Code. University of Lund, Lund, Sweden.

Eskilson, P. (1987). Thermal Analysis of Heat Extraction Boreholes. Ph.D. Thesis, University of Lund, Lund, Sweden.

Fisher, D. E., Rees, S. J., Padhmanabhan, S. K., & Murugappan, A. (2006). Implementation and validation of ground-source heat pump system models in an integrated building and system simulation environment. HVAC&R Research, 12(3A), 693-710.

Fossa, M. (2011). The temperature penalty approach to the design of borehole heat exchangers for heat pump applications. Energy and Buildings, 43(6), 1473-1479. doi:10.1016/j.enbuild.2011.02.020

Fossa, M., Cauret, O., & Bernier, M. (2009). Comparing the thermal performance of ground heat exchangers of various lengths. Proceedings of Effstock 2009, Stockholm, Sweden.(pp. 8).

Hellström, G., & Sanner, B. (1994). Software for dimensioning of deep boreholes for heat extraction. Proceedings of Calorstock 1994, Espoo/Helsinki, Finland.(pp. 195-202).

Ingersoll, L. R., Adler, F. T., Plass, H. J., & Ingersoll, A. C. (1950). Theory of earth heat exchangers for the heat pump. Heating, Piping & Air Conditioning, 22, 113-122.

Ingersoll, L. R., & Plass, H. J. (1948). Theory of the ground pipe heat source for the heat pump. Heating, Piping & Air Conditioning, 20(119), 119-122.

Lamarche, L. (2009). A fast algorithm for the hourly simulations of ground-source heat pumps using arbitrary response factors. Renewable Energy, 34(10), 2252-2258.

Lamarche, L. (2011). Analytical g-function for inclined boreholes in ground-source heat pump systems. Geothermics, 40(4), 241-249.

Lamarche, L., & Beauchamp, B. (2007a). A fast algorithm for the simulation of GCHP systems. ASHRAE Transactions, 113, 470-476.

Lamarche, L., & Beauchamp, B. (2007b). A new contribution to the finite line-source model for geothermal boreholes. Energy and Buildings, 39(2), 188-198.

Lamarche, L., Kajl, S., & Beauchamp, B. (2010). A review of methods to evaluate borehole thermal resistances in geothermal heat-pump systems. Geothermics, 39(2), 187-200.

Liu, X. (2005). Development and experimental validation of simulation of hydronic snow melting systems for bridges. Ph.D. Thesis, Oklahoma State University, Stillwater, OK.

Liu, X., & Hellstrom, G. (2006). Enhancements of an integrated simulation tool for ground-source heat pump system design and energy analysis. Proc. 10th International Conference on Thermal Energy Storage, Richard Stockton College of New Jersey.

Malayappan, V., & Spitler, J. D. (2013). Limitations of using uniform heat flux assumptions in sizing vertical borehole heat exchanger fields. Proceedings of Clima 2013, Prague, Czech Republic.

Marcotte, D., & Pasquier, P. (2008). Fast fluid and ground temperature computation for geothermal ground-loop heat exchanger systems. Geothermics, 37(6), 651-665.

Marcotte, D., & Pasquier, P. (2009). The effect of borehole inclination on fluid and ground temperature for GLHE systems. Geothermics, 38(4), 392-398.

Monzó, P., Acuña, J., Fossa, M., & Palm, B. (2013). Numerical generation of the temperature response factors for a borehole heat exchangers field. European Geothermal Congress 2013, Pisa, Italy.

Moreno, P., & Ramirez, A. (2008). Implementation of the Numerical Laplace Transform: A review. IEEE Transactions on power delivery, 23(4), 2599-2609.

Philippe, M., Bernier, M., & Marchio, D. (2009). Validity ranges of three analytical solutions to heat transfer in the vicinity of single boreholes. Geothermics, 38(4), 407-413.

Spitler, J. D. (2000). A design tool for commercial building loop heat exchangers. Fourth International Heat Pumps in Cold Climates Conference, Aylmer, Québec.

Stehfest, H. (1970). Algorithm 368, Numerical inversion of the Laplace transforms [D5]. Communications of the ACM, 13(1), 47-49.

Wedepohl, L. M. (1983). Power system transients: Errors incurred in the numerical inversion of the Laplace transforms. 26th Midwest Symposium on Circuits and Systems, Mexico.(pp. 174-178).

Yavuzturk, C., & Spitler, J. D. (1999). A short time step response factor model for vertical ground loop heat exchangers. ASHRAE Transactions, 105(2), 475-485.

Zeng, H. Y., Diao, N. R., & Fang, Z. H. (2002). A finite line-source model for boreholes in geothermal heat exchangers. Heat Transfer - Asian Research, 31(7), 558-567.

CHAPITRE 5 ARTICLE 3 : EFFECTS OF UNEQUAL BOREHOLE SPACING ON THE REQUIRED BOREHOLE LENGTH

Cimmino, M., & Bernier, M. (2014). Effects of unequal borehole spacing on the required borehole length. *ASHRAE Transactions*, 120(2), SE-14-013.

ABSTRACT

The aim of this paper is to show how the number and positioning of boreholes for a given land surface area can affect the fluid and ground temperature variations and the required borehole length. The methodology uses a g-function generation model and then uses temporal superposition to predict the variation of the fluid and borehole wall temperatures over 20 years of operation of the ground-source heat pump system. The cases of a 3 × 7 and 5 × 10 bore field are studied. Results show that the position of boreholes within a bore field of constant land area affect only slightly the required borehole length while the number of boreholes has a greater, albeit small, impact on the required length. For instance, for the 5 × 10 bore field, the total required borehole length increases by 0.9 % when boreholes are displaced towards the center and decreases by 2 % when the field was changed to a 5 × 9 configuration. In the latter case, the length of individual boreholes increased by 8.8 %.

5.1 Introduction

The design of a geothermal bore field consists in determining the number and length of boreholes required for the ground and heat transfer fluid temperatures to stay within an acceptable range. The temperature of the heat transfer fluid should not drop below a minimum fluid temperature $T_{f,min}$ or rise above a maximum fluid temperature $T_{f,max}$ to ensure proper heat pump operation. As a result of the extraction and injection of heat from and into the ground, the ground temperature varies during the operation of the ground source heat pump (GSHP) system. If the building loads are unbalanced, for example if more heat is extracted than injected during one full year, the temperature of the ground – and that of the fluid – will decrease from one year to the

next. This decrease (or increase in the case where more heat is injected than extracted) may lead to unacceptable ground temperature to ensure proper heat transfer from the ground to the fluid.

Typical bore field configurations consist of equally spaced boreholes on a rectangular grid. One such configuration is shown on Figure 5-1 for a field of 6 boreholes arranged on 2 rows.

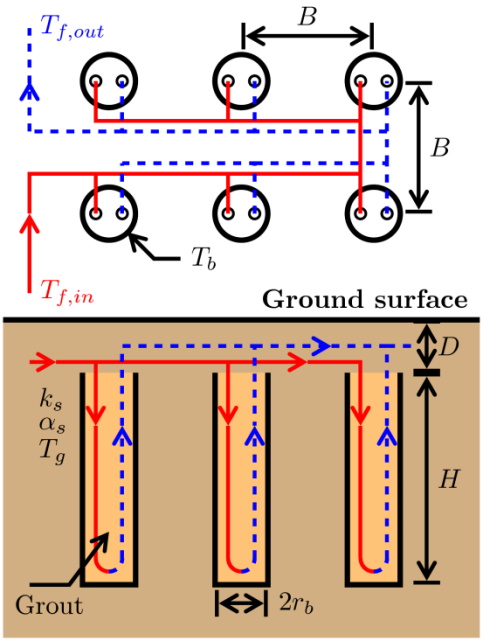

Figure 5-1: Field of 3 × 2 equally spaced boreholes arranged in a parallel configuration

In a bore field, a portion of the fluid temperature variation is associated with thermal interactions among boreholes. Thermal interactions depend on the size, number and position of the boreholes within the bore field. Different bore field configurations respond differently to the extraction and injection of heat into the ground and thus the required length of the boreholes differs between configurations.

The aim of this paper is to show how the number and positioning of boreholes for a given land surface area can affect the temperature variations and result in a variation of the required borehole length. The methodology uses the g-function generation model of Cimmino et al. (2013) to predict the variation of the borehole wall temperature and the temperature of the fluid exiting the bore field.

The methodology is applied to simulate two different bore fields: 3 × 7 and 5 × 10 equally spaced boreholes. A 20 year simulation of the bore fields is done using an unbalanced annual heat extraction profile. The required length of each bore field is identified. Then, the number and position of boreholes in the two fields are varied to study their effect on the g-function and on the required borehole length.

5.2 Literature review

5.2.1 Thermal response factors

Eskilson (1987) obtained thermal response factors for bore fields by solving the heat transfer between the boreholes and the ground using a finite difference approach. A number of ground heat exchanger design tools and energy simulation programs, e.g. EED (Hellström & Sanner, 1994), GLHEPRO (Spitler, 2000), EnergyPlus (Fisher et al., 2006), eQUEST (Liu & Hellstrom, 2006), use these g-functions to simulate the transient heat transfer between the boreholes and the ground. Values of g-functions for a number of bore field configurations are included within databases in each simulation program. Since the user has to choose among the provided bore fields which consist of equally spaced boreholes, the use of these tools restricts the design possibilities to those bore fields.

With the g-function approach, each borehole is modeled in a 2D radial-axial mesh. At each time step, the temperature distribution around every borehole is superposed to obtain the total temperature distribution in the bore field. The method of images is used to account for the constant ground surface temperature. The uniform borehole wall temperature (same for all boreholes) required to maintain the constant total heat extraction rate is then calculated. The temperature distribution at the end of each time step is calculated by forward explicit finite differences. The resulting response factors, called g-functions, give the non-dimensional borehole wall temperature drop due to a constant unit heat extraction rate at the borehole walls. According to Eskilson (1987), g-functions are defined by:

$$T_b = T_g - \frac{Q'_g}{2\pi k_s} \cdot g(t/t_s, r_b/H, B/H) \tag{5.1}$$

where T_b is the borehole wall temperature, T_g is the undisturbed ground temperature, Q'_g is the heat extraction rate per unit length of borehole, ks is the ground thermal conductivity, t/t_s is the non-dimensional time with $t_s = H^2/9\alpha_s$ the characteristic time, H is the length of an individual borehole, α_s is the ground thermal diffusivity, r_b is the borehole radius, and B is the spacing between two adjacent boreholes. g-functions give a direct relation between the heat extraction rate in the bore field and the temperature variation at the borehole walls : the greater is the value of the g-function, the greater is the temperature variation at the borehole walls for a given heat extraction rate. For $Q'_g/2\pi k_s$ = 1, the variation of the borehole wall temperature is equal to the g-function of the bore field. Values of g-functions for a field of 3 × 2 boreholes are shown on Figure 5-2. They are usually presented for a ratio r_b/H = 0.0005 and for various values of the B/H ratio. A ratio $B/H = \infty$ corresponds to the case of a single borehole.

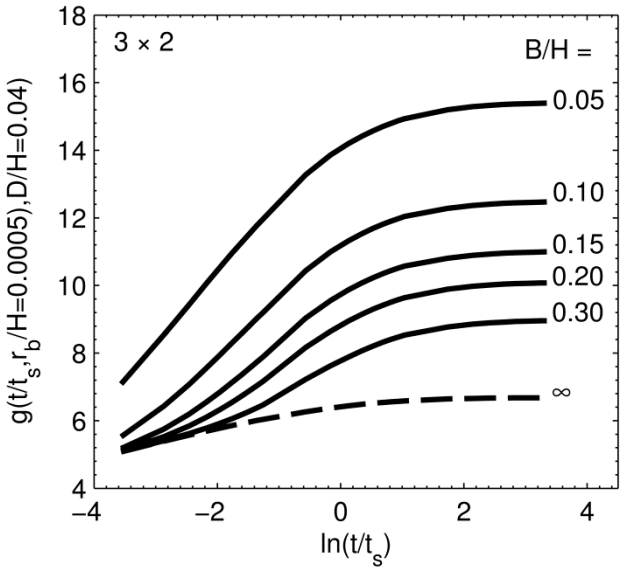

Figure 5-2: g-functions of a field of 3 × 2 boreholes

Thermal response factors for bore fields can also be obtained using analytical solutions. Ingersoll and Plass (1948) and Ingersoll et al. (1950; 1954) used both Kelvin's infinite line source (ILS) solution and the cylindrical heat source (CHS) solution from Carslaw and Jaeger (1946a) to obtain the variation of temperature near boreholes. Analytical solutions are superposed in space and time to account for thermal interaction between boreholes and time-varying heat extraction rates. Eskilson (1987) proposed the finite line source (FLS) for the approximation of the

g-functions. The solution is obtained by the spatial superposition of point heat sources over the length of the borehole:

$$T(r,z,t) = T_g - \frac{Q'}{4\pi k_s} \cdot \int_D^{H+D} \left[\frac{erfc\left(\frac{\sqrt{r^2+(z-s)^2}}{\sqrt{4\alpha_s t}}\right)}{\sqrt{r^2+(z-s)^2}} - \frac{erfc\left(\frac{\sqrt{r^2+(z+s)^2}}{\sqrt{4\alpha_s t}}\right)}{\sqrt{r^2+(z+s)^2}} \right] ds \tag{5.2}$$

where D is the buried depth of the borehole and erfc is the complementary error function. Eskilson obtained the borehole wall temperature by evaluating the FLS solution at mid-length ($z = D + H/2$) and at a radius $r = \sqrt{1.5} \cdot r_b$ corresponding to the radius of an ellipsoid having the same volume as the borehole, since the isotherms around a finite line source tend to resemble slightly distorted ellipsoids.

The FLS was latter reintroduced by Zeng et al. (2002) who evaluated the solution at mid-length and at the borehole radius to obtain the temperature at the borehole wall. The temperature at mid-length was chosen instead of the average temperature over the length of the borehole to avoid solving a double integral. Lamarche and Beauchamp (2007b) obtained a solution for the average temperature over the length of the borehole by simplifying the FLS for a buried depth $D = 0$. Claesson and Javed (2011) obtained a solution for $D \geq 0$ which gives the average temperature over the length of the borehole:

$$\bar{T}(r,t) = T_g - \frac{Q'}{4\pi k_s} \cdot \int_{1/\sqrt{4\alpha_s t}}^{\infty} \exp(-r^2 s^2) \cdot \frac{Y(Hs, Ds)}{Hs^2} \cdot ds \tag{5.3}$$

$$Y(h,d) = 2 \cdot \text{ierf}(h) + 2 \cdot \text{ierf}(h+2d) - \text{ierf}(2h+2d) - \text{ierf}(2d) \tag{5.4}$$

$$\text{ierf}(X) = X \cdot \text{erf}(X) - \frac{1}{\sqrt{\pi}}(1 - \exp(-X^2)) \tag{5.5}$$

where $\bar{T}$ is the average temperature over the length of the borehole at a distance r from its center, and erf is the error function. The FLS solution can be expressed in the form of a response factor, according to the definition of the g-function (Equation 5.2):

$$h_{FLS}(t,r,H,D) = \frac{1}{2} \cdot \int_{1/\sqrt{4\alpha_s t}}^{\infty} \exp(-r^2 s^2) \cdot \frac{Y(Hs,Ds)}{Hs^2} \cdot ds \tag{5.6}$$

where h_{FLS} is the borehole-to-borehole response factor.

The thermal response factor of a bore field can be obtained by the spatial superposition of the FLS solution, assuming that all boreholes have the same heat extraction rate. The thermal response factor is given by the average temperature variation of every borehole in the field:

$$g_{FLS}(t) = \frac{1}{N_b} \sum_{i=1}^{N_b} \sum_{j=1}^{N_b} h_{FLS}\left(t, d_{ij}, H, D\right) \tag{5.7}$$

$$d_{ij} = \begin{cases} r_b & \text{for } i = j \\ \sqrt{\left(x_i - x_j\right)^2 + \left(y_i - y_j\right)^2} & \text{for } i \neq j \end{cases} \tag{5.8}$$

where g_{FLS} is the thermal response factor for the bore field obtained using what is referred to here as classical superposition of the FLS, N_b is the number of boreholes in the field and (x_i, y_i) are the coordinates of the i^{th} borehole.

Fossa (2011) compared the thermal response factors obtained using the classical superposition of the FLS (Equation 5.7) with Eskilson's g-functions. The author noted that, for small values of the spacing to length ratio B/H and for large values of the non-dimensional time t/t_s, the classical superposition of the FLS overestimated Eskilson's g-functions.

Cimmino et al. (2013) used the FLS solution to generate g-functions while accounting for the variation of the heat extraction rates among boreholes. The authors accounted for thermal interaction among boreholes by imposing an average borehole wall temperature equal for all boreholes. Spatial and temporal superpositions are used to obtain a linear system of equation in the Laplace domain. The solution to the system of equations gives the normalized heat extraction rates of every borehole as well as the non-dimensional borehole wall temperature, which corresponds to the thermal response factor of the bore field. Results showed that the model gives a better approximation of Eskilson's g-functions than the classical superposition of the FLS. The method was recently improved to apply to fields of boreholes of unequal lengths and to consider a boundary condition of uniform temperature at the borehole walls (Cimmino & Bernier, 2014b).

The results showed that Eskilson's g-functions can be replicated accurately. The authors developed a software tool that generates g-functions based on user inputs of borehole dimensions and positions (Cimmino & Bernier, 2013).

5.2.2 Simulation using thermal response factors

The variation of the borehole wall temperature can be obtained through the temporal superposition of the thermal response factor:

$$T_b(t_k) = T_g - \sum_{i=1}^{k} \left[\frac{q'(t_i)}{2\pi k_s} \cdot g((t_k - t_{i-1})/t_s, r_b/H, B/H) \right] \tag{5.9}$$

where $q'(t_i) = Q'(t_i) - Q'(t_i - 1)$ is the heat extraction rate increment per unit borehole length, $t_i - t_{i-1} = \Delta t$ the simulation time step and $q'(t_1) = Q'(t_1)$. Equation 5.9 is also known as the temporal superposition of loads. As the number of simulation time steps increases, the number of terms in the sum of Equation 5.9 becomes larger and the temporal superposition of loads is increasingly long to compute.

Methods have been proposed by several authors to reduce the calculation time associated with temporal superposition. For instance, Yavuzturk and Spitler (1999) introduced load aggregation. The method consists in averaging the loads for times prior to $t^* = t_k - n_{ag} \cdot \Delta t$, where nag is the number of non-aggregated time steps. The number of terms in the summation of Equation 5.9 is then inferior or equal to $n_{ag} + 1$. This greatly reduces the number of terms in the summation and thereby reduces the time required for the simulation. The authors reduced the time required for a 20 year hourly simulation by 99%.

Bernier et al. (2004) improved the method of aggregation of loads by defining multiple aggregation groups. The multiple load aggregation algorithm (MLAA) consists in grouping the loads to be averaged in several groups, including a larger number of time steps as the time steps are farther away from t_k. Five groups are defined: the non-aggregated hourly loads, and the daily, weekly, monthly, and yearly loads. Optimization of the group sizes was done in order to maximize the precision of the temporal superposition of loads for a given calculation time.

A similar algorithm for the aggregation of loads was developed by Liu (2005), referred to as the "hierarchical load aggregation procedure". The hourly loads are grouped into a number of small,

medium and large aggregation blocks. While the size of each block is set, the number of blocks of each size is adapted at each time step according to the length of the load history. The algorithm is used in EnergyPlus for the simulation of ground source heat pump systems.

Lamarche and Beauchamp (2007a) proposed a non-history dependent algorithm for the temporal superposition of loads. The authors expressed the temporal superposition of the CHS solution in the form of a Green function. By inverting the order of integration, the temperature at the last time step can be obtained using only the ground load at the last time step and the solution from the previous time step. The authors obtained a simulation time of 1.39 s for a 2 year hourly simulation, whereas the same simulation was done in 25.1 s using the MLAA. Lamarche (2009) later generalized the algorithm to enable the use of any thermal response factor.

Marcotte and Pasquier (2008a) noted that the sum of Equation 5.9 is in fact a convolution product, which can be solved using Fourier transforms. Equation 5.9 is rewritten as:

$$T_b(t) = T_g - \mathcal{F}^{-1}\left(\mathcal{F}\left(\frac{q'(t)}{2\pi k_s}\right) \cdot \mathcal{F}\left(g(t/t_s, r_b/H, B/H)\right)\right) \tag{5.10}$$

where $\mathcal{F}$ and $\mathcal{F}^{-1}$ are the direct and inverse Fourier transforms.

The authors also proposed to subsample the evaluation of the FLS and interpolated the solution in order to obtain the FLS solution for all time steps of the simulation. Using a fast Fourier transform (FFT) algorithm and a cubic spline interpolant, the authors were able to achieve a 20 year simulation with an hourly time step for a field of 40 boreholes in less than a minute on a typical desktop computer. Cimmino et al. (2012) showed how the FFT can be used to simulate ground source heat pump systems with g-functions. The simulation time for a 20 year simulation with an hourly time step for a field of 3 × 6 boreholes was reduced by 3 orders of magnitude compared to a simulation performed using the MLAA.

5.2.3 Optimization of bore field geometry

Bore field optimization is rarely seen in ground heat exchanger design tools. Most design software tools serve the purpose of determining the required borehole length based on a bore field geometry given by the user. One exception is the latest version of EED (Blomberg, Claesson, Eskilson, Hellström, & Sanner, 2008) which provides an optimization tool to find the best bore

field configuration based on the required borehole length or the total cost. The software does successive simulation of all bore field configurations that fit into the specified available land area, varying the spacing between boreholes for each configuration. The available fields are, however, restricted to bore fields with evenly spaced boreholes. Another example is the program EWS (Huber, 2011), which lets the user input custom borehole positions in order to calculate a thermal response factor and simulate the bore field.

Beck et al. (2013) studied the effect of the borehole positions in a bore field on the temperature variation of the ground in the bore field. The positions of boreholes in a field of 36 boreholes on a 6 × 6 grid were varied and the ground temperatures were obtained from the simulation of the bore field using a given monthly variation of the heat extraction rates over 30 years. It was shown that positioning the boreholes on the perimeter of the field resulted in a lower temperature drop in the ground.

Kurevija et al. (2012) compared the cylindrical heat source solution and Eskilson's g-function for the simulation and sizing of a 7 × 6 and a 21 × 2 bore fields using a heating dominated load profile. It was shown that the required length obtained from the use of the CHS solution is greater than that calculated using Eskilson's g-functions. Additionally, the 21 × 2 bore field resulted in smaller fluid and ground temperature drops, and thus the 21 × 2 bore field achieved a smaller required borehole length than the 7 × 6 bore field. It was noted that thermal interactions are more important for more compact fields, in this case the 7 × 6 bore field.

Robert and Gosselin (2014) presented an optimization methodology for the total cost minimization of ground coupled heat pump systems. Optimization variables included the borehole length, the number and geometric configuration of boreholes on a rectangular grid, the spacing between boreholes and the portion of the building load assumed by the geothermal system. The authors demonstrated that the total cost is most importantly influenced by the length and number of boreholes. The uncertainty on the value of the ground thermal conductivity and the cost related with the evaluation of the thermal conductivity via thermal response tests (TRT) were also studied by the authors. It was shown that the evaluation of the ground thermal conductivity is mostly important when the thermal conductivity is low and the number of boreholes in the bore field is high.

5.3 Proposed methodology

The model proposed by Cimmino et al. (2013) is used to generate g-functions for the simulation and sizing of two bore fields. The base configuration of the two bore fields consist of 21 equally spaced boreholes on a rectangular 3 × 7 grid and 50 equally spaced boreholes on a rectangular 5 × 10 grid, as shown on Figure 5-3. The 3 × 7 bore field was selected based on the ground loads obtained for this study, as will be shown on Figure 5-4. The 5 × 10 bore field was included to validate that the results apply to larger bore fields. However, the methodology applies to other configurations and will be used to study variations of the two bore fields. Boreholes have a radius r_b, a length H and are buried at a depth D. The ground has a thermal conductivity k_s, a thermal diffusivity α_s and is initially at a temperature T_g. The ground surface is maintained at the initial ground temperature T_g.

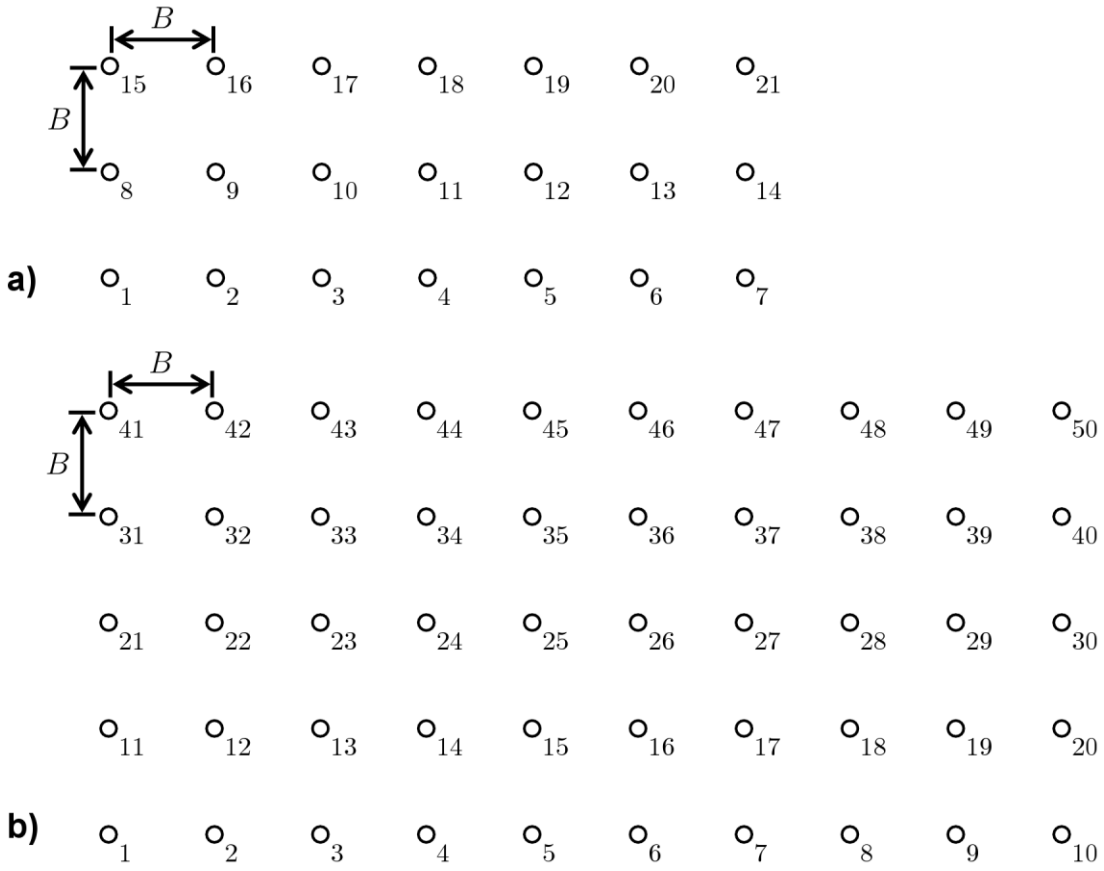

Figure 5-3: Identification of the boreholes in a 3 × 7 bore field and a 5 × 10 bore field

Boreholes are modeled as finite line sources with a uniform heat extraction rate over their entire length. The total heat extraction rate is constant but individual boreholes may have different heat extraction rates. The average over-the-length borehole wall temperature is assumed to be equal for every borehole in the field in accordance with Eskilson's g-function definition. This assumption is used to model the operation of boreholes connected in parallel. An equal borehole wall temperature for every borehole is justified provided that the inlet fluid temperature is equal for all boreholes and the temperature difference between inlet and outlet is small. In that case, the temperature at the borehole walls should tend to the same value. The condition of equal borehole wall temperature differs from the condition typically used when modelling boreholes using analytical heat source solutions, which is the condition of a uniform heat extraction rate equal for all boreholes.

5.3.1 Temporal superposition

The temperature variation at the wall of a borehole caused by the extraction of heat at another borehole is obtained by the temporal superposition of the borehole-to-borehole response factors:

$$\Delta T_{i\to j}(t_k) = -\sum_{p=1}^{k}\left[\frac{q_i'(t_p)}{2\pi k_s}\cdot h_{i\to j}(t_k - t_{p-1})\right] \tag{5.11}$$

$$h_{i\to j}(t) = h_{FLS}(t, d_{ij}, H, D) \tag{5.12}$$

$$d_{ij} = \begin{cases} r_b & \text{for } i = j \\ \sqrt{(x_i - x_j)^2 + (y_i - y_j)^2} & \text{for } u \neq j \end{cases} \tag{5.13}$$

where $\Delta T_{i\to j}$ is the temperature variation at the wall of borehole j, caused by the extraction of heat from borehole i, q_i' is the heat extraction rate increment per unit length of borehole i, (x_i, y_i) are the coordinates of borehole i. $h_{i\to j}$ is the borehole-to-borehole response factors from borehole i to borehole j.

5.3.2 Spatial superposition

The total temperature variation at the borehole walls is obtained by the sum of the temperature variations caused by every borehole:

$$\Delta T_b(t_k) = -\sum_{p=1}^{k}\sum_{i=1}^{N_b}\left[\frac{q_i'(t_p)}{2\pi k_s}\cdot h_{i\to j}(t_k - t_{p-1})\right] \tag{5.14}$$

where $\Delta T_b = T_b - T_g$ is the temperature variation at the borehole wall (same for all boreholes) and N_b is the number of boreholes in the bore field. Equation 5.14 can be evaluated for any borehole j to create a set of N_b equations with $N_b + 1$ unknowns (q_i' and ΔT_b). One last equation is required to complete the set. This last equation states that the sum of the heat extraction rate increments is equal to the ground load increment:

$$q_g(t_k) = \sum_{i=1}^{N_b}[H \cdot q_i'(t_k)] \tag{5.15}$$

5.3.3 System of equation in the Laplace domain

The complete set of equations (Equations 5.14 and 5.15) is however difficult to solve due to the sum involving the time variable in Equation 5.14. The set of equations can be turned into a simple system of linear equations using Laplace transforms. As noted by Marcotte and Pasquier (2008a), the summation in the time domain in Equation 5.14 is in fact a convolution product and can be replaced by a simple multiplication in the spectral domain. The Laplace transform is used here to avoid temporal aliasing which would occur when solving the system of equation using Fourier transforms. The Laplace transform pairs are expressed as:

$$F(s) = \mathcal{L}\big(f(t)\big) = \int_0^{\infty} f(t)\, exp(\text{-}st)\, dt \tag{5.16}$$

$$f(t) = \mathcal{L}^{\text{-}1}\big(F(s)\big) = \frac{1}{2\pi j}\int_{\sigma - j\infty}^{\sigma + j\infty} F(s)\, exp(st)\, ds \tag{5.17}$$

where $\mathcal{L}$ and $\mathcal{L}^{\text{-}1}$ are the direct and inverse Laplace transforms, f is an arbitrary function in the time domain, F is the corresponding-function in the Laplace domain, s is the complex frequency in the Laplace domain and $j = \sqrt{\text{-}1}$ is the imaginary number.

By imposing a variable change $s = \sigma + j\omega$ (Moreno & Ramirez, 2008), the Laplace transform can be obtained from the Fourier transform:

$$F(s) = \int_0^{\infty} [f(t)\, exp(\text{-}\sigma t)]\, exp(\text{-}j\omega t)\, dt = \mathcal{F}(h(t) \cdot exp(\text{-}\sigma t)) \tag{5.18}$$

$$f(t) = \frac{exp(\sigma t)}{2\pi} \int_{\text{-}\infty}^{+\infty} F(s)\, exp(j\omega t)\, d\omega = exp(\sigma t) \cdot \mathcal{F}^{-1}\big(H(s)\big) \tag{5.19}$$

where ω is the angular frequency in the Fourier domain and σ is a real positive constant. The value of σ should be large enough to avoid temporal aliasing and small enough to avoid distorting the results. The value of σ is chosen according to Wedepohl's criterion (Wedepohl, 1983):

$$\sigma = 2 \cdot \frac{\ln(N)}{t_{max}} \tag{5.20}$$

where N is the number of time steps in the simulation and t_{max} is the maximum value of the time variable.

Equation 5.14 and 5.15 are expressed in the Laplace domain:

$$\mathcal{L}(\Delta T_b) = \text{-} \sum_{i=1}^{N_b} \left[\mathcal{L}\left(\frac{q_i'}{2\pi k_s} \right) \cdot \mathcal{L}\big(h_{i \to j}\big) \right] \tag{5.21}$$

$$\mathcal{L}\big(q_g\big) = \sum_{i=1}^{N_b} [H \cdot \mathcal{L}(q_i')] \tag{5.22}$$

Equations 5.21 and 5.22 form a system of $N_b + 1$ linear equations, which can be written in matrix form:

$$\begin{bmatrix} 0 \\ \vdots \\ 0 \\ 0 \\ \mathcal{L}\left(\frac{\text{-}q_g}{2\pi k_s H} \right) \end{bmatrix} = \begin{bmatrix} \mathcal{L}(h_{1\to1}) & \dots & \mathcal{L}\big(h_{(N_b-1)\to1}\big) & \mathcal{L}\big(h_{N_b\to1}\big) & \text{-}1 \\ \vdots & \ddots & \vdots & \vdots & \vdots \\ \mathcal{L}\big(h_{1\to(N_b-1)}\big) & \dots & \mathcal{L}\big(h_{(N_b-1)\to(N_b-1)}\big) & \mathcal{L}\big(h_{N_b\to(N_b-1)}\big) & \text{-}1 \\ \mathcal{L}\big(h_{1\to N_b}\big) & \dots & \mathcal{L}\big(h_{(N_b-1)\to N_b}\big) & \mathcal{L}\big(h_{N_b\to N_b}\big) & \text{-}1 \\ 1 & \dots & 1 & 1 & 0 \end{bmatrix} \begin{bmatrix} \mathcal{L}\left(\frac{\text{-}q_1'}{2\pi k_s} \right) \\ \vdots \\ \mathcal{L}\left(\frac{\text{-}q_{N_b-1}'}{2\pi k_s} \right) \\ \mathcal{L}\left(\frac{\text{-}q_{N_b}'}{2\pi k_s} \right) \\ \mathcal{L}(\Delta T_b) \end{bmatrix} \tag{5.23}$$

The system of equations is solved for each term of the Laplace transforms. The solution of the system gives the variation of the borehole wall temperature and the heat extraction rates for each borehole.

5.4 Application

The methodology presented above is used to study borehole positioning in two bore fields over a period of 20 years. The first bore field consists in 21 boreholes on 3 rows, namely the 3 × 7 bore field, and the second bore field consists in 50 boreholes on 5 rows, namely the 5 × 10 bore field.

Ground loads for the 3 × 7 bore field are obtained from the simulation of a two-story office building located in Montreal, Quebec, using eQUEST. Ground loads are obtained from the building heating and cooling loads, which are weighted to account for heat pump efficiency in heating and cooling. The hourly ground loads are shown on Figure 5-4a, heat extracted from the ground is shown as positive. The ground loads are heating dominated (i.e. more heat is extracted than injected into the ground on an annual basis). Ground loads for the 5 × 10 bore field are obtained from the loads of the 3 × 7 bore field, which are multiplied by a factor of 2. The hourly ground loads are shown on Figure 5-4b. The peak heat extraction and heat injection rates, the total heat extracted and injected during one year and the yearly average heat extraction rate are shown in Table 5-1.

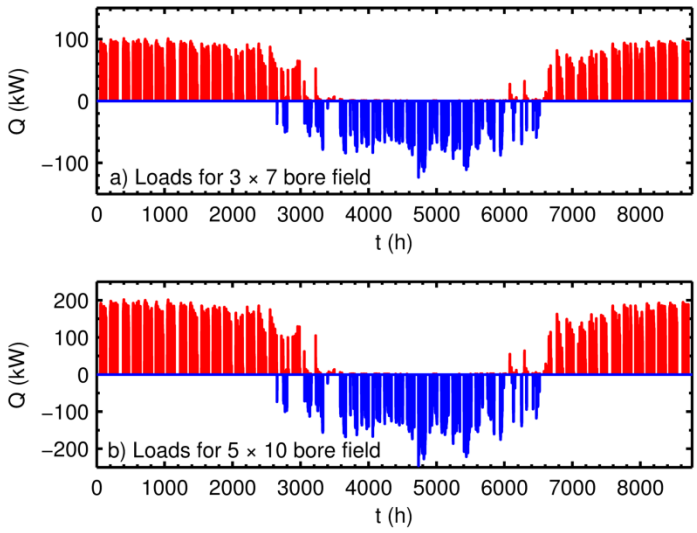

Figure 5-4: Ground loads for a) the 3 × 7 bore field and b) the 5 × 10 bore field

Table 5-1: Peak, total and average ground heat transfer rates for the 3 × 7 and 5 × 10 bore field

	3 × 7 bore field	5 × 10 bore field
Peak heat extraction rate, kW (kBtu/h)	100.8 (344)	201.3 (687)
Peak heat injection rate, kW (kBtu/h)	123.2 (420)	246.4 (841)
Total heat extracted, kWh (MBtu)	86 993 (297)	173 986 (594)
Total heat injected, kWh (MBtu)	46 115 (157.4)	92 230 (315)
Average heat extraction rate imbalance, kW (kBtu/h)	4.67 (15.93)	9.34 (31.9)

For both cases, the bore fields consist of boreholes on a rectangular grid with a spacing B = 7 m (23 ft). Boreholes are buried at a distance D = 2 m (6.5 ft) from the ground surface, have a radius r_b = 0.075 m (3 in.) and a thermal resistance R_b = 0.1 m-K/W (0.0144 h-ft^2-°F/Btu-in.). Boreholes are connected in parallel. The total fluid flow rate in the bore field is $\dot{m}$ = 7 L/s (111 Gal/min) for the 3 × 7 bore field and $\dot{m}$ = 16 L/s (254 Gal/min) for the 5 × 10 bore field. The fluid has a density ρ = 1015 kg/m^3 (63.4 lb/ft^3) and a thermal capacity c_p = 3.97 kJ/kg-K (0.948 Btu/lb-°F). The thermal conductivity of the ground is k_s = 2 W/m-K (1.16 Btu/h-ft-°F) and the thermal diffusivity of the ground is α_s = 1 × 10^{-6} m^2/s (1.08 × 10^{-5} ft^2/s). The ground is initially at a temperature T_g = 10°C (50°F).

5.4.1 Bore field sizing

The fluid temperature at the outlet of the bore field is obtained from the borehole wall temperature, assuming a linear variation of the fluid temperature inside the boreholes:

$$T_{f,out}(t) = T_b(t) - \frac{Q_g(t)}{N_b \cdot H} R_b + \frac{Q_g(t)}{2\dot{m}c_p} \tag{5.24}$$

The borehole wall temperature is obtained from the temporal superposition of the g-function (Equation 5.9). For both bore fields, the minimum borehole length required to have a minimum outlet fluid temperature of 0°C (32°F) is identified. The fluid temperature variation obtained from the 20 years of hourly simulations for both fields are shown on Figure 5-5. For the 3 × 7 bore

field, the minimum required borehole length is 121 m (397 ft). As shown on Figure 5-5a, the minimum fluid temperature is attained after 20 years. Since the ground loads are heating dominated, the fluid temperature gets lower from year to year. For the 5 × 10 bore field, the minimum borehole length is 113 m (371 ft). As was the case for the 3 × 7 bore field, Figure 5-5b shows that the minimum fluid temperature is attained after 20 years.

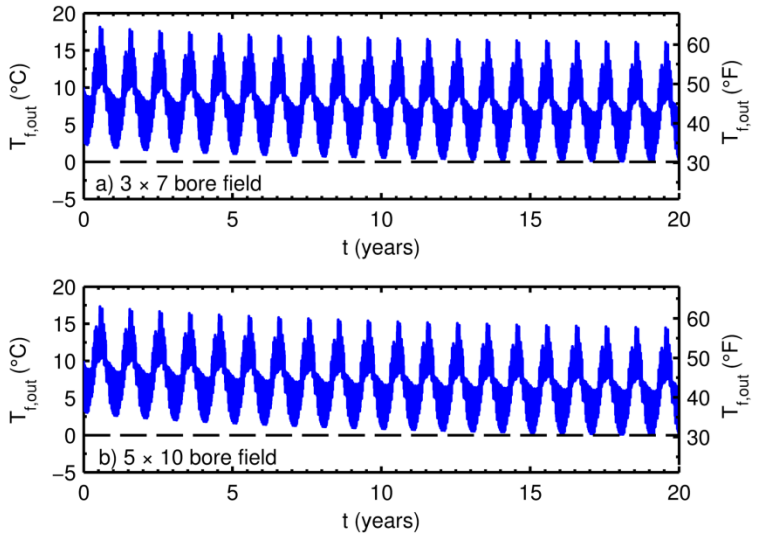

Figure 5-5: Variation of the outlet fluid temperature for a) the 3 × 7 bore field and b) the 5 × 10 bore field

5.5 Bore field optimization

Two strategies are examined to reduce the required borehole length in the bore fields, given the same land area. The first strategy consists in displacing the boreholes in the bore fields, either away from or towards the center of the field. The second strategy consists in removing or adding boreholes to the bore field. Each strategy is first compared with the base bore fields using their respective g-functions. The effect of the change in bore field configuration on the required borehole length is then studied.

5.5.1 Displacing boreholes in the bore field

Previous studies have shown that the boreholes located near the center of the field tend to extract less heat over time due to the fact that the temperature in the center of the bore field drops faster than on the perimeter of the field. It may then be advantageous to use unequal borehole spacing

to reduce the total required borehole length. As was the case above, the bore fields consist of 21 boreholes distributed on 3 rows and 50 boreholes distributed on 5 rows. However, in contrast to the bore fields studied in the previous section, the spacing between two adjacent boreholes on the same row varies. Unequal borehole spacing in the other perpendicular direction could also be envisioned with the proposed methodology. However, in the present case, only the borehole spacing in one direction is varied. These new bore field configurations are shown on Figure 5-6. The bore field occupies the same land area as the bore fields shown on Figure 5-3 and the average spacing between two adjacent boreholes on the same row is thus B = 7 m (23 ft). The spacing between boreholes grows with a factor fi towards the center of the bore field.

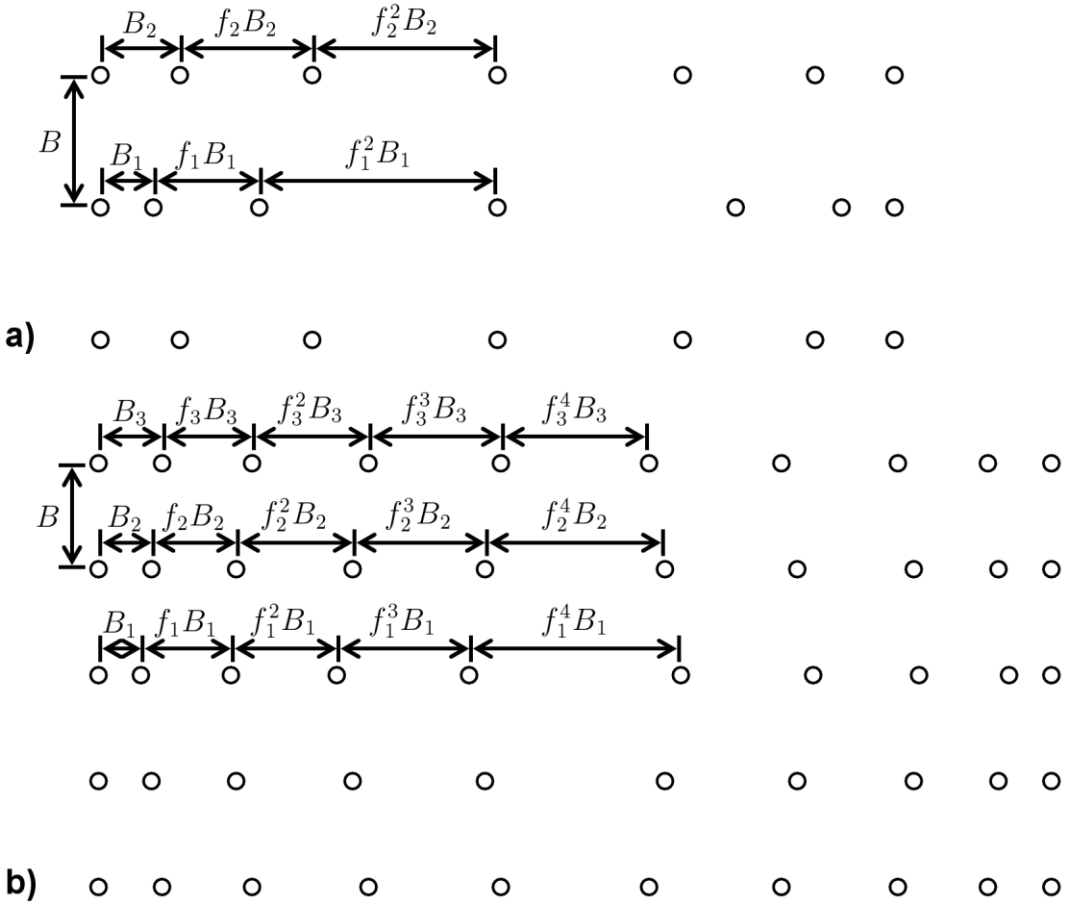

Figure 5-6: Fields of 3 × 7 and 5 × 10 unevenly spaced boreholes

The g-function of the base field of 21 boreholes is compared to a bore field where boreholes are displaced away the center of the bore field, with B_1 = 3 m (9.8 ft), B_2 = 5 m (16.4 ft), f_1 = 2, and

f_2 = 1.36; and to a bore field where boreholes are displaced towards the center of the bore field, with B_1 = 12 m (39 ft), B_2 = 9.2 m (30 ft), f_1 = 0.5, and f_2 = 0.74. The g-functions are compared on Figure 5-7, for a common length H = 121 m. It is shown that the impact of the changes on the g-function is negligible. This means that the borehole wall temperature response is about the same for each configuration. For example, after 20 years, i.e. for $\ln(t/t_s)$ = -0.95, the g-functions show a difference of -0.56 % and 1.65 % with the base field when the boreholes are displaced away from the center of the field and towards the center of the field, respectively. The impact on the required borehole length is also relatively very small : the required borehole length for the field with the boreholes displaced away from the center is H = 121 m (397 ft) (same as the equally-spaced bore field) and the required borehole length for the field with the boreholes displaced towards the center is H = 122 m (400 ft).

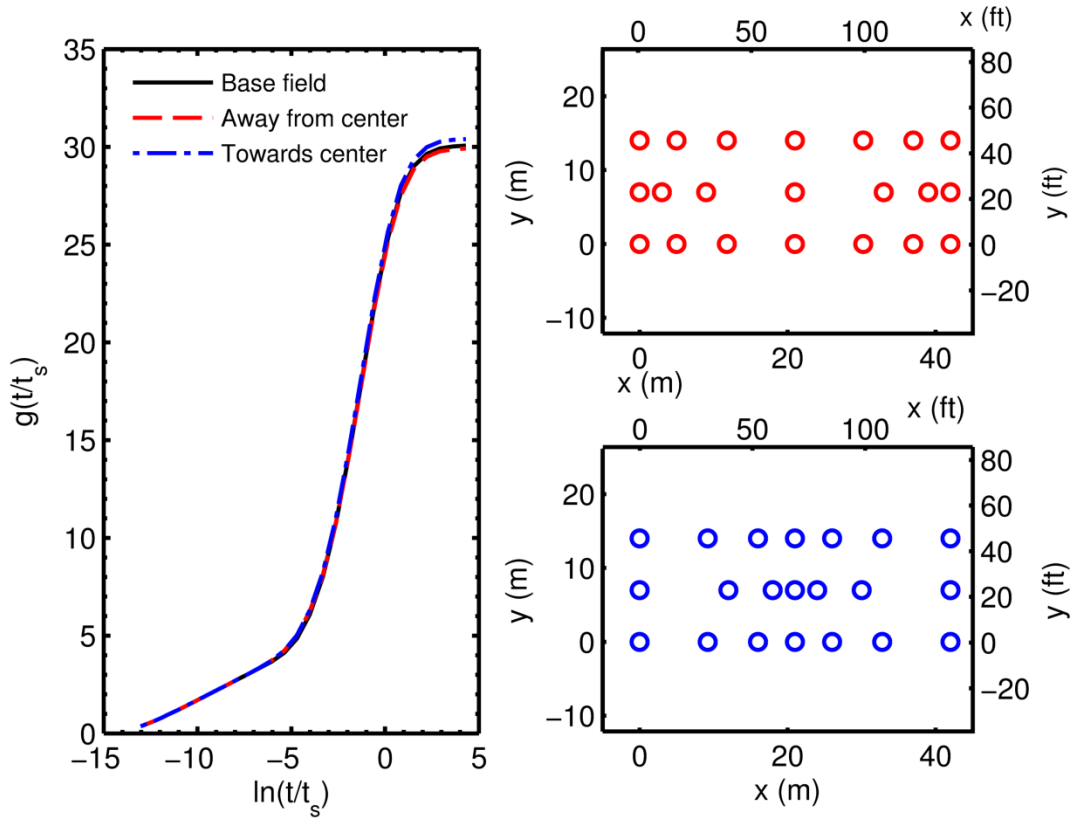

Figure 5-7: g-functions of a 3 × 7 bore field with equal and unequal spacing between boreholes

The same comparison is made for the field of 50 boreholes. The base configuration is compared to a bore field with the boreholes displaced away from the center, with B_1 = 3 m (9.8 ft), B_2 = 4.5 m (14.8 ft), B_3 = 6 m (19.7 ft), f_1 = 1.49, f_2 = 1.25, and f_3 = 1.09; and to a bore field with the boreholes displaced towards the center, with B_1 = 11.6 m (38 ft), B_2 = 9.46 m (31 ft), B_3 = 7.86 m (26 ft), f_1 = 0.71, f_2 = 0.83, and f_3 = 0.93. The g-functions are compared on Figure 5-8, for a common length H = 113 m (371 ft). Once again, the impact of the changes on the g-function is negligible. For example, after 20 years, the difference between the g-function of the field with the boreholes displaced away from the center of the field and the g-function of the base field is -0.48 %. The difference between the g-function of the field with the boreholes displaced towards the center of the field and the g-function of the base field is 0.73 %. The required lengths are H = 113 m (371 ft) (same as the equally-spaced boreholes) for the field with the boreholes displaced away from the center and H = 114 m (374 ft) for the field with the boreholes displaced towards the center.

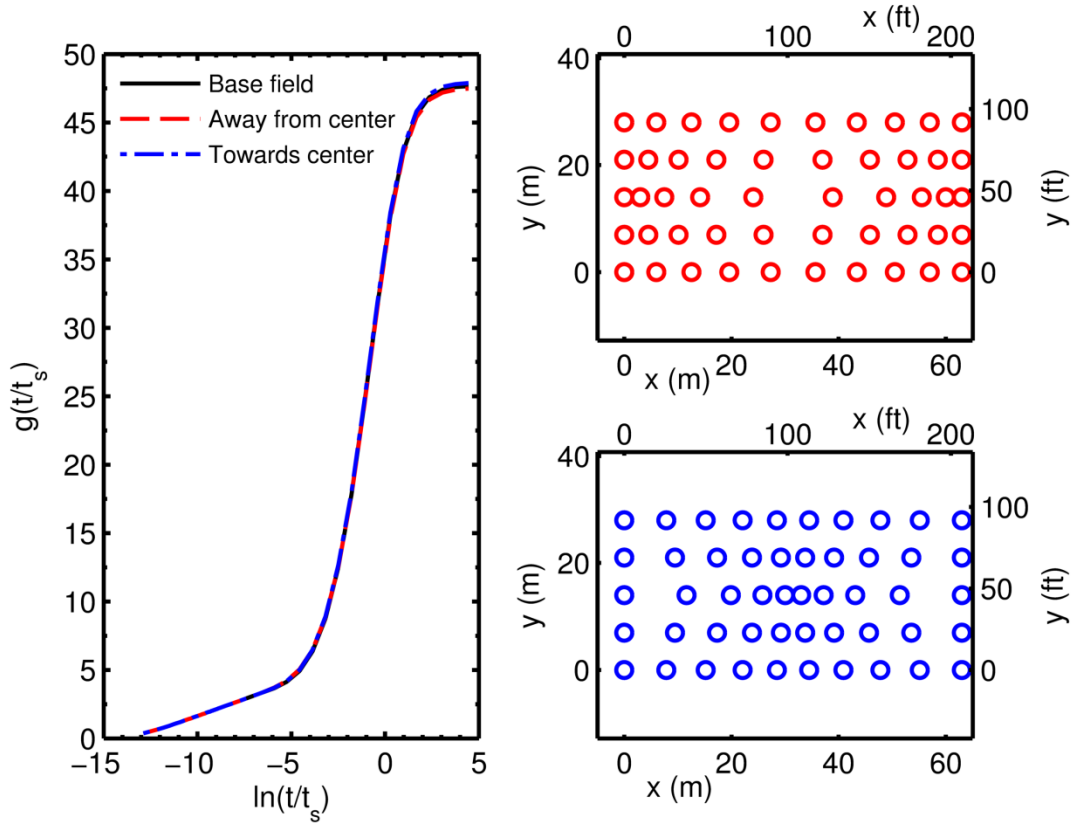

Figure 5-8: g-functions of a 5 × 10 bore field with equal and unequal spacing between boreholes

5.5.2 Removing or adding boreholes

The effect of removing and adding boreholes to the bore field is now studied. The 3 × 7 bore field is compared to a 3 × 6 bore field and to a 3 × 8 bore field, with the horizontal spacing B_{hor} adjusted so the bore field occupies the same land area. The horizontal spacing is thus B_{hor} = 8.4 m (28 ft) for the 3 × 6 bore field and B_{hor} = 6.0 m (19.7 ft) for the 3 × 8 bore field. The g-functions are compared on Figure 5-9 for the same total borehole length $N_b \cdot H$ = 2541 m (8337 ft). The characteristic time t_s is calculated for H = 121 m (397 ft) so the non-dimensional time axis of the g-function graph is coherent between the 3 bore fields. The 3 × 6 bore field shows a reduction of the g-function while the 3 × 8 bore field shows an increase of the g-function value. The reduction of the g-function is 10.0 % at t = 20 years for the 3 × 6 bore field. The increase is 9.41 % at t = 20 years for the 3 × 8 bore field. These variations are explained by the fact that an increase in the number of boreholes reduces the distance between boreholes and thereby increase the effect of thermal interactions. Furthermore, an increase in the number of boreholes is accompanied by a decrease in the length of the individual boreholes. The reduction in length effectively reduces the ground volume occupied by the bore field and therefore reduces the ground volume from which the bore field can extract heat. A variation of the required borehole length is expected as a consequence of the changes in the g-function values. Indeed, the required total borehole length is 2484 m (8150 ft) for the 3 × 6 bore field and 2592 m (8504 ft) for the 3 × 8 bore field. The individual borehole lengths are then H = 138 m (453 ft) and H = 108 m (354 ft), respectively.

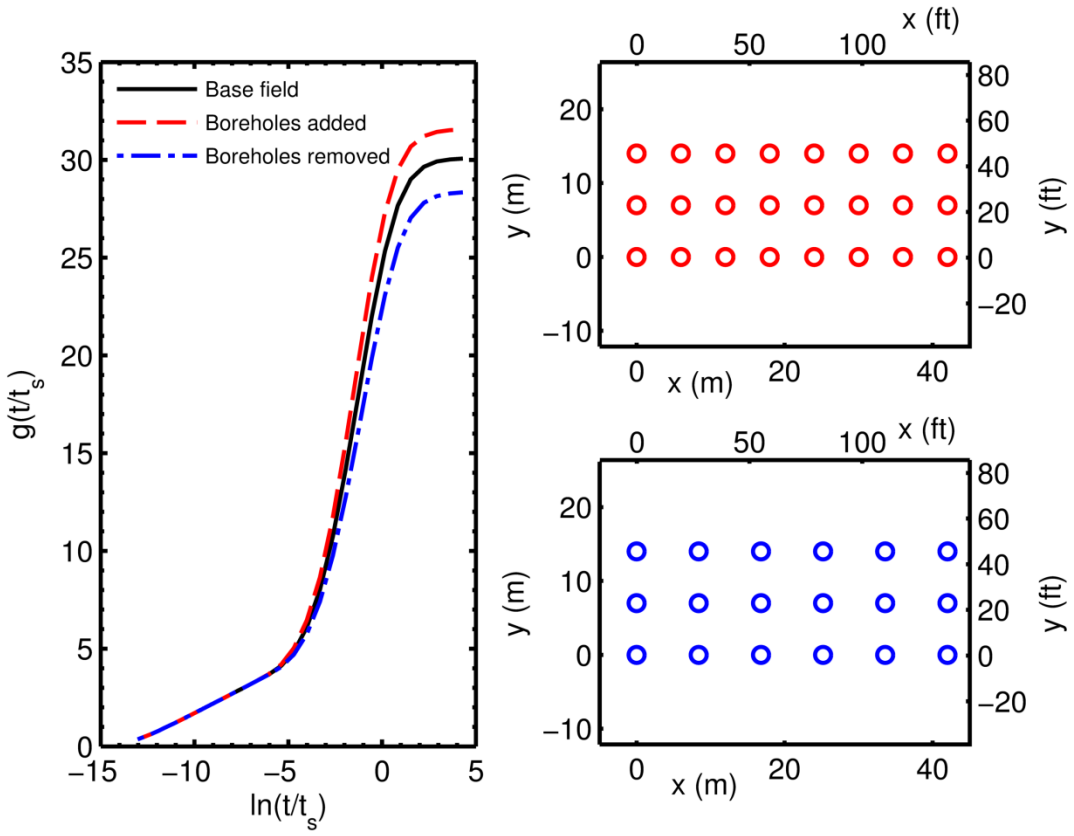

Figure 5-9: g-function of a 3 × 7 bore field with compared with the g-functions of a 3 × 8 and a 3 × 6 bore field

The same strategy is used on the 5 × 10 bore field, which is compared to a 5 × 9 bore field and to a 5 × 11 bore field. The horizontal spacing is B_{hor} = 7.9 m (26 ft) for the 5 × 9 bore field and B_{hor} = 6.3 m (21 ft) for the 5 × 11 bore field. The g-functions are compared on Figure 5-10 for the same total borehole length $N_b \cdot H$ = 5650 m (18537 ft). The characteristic time t_s is calculated for H = 113 m (371 ft). The results are similar to the 3 × 7 bore field, as the g-functions are reduced for the field with removed boreholes and increased for the field with added boreholes. The reduction of the g-function is 6.88 % at t = 20 years for the 5 × 9 bore field. The increase is 6.47 % at t = 20 years for the 5 × 11 bore field. The required total borehole length is reduced to 5535 m (18159 ft) for the 5 × 9 bore field and increased to 5775 m (18947 ft) for the 5 × 11 bore field. The individual borehole lengths are then H = 123 m (404 ft) and H = 105 m (344 ft), respectively.

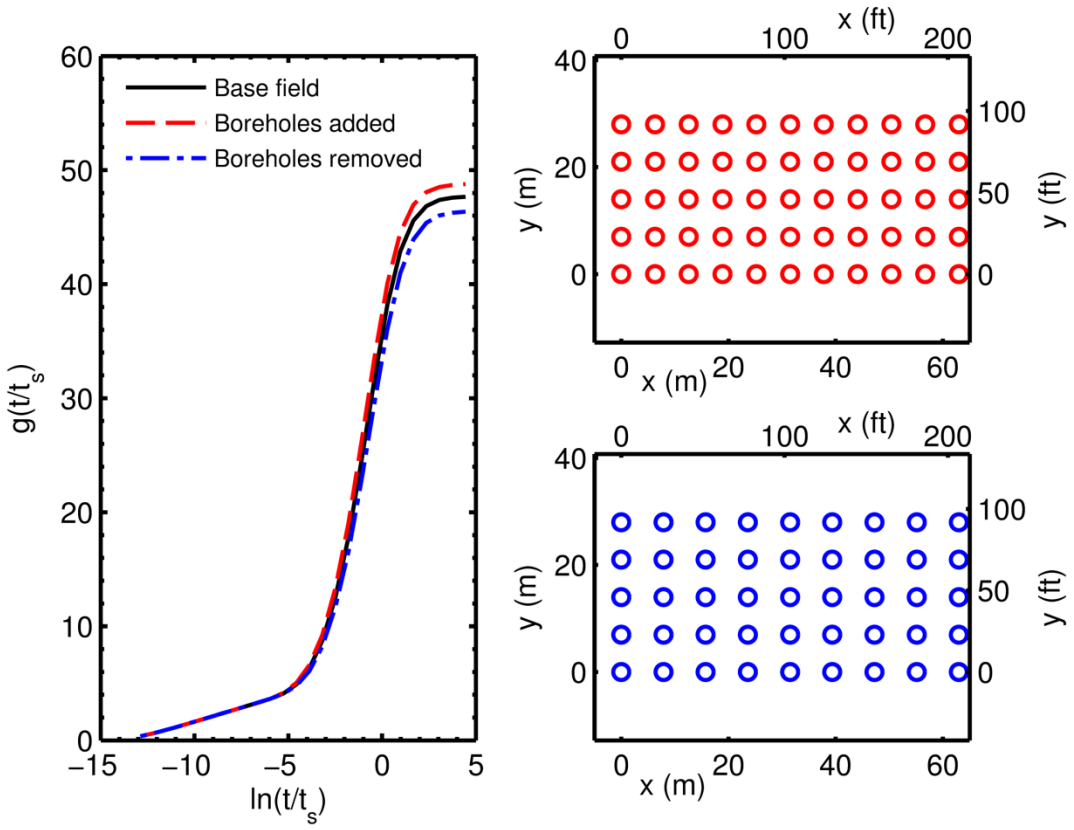

Figure 5-10: g-function of a 5 × 10 bore field with compared with the g-functions of a 5 × 11 and a 5 × 9 bore field

The required individual and total borehole lengths are summarized in Table 5-2 for the two bore fields and each strategy. It is shown that displacing boreholes in the field has relatively little impact on the required borehole length. Results presented here seem to indicate that it is not beneficial to displace boreholes inside the bore field, as it does not decrease the required length. However, small variations of the borehole positions have negligible effects on the required borehole length. This has an important implication for designers and drillers : the positioning of boreholes can be altered, within a given land area, without affecting the performance of the system

Removing boreholes from the bore fields reduces the total required length while adding boreholes increases the total required length. Removing 3 boreholes from the 3 × 7 bore field reduces the total required length by 2.2% while increasing the individual borehole length by 14.0%. Removing 5 boreholes from the 5 × 10 bore field reduces the total required length by 2.0% while

increasing the individual borehole length by 8.8%. These values are valid for a borehole resistance of 0.1 m-K/W (0.0144 h-ft^2-°F/Btu-in.). The variation of the required length correlates with the variation of the g-function value: a reduction of the g-function is seen in cases where the required length is reduced, as shown in Table 5-3.

Table 5-2: Required Borehole Length of the Bore Fields and Relative Change of the Total Required Length

Strategy	3 × 7 bore field			5 × 10 bore field		
	Required length, m (ft)	Total length, m (ft)	Relative change*	Required length, m (ft)	Total length, m (ft)	Relative change*
Base	121 (397)	2541 (8337)	0	113 (371)	5650 (18537)	0
Displacing away from center	121 (397)	2541 (8337)	0	113 (371)	5650 (18537)	0
Displacing towards center	122 (400)	2562 (8406)	+0.8%	114 (374)	5700 (18701)	+0.9%
Removing boreholes	138 (453)	2484 (8150)	-2.2%	123 (404)	5535 (18159)	-2.0%
Adding boreholes	108 (354)	2592 (8504)	+2.0%	105 (344)	5775 (18947)	+2.2%

***Relative to the base configuration. For R_b = 0.1 m-K/W (0.0144 h-ft^2-°F/Btu-in.), $\dot{m}$ = 7 L/s (111 Gal/min) for the 3 × 7 bore field and $\dot{m}$ = 16 L/s (254 Gal/min) for the 5 × 10 bore field.**

Table 5-3: g-function Values at t = 20 years and Relative Change with the Base Configuration

Strategy	3 × 7 bore field			5 × 10 bore field		
	g-function at t = 20 years	Relative change*	Relative change in required length*	g-function at t = 20 years	Relative change*	Relative change in required length*
Base	19.8	0	0	27.5	0	0
Displacing away from center	19.7	-0.5%	0	27.3	-0.5%	0
Displacing towards center	20.1	+1.7%	+0.8%	27.7	+0.7%	+0.9%
Removing boreholes	17.8	-10%	-2.2%	25.6	-6.9%	-2.0%
Adding boreholes	21.6	+9.4%	+2.0%	29.3	+6.5%	+2.2%

***Relative to the base configuration. For R_b = 0.1 m-K/W (0.0144 h-ft^2-°F/Btu-in.), $\dot{m}$ = 7 L/s (111 Gal/min) for the 3 × 7 bore field and $\dot{m}$ = 16 L/s (254 Gal/min) for the 5 × 10 bore field.**

The variation of the required borehole length as a result of each strategy is also studied for varying ground thermal properties. Table 5-4 shows the required individual and total borehole lengths of the 3 × 7 bore field for ground thermal conductivities of 1.7 W/m-K (0.98 Btu/h-ft-°F), 2.0 W/m-K (1.16 Btu/h ft °F) and 2.3 W/m-K (1.33 Btu/h-ft-°F). Table 5-5 shows the required individual and total borehole lengths of the 3 × 7 bore field for ground thermal diffusivities of 0.5×10^{-6} m^2/s (0.54×10^{-5} ft^2/s), 1.0×10^{-6} m^2/s (1.08×10^{-5} ft^2/s) and 1.5×10^{-6} m^2/s (1.61×10^{-5} ft^2/s). The results are similar to the results of Table 5-2: displacing the boreholes does not reduce the required borehole length significantly and a reduction of the total required length is obtained only when removing boreholes from the bore field. The relative change in the total required length is greater with lower ground thermal conductivity and higher ground thermal diffusivity.

Table 5-4: Required Borehole Length of the Bore Fields and Relative Change of the Total Required Length for Varying Ground Thermal Conductivity

	k_s = 1.7 W/m-K (0.98 Btu/h-ft-°F)			k_s = 2 W/m-K (1.16 Btu/h-ft-°F)			k_s = 2.3 W/m-K (1.33 Btu/h-ft-°F)		
	Required length, m (ft)	Total length, m (ft)	Relative change*	Required length, m (ft)	Total length, m (ft)	Relative change*	Required length, m (ft)	Total length, m (ft)	Relative change*
Base	136 (446)	2856 (9370)	0	121 (397)	2541 (8337)	0	110 (361)	2310 (7579)	0
Displacing away from center	137 (449)	2877 (9439)	+0.7%	121 (397)	2541 (8337)	0	110 (361)	2310 (7579)	0
Displacing towards center	138 (453)	2898 (9508)	+1.5%	122 (400)	2562 (8406)	+0.8%	111 (364)	2331 (7648)	+0.9%
Removing boreholes	155 (509)	2790 (9154)	-2.3%	138 (453)	2484 (8150)	-2.2%	126 (413)	2268 (7441)	-1.8%
Adding boreholes	122 (400)	2928 (9606)	+2.5%	108 (354)	2592 (8504)	+2.0%	98 (322)	2352 (7717)	+1.8%

***Relative to the base configuration. For R_b = 0.1 m-K/W (0.0144 h-ft^2-°F/Btu-in.), $\dot{m}$ = 7 L/s (111 Gal/min), $\alpha_s = 1.0 \times 10^{-6}$ m^2/s (1.08×10^{-5} ft^2/s).**

Table 5-5: Required Borehole Length of the Bore Fields and Relative Change of the Total Required Length for Varying Ground Thermal Diffusivity

	$\alpha_s = 0.5 \times 10^{-6}$ m^2/s (0.54×10^{-5} ft^2/s)			$\alpha_s = 1.0 \times 10^{-6}$ m^2/s (1.08×10^{-5} ft^2/s)			$\alpha_s = 1.5 \times 10^{-6}$ m^2/s (1.61×10^{-5} ft^2/s)		
	Required length, m (ft)	Total length, m (ft)	Relative change*	Required length, m (ft)	Total length, m (ft)	Relative change*	Required length, m (ft)	Total length, m (ft)	Relative change*
Base	106 (348)	2226 (7303)	0	121 (397)	2541 (8337)	0	131 (430)	2751 (9026)	0
Displacing away from center	106 (348)	2226 (7303)	0	121 (397)	2541 (8337)	0	131 (430)	2751 (9026)	0
Displacing towards center	107 (351)	2247 (7372)	+0.9%	122 (400)	2562 (8406)	+0.8%	132 (433)	2772 (9094)	+0.8%
Removing boreholes	122 (400)	2196 (7205)	-1.3%	138 (453)	2484 (8150)	-2.2%	148 (486)	2664 (8740)	-3.2%
Adding boreholes	95 (312)	2280 (7480)	+2.4%	108 (354)	2592 (8504)	+2.0%	117 (384)	2808 (9213)	+2.1%

***Relative to the base configuration. For R_b = 0.1 m-K/W (0.0144 h-ft^2-°F/Btu-in.), $\dot{m}$ = 7 L/s (111 Gal/min), k_s = 2.0 W/m-K (1.16 Btu/h-ft-°F).**

5.6 Discussion

5.6.1 g-functions

The present study shows that the g-function is a useful tool for the comparison of bore field configurations. In all presented cases, an increase of the g-function caused an increase of the total required length while a reduction of the g-function caused a reduction of the total required length. g-functions can thus be used in early design stages to compare different bore field layouts and select the most promising designs. Simulation of the system is still required to identify the required borehole length.

5.6.2 Practical limit of the strategies

The present study analyzed the effects of adding and removing boreholes on the total required borehole length. It was shown that removing boreholes reduces the total required borehole length but increased the individual borehole length. In practice, there are technical and economical limits to the length of a borehole. This limits the number of boreholes that can be removed from a bore field. In general, to reduce the total required borehole length, a bore field should have the least possible amount of boreholes covering the available land area.

5.7 Conclusion

A model of the thermal response of bore fields (Cimmino, Bernier, & Adams, 2013) is adapted for the simulation of ground source heat pump systems. The model accounts for thermal interactions among boreholes by imposing a borehole wall temperature equal for all boreholes. The model is used to produce g-functions for fields of 21 (3 × 7) and 50 (5 × 10) boreholes and simulate the bore fields to obtain the total required borehole length for each field.

Four strategies, consisting in displacing boreholes away or towards the center of the bore field and adding or removing boreholes from the bore field, are tested to study their impact on the total required borehole length. It is shown that removing boreholes from the bore fields leads to a reduction of the total required length and adding boreholes increases the total required length. Displacing boreholes inside the bore field has a relatively small impact on the total required length. Removing 3 boreholes from the 3 × 7 bore field led to a reduction of 2.2% of the total required length, but increased the individual length of the boreholes by 14.0%. Removing 5 boreholes from the 5 × 10 bore field led to a reduction of 2.0% of the total required length, but increased the individual length of the boreholes by 8.8%. It was shown that the g-function can be used to identify the configuration with the lowest total required length. Similar results were obtained when using different values of ground thermal conductivity and ground thermal diffusivity. The relative change in the total required length was shown to be greater with lower ground thermal conductivity and higher ground thermal diffusivity.

5.8 Acknowledgements

This work was partly funded by the NSERC Smart Net-Zero Energy Buildings Strategic Research Network (SNEBRN). The authors also wish to thank the Canadian GeoExchange Coalition and the American Society of Heating, Refrigerating and Air-Conditioning Engineers (ASHRAE) for a scholarship and a Grant-in-aid awarded to the first author.

5.9 Nomenclature

SYMBOLS

B : Borehole spacing (m, ft)

c_p : Fluid thermal capacity (kJ/kg-K, Btu/lb-°F)

D : Borehole buried depth (m, ft)

f_i : Bore field form factor for row i

$\mathcal{F}, \mathcal{F}^{-1}$: Direct and inverse Fourier transforms

g : g-function

H : Borehole length (m, ft)

h : Borehole-to-borehole response factors

k_s : Ground thermal conductivity (W/m-K, Btu/h-ft-°F)

$\mathcal{L}, \mathcal{L}^{-1}$: Direct and inverse Laplace transforms

$\dot{m}$: Fluid flow rate (L/s, Gal/min)

N : Number of time steps

N_b : Number of boreholes

$Q, '$: Heat extraction rate, heat extraction rate per unit borehole length (kW/m, kBtu/h)

$q, '$: Heat extraction rate increment, heat extraction rate increment per unit borehole length (kW/m, kBtu/h)

R_b : Borehole thermal resistance (m K/W, h-ft2-°F/Btu-in.)

r_b : Borehole radius (m, in.)

$T, \Delta T$: Temperature, temperature variation (°C, °F)

$t, \Delta t$: Time, time-step (s)

t_s : Bore field characteristic time (s)

GREEK SYMBOLS

α_s : Ground thermal diffusivity (m^2/s, ft^2/s)

σ : Damping coefficient for the numerical Laplace transform (1/s)

ρ : Fluid density (kg/m^3, lb/ft^3)

SUBSCRIPTS

b : Borehole wall

g : Ground

hor : Horizontal

i, j : Boreholes i and j

$i \rightarrow j$: From borehole i to borehole j

max : Maximum

min : Minimum

out : Outlet

5.10 References

Beck, M., Bayer, P., de Paly, M., Hechy-Méndez, J., & Zell, A. (2013). Geometric arrangement and operation mode adjustment in low-enthalpy geothermal borehole fields for heating. Energy, 49(1), 434-443.

Bernier, M. A., Pinel, P., Labib, R., & Paillot, R. (2004). A multiple load aggregation algorithm for annual hourly simulations of GCHP systems. HVAC&R Research, 10(4), 471-487.

Blomberg, T., Claesson, J., Eskilson, P., Hellström, G., & Sanner, B. (2008). EED 3.0 - Earth Energy Designer. Tiré de http://www.buildingphysics.com/manuals/EED3.pdf

Carslaw, H. S., & Jaeger, J. C. (1946a). Chapter 13, The Laplace transformation: Problems on the cylinder and sphere. In O. U. Press (dir.), Conduction of Heat in Solids. (2nde éd., pp. 327-352). Oxford: Oxford University.

Cimmino, M., & Bernier, M. (2013). Preprocessor for the generation of g-functions used in the simulation of geothermal systems. Proceedings of BS2013, Chambéry, France.

Cimmino, M., & Bernier, M. (2014). A semi-analytical method to generate g-functions for geothermal bore fields. International Journal of Heat and Mass Transfer, 70(c), 641-650.

Cimmino, M., Bernier, M., & Adams, F. (2013). A contribution towards the determination of g-functions using the finite line source. Applied Thermal Engineering, 51(1-2), 401-412.

Cimmino, M., Bernier, M., & Pasquier, P. (2012). Utilisation des g-functions de Eskilson pour la simulation de systèmes géothermiques. Proceedings of eSim 2012, Halifax NS.(pp. 282-295).

Claesson, J., & Javed, S. (2011). An analytical method to calculate borehole fluid temperatures for time-scales from minutes to decades. ASHRAE Transactions, 117(2), 279-288.

Eskilson, P. (1987). Thermal Analysis of Heat Extraction Boreholes. Ph.D. Thesis, University of Lund, Lund, Sweden.

Fisher, D. E., Rees, S. J., Padhmanabhan, S. K., & Murugappan, A. (2006). Implementation and validation of ground-source heat pump system models in an integrated building and system simulation environment. HVAC&R Research, 12(3A), 693-710.

Fossa, M. (2011). The temperature penalty approach to the design of borehole heat exchangers for heat pump applications. Energy and Buildings, 43(6), 1473-1479. doi:10.1016/j.enbuild.2011.02.020

Hellström, G., & Sanner, B. (1994). Software for dimensioning of deep boreholes for heat extraction. Proceedings of Calorstock 1994, Espoo/Helsinki, Finland.(pp. 195-202).

Huber, A. (2011). Program EWS: Calculation of Borehole Heat Exchangers. Zürich, Swiss.

Ingersoll, L. R., Adler, F. T., Plass, H. J., & Ingersoll, A. C. (1950). Theory of earth heat exchangers for the heat pump. Heating, Piping & Air Conditioning, 22, 113-122.

Ingersoll, L. R., & Plass, H. J. (1948). Theory of the ground pipe heat source for the heat pump. Heating, Piping & Air Conditioning, 20(119), 119-122.

Ingersoll, L. R., Zobel, O. J., & Ingersoll, A. C. (1954). Theory of earth heat exchanger for the heat pump Heat Conduction: With Engineering, Geological and Other Applications. (2nde éd., pp. 240-271): McGraw-Hill.

Kurevija, T., Vulin, D., & Krapec, V. (2012). Effect of borehole array geometry and thermal interferences on geothermal heat pump system. Energy Conversion and Management, 60, 134-142.

Lamarche, L. (2009). A fast algorithm for the hourly simulations of ground-source heat pumps using arbitrary response factors. Renewable Energy, 34(10), 2252-2258.

Lamarche, L., & Beauchamp, B. (2007a). A fast algorithm for the simulation of GCHP systems. ASHRAE Transactions, 113, 470-476.

Lamarche, L., & Beauchamp, B. (2007b). A new contribution to the finite line-source model for geothermal boreholes. Energy and Buildings, 39(2), 188-198.

Liu, X. (2005). Development and experimental validation of simulation of hydronic snow melting systems for bridges. Ph.D. Thesis, Oklahoma State University, Stillwater, OK.

Liu, X., & Hellstrom, G. (2006). Enhancements of an integrated simulation tool for ground-source heat pump system design and energy analysis. Proc. 10th International Conference on Thermal Energy Storage, Richard Stockton College of New Jersey.

Marcotte, D., & Pasquier, P. (2008). Fast fluid and ground temperature computation for geothermal ground-loop heat exchanger systems. Geothermics, 37(6), 651-665.

Moreno, P., & Ramirez, A. (2008). Implementation of the Numerical Laplace Transform: A review. IEEE Transactions on power delivery, 23(4), 2599-2609.

Robert, F., & Gosselin, L. (2014). New methodology to design ground coupled heat pump systems based on total cost minimization. Applied Thermal Engineering, 62(2), 481-491.

Spitler, J. D. (2000). A design tool for commercial building loop heat exchangers. Fourth International Heat Pumps in Cold Climates Conference, Aylmer, Québec.

Wedepohl, L. M. (1983). Power system transients: Errors incurred in the numerical inversion of the Laplace transforms. 26th Midwest Symposium on Circuits and Systems, Mexico.(pp. 174-178).

Yavuzturk, C., & Spitler, J. D. (1999). A short time step response factor model for vertical ground loop heat exchangers. ASHRAE Transactions, 105(2), 475-485.

Zeng, H. Y., Diao, N. R., & Fang, Z. H. (2002). A finite line-source model for boreholes in geothermal heat exchangers. Heat Transfer - Asian Research, 31(7), 558-567.

CHAPITRE 6 ARTICLE 4 : EXPERIMENTAL DETERMINATION OF THE G-FUNCTION OF A SMALL-SCALE GEOTHERMAL BOREHOLE

Cimmino, M., & Bernier, M. (2014). Experimental determination of the g-function of a small-scale geothermal borehole. Soumis à *Geothermics* le 1er novembre 2014.

ABSTRACT

An experimental setup was built to obtain the experimental g-function of a small-scale borehole. The experimental g-function is calculated from the measured borehole wall temperature and the net heat injection rate into a 400 mm long borehole inserted in a 2 m^3 sand tank with known thermal properties. With such a small length it is possible to reach a steady-state condition after a 168 h long test. The experimental g-function of the borehole is compared to the g-function obtained from an analytical model based on the finite line source solution. The difference between the experimental and analytical g-functions is 4.7% after one week but the two curves remain within the experimental uncertainty bands. The air temperature variations during the test are shown to have a relatively significant effect on the results.

6.1 Introduction

Thermal response factors, or g-functions, have been used for a number of years to design and simulate geothermal bore fields (Fisher et al., 2006; Hellström & Sanner, 1994; Liu & Hellstrom, 2006; Spitler, 2000).

The concept of thermal response factors was introduced by Eskilson (1987) and has been reviewed rencently by Bernier (2014). Eskilson's g-functions give the variation of the borehole wall temperature T_b in a bore field in response to a constant average heat extraction rate per borehole length $\bar{Q}$:

$$T_b = T_g - \frac{\bar{Q}}{2\pi k_s} \cdot g(t/t_s, r_b/H, B/H, D/H) \quad (6.1)$$

where T_g is the undisturbed ground temperature, k_s is the ground thermal conductivity and g is the g-function of the bore field. g-Functions vary according to four non-dimensional parameters: the non-dimensional time t/t_s, with t_s $(= H^2/9\alpha_s)$ the characteristic time of the bore field, H the borehole length and α_s the ground thermal diffusivity; the non-dimensional borehole radius r_b/H, with r_b the borehole radius; the non-dimensional borehole spacing B/H, with B the distance between two adjacent boreholes; and the non-dimensional buried depth D/H, with D the buried depth of the boreholes. The various dimensional parameters of a single borehole are illustrated on Figure 6-1.

A graphical representation of a g-function for a single borehole is given in Figure 6-2. This figure shows the variation of the g-function for $r_b/H = 0.0005$ and $D/H = 0.025$ as a function of $\ln(t/t_s)$. As shown by Cimmino and Bernier (2014b) the g-function graphs for bore fields consists of four regions. In the case of single boreholes, borehole to borehole interaction is not a concern and the g-function curve can be decomposed into three different regions as shown in Figure 6-2. The first region, for non-dimensional times up to approximately $\ln(t/t_s) = -2.3$, is characterized by one-dimensional radial heat conduction. At these times, the borehole does not interact with the ground surface or the ground below the borehole and the g-function can be approximated by the infinite line source analytical solution. The second region, ranging from approximately $\ln(t/t_s) = -2.3$ to $\ln(t/t_s) = 2.3$, is characterized by two-dimensional radial-axial heat conduction. In this region, the borehole interacts with the ground surface and the ground below the borehole and the g-function tends to its steady-state value. The third region, starting approximately at $\ln(t/t_s) = 2.3$, is characterized by steady-state heat transfer. The borehole is in thermal equilibrium and the extraction of heat does not further decrease the borehole wall temperature.

The g-function is non-dimensional, and is therefore valid for any ground thermal properties and for any borehole with equal non-dimensional radius r_b/H and non-dimensional buried depth D/H. For example, a borehole with a radius r_b = 0.05 m, a length H = 100 m and a buried depth D = 2 m has the same g-function as a borehole with a radius r_b = 0.075 m, a length H = 150 m

and a buried depth D = 3 m. Finally, it is important to note that g-function graphs are valid for specific values of the r_b/H ratio.

The objective of this study is to experimentally evaluate the g-function of a single borehole. Since the evaluation of the complete g-function curve using measurements on a real-scale borehole is impractical (i.e. a non-dimensional $\ln(t/t_s) = 2$ corresponds to a time t = 300 years for a typical 100 m borehole), a small-scale borehole installation with a borehole length of 400 mm was built to evaluate the experimental g-function with a test period of only one week. The borehole is fully instrumented and is installed into a sand tank with known thermal properties.

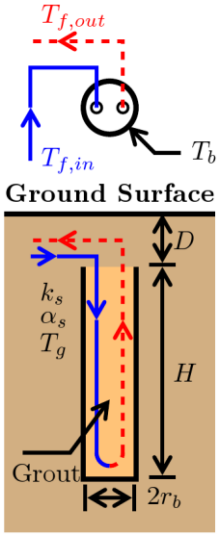

Figure 6-1: Typical borehole geometry

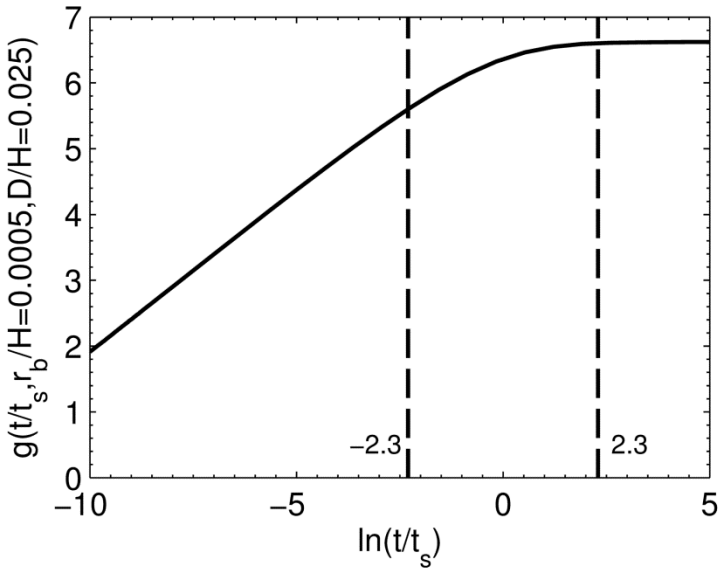

Figure 6-2: g-function of a single borehole with three distinct regions

6.2 Litterature review

6.2.1 Thermal response factors

Eskilson's g-functions were obtained using a finite difference method to solve the transient heat conduction problem inside a bore field. The ground surrounding each individual borehole was modeled in a 2-D radial axial grid. The total temperature variation in the ground was calculated by spatial superposition of the temperature field surrounding each borehole. A zero temperature condition at the ground surface was obtained by the method of images, superposing a temperature field of opposite sign for each borehole, using the ground surface as the axis of symmetry. A uniform borehole wall temperature, equal for all boreholes, was used as a boundary condition. The required borehole wall temperature to obtain a constant average heat extraction rate is calculated at each time step. The numerical model used to generate g-functions is described in the Superposition Borehole Model (SBM) manual for computer code (Eskilson, 1986). A complete review of Eskilson's g-functions was presented by Cimmino et al. (2013).

Analytical solutions are often used to calculate thermal response factors. The infinite line source (ILS) and Carslaw and Jaeger's cylindrical heat source (CHS) analytical solutions (Carslaw &

Jaeger, 1946b) were used by Ingersoll et al. (1950; 1948) to predict temperature variations in ground heat exchangers. The cylindrical heat source solution gives the temperature variation in a semi-infinite ground region for $r \geq r_b$ for a constant heat injection rate at the borehole wall, i.e. at $r = r_b$. It is noted by Ingersoll et al. that the ILS can be used as an approximation of the CHS for times greater than $t = 20r_b^2/\alpha_s$, the relative difference between the ILS and the CHS is then 2.6% (Philippe et al., 2009). An upper bound of validity was given by Eskilson at $t = t_s/10$, when axial effects start appearing.

Eskilson (1987) proposed to use the finite line source (FLS) solution to approximate the g-function of a single borehole. The temperature variation around the borehole is obtained by the spatial integration of the point heat source solution along the length of the borehole. The ground surface temperature is maintained at the initial ground temperature by superimposing a line source of opposite sign above the ground surface. The g-function of a bore field would be obtained by spatial superposition of the FLS, using one line source per borehole.

Zeng et al. (2002) used the spatial superposition of the FLS solution to approximate g-functions. The borehole wall temperature was given by the integral mean temperature at $r = r_b$ over the length of the borehole. A simplified solution was presented by Lamarche and Beauchamp (2007b) for the case $D = 0$, then by Costes and Peysson (2008) and Claesson and Javed (2011) for the case $D \geq 0$. Fossa (2011) compared g-functions obtained by spatial superposition of the FLS solution to Eskilson's g-functions. The FLS solution overestimated Eskilson's g-functions as the number of boreholes increased and the spacing between boreholes decreased.

Cimmino et al. (2013) and Cimmino and Bernier (2014b) used the FLS solution to model the variation of the heat extraction rate among boreholes and along the length of each borehole. Each borehole was broken down into segments, each segment modeled by a finite line source. The temperature at the wall of each borehole segment was obtained from the spatial and temporal superposition of the FLS solution. A system of equations was built in the Laplace domain and solved by imposing an equal wall temperature for all borehole segments, as done by Eskilson in his numerical model. The g-functions obtained with the FLS were compared to Eskilson's g-functions for bore fields ranging from 1 borehole to 12 × 12 boreholes. The difference was less than 5% in most cases. The authors developed a software tool that generates g-functions based on user input of borehole positions and lengths (Cimmino & Bernier, 2013).

Monzó et al. (2014) used a finite element model to calculate the g-function of a field of 3 × 2 boreholes. The uniform temperature boundary condition at the borehole walls was obtained by modelling the boreholes as highly conductive cylinders. The cylinders are thermally connected above ground through a highly conductive bar. A unit heat transfer rate is applied as a boundary condition on the top surface of the bar. Heat is transferred to the ground through the highly conductive material. The g-function obtained with the finite element model was in agreement with Eskilson's g-function.

6.2.2 Field validation and laboratory validation of geothermal borehole models

Yavuzturk and Spitler (2001) compared a 2-D finite volume model of the short-term response of a borehole heat exchanger (Yavuzturk & Spitler, 1999; Yavuzturk et al., 1999) to monitored field data of an elementary school geothermal system of 120 boreholes. Predicted heat pump entering fluid temperature (EFT) and heat pump energy consumption were compared to monitored data over a period of one year. Yavuzturk et al. (2009) later presented a 1-D finite element model of the short-term response of a borehole heat exchanger. The model was compared to measurements from a thermal response test.

Zarella et al. (2011) developed a capacity resistance model (CARM) of a 4 pipe borehole configuration. The borehole was modelled as a thermal resistance circuit with thermal capacity nodes located at the center of the borehole and at the borehole wall. The thermal capacitance of the fluid within the pipes is also considered. The model was coupled with another capacity resistance model of the soil (De Carli, Tonon, Zarrella, & Zecchin, 2010) and validated using measured data from a thermal response test. The measured and predicted outlet fluid temperatures were within 1°C over the test period of 13 days.

Bauer et al. (2011) developed a 3-D model of the short-term response of a borehole, based on a thermal resistance and capacity model (TRCM) of the borehole (Bauer et al., 2010). The borehole cross-section is modeled as a thermal resistance circuit with thermal capacity nodes representing the thermal capacitance of the grout surrounding each pipe. The model was validated against a thermal response test. Pasquier and Marcotte (2012, 2014) proposed an improved thermal resistance and capacity model. The grout was divided into sub-volumes for each pipe and the

core. The sub-volumes were then separated into several thermal resistances and thermal capacity nodes. The model was validated against a thermal response test and reference measurements from a laboratory thermal response test (Beier et al., 2011).

Gu and O'Neal (1998) built a small-scale test facility for the simulation of borehole heat exchanger. The test facility consisted of a 1.2 m grouted borehole inserted into a 1.2 m deep soil tank of 0.8 m diameter. The soil inside the tank was partially saturated with water. A test period of 72 minutes on the experimental setup was equivalent to one day of operation on a real scale installation due to the reduction in scale. The facility was used to validate a short-term borehole with different grouting materials.

Beier et al. (2011) built a 18 m long horizontal sandbox filled with fully saturated sand. A borehole is installed horizontally in the center of the sandbox. The borehole consists of a high density polyethylene (HDPE) U-tube inserted in an aluminum pipe that serves as the borehole wall. The space between the U-tube and the aluminum pipe was filled with grout. The thermal conductivities of the saturated sand and the grout were measured using a thermal probe. The sandbox was used to run two thermal response tests. The available measurement data were used by other researchers to validate borehole models (M. Li & Lai, 2013; Pasquier & Marcotte, 2014).

Eslami-Nejad and Bernier (2012) designed an experimental setup to validate a numerical model of the heat transfer in saturated soil with ground freezing. The setup consists of a 0.5 m high saturated sand tank of 0.43 m diameter. A 22 mm diameter copper pipe is inserted at the center of the tank and a cold solution was run through the pipe to freeze the sand close to the copper pipe. Temperature measurements in the sand tank were used to successfully validate the numerical model.

Kramer et al. (2014) built a test setup for geothermal pile heat exchangers. The setup consists of a 2.13 m tall and 1.83 m wide dry sand tank with a 1.38 m long concrete geothermal pile in its center. A polyvinyl chloride (PVC) U-tube is installed in the geothermal pile. An array of thermocouples is placed in the sand on two planes parallel to the pile axis to measure the 2-D temperature field in the sand tank. The authors studied the performance of the geothermal pile under various heating, cooling and successive cooling and heating scenarios with different fluid flow rates and initial temperature conditions.

Erol and François (2014) evaluated experimentally the thermal, mechanical and hydraulic properties of different grout mixtures. The permeability, viscosity, compression strength and thermal conductivity of commercial silica sand-based and bentonite-based grout mixtures were compared to that of thermally enhanced grout mixtures using graphite. The thermal resistance of boreholes with different grout mixtures were then evaluated during thermal response tests on short boreholes installed in a 1 m^3 sandbox. The temperature variations in the sandbox and at the borehole wall measured during the test were in good agreement with the variations predicted by the finite line source model. A 5% addition of graphite into grout mixtures showed to provide a significant positive effect on the thermal properties of the grout mixtures.

Salim-Shirazi and Bernier (2014) designed and constructed a small-scale setup for the study of transient heat transfer of geothermal boreholes. The setup consists of a 1.35 m tall and 1.4 m diameter sand tank. A 1.23 m long borehole is installed at the center of the tank and hot water is circulated into the borehole during a 73 h heat injection period. Sand and borehole wall temperatures are measured by an array of thermocouples installed on a string rack into the sand tank. Thermocouples are installed at four different radial distances, four different depths and 4 different azimutal positions. A successful comparison with temperatures predicted by a 2-D finite volume model of the sand tank established the validity of the sand tank instrumentation and data processing.

It appears from the surveyed literature that there has not yet been an attempt to determine g-functions experimentally over the three regions identified earlier in relation to Figure 6-2.

6.3 Analytical model

There are no reported g-function corresponding to the r_b/H ratio used in the experiments. Therefore, a specific g-function is derived analytically based on a well-established methodology. The model uses the finite line source to calculate the g-function of a single vertical borehole for the geometry shown on Figure 6-1. The model is an adaptation of a general model to calculate the g-functions of fields of multiple boreholes using the finite line source presented by Cimmino and Bernier (2014b). As shown on Figure 6-3, the borehole is divided into n_q segments (four on this figure) and arrows represent interactions between segments on the finite line and segments on the borehole radius, r_b. The borehole has a length H and is buried at a distance D from the ground

surface. The ground has a thermal conductivity k_s and a thermal diffusivity α_s. In accordance with Eskilson's boundary condition, it is assumed that the borehole wall temperature is uniform along the length of the borehole and that the temperature at the ground surface is constant and equal to the initial ground temperature T_g. The g-function is obtained by calculating the borehole wall temperature resulting from the extraction of heat at a constant average heat extraction rate per unit length $\bar{Q}$. This results in different heat extraction rate per unit length for each segment.

6.3.1 Segment-to-segment response factors

As shown on Figure 6-3, each segment u has the same length $H_u\ (= H/n_q)$ and is therefore buried at a distance $D_u\ (= D + (u-1)\cdot H/n_q)$ from the ground surface. The temperature variation $\Delta T_{u\to v}$ at the wall of the v^{th} borehole segment caused by the extraction of heat at the u^{th} finite line segment at a constant rate per unit length Q_u is obtained from the finite line source solution (Cimmino & Bernier, 2014b):

$$\Delta T_{u\to v}(t_k) = -\frac{Q_u}{2\pi k_s}\cdot h_{u\to v}(t_k) \tag{6.2}$$

$$\begin{aligned} h_{u\to v}(t) = \frac{1}{2H_v}\int_{1/\sqrt{4\alpha_s t}}^{\infty} \frac{1}{s^2} exp(-{r_b}^2 s^2)\Big[ierf\big((D_v - D_u + H_v)\mathrm{s}\big) \\ - ierf\big((D_v - D_u)\mathrm{s}\big) + ierf\big((D_v - D_u - H_u)\mathrm{s}\big) \\ - ierf\big((D_v - D_u + H_v - H_u)\mathrm{s}\big) + ierf\big((D_v + D_u + H_v)\mathrm{s}\big) \\ - ierf\big((D_v + D_u)\mathrm{s}\big) + ierf\big((D_v + D_u + H_u)\mathrm{s}\big) \\ - ierf\big((D_v + D_u + H_v + H_u)\mathrm{s}\big)\Big] ds \end{aligned} \tag{6.3}$$

$$ierf(\mathrm{X}) = \int_0^X erf(x')\,dx' = X\,erf(X) - \frac{1}{\sqrt{\pi}}(1 - exp(-X^2)) \tag{6.4}$$

where $h_{u\to v}$ is the segment-to-segment response factor of the u^{th} finite line segment onto the v^{th} borehole segment and erf is the error function.

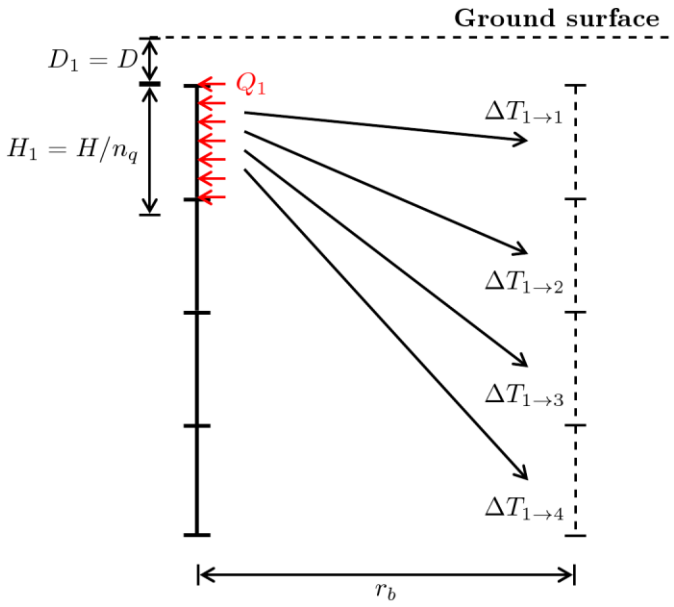

Figure 6-3: Decomposition of a borehole into $n_q = 4$ finite line sources

6.3.2 Temporal and spatial superposition

For a succession of heat extraction rates $Q_u(t_p)$ at the u^{th} finite line segment, starting at time t_{p-1} until time t_p, the temperature variation at the wall of the v^{th} borehole segment at time tk is obtained from the temporal superposition of the finite line source solution:

$$\Delta T_{u\to v}(t_k) = -\sum_{p=1}^{k}\left[\frac{q_u(t_p)}{2\pi k_s}\cdot h_{u\to v}(t_k - t_{p-1})\right] \tag{6.5}$$

where $q_u(t_p) = Q_u(t_p) - Q_u(t_{p-1})$ is the heat extraction rate increment of the u^{th} finite line segment, with $Q_u(t_0) = 0$ and $\Delta t = t_p - t_{p-1}$ the calculation time step.

The total temperature variation at the wall of the v^{th} borehole segment is the sum of the temperature variations caused by all finite line segments:

$$\Delta T_b(t_k) = -\sum_{p=1}^{k}\sum_{u=1}^{n_q}\frac{q_u(t_p)}{2\pi k_s}h_{u\to v}(t_k - t_{p-1}) \tag{6.6}$$

where $\Delta T_b = T_b - T_g$ is the total temperature variation a the borehole wall, equal for all borehole segments.

Equation 6.6 can be evaluated for all n_q borehole segments to form a set of n_q equations with $n_q + 1$ unkowns (q_u and ΔT_b). The set of equations is completed by setting the average heat extraction rate per unit borehole length as constant:

$$\bar{q}(t_k) = \frac{\sum_{u=1}^{n_q} q_u(t_k)}{n_q} = \begin{cases} \bar{Q} & \text{for } t_k = t_1 \\ 0 & \text{for } t_k \neq t_1 \end{cases} \tag{6.7}$$

where $\bar{q}$ is the average heat extraction rate increment of the finite line segments.

Equations 6.6 and 6.7 are rewritten in non-dimensional form:

$$\Theta_b(t_k) = \sum_{p=1}^{k} \sum_{u=1}^{n_q} \tilde{q}_u(t_p) h_{u \to v}(t_k - t_{p-1}) \tag{6.8}$$

$$\tilde{q}(t_k) = \frac{\sum_{u=1}^{n_q} \tilde{q}_u(t_k)}{n_q} = \begin{cases} 1 & \text{for } t_k = t_1 \\ 0 & \text{for } t_k \neq t_1 \end{cases} \tag{6.9}$$

where $\Theta_b = \frac{\Delta T_b}{-\bar{Q}/2\pi k_s}$ is the non-dimensional temperature variation at the borehole wall, which corresponds to the g-function of the borehole (Equation 6.1), and $\tilde{q}_u = q_u/\bar{Q}$ is the normalized heat extraction rate increment.

6.3.3 System of equations in the Laplace domain

The summation over the time variable in Equation 6.8 makes the system of equations difficult to solve directly since the value of the g-function at time t_k is dependent on the values of the normalized heat extraction rate increments at all times prior to t_k. However, this summation is in fact a convolution product (Marcotte & Pasquier, 2008a) and can be replaced by a multiplication in the Laplace domain. The Laplace transform pairs are expressed as:

$$F(s) = \mathcal{L}\big(f(t)\big) = \int_0^{\infty} f(t)\, exp(-st)\, dt \tag{6.10}$$

$$f(t) = \mathcal{L}^{-1}\big(F(s)\big) = \frac{1}{2\pi j}\int_{\sigma-j\infty}^{\sigma+j\infty} F(s)\, exp(st)\, ds \tag{6.11}$$

where $\mathcal{L}$ and $\mathcal{L}^{-1}$ are the direct and inverse Laplace transforms, f is an arbitrary function in the time domain and F the corresponding function in the Laplace domain, s is the complex frequency in the Laplace domain and $j = \sqrt{-1}$ is the imaginary number.

The Laplace transform can be obtained from the Fourier transform using a variable change $s = \sigma + j\omega$ (Moreno & Ramirez, 2008):

$$F(s) = \int_0^{\infty} [f(t)\, exp(-\sigma t)]\, exp(-j\omega t)\, dt = \mathcal{F}(f(t) \cdot exp(-\sigma t)) \tag{6.12}$$

$$f(t) = \frac{exp(\sigma t)}{2\pi}\int_{-\infty}^{+\infty} F(s)\, exp(j\omega t)\, d\omega = exp(\sigma t) \cdot \mathcal{F}^{-1}\big(F(s)\big) \tag{6.13}$$

where ω is the angular frequency in the Fourier domain, $\mathcal{F}$ and $\mathcal{F}^{-1}$ are the direct and inverse Fourier transforms and σ is a real positive constant.

The Laplace transform can be calculated numerically using a fast Fourier transform (FFT) algorithm. Since the heat extraction rate increments $q_u(t_k)$ are only defined for $t \geq t_1 = \Delta t$, a variable change $t_k^* = t_k - \Delta t$ is needed prior to the evaluation of the functions $exp(-\sigma t)$ and $exp(\sigma t)$ during the direct and inverse Laplace transforms. The damping coefficient σ is selected according to Wedepohl's criterion (Wedepohl, 1983):

$$\sigma = 2 \cdot \frac{\ln(N_t)}{t_{max}}, \tag{6.14}$$

where N_t is the total number of time steps and t_{max} is the maximum value of the time variable t^*.

The system of equations (Equations 6.8 and 6.9) is rewritten in the Laplace domain:

$$\mathcal{L}(\Theta_b) = \sum_{u=1}^{n_q} \mathcal{L}(\tilde{q}_u)\mathcal{L}(h_{u\to v}) \tag{6.15}$$

$$\mathcal{L}(\tilde{q}) = \frac{\sum_{u=1}^{n_q} \mathcal{L}(\tilde{q}_u)}{n_q}. \tag{6.16}$$

The solution to the system of equations gives the g-function of the borehole.

6.3.4 g-functions of short boreholes

The analytical model based on the finite line source solution is only valid for long boreholes, for which the line source approximation is valid (i.e. $r_b/H \ll 1$). For a short borehole, the finite line source solution overestimates the heat extraction rates required at both ends of the borehole to maintain a uniform borehole wall temperature along the length of the borehole and leads to an underestimation of the g-function. The g-function can still be obtained by calculating the g-function for a borehole radius $r^* = 0.0005 \cdot H$ and then correcting the g-function using the non-dimensional thermal resistance of an annulus (Eskilson, 1987):

$$g(t, r_b/H) = g(t, r^*/H) - \ln(r_b/r^*) \tag{6.17}$$

The g-functions obtained using this approach were verified with an implementation of Eskilson's Superposition Borehole Model (SBM) (Eskilson, 1986). Although not shown in the results section, the analytical g-function of a small-scale borehole is equivalent to the numerical g-function obtained using the SBM. Analytical g-functions for bore fields were also previously verified with the SBM by Cimmino and Bernier (2014b). Thus, the analytical determination of g-functions can be used with confidence.

6.4 Experimental setup

A small-scale borehole was designed and built to validate the g-function curve for a single borehole. This proved to be difficult mainly because of the small borehole dimensions which required the precise assembly of various parts and the injection of a relatively small amount of power.

Referring back to Equation 6.1, the experimental determination of the g-function requires the injection of a constant amount of power for a period of one week and the measurement of the borehole wall temperature. With these two measurements and with a knowledge of the ground

thermal properties, it is possible to evaluate the time evolution of the g-function. The amount of injected power was of the order of 8 to 9 Watts and needed to be precisely controlled. This power level was chosen so as to remain under 80°C, the temperature limit of the constant temperature bath bath feeding the thermal guard ring. The measured injected power relies on a differential temperature measurement from a thermopile. A precise calibration of the heat losses from the thermopile to the active borehole length was required for an accurate determination of the net injected power into the sand tank.

An overview of the final borehole assembly is shown in Figure 6-4 and schematic representations are presented in Figures 6-5 and 6-6. An active borehole length H of 400 mm was chosen such as to reach a quasi-steady state condition for a non-dimensional time $\ln(t/t_s) = 2$ at the end of a week-long (168 h) experiment. The borehole is inserted into a 2 m^3 sand tank (Ali Salim Shirazi & Bernier, 2014). Water is pumped through the borehole in a closed circuit using a peristaltic pump. Heat is injected into the water loop by a computer-controlled electric heater. Thermocouple probes are used to measure the borehole wall, sand, fluid, and air temperatures.

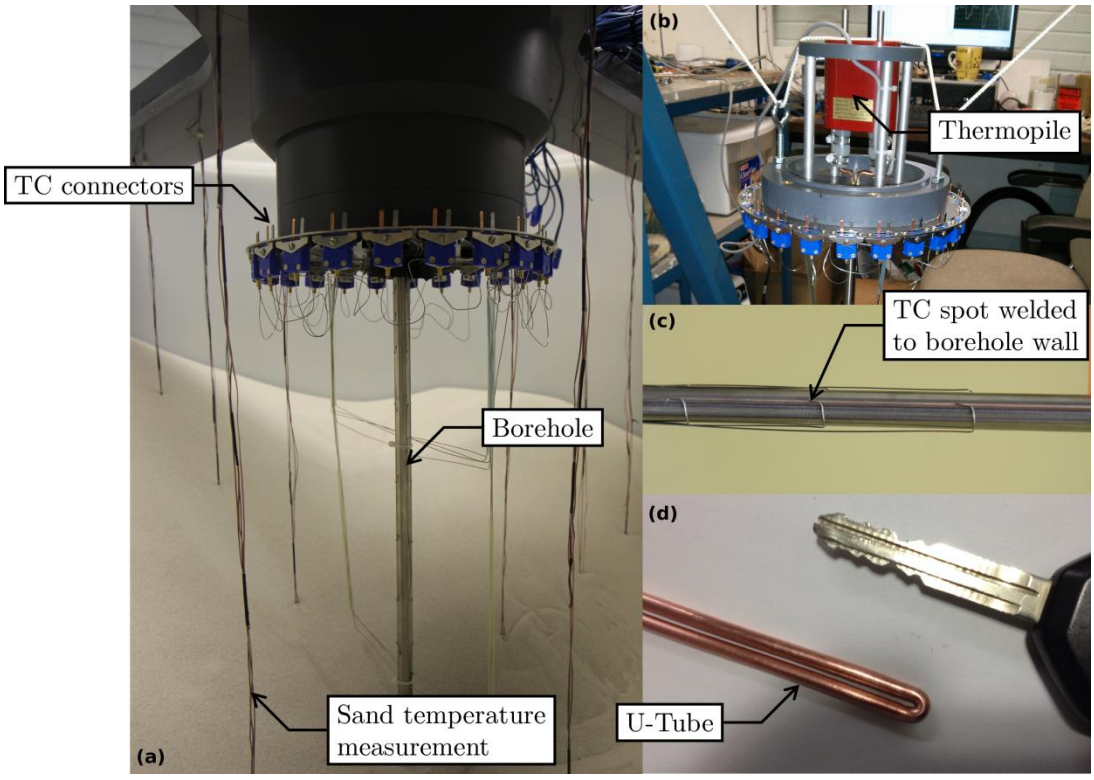

Figure 6-4: Overview of the experimental setup: (a) Small-scale borehole in sand tank, (b) Inside of the thermopile enclosure, (c) Thermocouples welded onto the borehole wall and (d) U-Tube

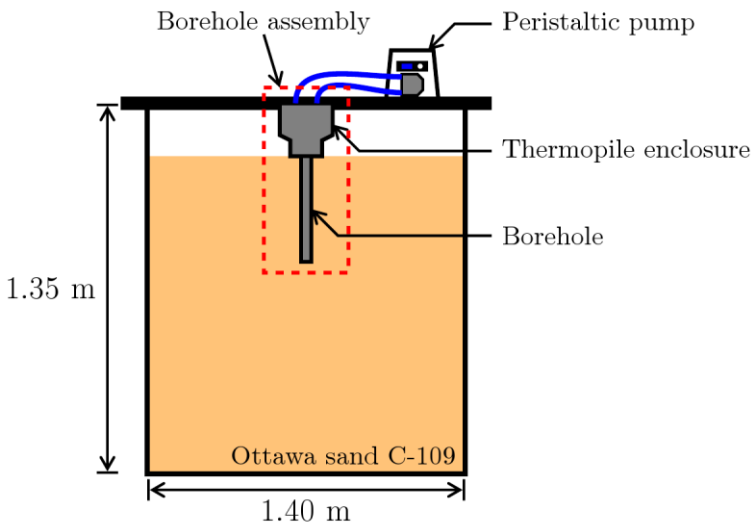

Figure 6-5: Schematic representation of the small-scale test setup

6.4.1 Borehole assembly

The borehole assembly consists of a copper U-tube of 0.125 in. nominal diameter (see Figure 6-6) inserted into a stainless steel tube of 0.5 in. nominal diameter, as shown in Figure 6-7. Polyphenylene oxide (PPO) spacers are used to maintain the spacing between the two U-tube pipes constant at 5.1 mm. The remaining space between the U-tube and the stainless steel tube is filled with fine grade sand which acts as the grout in this case.

As shown in Figure 6-6, the active portion of the borehole starts 19 mm below the thermopile enclosure. The portion of the stainless steel tube above the sand surface is filled with fine cork dust that acts as insulation. The outside of that tube portion is insulated using 12 mm thick closed cell foam insulation. Two type T thermocouples (marked as TC on Figure 6-6) measure the borehole inlet and outlet water temperatures. The temperature difference between the borehole water inlet and outlet is measured by a 20-junction thermopile. The thermopile has a ± 0.04°C accuracy on the temperature difference measurement. It is located inside a PVC enclosure filled with granulated cork to limit heat losses between the temperature difference measurement section and the active portion of the borehole. Water is run through a thermal guard, consisting of a Viton tubing spiral loop located on the outer wall of the thermopile enclosure, at the same temperature

as the water inside the U-tube (measured by the thermocouples at the inlet and outlet of the thermopile enclosure) to further reduce the heat losses. A constant temperature bath is used to control the water temperature inside the thermal guard.

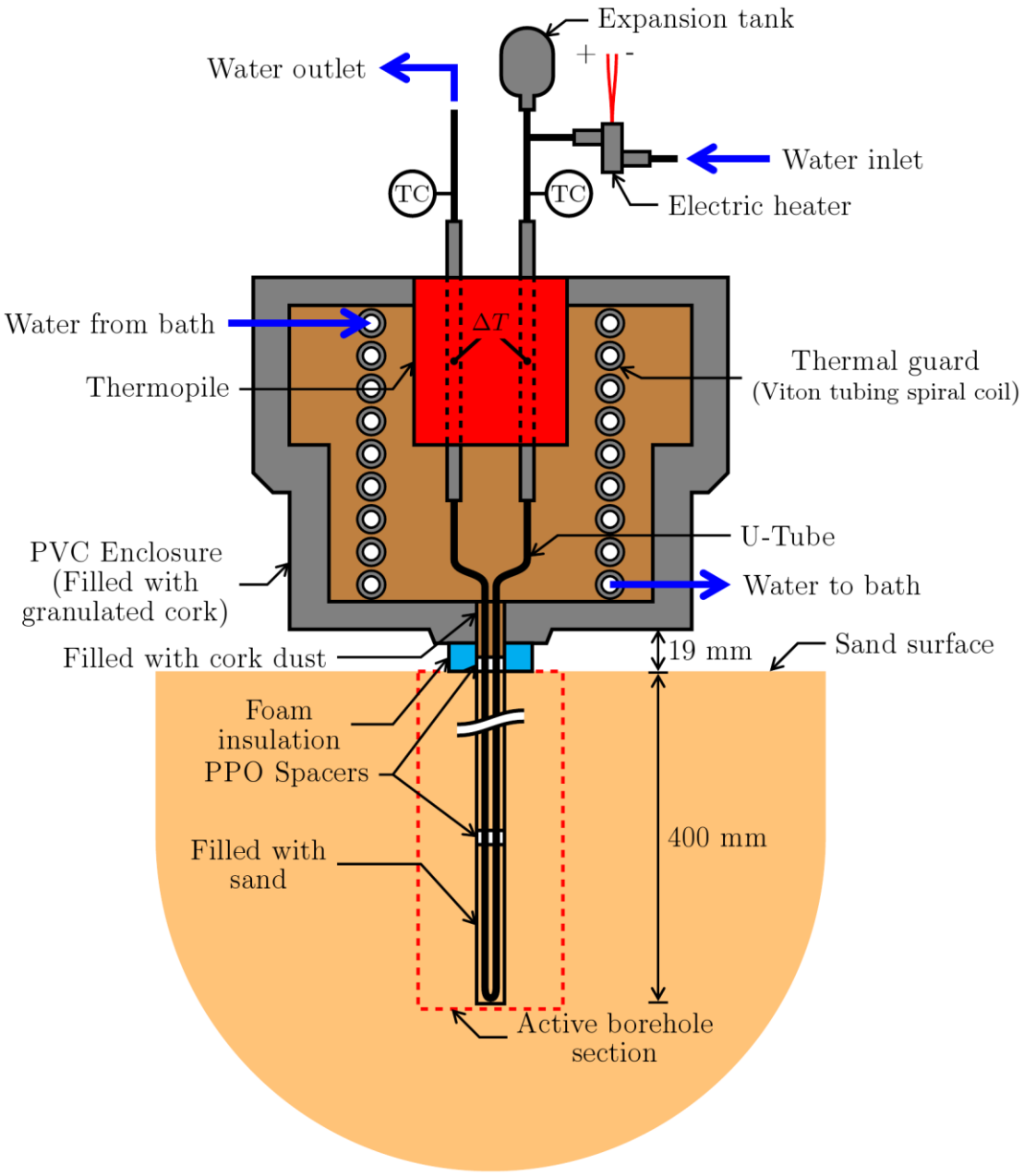

Figure 6-6: Schematic representation of the borehole assembly

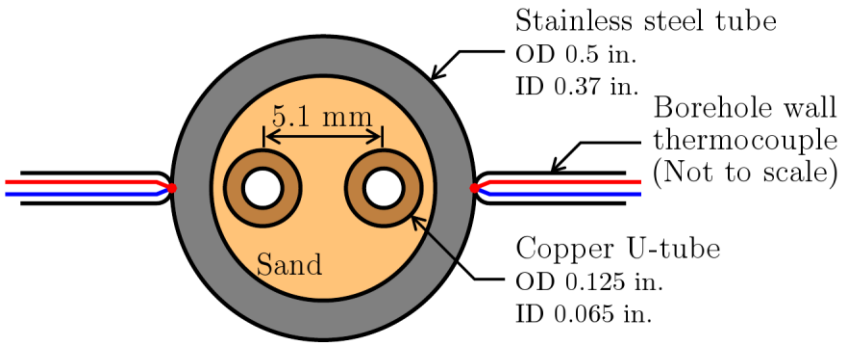

Figure 6-7: Borehole cross-section

A total of 22 type T thermocouples are used to measure the temperatures along the borehole wall. The thermocouples are enclosed in a 0.020 in. diameter stainless steel sheath. They are spot welded to the borehole wall (see Figures 6-4d and 6-7). Thermocouples are located in pairs at positions z = 5, 25, 50, 100, 150, 200, 250, 300, 350, 375 and 395 mm along the active length of the borehole. The borehole wall thermocouples were calibrated by immersion in a constant temperature bath at each 5°C temperature increment between 25°C and 80°C. A single second degree polynomial is used for all thermocouples. The standard deviation between the bath temperatures and the calibrated thermocouple measurements is ± 0.05°C. The standard uncertainty of the reference temperature sensor used during the calibration is ± 0.11°C. Combining these two uncertainties leads to an uncertainty of ± 0.12°C for the borehole thermocouple measurements.

6.4.2 Sand tank

The sand tank consists of a cylindrical polyethylene tank filled with Ottawa sand *C-109*. The tank circumference is insulated with 25 mm thick closed cell foam insulation. The tank rests on a 50 mm layer of rigid insulation. Ottawa sand *C-109* is a graded pure quartz sand with well documented thermal properties (Tarnaski, Momose, & Leong, 2011; Tarnaski, Momose, Leong, Bovesecchi, & Coppa, 2009). The thermal conductivity of the sand was measured using a thermal needle probe and was determined to be k_s = 0.262 W/m-K. An accuracy of 2% is assumed on the evaluated thermal conductivity. The thermal diffusivity of the sand is $\alpha_s = 2.01 \cdot 10^{-7}$ m^2/s.

6.4.3 Equipment, data acquisition and control

Water is pumped through the borehole circuit using a Masterflex® peristaltic pump with a high performance pump head. The pump drive allows control over the pump speed from 1 rpm to 100 rpm with a 0.1 rpm resolution. The accuracy of the speed control is assumed to be inferior to ± 0.1 rpm based on the calibration report.

Heat is injected into the water loop using a DC electric cartridge heater rated at 50 W at 24 V. The DC voltage at the electric heater is provided by a Sorensen XT 30-2 programmable DC power supply. The heating power of the electric heater was controlled via a virtual LabView PID to maintain a stable net heat injection rate into the sand over the test period of 168 h. At any time during the test, the data acquisition system evaluates the water temperature difference required at the thermopile to obtain a total heat injection rate equal to the sum of the desired net heat injection rate into the sand tank and the calculated heat losses through the thermopile enclosure. The evaluated water temperature difference is then used as the set-point for the virtual PID.

6.4.4 Calibration of the thermopile enclosure heat losses

The accurate measurement of the heat injection rate through the borehole into the sand tank is a crucial part of determining the g-function experimentally. During tests, the heat injection rate is determined from an energy balance using the water temperature difference measured by the thermopile. However, the heat injection rate during the experiments is small (i.e. ~8.67 W) and the heat losses through the thermopile enclosure between the measurement of the temperature difference at the thermopile and the active portion of the borehole cannot be neglected.

A calibration test was conducted to quantify the heat losses from the thermopile enclosure to the borehole inlet. For these tests the active borehole section was removed and replaced by a short 180° bend as shown in Figure 6-8. Thus, measured heat losses excluded the active borehole section. Water is run through the set-up at the same flow rate, $\dot{V}$ = 30.1 mL/min, as for the final experiment. The inlet and outlet water temperatures are measured by two type T thermocouples (marked as TC in Figure 6-6). The air temperature surrounding the calibration enclosure is measured by a type T thermocouple placed next to the enclosure.

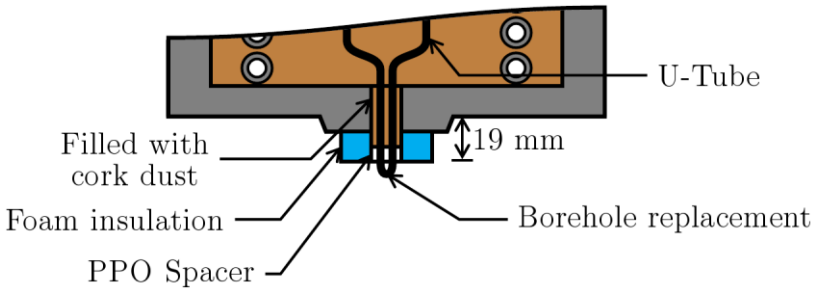

Figure 6-8: Schematic representation of the calibration assembly

After several preliminary tests, it was found that a simple lumped capacitance model of the section between the thermopile and the active borehole section was adequate to predict the time evolution of the heat losses. The resulting RC circuit is shown in Figure 6-9, where T_1 is the inner node temperature of the enclosure, C_1 is the corresponding node thermal capacitance, R_1, R_2 are the thermal resistances between nodes, $\bar{T}_f$ is the average of the measured inlet and outlet water temperatures, and T_{air} is the measured air temperature. The objective of the calibration test is thus to evaluate R_1, R_2 and C_1.

Heat loss calibration tests required two constant temperature baths, one to feed the test assembly and another to supply the thermal guard ring. The inlet temperature to the thermopile from the first bath was kept constant during a start-up period of 15 minutes before increasing linearly up to a temperature of 70 °C over a period of 1 hour. The bath water temperature was then kept constant at 70 °C for 7 hours. A second bath was used to keep the circulating water in the thermal guard ring at the same average temperature as the one circulating in the thermopile. The water and air temperatures and the water temperature difference at the thermopile were measured every second for the full duration of the calibration tests. Two calibration tests were performed. Measurements from the first test were used to obtain R_1, R_2 and C_1. The temperatures T_1 at time $t + \Delta t$ are obtained using an explicit scheme:

$$T_1(t + \Delta t) = T_1(t) + \left(\frac{\bar{T}_f(t) - T_1(t)}{R_1} + \frac{T_{air}(t) - T_1(t)}{R_2} \right) \frac{\Delta t}{C_1} \tag{6.18}$$

$$Q_{loss}(t) = \left(\frac{\bar{T}_f(t) - T_1(t)}{R_1} \right) \tag{6.19}$$

where Δt = 1 s is the measurement period. The parameters R_1, R_2 and C_1 are obtained using a line-search algorithm to minimize the root mean square difference between the measured and calculated heat losses. The values of the calibrated parameters are R_1 = 3.86°C/W, R_2 = 27.8°C/W and C_1 = 325 J/°C. A comparison of the measured and calculated heat losses is presented on Figure 6-10. A few blimps in the data can be observed and are probably caused by air bubbles in the circuit. However, these deviations have no incidence on the calibration results. Heat losses are of the order of 1.2 Watts when the inlet temperature is ≈ 62°C. As shown on Figure 6-10, the lumped capacitance model is able to correctly predict the measured heat losses. The standard deviation between the measured and calculated values after the initial 15 minute transient period are 0.067 W and 0.069 W for the first and second tests, respectively. A standard uncertainty equivalent to twice the standard deviation, i.e. ± 0.14 W, is assumed for the heat losses.

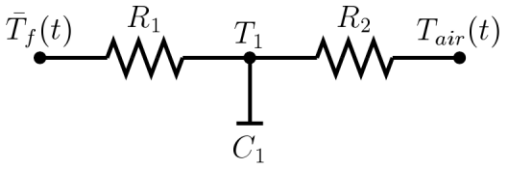

Figure 6-9: Lumped capacitance model of the thermopile enclosure

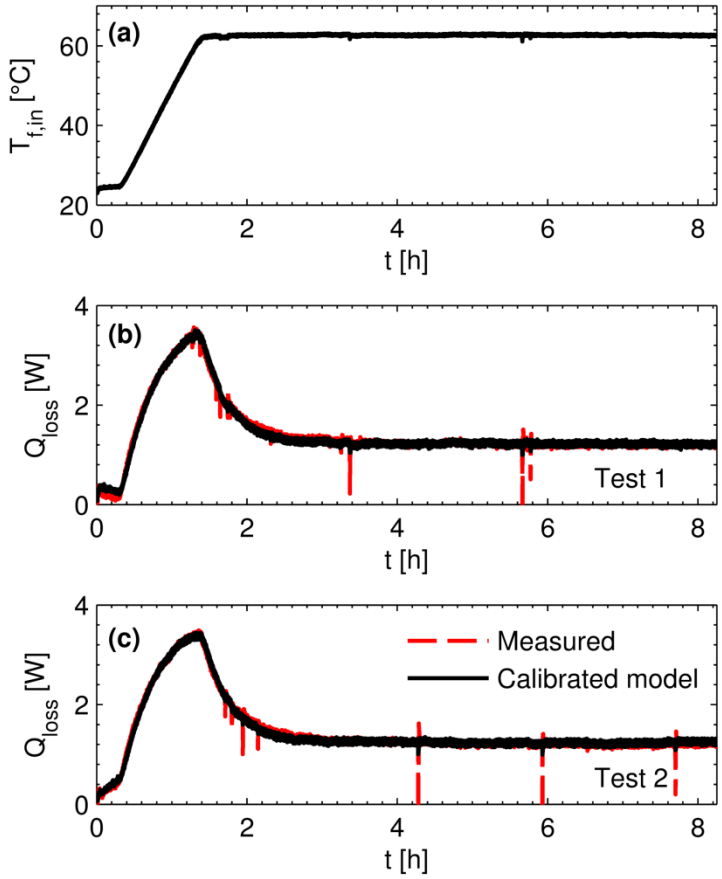

Figure 6-10: Inlet water temperature (a) and heat losses during the first (b) and second (c) calibration tests

6.4.5 Data reduction

The borehole wall temperature is obtained from the weighted average of the 22 measured temperatures along the length of the borehole using the trapezoidal rule. The temperatures above the first thermocouple and below the last thermocouple are assumed to be uniform and equal to the thermocouple measurement. The borehole wall temperature T_b at time t_k is thus given by:

$$T_b(t_k) = \frac{\sum_{i=1}^{11} \frac{\left(T_{E,i}(t_k) + T_{W,i}(t_k)\right)}{2} \Delta z_i}{H} \tag{6.20}$$

$$\Delta z_i = \frac{z_{i+1} - z_{i-1}}{2}, \qquad \Delta z_1 = \frac{z_2 - z_1}{2} + z_1, \qquad \Delta z_{11} = \frac{z_{11} - z_{10}}{2} + H - z_{11} \tag{6.21}$$

where $T_{E,i}$ and $T_{W,i}$ are the temperature measurements of the i^{th} thermocouples along the length of the borehole on the downward and the upward flow side, respectively and z_i is the position of the i^{th} thermocouples along the length of the borehole. Thermocouple positions were given earlier in section 6.4.1.

The net heat injection rate into the sand tank Q_{sand} is calculated by subtracting the calculated heat losses Q_{loss} (Equations 18 and 19) from the total heating power Q_{total} obtained from an energy balance on the water at the thermopile:

$$Q_{sand}(t_k) = Q_{total}(t_k) - Q_{loss}(t_k) \tag{6.22}$$

$$Q_{total}(t_k) = \dot{V}\rho_w c_{p,w}\Delta T(t_k) \tag{6.23}$$

where $\dot{V}$ is the volumetric flow rate in the borehole, ρ_w is the water density, $c_{p,w}$ is the specific heat of the water, and $\Delta T(t_k)$ is the temperature difference measured by the thermopile at time t_k.

The borehole wall temperature is averaged every five minutes to dampen the random variations of the temperatures measured by the thermocouples, mainly caused by the variation of the net heat injection rate into the sand tank:

$$\bar{T}_{b,n} = \frac{\sum_{k=(N-1)n+1}^{Nn} T_b(t_k)}{N} \tag{6.24}$$

where $\bar{T}_{b,n}$ is the average borehole wall temperature over five minutes after $5n$ minutes of operation, $N = 300$ is the number of temperatures averaged over the five minute period.

The average initial ground temperature $\bar{T}_g$ is calculated from the average borehole wall temperature over the first ten seconds of operation, before any heat has been injected into the sand tank:

$$\bar{T}_g = \frac{\sum_{k=1}^{10} T_b(t_k)}{10} \tag{6.25}$$

The average net heat injection rate into the sand tank per unit borehole length $\bar{Q}_n$ since the start of the test is calculated every five minutes:

$$\bar{Q}_n = \frac{\sum_{k=1}^{Nn} Q_{sand}\,(t_k)}{NnH} \tag{6.26}$$

Finally, the experimental g-function is obtained using the definition of the g-function (Equation 6.1):

$$\bar{g}_n = \frac{\bar{T}_{b,n} - \bar{T}_g}{\bar{Q}_n / 2\pi k_s} \tag{6.27}$$

6.5 Results

6.5.1 Net heat injection rate into the sand tank

Water was circulated into the borehole section at a constant flow rate $\dot{V}$ = 30.1 mL/min. Measurements from all thermocouples, the thermopile and the power supply were recorded every second over the test period of 168h. The average initial temperature of the sand tank was $\bar{T}_g$ = 23.0 °C.

The average net heat injection rate into the sand tank since the start of the test (Equation 6.26) and the calculated heat losses using the calibrated lumped capacitance model (Equations 6.18 and 6.19) are shown in Figure 6-11. The average net heat injection increases rapidly at the start of the test (98 % of the final value is attained after 13 h) and reaches 8.67 W at the end of the test (t = 168 h). The variation of the average net injection rate at the start of the test is due to the rapid variation of the water temperature inside the borehole which could not be perfectly controlled by the electric heater PID controller. There are some small variations in the value of the net injection rate Q_{sand} (not shown on Figure 6-11) and the standard deviation between all the net heat injection rates into the sand tank, calculated every second, is 0.16 W.

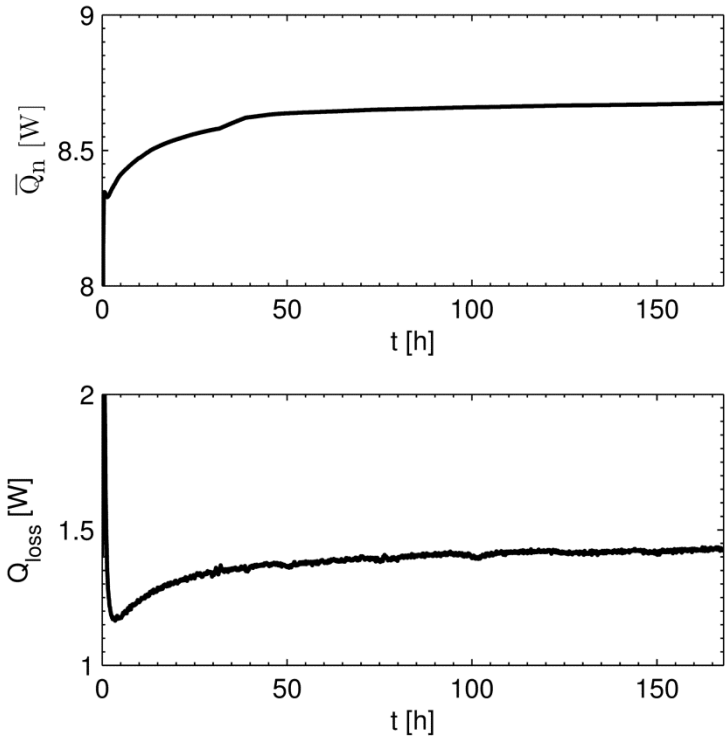

Figure 6-11: Average heat injection rate into the ground (a) and heat losses through the thermopile enclosure (b)

6.5.2 Depth variation of the borehole wall temperature

The variation of the borehole wall temperature along the length of the borehole after 1 h, 6 h, 12 h, 24 h and 168 h of operation is shown on Figure 6-12. The temperatures shown are the average of the temperatures on each side of the borehole. The temperature profiles have similar shapes: the temperature from z = 25 mm to z = 375 mm is almost uniform, with only a 2.0°C maximum difference a t = 168 h. The thermocouples at z = 5 mm and z = 395 mm show that the heat interaction with the sand surface and the sand below the borehole causes the temperature to drop at both ends of the borehole.

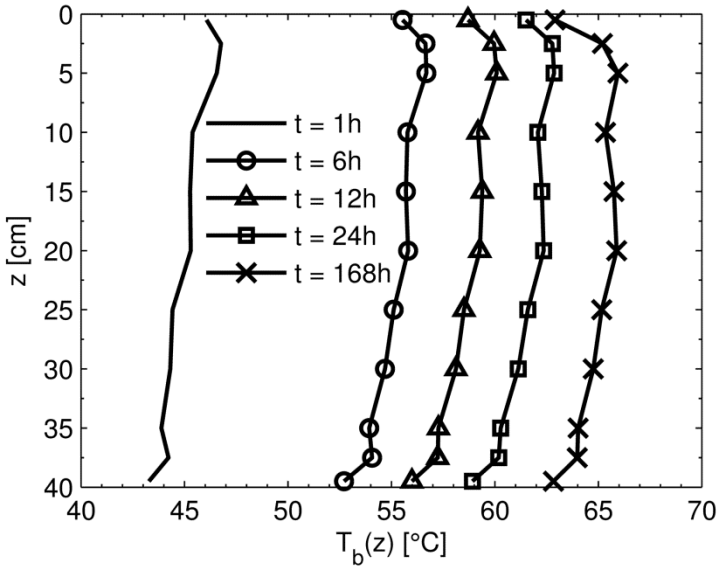

Figure 6-12: Borehole wall temperature profiles during the test

6.5.3 Experimental g-function

The experimental g-function is determined from the five minute average borehole wall temperature and the average net heat injection rate into the sand tank from the active borehole section. Appendix A presents the calculation procedure involved in the determination of the uncertainty on the experimental g-function. The experimental g-function is compared to the theoretical g-function determined analytically on Figure 6-13 as a function of the logarithmic time $\ln(t/t_s)$. Both curves follow the same trend in the first region: the g-function increases linearly on the logarithmic time scale up until a time $t = t_s/10$ = 2.45 h ($\ln(t/t_s) =$ -2.3) where axial heat transfer effects become significant. Then, the rate of increase of the g-function decreases up to the end of the test where it reaches a plateau indicating that steady-state is reached. The agreement between the two curves is very good in the linear portion. Near ($\ln(t/t_s) =$ -2.3), the two curves start to split apart. At t = 168 h ($\ln(t/t_s) = 1.92$), the value of the experimental g-function is 3.19 and the value of the theoretical g-function is 3.04, representing a 4.7% difference. Globally, the theoretical g-function underestimates the experimental g-function for all times greater than 75 minutes ($\ln(t/t_s) =$ -3) but stays within the bounds of uncertainty.

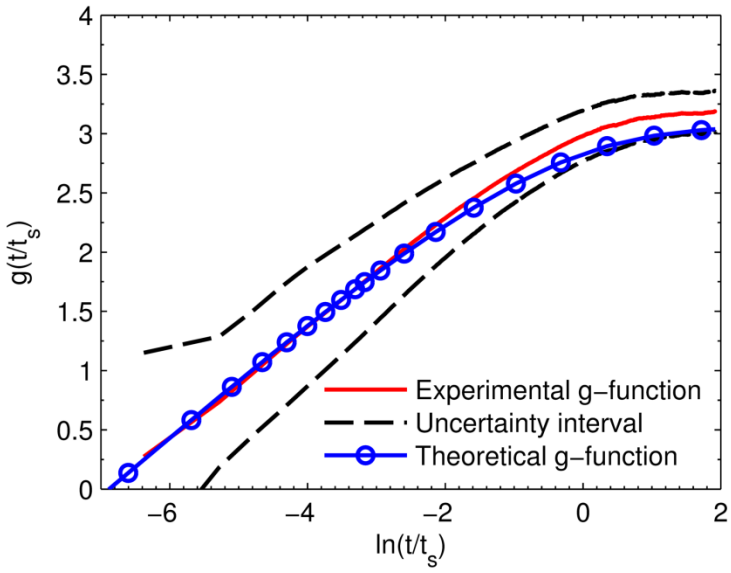

Figure 6-13: Experimentally determined g-function of the small-scale borehole

The differences between the experimental and theoretical g-functions are partly due to the variation of the air temperature above the sand during the test. Figure 6-14 shows the variation of the five minute average air temperature during the test. The air temperature varied between 24°C and 25°C during the test, 1°C to 2°C above the initial sand temperature. The air temperature variations are due to the heat generated by the borehole itself which could not be entirely evacuated from area above the sand surface and the daily variations of the air temperature in the laboratory during the week. The air temperature variations are not represented in the analytical model and the borehole wall temperature can be affected by these variations.

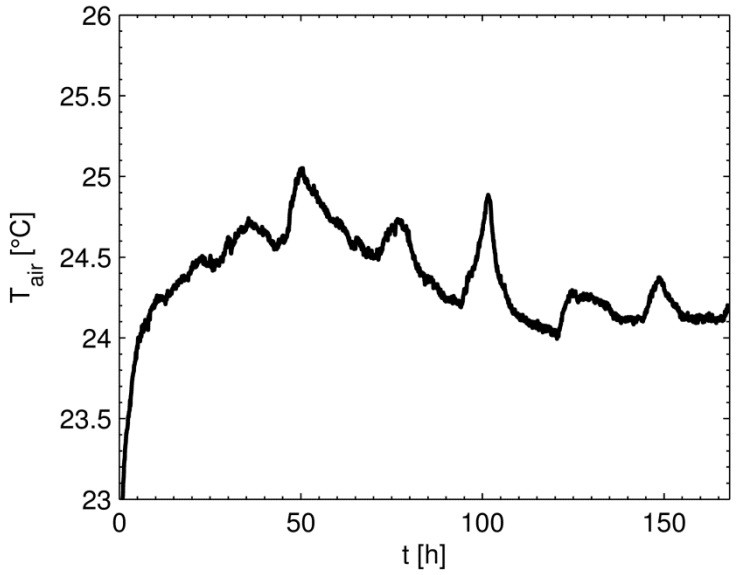

Figure 6-14: Variation of the air temperature above the sand during the test

It is possible to correct the sand temperature for the air temperature variations using a one-dimensional semi-infinite model of the sand tank. The sand temperature at any depth z due to the variation of the sand surface temperature is (Carslaw & Jaeger, 1946a):

$$\mathcal{L}\left(T_g^*(z,t) - \bar{T}_g\right) = \mathcal{L}\left(\bar{T}_{air}(t) - \bar{T}_g\right) \cdot \mathcal{L}\left(f_s(z,t)\right) \tag{6.28}$$

$$f_s(z,t) = \frac{z}{2\sqrt{\pi\alpha_s t^3}} exp\left(-{z^2}/{4\alpha_s t}\right) \tag{6.29}$$

where $T_g^*(z,t)$ is the corrected sand temperature at depth z and $\bar{T}_{air}(t)$ is the five minute average air temperature assumed to be equal to the sand surface temperature.

The average corrected sand temperature over the borehole length is obtained by integration of the solution (Equations 6.28 and 6.29) over the borehole length:

$$\mathcal{L}\left(\bar{T}_g^*(t) - \bar{T}_g\right) = \mathcal{L}\left(\bar{T}_{air}(t) - \bar{T}_g\right) \cdot \mathcal{L}\left(F_s(z,t)\right) \tag{6.30}$$

$$F_s(z,t) = \sqrt{\frac{\alpha_s}{\pi t}}\left[exp\left(\frac{D^2}{4\alpha_s t}\right) - exp\left(\frac{(D+H)^2}{4\alpha_s t}\right)\right] \tag{6.31}$$

where $\bar{T}_g^*$ is the corrected sand temperature at the borehole wall.

Figure 6-15 shows a comparison of the measured 5 minute average borehole wall temperature and the predicted borehole wall temperature using the theoretical g-function. The predicted borehole wall is calculated for the initial sand temperature (Equation 6.25) and for the corrected sand temperature (Equations 6.30 and 6.31). The difference between the measured and predicted borehole wall temperatures reaches 2.18°C after 32 h of operation and decreases to 1.98°C at t = 168 h. Using the corrected ground temperature at the borehole wall, the differences at t = 32 h and t = 168 h are 1.63°C and 1.14°C, respectively. Relative to the temperature rise at the borehole wall, $\bar{T}_{b,n} - \bar{T}_g^*$, the differences are small: 4.1% and 2.8% at t = 32 h and t = 168 h, respectively.

The comparison of the predicted and corrected borehole wall temperatures shows that the effect of the air temperature variations on the measured borehole wall temperatures was non-negligible. In perfect conditions, the air temperature should be kept constant at the initial sand temperature $\bar{T}_g$ = 23.0°C. However, as shown on Figure 6-12, the air temperature was greater than the initial sand temperature during the test and the measured g-function thus gives an over-prediction of the g-function of the borehole.

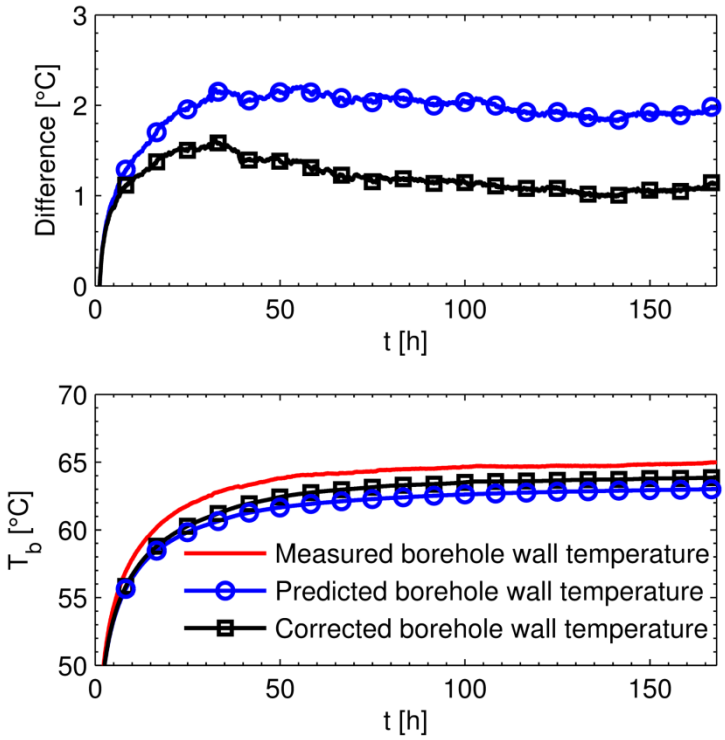

Figure 6-15: Comparison of the measured and predicted borehole wall temperatures

6.6 Conclusion

An analytical model based on the finite line source solution for the calculation of the g-function of a borehole is presented. The borehole is divided into segments and each borehole segment is modelled as a finite line source. The wall temperature of each segment, equal for all segments, is determined from the temporal superposition and spatial superposition in the Laplace domain of the heat extraction rates of all borehole segments. The g-function of the borehole is determined by solving a system of equations for a constant average heat extraction rate per borehole length.

An experimental setup was built to obtain, apparently for the first time, experimental g-functions. The temperature along the wall of a 400 mm long small-scale borehole installed into a sand tank is measured over the course of a 168 h test. The total heat injection rate is obtained from a differential temperature measurement by a 20-junction thermopile and from the flow rate given by a calibrated peristaltic pump. A calibration of the thermopile enclosure allows to quantify the

heat losses through the thermopile enclosure and to evaluate the net heat injection rate into the sand tank. The net heat injection rate into the sand tank is maintained constant throughout the test using a PID controller.

The experimental g-function is calculated from the measured borehole wall temperature and the net heat injection rate into the sand tank. A comparison with the analytical g-function shows that the agreement between the measured and theoretical g-functions is very good up until the non-dimensional time $\ln(t/t_s) = -2.3$ where differences between the two curves become apparent. The analytical model underestimates the experimental g-function by 4.7% at steady-state, after 168 hours. However, the theoretical g-function is within the limits of uncertainty of the experimental g-function throughout the test. The borehole wall temperature predicted by the analytical model is 1.98°C below the measured borehole wall temperature at t = 168 h. Part of this discrepancy is probably due to the fact that the air temperature above the sand was approximately 1 to 2°C above the initial sand temperature during the test. By correcting the sand temperature for the variation of the air temperature during the test, the difference between the predicted and measured borehole wall temperatures is reduced to 1.14°C.

Certain recommendations can be drawn from the results presented in the paper for future experiments on small-scale boreholes. First, ambient temperature should be kept constant during the tests. Our results showed that an increase of the ambient temperature of 1 to 2°C can increase the wall temperature of a 400 mm borehole by close to 1°C. Second, the precision of the experimental g-function could be improved by limiting the uncertainty of the net injection rate into the sand tank. In this study, the uncertainty of the net injection rate into the sand tank was the biggest factor in the uncertainty of the experimental g-function. The uncertainty could be reduced by further limiting the heat losses or by increasing the size of the borehole to increase the net heating rate that can be injected into the sand tank.

6.7 Acknowledgements

This work was partly funded by the NSERC Smart Net-Zero Energy Buildings Strategic Research Network (SNEBRN) and by EDF. The first author received scholarships from the Canadian GeoExchange Coalition and the Natural Sciences and Engineering Research Council of

Canada and a Grant-in-aid award from the American Society of Heating, Refrigerating and Air-Conditioning Engineers (ASHRAE).

6.8 Appendix A: Uncertainty analysis

The standard uncertainty of the experimental g-function is obtained using the propagation of uncertainties technique (Figliola & Beasley, 2011). The propagation of uncertainties is calculated under the assumption of a normal distribution of the measurement errors and for a 95% confidence on the expanded uncertainty. The standard uncertainty of a measured value is thus half of the total uncertainty. The standard uncertainty of the experimental g-function is calculated using the method of partial derivatives for the independent variables in Equation 6.27:

$$u^2(\bar{g}_n) = \left(\frac{2\pi k_s}{\bar{Q}_n} u(\bar{T}_{b,n})\right)^2 + \left(\frac{2\pi k_s}{\bar{Q}_n} u(\bar{T}_g)\right)^2 + \left(\frac{\bar{T}_{b,n} - \bar{T}_g}{\bar{Q}_n^2/2\pi k_s} u(\bar{Q}_n)\right)^2 + \left(\frac{2\pi(\bar{T}_{b,n} - T_g)}{\bar{Q}_n} u(k_s)\right)^2 \quad (6.32)$$

where $u(X)$ is the standard uncertainty of variable X, with $u(k_s) = \pm 0.0026$ W/m-K. The uncertainty over the non-dimensional time $\ln(t/t_s)$ due to the uncertainty over the thermal diffusivity was neglected. For instance, a variation of ± 5% for the thermal diffusivity causes a variation of ± 0.05 for the non-dimensional time.

The standard uncertainty of the borehole wall temperature is the combination of the random standard uncertainty of the thermocouple measurements along the length of the borehole and the calibration standard uncertainty of the thermocouples. The thermocouple measurements are not independent and the random standard uncertainty of the borehole wall temperature must be corrected for correlated uncertainties:

$$
\begin{aligned}
u^2(\bar{T}_{b,n}) = & \sum_{i=1}^{11}\left[\left(\frac{\Delta z_i}{2H}\sigma_n(T_{E,i})\right)^2 + \left(\frac{\Delta z_i}{2H}\sigma_n(T_{W,i})\right)^2\right] \\
& + 2\sum_{i=1}^{11}\sum_{j=1}^{i-1}\left[\frac{\Delta z_i \Delta z_j}{4H^2}\left(\rho_n(T_{E,i},T_{E,j})\sigma_n(T_{E,i})\sigma_n(T_{E,j})\right)\right] \\
& + 2\sum_{i=1}^{11}\sum_{j=1}^{i-1}\left[\frac{\Delta z_i \Delta z_j}{4H^2}\left(\rho_n(T_{E,i},T_{W,j})\sigma_n(T_{E,i})\sigma_n(T_{W,j})\right)\right] \\
& + 2\sum_{i=1}^{11}\sum_{j=1}^{i-1}\left[\frac{\Delta z_i \Delta z_j}{4H^2}\left(\rho_n(T_{W,i},T_{W,j})\sigma_n(T_{W,i})\sigma_n(T_{W,j})\right)\right] \\
& + u_c^2(T)
\end{aligned}
\tag{6.33}
$$

where $\sigma_n(T_{E,i})$ and $\sigma_n(T_{W,i})$ are the standard deviation of the temperature measurements of the i^{th} thermocouples on the downward flow side and the upward flow side used in the calculation of the n^{th} average borehole wall temperature (Equation 6.24), $\rho_n(T_{E,i},T_{E,j})$ is the correlation coefficient between the temperature measurements of the i^{th} and j^{th} thermocouples on the downward flow side used in the calculation of the n^{th} average borehole wall temperature and $u_c(T) = \pm\ 0.12°\text{C}$ is the calibration standard uncertainty of the thermocouples. During the test, the random standard uncertainty was found to be negligible compared to the calibration standard uncertainty of the thermocouples for times $t > 50$ min and the standard uncertainty of the borehole wall temperature is thus equal to the calibration standard uncertainty of the thermocouples. The standard uncertainty of the average initial ground temperature $\bar{T}_g$ is obtained in the same manner from the thermocouple measurements of the first ten seconds of operation.

The standard uncertainty of the average net heat injection rate into the sand tank is the combination of the propagation of uncertainties for the water volumetric flow rate and the temperature difference at the thermopile, the calibration standard uncertainty of the heat losses through the thermopile enclosure and the random standard uncertainty of the average net heat injection rate into the sand tank:

$$u^2(\bar{Q}_n) = \left(\frac{\rho_w c_{p,w} \Delta T}{H} u(\dot{V})\right)^2 + \left(\frac{\dot{V} \rho_w c_{p,w}}{H} u(\Delta T)\right)^2 + \left(\frac{1}{H} u_c(Q_{loss})\right)^2 + \sigma_n(\bar{Q}_n)^2 \quad (6.34)$$

where $u(\dot{V})$ = ± 0.09 mL/min is the standard uncertainty of the volumetric flow rate supplied by the peristaltic pump, $u(\Delta T)$ = ± 0.02°C is the standard uncertainty of the temperature difference measured by the thermopile, $u_c(Q_{loss})$ = ± 0.14 W is the calibration standard uncertainty of the heat losses through the thermopile enclosure and $\sigma_n(\bar{Q}_n)$ is the standard deviation of the net heat injection rates per unit borehole length used in the calculation of the n^{th} average heat injection rate into the sand tank (Equation 6.26).

The expanded uncertainty of the experimental g-function $U(\bar{g}_n)$ is calculated for a 95% confidence level, assuming a normal distribution of the measurement errors:

$$U(\bar{g}_n) = 2 \cdot u(\bar{g}_n) \quad (6.35)$$

The expanded uncertainty of the experimental g-function is maximum at the start of the test, when the net injection rate into the sand tank still varies, and decreases with time as the net injection rate and the borehole wall temperature reach steady-state. Table 6-1 shows the absolute and relative expanded uncertainty after 1, 6, 12, 24 and 168 h. Values of $U(\bar{g}_n)$ are shown on Figure 6-13.

Table 6-1: Absolute and relative expanded uncertainty of the experimental g-function

t [h]	1	6	12	24	168
$\ln(t/t_s)$	-3.2	-1.4	-0.72	-0.02	1.92
$\bar{g}_n$	1.68	2.51	2.77	2.97	3.19
$U(\bar{g}_n)$	0.44	0.29	0.24	0.22	0.17
$U(\bar{g}_n)/\bar{g}_n$ [%]	26.5	11.4	8.9	7.2	5.4

6.9 References

Bauer, D., Heidemann, W., & Diersch, H.-J. (2011). Transient 3D analysis of borehole heat exchanger modeling. Geothermics, 40(4), 250-260.

Bauer, D., Heidemann, W., Müller-Steinhagen, H., & Diersch, H.-J. (2010). Thermal resistance and capacity models for borehole heat exchangers. International Journal of Energy Research, 35(4), 312-320.

Beier, R. A., Smith, M. D., & Spitler, J. D. (2011). Reference data sets for vertical borehole ground heat exchanger models and thermal response test analysis. Geothermics, 40(1), 79-85.

Bernier, M. (2014). Sizing and simulating bore fields using thermal response factors (Keynote presentation). 11th IEA 2014 Heat Pump conference.

Carslaw, H. S., & Jaeger, J. C. (1946a). Chapter 2, Linear flow of heat: the infinite and semi-infinite solid. In O. U. Press (dir.), Conduction of Heat in Solids. (2nde éd., pp. 50-91). Oxford: Oxford University.

Carslaw, H. S., & Jaeger, J. C. (1946b). Chapter 13, The Laplace transformation: Problems on the cylinder and sphere. In O. U. Press (dir.), Conduction of Heat in Solids. (2nde éd., pp. 327-352). Oxford: Oxford University.

Cimmino, M., & Bernier, M. (2013). Preprocessor for the generation of g-functions used in the simulation of geothermal systems. Proceedings of BS2013, Chambéry, France.

Cimmino, M., & Bernier, M. (2014b). A semi-analytical method to generate g-functions for geothermal bore fields. International Journal of Heat and Mass Transfer, 70(c), 641-650.

Cimmino, M., Bernier, M., & Adams, F. (2013). A contribution towards the determination of g-functions using the finite line source. Applied Thermal Engineering, 51(1-2), 401-412.

Claesson, J., & Javed, S. (2011). An analytical method to calculate borehole fluid temperatures for time-scales from minutes to decades. ASHRAE Transactions, 117(2), 279-288.

Costes, V., & Peysson, P. (2008). Capteurs géothermiques verticaux enterrés : Validation expérimentale de nouveaux modèles développés dans l'environnement TRNSYS. Tiré de École Polytechnique de Montréal.

De Carli, M., Tonon, M., Zarrella, A., & Zecchin, R. (2010). A computational capacity resistance model (CaRM) for vertical ground-coupled heat exchangers. Renewable Energy, 35(7), 1537-1550.

Erol, S., & François, B. (2014). Efficiency of various grouting materials for borehole heat exchangers. Applied Thermal Engineering, 70(1), 788-799.

Eskilson, P. (1986). Superposition Borehole Model: Manual for Computer Code. University of Lund, Lund, Sweden.

Eskilson, P. (1987). Thermal Analysis of Heat Extraction Boreholes. Ph.D. Thesis, University of Lund, Lund, Sweden.

Eslami-nejad, P., & Bernier, M. (2012). Freezing of geothermal borehole surroundings: A numerical and experimental assessment with applications. Applied Energy, 98(0), 333-345.

Figliola, R. S., & Beasley, D. E. (2011). Chapter 5, Uncertainty Analysis Theory and Design for Mechanical Measurements. (5the éd., pp. 161-208): Wiley.

Fisher, D. E., Rees, S. J., Padhmanabhan, S. K., & Murugappan, A. (2006). Implementation and validation of ground-source heat pump system models in an integrated building and system simulation environment. HVAC&R Research, 12(3A), 693-710.

Fossa, M. (2011). The temperature penalty approach to the design of borehole heat exchangers for heat pump applications. Energy and Buildings, 43(6), 1473-1479.

Gu, Y., & O'Neal, D. L. (1998). Modelling the effect of backfills on U-tube ground coil performance. ASHRAE Transactions, 104, 356-365.

Hellström, G., & Sanner, B. (1994). Software for dimensioning of deep boreholes for heat extraction. Proceedings of Calorstock 1994, Espoo/Helsinki, Finland.(pp. 195-202).

Ingersoll, L. R., Adler, F. T., Plass, H. J., & Ingersoll, A. C. (1950). Theory of earth heat exchangers for the heat pump. Heating, Piping & Air Conditioning, 22, 113-122.

Ingersoll, L. R., & Plass, H. J. (1948). Theory of the ground pipe heat source for the heat pump. Heating, Piping & Air Conditioning, 20(119), 119-122.

Kramer, C. A., Ghasemi-Fare, O., & Basu, P. (2014). Laboratory thermal performance tests on a model heat exchanger pile in sand. Geotechnical and Geological Engineering, 1-19.

Lamarche, L., & Beauchamp, B. (2007). A new contribution to the finite line-source model for geothermal boreholes. Energy and Buildings, 39(2), 188-198.

Li, M., & Lai, A. C. K. (2013). Analytical model for short-time responses of ground heat exchangers with u-shaped tubes: Model development and validation. Applied Energy, 104(April), 510-516.

Liu, X., & Hellstrom, G. (2006). Enhancements of an integrated simulation tool for ground-source heat pump system design and energy analysis. Proc. 10th International Conference on Thermal Energy Storage, Richard Stockton College of New Jersey.

Marcotte, D., & Pasquier, P. (2008). Fast fluid and ground temperature computation for geothermal ground-loop heat exchanger systems. Geothermics, 37(6), 651-665.

Monzó, P., Mogensen, P., & Acuña, J. (2014). A novel numerical model for the thermal response of borehole heat exchanger fields. 11th IEA Heat Pump Conference 2014, Montréal (Québec), Canada.

Moreno, P., & Ramirez, A. (2008). Implementation of the Numerical Laplace Transform: A review. IEEE Transactions on power delivery, 23(4), 2599-2609.

Pasquier, P., & Marcotte, D. (2012). Short-term simulation of ground heat exchanger with an improved TRCM. Renewable Energy, 46, 92-99.

Pasquier, P., & Marcotte, D. (2014). Joint use of quasi-3D response model and spectral method to simulate borehole heat exchanger. Geothermics, 51, 281-299.

Philippe, M., Bernier, M., & Marchio, D. (2009). Validity ranges of three analytical solutions to heat transfer in the vicinity of single boreholes. Geothermics, 38(4), 407-413.

Salim Shirazi, A., & Bernier, M. (2014). A small-scale experimental apparatus to study heat transfer in the vicinity of geothermal boreholes. HVAC&R Research, 20(7), 819-827.

Spitler, J. D. (2000). A design tool for commercial building loop heat exchangers. Fourth International Heat Pumps in Cold Climates Conference, Aylmer, Québec.

Tarnaski, V. R., Momose, T., & Leong, W. H. (2011). Thermal conductivity of standard sands II. Saturated conditions. International Journal of Thermophysics, 32(5), 984-1005.

Tarnaski, V. R., Momose, T., Leong, W. H., Bovesecchi, G., & Coppa, P. (2009). Thermal conductivity of standard sands. Part I. Dry-state conditions. International Journal of Thermophysics, 30(3), 949-968.

Wedepohl, L. M. (1983). Power system transients: Errors incurred in the numerical inversion of the Laplace transforms. 26th Midwest Symposium on Circuits and Systems, Mexico.(pp. 174-178).

Yavuzturk, C., Chiasson, A. D., & Nydahl, J. E. (2009). Simulation model for ground loop heat exchangers. ASHRAE Transactions, 115(2), 45-59.

Yavuzturk, C., & Spitler, J. D. (1999). A short time step response factor model for vertical ground loop heat exchangers. ASHRAE Transactions, 105(2), 475-485.

Yavuzturk, C., & Spitler, J. D. (2001). Field validation of a short time step model for vertical ground-loop heat exchangers. ASHRAE Transactions, 107(1), 751-759.

Yavuzturk, C., Spitler, J. D., & Rees, S. J. (1999). A transient two-dimensional finite volume model for the simulation of vertical U-tube ground heat exchangers. ASHRAE Transactions, 105(2), 465-474.

Zarrella, A., Scarpa, M., & De Carli, M. (2011). Short time step analysis of vertical ground-coupled heat exchangers: The approach of CaRM. Renewable Energy, 39(9), 2357-2367.

Zeng, H. Y., Diao, N. R., & Fang, Z. H. (2002). A finite line-source model for boreholes in geothermal heat exchangers. Heat Transfer - Asian Research, 31(7), 558-567.

6.10 Nomenclature

SYMBOLS

α_s Thermal diffusivity of the sand or soil [m^2/s]

B Borehole spacing [m]

C_1 Thermal capacity of the inner node of the lumped capacitance model [J/°C]

$c_{p,w}$ Water specific heat [J/kg-K]

D Buried depth of a borehole or borehole segment [m]

g	g-function [-]
H	Length of a borehole or borehole segment [m]
k_s	Thermal conductivity of the sand or soil [W/m-K]
n_q	Number of borehole segments [-]
Q	Heat extraction or injection rate per unit borehole length [W/m]
Q_{loss}	Heat losses from the thermopile enclosure [W]
Q_{sand}	Net heat injection rate into the sand tank [W]
Q_{total}	Total heating power [W]
$\bar{Q}$	Average heat extraction or injection rate per unit borehole length [W/m]
q	Heat extraction rate increment per unit borehole length [W/m]
$\bar{q}$	Average heat extraction rate increment per unit borehole length [W/m]
$\tilde{q}$	Normalized heat extraction rate increment per unit borehole length [W/m]
R_1, R_2	Thermal resistances of the lumped capacitance model [°C/W]
r_b	Borehole radius [m]
ρ_n	Correlation coefficient of measured values
ρ_w	Water density [kg/m^3]
σ	Damping coefficient (Numerical Laplace transform) [s^{-1}]
σ_n	Standard deviation of measured values [-]
T_{air}	Air temperature [°C]
T_b	Borehole wall temperature [°C]
T_E	Temperature measured on the downward flow side [°C]
T_f	Fluid temperature [°C]
T_g	Initial ground temperature [°C]
T_W	Temperature measured on the upward flow side [°C]

ΔT Measured water temperature difference [°C]

ΔT_b Temperature variation at the borehole wall [°C]

t Time [s]

t_s Borehole characteristic time [s]

Δt Measurement period [s]

U Expanded uncertainty

u Standard uncertainty

$\dot{V}$ Water flow rate [mL/min]

SUBSCRIPTS

c Calibration

i,j Thermocouple indexes

in Inlet

k,p Time indexes

n Index of average measurement

out Outlet

u,v Borehole or line segment indexes

CHAPITRE 7 DISCUSSION GÉNÉRALE

Les objectifs principaux de la thèse sont de développer un modèle pour le calcul des facteurs de réponse thermique des champs de puits géothermiques et de déterminer expérimentalement le facteur de réponse thermique d'un puits géothermique.

7.1 Contributions principales de la thèse

La revue de la littérature (Chapitre 1) a identifié les différences entre les modèles analytiques et les modèles numériques (Eskilson, 1987) pour le calcul des facteurs de réponse thermique (g-functions) des champs de puits géothermiques. Le Chapitre 3 offre une première contribution vers le développement d'un modèle analytique pour le calcul des facteurs de réponse thermique. Une méthode est proposée afin d'obtenir les facteurs de réponse thermique en imposant une température moyenne (sur la longueur) à la paroi égale pour tous les puits. La superposition spatiale et la superposition temporelle de la solution de la source ligne finie sont utilisées afin de construire un système d'équation liant les taux d'extraction de chaleur de chacun des puits à la température moyenne à la paroi des puits. La solution du système, construit dans le domaine de Laplace, donne le facteur de réponse thermique du champ de puits. Une méthode est également proposée pour réduire la taille du système d'équations par l'utilisation des symétries.

Le Chapitre 4 complète le modèle du chapitre précédent en présentant un modèle plus général, applicable à des champs de puits de longueurs inégales, pour le calcul des facteurs de réponse thermique. Les puits sont divisés en segments afin de considérer la variation des taux d'extraction de chaleur sur la longueur des puits. Une solution étendue de la source ligne finie permet de calculer la température à la paroi de chacun des segments de puits par l'utilisation de la superposition temporelle et de la superposition spatiale. Similairement au Chapitre 3, un système d'équations est construit dans le domaine de Laplace pour calculer les facteurs de réponse thermique. Les facteurs de réponse thermique sont également comparés à ceux utilisant une condition frontière de taux d'extraction de chaleur uniforme et égale pour tous les puits et à ceux utilisant une condition frontière de taux d'extraction de chaleur uniforme pour chaque puits et de température moyenne égale pour tous les puits (tel que présenté au Chapitre 3). Les facteurs de réponse thermique calculés en utilisant la condition de température uniforme à la paroi des puits et égale pour tous les puits sont en accord avec les g-functions d'Eskilson (1987) tandis que les

deux autres conditions frontières mènent à une surestimation des g-functions d'Eskilson. Des différences sont observées pour les champs de puits à une seule rangée ($1 \times N$ puits). Les erreurs seraient dues à la procédure d'interpolation utilisée lors de la superposition spatiale dans le modèle par différences finies. L'étude de la dépendance des facteurs de réponse par rapport au nombre de segments de puits considéré montre que 12 segments sont suffisants dans la plupart des cas.

Le modèle présenté au Chapitre 4 constitue une importante contribution, car les logiciels de dimensionnement utilisent des facteurs de réponse thermique calculés à partir de la solution de la source linéique finie, qui surestime les g-functions d'Eskilson, ou bien des g-functions tabulées disponibles que pour un nombre restreint de configurations de champs de puits. Le modèle permet de calculer rapidement les facteurs de réponse thermique de n'importe quel champ de puits (environ 7 minutes pour un champ de 10 × 10 puits). Un préprocesseur pour le calcul des facteurs de réponse thermiques a été développé dans Matlab et présenté à la conférence BS2013 (Cimmino & Bernier, 2013). L'interface du préprocesseur est montrée à la Figure 7-1. Le préprocesseur permet de générer et d'exporter les facteurs de réponse thermique de champs de puits ayant des longueurs et des profondeurs de tête de puits inégales et des positions arbitraires.

Le Chapitre 5 présente une application du modèle analytique à la simulation et au dimensionnement de systèmes géothermiques. Des champs de puits sont dimensionnés pour deux scénarios de charges au sol à partir de simulations sur 20 ans d'opération. L'effet du positionnement et du nombre de puits sur la longueur requise des puits est étudié. Pour une surface de terrain donnée, l'analyse montre que la position des puits à l'intérieur du champ a très peu d'impact sur la longueur requise des puits. La longueur totale requise pour les champs de 3 × 7 et 5 × 10 puits étudiés varie de moins de 1% lorsque la position des puits est modifiée. Le retrait des puits a un effet plus important: la longueur totale est réduite d'environ 2% lorsque 3 puits sont retirés du champ de 3 × 7 et 5 puits sont retirés du champ de 5 × 10 puits.

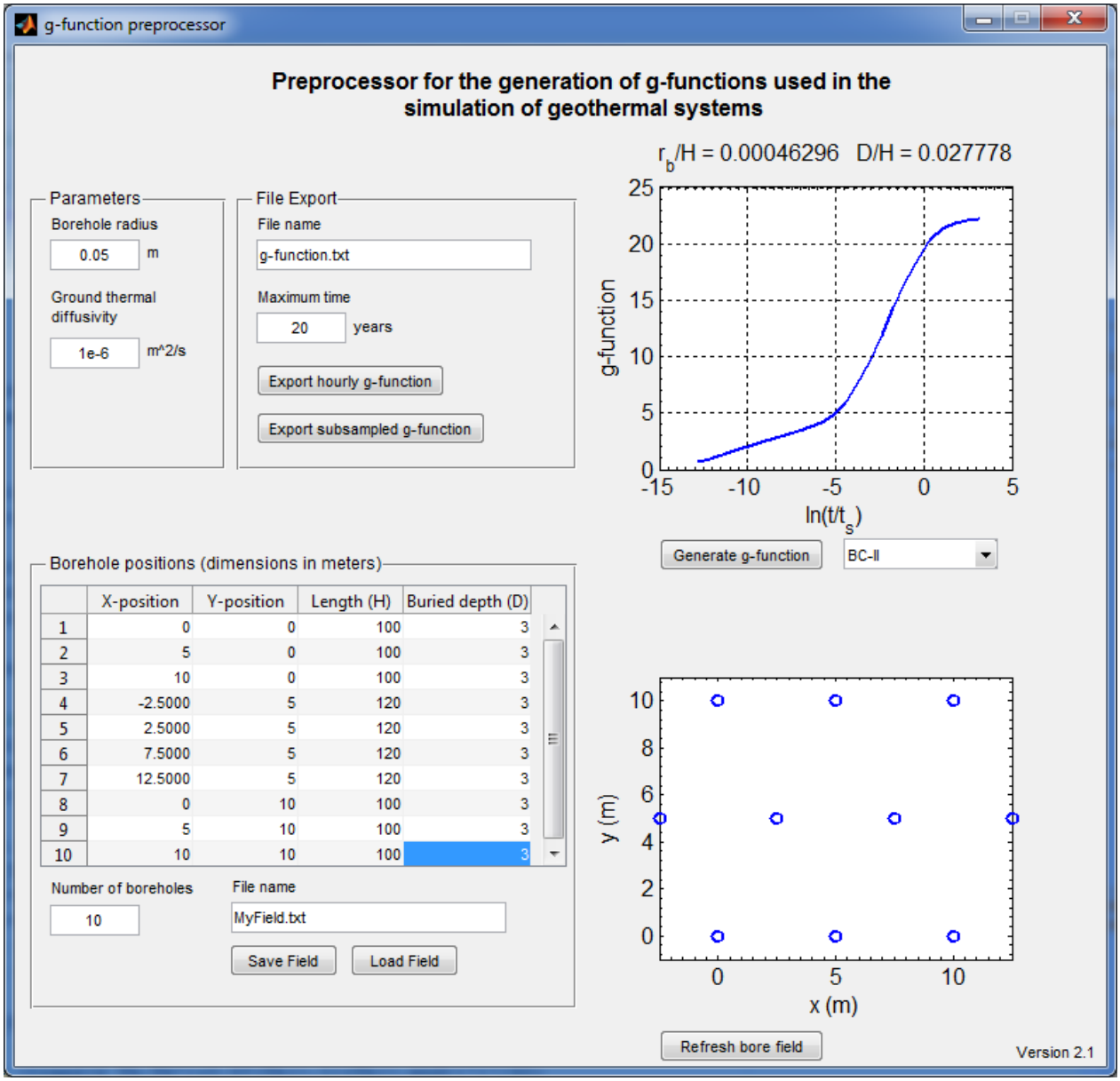

Figure 7-1: Interface du préprocesseur

Le Chapitre 6 aborde le second objectif de la thèse, soit la détermination expérimentale du facteur de réponse thermique d'un puits géothermique. La variation de la température à la paroi d'un puits miniature de 400 mm de longueur installé dans un réservoir de sable est mesurée au cours d'un test d'une semaine. La puissance thermique injectée dans le sable est maintenue constante durant tout le test. Le facteur de réponse thermique du puits est obtenu à partir des mesures de température à la paroi du puits et de la puissance thermique injectée. La différence entre le

facteur de réponse thermique obtenu expérimentalement et celui obtenu à partir du modèle analytique est de 4.7% après une semaine, ce qui représente une différence de 2.0°C entre la température prédite par le modèle analytique et la température mesurée à la paroi du puits. La g-function théorique est à l'intérieure de l'intervalle d'incertitude de la g-function expérimentale pour toute la durée de l'essai. En corrigeant la température du sol pour tenir compte de la variation de la température de l'air ambiant, l'écart entre la température prédite par le modèle analytique et la température mesurée à la paroi du puits est réduit à 1.1°C, soit 2.8% de la variation de température à la paroi du puits. La détermination expérimentale du facteur de réponse thermique d'un puits géothermique est une contribution importante, car elle n'a jamais été tentée auparavant. D'ailleurs, la température à la paroi du puits atteint le régime permanent avant la fin du test, ce qui n'a jamais été mesuré sur un puits géothermique. L'expérience permet alors de confirmer la validité du modèle analytique pour le calcul de la réponse à long terme d'un puits géothermique. Les résultats présentés au Chapitre 6 permettent d'établir des recommandations pour la réduction de l'incertitude expérimentale lors d'essais futurs.

CONCLUSION ET RECOMMANDATIONS

Tel que mentionné au chapitre précédent, le modèle analytique présenté dans la thèse pour le calcul des facteurs de réponse thermique est en mesure de reproduire avec précision les facteurs de réponse thermique autrefois obtenus avec des modèles numériques. Cependant, du travail supplémentaire est requis afin de déterminer la validité de ces facteurs de réponse thermique pour les champs de puits géothermiques.

La condition frontière à la paroi des puits pour le calcul des facteurs de réponse thermique doit être étudiée davantage. En effet, la résistance thermique des puits, de même que le débit circulant dans chacun des puits, peuvent affecter les profils de température et de taux d'extraction de chaleur de chacun des puits du champ et ainsi avoir un impact sur la réponse thermique à long terme. Il sera donc nécessaire de compléter le modèle afin de considérer le transfert de chaleur entre le fluide caloporteur et la paroi des puits.

Des écarts ont été notés entre les facteurs de réponse thermique évalués avec le modèle analytique et les g-functions d'Ekilson pour les champs de puits à une seule rangée. Des améliorations au modèle SBM, ou bien le développement d'un nouveau modèle numérique permettraient de diminuer les écarts et de valider les facteurs de réponse des champs de puits à une seule rangée.

Il serait intéressant d'étendre le modèle analytique afin de modéliser les champs de puits connectés en série. Il serait possible de considérer des puits à un tube en U (Marcotte & Pasquier, 2014) ou bien des puits à deux circuits indépendants (Eslami-Nejad & Bernier, 2011).

Afin de rendre le modèle disponible aux ingénieurs de la pratique, l'implémentation du modèle dans les logiciels de simulation est envisagée. La tâche a déjà débuté pour l'implémentation du modèle dans le logiciel de simulation TRNSYS (Godefroy, 2014) et dans le logiciel de dimensionnement et de simulation de système géothermiques GEOEASE, propriété d’EDF.

Le banc d'essai utilisé pour la détermination expérimentale du facteur de réponse thermique d'un puits géothermique peut également être amélioré. L'importance des pertes de chaleur vis-à-vis l'évaluation de la puissance thermique injectée dans le réservoir de sable pourrait être réduite en augmentant la puissance thermique injectée dans le sable. L'augmentation de la longueur du puits et l'utilisation d'un sable à plus grande conductivité thermique permettraient d'augmenter la

puissance thermique pouvant être injectée dans le réservoir de sable. Finalement, le banc d'essai pourrait être modifié pour la détermination des facteurs de réponse thermique de champs de puits.

BIBLIOGRAPHIE

Abdelaziz, S. L., Ozudogru, T. Y., Olgun, C. G., & Martin Ii, J. R. (2014). Multilayer finite line source model for vertical heat exchangers. *Geothermics, 51*(0), 406-416.

Acuña, J., Fossa, M., Monzó, P., & Palm, B. (2012). *Numerically generated g-functions for ground-coupled heat pump applications*. Proceedings of the 2012 COMSOL conference in Milan, Milan.

Al-Khoury, R. (2010). Spectral framework for geothermal borehole heat exchangers. *International journal of numerical methods for heat & fluid flow, 20*(7), 773-793.

Al-Khoury, R. (2012). A spectral model for shallow geothermal systems. *International journal of numerical methods for heat & fluid flow, 22*(1), 49-72.

ASHRAE. (2011). Chapter 34: Geothermal Energy. In ASHRAE (dir.), *ASHRAE Handbook - HVAC Applications*. (pp. 34.31-34.20). Atlanta: American Society of Heating, Refrigerating and Air-Conditioning Engineers.

Austin, W. A. I., Yavuzturk, C., & Spitler, J. D. (2000). Development of an in-situ system and analysis procedure for measuring ground thermal properties. *ASHRAE Transactions, 106*, 365-379.

Bandos, T. V., Montero, Á., Fernández de Córdoba, P. J., & Urchueguía, J. F. (2011). Improving parameter estimates obtained from thermal response tests: Effect of ambient air temperature variations. *Geothermics, 40*(2), 136-143.

Bandos, T. V., Montero, Á., Fernández, E., Santander, J. L. G., Isidro, J. M., Pérez, J. (2009). Finite line-source model for borehole heat exchangers: effect of vertical temperature variations. *Geothermics, 38*(2), 263-270.

Bandyopadhyay, G., Gosnold, W., & Mann, M. (2008). Analytical and semi-analytical solutions for short-time transient response of ground heat exchangers. *Energy and Buildings, 40*(10), 1816-1824.

Bandyopadhyay, G., Kulkarni, M., & Mann, M. (2008). A New Approach to Modeling Ground Heat Exchangers in the Initial Phase of Heat-Flux Build Up. *ASHRAE Transactions, 114*(2), 428-439.

Baudoin, A. (1988). *Stockage intersaisonnier de chaleur dans le sol par batterie d'échangeurs baionnette verticaux; modèle de prédimensionnement.* Ph.D. Thesis, Université de Reims Champagne-Ardenne, France.

Bauer, D., Heidemann, W., & Diersch, H.-J. (2011). Transient 3D analysis of borehole heat exchanger modeling. *Geothermics, 40*(4), 250-260.

Bauer, D., Heidemann, W., Müller-Steinhagen, H., & Diersch, H.-J. (2010). Thermal resistance and capacity models for borehole heat exchangers. *International Journal of Energy Research, 35*(4), 312-320.

Beck, M., Bayer, P., de Paly, M., Hechy-Méndez, J., & Zell, A. (2013). Geometric arrangement and operation mode adjustment in low-enthalpy geothermal borehole fields for heating. *Energy, 49*(1), 434-443.

Beier, R. A., & Smith, M. D. (2003). Minimum duration of in-situ tests on vertical boreholes. *ASHRAE Transactions, 109*(2), 475-486.

Beier, R. A., Smith, M. D., & Spitler, J. D. (2011). Reference data sets for vertical borehole ground heat exchanger models and thermal response test analysis. *Geothermics, 40*(1), 79-85.

Bennet, J., Claesson, J., & Hellstrom, G. (1987). *Multipole method to compute the conductive heat flows to and between pipes in a composite cylinder*. Tiré de Lund Institue of Technology.

Bernier, M. (2000). *A Review of the Cylindrical Heat Source Method for the Design and Analysis of Vertical Ground-Coupled Heat Pump Systems*. 4th International Conference on Heat Pumps in Cold Climates.

Bernier, M. (2001). Ground-coupled Heat pump system simulation. *ASHRAE Transactions, 107*(1), 605-616.

Bernier, M. (2014). *Sizing and simulating bore fields using thermal response factors (Keynote presentation)*. 11th IEA 2014 Heat Pump conference.

Bernier, M., Pinel, P., Labib, R., & Paillot, R. (2004). A multiple load aggregation algorithm for annual hourly simulations of GCHP systems. *HVAC&R Research, 10*(4), 471-487.

Bernier, M., & Salim Shirazi, A. (2007). *Solar Heat Injection into Boreholes : a Preliminary Analysis*. 2nd Canadian Solar Buildings Conference, Calgary.

Blomberg, T., Claesson, J., Eskilson, P., Hellström, G., & Sanner, B. (2008). EED 3.0 - Earth Energy Designer. Tiré de http://www.buildingphysics.com/manuals/EED3.pdf

Carslaw, H. S., & Jaeger, J. C. (1946a). Chapter 2, Linear flow of heat: the infinite and semi-infinite solid. In O. U. Press (dir.), *Conduction of Heat in Solids*. (2nd^{e} éd., pp. 50-91). Oxford: Oxford University.

Carslaw, H. S., & Jaeger, J. C. (1946b). Chapter 13, The Laplace transformation: Problems on the cylinder and sphere. In O. U. Press (dir.), *Conduction of Heat in Solids*. (2nd^{e} éd., pp. 327-352). Oxford: Oxford University.

Carslaw, H. S., & Jaeger, J. C. (1946c). The Laplace transformation: Problems in linear flow. In O. U. Press (dir.), *Conduction of Heat in Solids*. (2^{e} éd., pp. 297-326). Oxford: Oxford University.

Chapuis, S. (2009). *Stockage thermique saisonnier dans un champ de puits géothermiques verticaux en boucle fermée*. Master's Thesis, École Polytechnique de Montréal, Montréal.

Chapuis, S., & Bernier, M. (2009). *Seasonal storage of solar energy in borehole heat exchangers*. 11th International IBPSA conference, Glasgow.

Cimmino, M., & Bernier, M. (2013). *Preprocessor for the generation of g-functions used in the simulation of geothermal systems*. Proceedings of BS2013, Chambéry, France.

Cimmino, M., & Bernier, M. (2014a). Effects of unequal borehole spacing on the required borehole length. *ASHRAE Transactions, 120*(2), SE-14-013.

Cimmino, M., & Bernier, M. (2014b). A semi-analytical method to generate g-functions for geothermal bore fields. *International Journal of Heat and Mass Transfer, 70*(c), 641-650.

Cimmino, M., Bernier, M., & Adams, F. (2013). A contribution towards the determination of g-functions using the finite line source. *Applied Thermal Engineering, 51*(1-2), 401-412.

Cimmino, M., Bernier, M., & Cauret, O. (2013). Validation d'un modèle pour la simulation de capteurs géothermiques compacts. *XIe Colloque Interuniversitaire Franco-Québecois sur la Thermique des Systèmes, Reims, France*.(pp. 277-282).

Cimmino, M., Bernier, M., & Pasquier, P. (2012). Utilisation des g-functions de Eskilson pour la simulation de systèmes géothermiques. *Proceedings of eSim 2012, Halifax NS.*(pp. 282-295).

Claesson, J., & Bennet, J. (1987). *Multipole method to compute the conductive heat flows to and between pipes in a cylinder*. Tiré de Lund Institute of Technology.

Claesson, J., & Hellström, G. (2011). Multipole method to calculate borehole thermal resistances in a borehole heat exchanger. *HVAC&R Research, 17*(6), 895-911.

Claesson, J., & Javed, S. (2011). An analytical method to calculate borehole fluid temperatures for time-scales from minutes to decades. *ASHRAE Transactions, 117*(2), 279-288.

Claesson, J., & Javed, S. (2012). A load-aggregation method to calculate extraction temperatures of borehole heat exchangers. *ASHRAE Transactions, 118*(1), 530-539.

Cooper, L. Y. (1976). Heating of a cylindrical cavity. *International Journal of Heat and Mass Transfer, 19*, 575-577.

Costes, V., & Peysson, P. (2008). *Capteurs géothermiques verticaux enterrés : Validation expérimentale de nouveaux modèles développés dans l'environnement TRNSYS*. Tiré de École Polytechnique de Montréal.

Cui, P., Li, X., Man, Y., & Fang, Z. (2011). Heat transfer analysis of pile geothermal heat exchangers with spiral coils. *Applied Energy, 88*(11), 4113-4119.

Cui, P., Yang, H., & Fang, Z. (2006). Heat transfer analysis of ground heat exchangers with inclined boreholes. *Applied Thermal Engineering, 26*(11-12), 1169-1175.

De Carli, M., Tonon, M., Zarrella, A., & Zecchin, R. (2010). A computational capacity resistance model (CaRM) for vertical ground-coupled heat exchangers. *Renewable Energy, 35*(7), 1537-1550.

Diao, N. R., Zeng, H. Y., & Fang, Z. H. (2004). Improvement in modeling of heat transfer in vertical ground heat exchangers. *HVAC&R Research, 10*(4), 459-470.

Duan, X., & Naterer, G. F. (2008a). Ground heat transfer from a varying line source with seasonal temperature fluctuations. *Journal of Heat Transfer, 130*(11), 1-10.

Duan, X., & Naterer, G. F. (2008b). Ground thermal response to heat conduction in a power transmission tower foundation. *Heat and Mass Transfer, 44*(5), 547-558.

Duan, X., Naterer, G. F., Lu, M., & Mueller, W. (2007). Transient heat conduction from a vertical rod buried in a semi-infinite medium with variable heating strength. *Heat and Mass Transfer, 43*(6), 547-557.

Erol, S., & François, B. (2014). Efficiency of various grouting materials for borehole heat exchangers. *Applied Thermal Engineering, 70*(1), 788-799.

Eskilson, P. (1986). *Superposition Borehole Model: Manual for Computer Code.* University of Lund, Lund, Sweden.

Eskilson, P. (1987). *Thermal Analysis of Heat Extraction Boreholes.* Ph.D. Thesis, University of Lund, Lund, Sweden.

Eskilson, P., & Claesson, J. (1988). Simulation model for thermally interacting heat extraction boreholes. *Numerical heat transfer, 13*(2), 149-165.

Eslami-Nejad, P., & Bernier, M. (2011). Coupling of geothermal heat pumps with thermal solar collectore using double U-tube boreholes with two independent circuits. *Applied Thermal Engineering, 31*(14-5), 3066-3077.

Eslami-nejad, P., & Bernier, M. (2012). Freezing of geothermal borehole surroundings: A numerical and experimental assessment with applications. *Applied Energy, 98*(0), 333-345.

Figliola, R. S., & Beasley, D. E. (2011). Chapter 5, Uncertainty Analysis *Theory and Design for Mechanical Measurements*. (5th^{e} éd., pp. 161-208): Wiley.

Fisher, D. E., Rees, S. J., Padhmanabhan, S. K., & Murugappan, A. (2006). Implementation and validation of ground-source heat pump system models in an integrated building and system simulation environment. *HVAC&R Research, 12*(3A), 693-710.

Fossa, M. (2011). The temperature penalty approach to the design of borehole heat exchangers for heat pump applications. *Energy and Buildings, 43*(6), 1473-1479.

Fossa, M., Cauret, O., & Bernier, M. (2009). Comparing the thermal performance of ground heat exchangers of various lengths. *Proceedings of Effstock 2009, Stockholm, Sweden*.(pp. 8).

Gehlin, S. E. A., & Hellström, G. (2003). Comparison of four models for thermal response test evaluation. *ASHRAE Transactions, 109*, 131-142.

Gehlin, S. E. A., & Nordell, B. (2003). Determining undisturbed ground temperature for thermal response test. *ASHRAE Transactions, 109*, 151-156.

Godefroy, V. (2014). *Élaboration et validation d'une suite évolutive de modèles d'échangeurs géothermiques verticaux.* (Mémoire de maîtrise), Polytechnique Montréal, Montréal.

Gu, Y., & O'Neal, D. L. (1998). Modelling the effect of backfills on U-tube ground coil performance. *ASHRAE Transactions, 104*, 356-365.

Hellstrom, G. (1989). *Duct ground heat storage model: Manual for computer code*. Tiré de University of Lund, Department of Mathematical Physics.

Hellstrom, G. (1991). *Ground heat storage: Thermal analysis of duct storage systems.* PhD, University of Lund, Lund, Sweden.

Hellström, G., & Sanner, B. (1994). Software for dimensioning of deep boreholes for heat extraction. *Proceedings of Calorstock 1994, Espoo/Helsinki, Finland*.(pp. 195-202).

Huber, A. (2011). *Program EWS: Calculation of Borehole Heat Exchangers.* Zürich, Swiss.

Ingersoll, L. R., Adler, F. T., Plass, H. J., & Ingersoll, A. C. (1950). Theory of earth heat exchangers for the heat pump. *Heating, Piping & Air Conditioning, 22*, 113-122.

Ingersoll, L. R., & Plass, H. J. (1948). Theory of the ground pipe heat source for the heat pump. *Heating, Piping & Air Conditioning, 20*(119), 119-122.

Ingersoll, L. R., Zobel, O. J., & Ingersoll, A. C. (1954). Theory of earth heat exchanger for the heat pump *Heat Conduction: With Engineering, Geological and Other Applications*. (2nd^{e} éd., pp. 240-271): McGraw-Hill.

Jaeger, J. C. (1944). XVIII. Some problems involving line sources in conduction of heat. *The London, Edinburgh and Dublin philosophical magazine and journal of science, 35*(242), 169-179.

Javed, S., & Claesson, J. (2011). New analytical and numerical solutions for the short-term analysis of vertical ground heat exchangers. *ASHRAE Transactions, 117*(1), 3-12.

Javed, S., Claesson, J., & Fahlén, P. (2010). Analytical modelling of short-term response of ground heat exchangers in ground source heat pump systems. *Proceedings of the 10th REHVA world congress; Clima 2010, Antalya Turkey*. Clima 2010.

Javed, S., Fahlén, P., & Claesson, J. (2009). Vertical ground heat exchangers: A review of heat flow models. *Proceedings of the 11th international conference on thermal energy storage; Effstock 2009, Stockholm Sweden*. Effstock 2009.

Kim, E.-J., Roux, J.-J., Bernier, M. A., & Cauret, O. (2011). Three-dimensional numerical modeling of vertical ground heat exchangers: Domain decomposition and state model reduction. *HVAC&R Research, 17*(6), 912-927.

Kim, E.-J., Roux, J.-J., Rusaouen, G., & Kuznik, F. (2010). Numerical modelling of geothermal vertical heat exchangers for the short time analysis using the state model size reduction technique. *Applied Thermal Engineering, 30*(6-7), 706-714.

Kramer, C. A., Ghasemi-Fare, O., & Basu, P. (2014). Laboratory thermal performance tests on a model heat exchanger pile in sand. *Geotechnical and Geological Engineering*, 1-19.

Kurevija, T., Vulin, D., & Krapec, V. (2012). Effect of borehole array geometry and thermal interferences on geothermal heat pump system. *Energy Conversion and Management, 60*, 134-142.

Lamarche, L. (2009). A fast algorithm for the hourly simulations of ground-source heat pumps using arbitrary response factors. *Renewable Energy, 34*(10), 2252-2258.

Lamarche, L. (2011). Analytical g-function for inclined boreholes in ground-source heat pump systems. *Geothermics, 40*(4), 241-249.

Lamarche, L., & Beauchamp, B. (2007a). A fast algorithm for the simulation of GCHP systems. *ASHRAE Transactions, 113*, 470-476.

Lamarche, L., & Beauchamp, B. (2007b). A new contribution to the finite line-source model for geothermal boreholes. *Energy and Buildings, 39*(2), 188-198.

Lamarche, L., & Beauchamp, B. (2007c). New solutions for the short-time analysis of geothermal vertical boreholes. *International Journal of Heat and Mass Transfer, 50*(7-8), 1408-1419.

Lamarche, L., Kajl, S., & Beauchamp, B. (2010). A review of methods to evaluate borehole thermal resistances in geothermal heat-pump systems. *Geothermics, 39*(2), 187-200.

Li, M., & Lai, A. C. K. (2012a). Heat-source solutions to heat conduction in anisotropic media with application to pile and borehole ground heat exchangers. *Applied Energy, 96*, 451-458.

Li, M., & Lai, A. C. K. (2012b). New temperature response functions (G functions) for pile and borehole ground heat exchangers based on composite-medium line-source theory. *Energy, 38*(1), 255-263.

Li, M., & Lai, A. C. K. (2013). Analytical model for short-time responses of ground heat exchangers with u-shaped tubes: Model development and validation. *Applied Energy, 104*(April), 510-516.

Li, M., Li, P., Chan, V., & Lai, A. C. (2014). Full-scale temperature response function (G-function) for heat transfer by borehole ground heat exchangers (GHEs) from sub-hour to decades. *Applied Energy, 136*, 197-205.

Li, Z. (2012). A new constant heat flux model for vertical U-tube ground heat exchangers. *Energy and Buildings, 45*, 311-316.

Li, Z., & Zheng, M. (2009). Development of a numerical model for the simulation of vertical U-tube ground heat exchangers. *Applied Thermal Engineering, 29*(5-6), 920-924.

Liu, X. (2005). *Development and experimental validation of simulation of hydronic snow melting systems for bridges.* Ph.D. Thesis, Oklahoma State University, Stillwater, OK.

Liu, X., & Hellstrom, G. (2006). Enhancements of an integrated simulation tool for ground-source heat pump system design and energy analysis. *Proc. 10th International Conference on Thermal Energy Storage, Richard Stockton College of New Jersey*.

Loveridge, F., & Powrie, W. (2013). Temperature response functions (G-functions) for single pile heat exchangers. *Energy, 57*(0), 554-564.

Loveridge, F., & Powrie, W. (2014). G-Functions for multiple interacting pile heat exchangers. *Energy, 64*(0), 747-757.

Malayappan, V., & Spitler, J. D. (2013). *Limitations of using uniform heat flux assumptions in sizing vertical borehole heat exchanger fields*. Proceedings of Clima 2013, Prague, Czech Republic.

Man, Y., Yang, H., Diao, N., Liu, J., & Fang, Z. (2010). A new model and analytical solutions for borehole and pile ground heat exchangers. *International Journal of Heat and Mass Transfer, 53*(13-14), 2593-2601.

Man, Y., Yang, H., Spitler, J. D., & Fang, Z. (2011). Feasibility study on novel hybrid ground coupled heat pump system with nocturnal cooling radiator for cooling load dominated buildings. *Applied Energy, 88*(11), 4160-4171.

Marcotte, D., & Pasquier, P. (2008a). Fast fluid and ground temperature computation for geothermal ground-loop heat exchanger systems. *Geothermics, 37*(6), 651-665.

Marcotte, D., & Pasquier, P. (2008b). On the estimation of thermal resistance in borehole thermal conductivity test. *Renewable Energy, 33*(11), 2407-2415.

Marcotte, D., & Pasquier, P. (2009). The effect of borehole inclination on fluid and ground temperature for GLHE systems. *Geothermics, 38*(4), 392-398.

Marcotte, D., & Pasquier, P. (2014). Unit-response function for ground heat exchanger with parallel, series or mixed borehole arrangement. *Renewable Energy, 68*, 14-24.

Marcotte, D., Pasquier, P., Sherrif, F., & Bernier, M. A. (2010). The importance of axial effects for borehole design of geothermal heat-pump systems. *Renewable Energy, 35*(4), 763-770.

Monzó, P., Acuña, J., Fossa, M., & Palm, B. (2013). *Numerical generation of the temperature response factors for a borehole heat exchangers field*. European Geothermal Congress 2013, Pisa, Italy.

Monzó, P., Mogensen, P., & Acuña, J. (2014). *A novel numerical model for the thermal response of borehole heat exchanger fields*. 11th IEA Heat Pump Conference 2014, Montréal (Québec), Canada.

Moreno, P., & Ramirez, A. (2008). Implementation of the Numerical Laplace Transform: A review. *IEEE Transactions on power delivery, 23*(4), 2599-2609.

Nouanegue, H.-F., Shirazi, A. S., & Bernier, M. (2009). *Extracted heat from geothermal boreholes: where does the energy come from?* 4th Canadian Solar Buildings Conference, Toronto, Ontario.

Pasquier, P., & Marcotte, D. (2012). Short-term simulation of ground heat exchanger with an improved TRCM. *Renewable Energy, 46*, 92-99.

Pasquier, P., & Marcotte, D. (2013). Efficient computation of heat flux signals to ensure the reproduction of prescribed temperatures at several interacting heat sources. *Applied Thermal Engineering, 59*(1), 515-526.

Pasquier, P., & Marcotte, D. (2014). Joint use of quasi-3D response model and spectral method to simulate borehole heat exchanger. *Geothermics, 51*, 281-299.

Philippe, M., Bernier, M., & Marchio, D. (2009). Validity ranges of three analytical solutions to heat transfer in the vicinity of single boreholes. *Geothermics, 38*(4), 407-413.

Robert, F., & Gosselin, L. (2014). New methodology to design ground coupled heat pump systems based on total cost minimization. *Applied Thermal Engineering, 62*(2), 481-491.

Salim Shirazi, A., & Bernier, M. (2013). Thermal capacity effects in borehole ground heat exchangers. *Energy and Buildings, 67*(0), 352-364.

Salim Shirazi, A., & Bernier, M. (2014). A small-scale experimental apparatus to study heat transfer in the vicinity of geothermal boreholes. *HVAC&R Research, 20*(7), 819-827.

Sherrif, F. (2007). *Génération de facteurs de réponse pour champs de puits géothermiques verticaux.* MA Sc, École Polytechnique de Montréal, Montreal.

Shonder, J. A., & Beck, J. V. (1999). Determining effective soil formation thermal properties from field data using parameter estimation technique. *ASHRAE Transactions, 105*, 458-466.

Spitler, J. D. (2000). *A design tool for commercial building loop heat exchangers*. Fourth International Heat Pumps in Cold Climates Conference, Aylmer, Québec.

Stehfest, H. (1970). Algorithm 368, Numerical inversion of the Laplace transforms [D5]. *Communications of the ACM, 13*(1), 47-49.

Tarnaski, V. R., Momose, T., & Leong, W. H. (2011). Thermal conductivity of standard sands II. Saturated conditions. *International Journal of Thermophysics, 32*(5), 984-1005.

Tarnaski, V. R., Momose, T., Leong, W. H., Bovesecchi, G., & Coppa, P. (2009). Thermal conductivity of standard sands. Part I. Dry-state conditions. *International Journal of Thermophysics, 30*(3), 949-968.

Wedepohl, L. M. (1983). Power system transients: Errors incurred in the numerical inversion of the Laplace transforms. *26th Midwest Symposium on Circuits and Systems, Mexico*.(pp. 174-178).

Yang, H., Cui, P., & Fang, Z. (2010). Vertical-borehole ground-coupled heat pumps: A review of models and systems. *Applied Energy, 87*(1), 16-27.

Yang, Y., & Li, M. (2014). Short-time performance of composite-medium line-source model for predicting responses of ground heat exchangers with single U-shaped tube. *International Journal of Thermal Sciences, 82*, 130-137.

Yavuzturk, C., Chiasson, A. D., & Nydahl, J. E. (2009). Simulation model for ground loop heat exchangers. *ASHRAE Transactions, 115*(2), 45-59.

Yavuzturk, C., & Spitler, J. D. (1999). A short time step response factor model for vertical ground loop heat exchangers. *ASHRAE Transactions, 105*(2), 475-485.

Yavuzturk, C., & Spitler, J. D. (2001). Field validation of a short time step model for vertical ground-loop heat exchangers. *ASHRAE Transactions, 107*(1), 751-759.

Yavuzturk, C., Spitler, J. D., & Rees, S. J. (1999). A transient two-dimensional finite volume model for the simulation of vertical U-tube ground heat exchangers. *ASHRAE Transactions, 105*(2), 465-474.

Zanchini, E., & Lazzari, S. (2013). Temperature distribution in a field of long Borehole Heat Exchangers (BHEs) subjected to a monthly averaged heat flux. *Energy, 59*(0), 570-580.

Zanchini, E., & Lazzari, S. (2014). New g-functions for the hourly simulation of double U-tube borehole heat exchanger fields. *Energy, 70*(0), 444-455.

Zarrella, A., Scarpa, M., & De Carli, M. (2011). Short time step analysis of vertical ground-coupled heat exchangers: The approach of CaRM. *Renewable Energy, 39*(9), 2357-2367.

Zeng, H. Y., Diao, N. R., & Fang, Z. (2003). Heat transfer analysis of boreholes in vertical ground heat exchangers. *International Journal of Heat and Mass Transfer, 46*(23), 4467-4481.

Zeng, H. Y., Diao, N. R., & Fang, Z. H. (2002). A finite line-source model for boreholes in geothermal heat exchangers. *Heat Transfer - Asian Research, 31*(7), 558-567.

ANNEXE A - CORRECTIONS AUX TABLEAUX DE LA SECTION 3.9

Les tableaux 3-1 à 3-6 présentés à la section 3.9 comportent des erreurs dues à un calcul erroné des transformées de Laplace numériques[2]. La transformée de Laplace est définie pour $t \geq 0$ (Équations 3.29 et 3.31). Or le taux d'extraction de chaleur total et les facteurs de réponse puits-à-puits et groupe-à-puits sont donnés pour $t \geq t_1 = \Delta t$. L'utilisation de la transformée de Laplace numérique requiert alors un changement de variable $t_k^* = t_k - \Delta t$ avant le calcul du coefficient d'amortissement σ et des fonctions $exp(\text{-}\sigma t)$ et $exp(\sigma t)$.

Le coefficient d'amortissement corrigé devient:

$$\sigma = 2 \cdot \frac{\ln(N)}{t_{max}}$$
$$\sigma = 2 \cdot \frac{\ln(6)}{(15\,768\,000\text{s} - 2\,628\,000\text{s})} = 2.73 \times 10^{-7}\ \text{s}^{-1} \tag{8.1}$$

Les nouveaux résultats suite à l'utilisation du coefficient d'amortissement corrigé sont presentés aux tableaux A-1 à A-6.

Le système d'équations matriciel dans le domaine de Laplace pour l'obtention des taux d'extraction de chaleur pour le premier pas de temps fréquentiel est alors:

$$\begin{bmatrix} 0 \\ 0 \\ \mathcal{L}(q_t')_1 \end{bmatrix} = \begin{bmatrix} \mathcal{L}(G_{11})_1 & \mathcal{L}(G_{12})_1 & \text{-}1 \\ \mathcal{L}(G_{21})_1 & \mathcal{L}(G_{22})_1 & \text{-}1 \\ n_1 & n_2 & 0 \end{bmatrix} \begin{bmatrix} \mathcal{L}(q_1')_1 \\ \mathcal{L}(q_2')_1 \\ \mathcal{L}(\Theta_b)_1 \end{bmatrix}$$
$$\begin{bmatrix} 0 \\ 0 \\ 6.00 \end{bmatrix} = \begin{bmatrix} 2.46 & \text{-}0.00953 & \text{-}1 \\ \text{-}0.0191 & 2.46 & \text{-}1 \\ n_1 & n_2 & 0 \end{bmatrix} \begin{bmatrix} \mathcal{L}(q_1')_1 \\ \mathcal{L}(q_2')_1 \\ \mathcal{L}(\Theta_b)_1 \end{bmatrix} \tag{8.2}$$

[2] Merci au professeur Louis Lamarche (École de technologie supérieure, Montréal) pour avoir repéré ces erreurs.

Table A-1: Facteurs de réponse puits-à-puits pour un champ de 3 × 2 puits

function	time [yr/12]					
	1	2	3	4	5	6
g_0'	3.87	4.20	4.40	4.54	4.65	4.73
g_1'	1.44E-02	7.89-02	1.53E-01	2.23E-01	2.86E-01	3.43E-01
g_2'	3.48E-06	7.46E-04	5.10E-03	1.42E-02	2.70E-02	4.24E-02
g_3'	7.52E-04	1.43E-02	4.29E-02	7.81E-02	1.15E-01	1.52E-01
g_4'	2.62E-07	1.87E-04	1.92E-03	6.53E-03	1.41E-02	2.41E-02

Table A-2: Facteurs de réponse groupe-à-puits et incrément de taux d'extraction de chaleur total pour un champ de 3 × 2 puits

function	time [yr/12]					
	1	2	3	4	5	6
G_{11}	3.88	4.28	4.56	4.78	4.97	5.14
G_{12}	1.52E-02	9.32E-02	1.96E-01	3.01E-01	4.01E-01	4.94E-01
G_{21}	3.03E-02	1.86E-01	3.93E-01	6.03E-01	8.03E-01	9.88E-01
G_{22}	3.88	4.28	4.55	4.76	4.93	5.08
q_t'	6	0	0	0	0	0
$\exp(-\sigma(t-\Delta t))$	1.00	0.49	0.24	0.12	0.06	0.03

Table A-3: Transformée de Laplace numérique des facteurs de réponse groupe-à-puits de l'incrément de taux d'extraction de chaleur total

function	Angular frequency ω [rad/yr]					
	−37.7	−25.1	−12.6	0.0	12.6	25.1
$\mathcal{L}(G_{11})$	2.46	2.63+0.991j	3.76+2.39j	8.04	3.76-2.39j	2.63-0.991j
$\mathcal{L}(G_{12})$	-0.00953	-0.017 +0.0067j	-0.025 +0.048j	0.179	-0.025 -0.048j	-0.014 -0.0067j
$\mathcal{L}(G_{21})$	-0.0191	-0.028 +0.0013j	-0.050 +0.097j	0.358	-0.050 -0.097j	-0.028 -0.0013j
$\mathcal{L}(G_{22})$	2.46	2.63+0.991j	3.76+2.39j	8.03	3.76-2.39j	2.63-0.992j
$\mathcal{L}(q_t')$	6.00	6.00	6.00	6.00	6.00	6.00

Table A-4: Transformée de Laplace numérique des increments de taux d'extraction de chaleur et de la temperature moyenne adimensionnelle à la paroi des puits

function	Angular frequency ω [rad/yr]					
	−37.7	−25.1	−12.6	0.0	12.6	25.1
$\mathcal{L}(\mathrm{q}_1')$	0.999	0.999 + 0.0014j	1.001 + 0.0041j	1.01	1.001 - 0.0041j	0.999 - 0.0014j
$\mathcal{L}(\mathrm{q}_2')$	1.002	1.002 - 0.0027j	0.999 - 0.0081j	0.99	0.999 + 0.0081j	1.002 + 0.0027j
$\mathcal{L}(\Theta_\mathrm{b})$	2.45	2.62 +1.00j	3.72 + 2.45j	8.28	3.72 – 2.45j	2.62 – 1.00j

Table A-5: Incréments de taux d'extraction de chaleur et temperature moyenne adimensionelle à la paroi des puits dans le domaine du temps

function	time [yr/12]					
	1	2	3	4	5	6
$\exp\big(\sigma(t-\Delta t)\big)$	1.00	2.05	4.19	8.59	17.58	36.00
q_1'	1.001	0.0067	0.0080	0.0072	0.0060	0.0050
q_2'	0.998	-0.0134	-0.0159	-0.0143	-0.0120	-0.0099
Θ_b	3.90	4.41	4.82	5.18	5.49	5.78

Table A-6: Taux d'extraction de chaleur pour un champ de 3 × 2 puits

function	Time [yr/12]					
	1	2	3	4	5	6
q_1	1.001	1.008	1.016	1.023	1.029	1.034
q_2	0.998	0.985	0.969	0.955	0.943	0.933